Stellar exotica in the field and globular clusters

Dissertation
zur
Erlangung des Doktorgrades (Dr. rer. nat.)
der
Mathematisch-Naturwissenschaftlichen Fakultät
der
Rheinischen Friedrich-Wilhelms-Universität Bonn

vorgelegt von
Santana Mansfield
aus
Bristol, UK

Bonn, 2024

Angefertigt mit Genehmigung der Mathematisch-Naturwissenschaftlichen Fakultät der Rheinischen Friedrich-Wilhelms-Universität Bonn

Gutachter/Betreuer: Prof. Dr. Pavel Kroupa
Gutachter: Prof. Dr. Karl Menten

Tag der Promotion: 29 August 2024
Erscheinungsjahr: 2024

"The stars are
long gone but
we can still
see their glow
long after they've
skidded off into oblivion"
– *Volbeat*

List of publications

This thesis consists of the following publications:

Far-ultraviolet investigation into the galactic globular cluster M30 (NGC 7099): I. Photometry and radial distributions
Santana Mansfield, Andrea Dieball, Pavel Kroupa, Christian Knigge, David R Zurek, Michael Shara, Knox S Long
Monthly Notices of the Royal Astronomical Society, Volume 511, Issue 3, April 2022
DOI: 10.1093/mnras/stac242, arXiv: 2202.04913 [astro-ph.SR]

Far-ultraviolet investigation into the galactic globular cluster M30 (NGC 7099): II. Potential X-ray counterparts and variable sources
Santana Mansfield, Andrea Dieball, Pavel Kroupa, Christian Knigge, David R. Zurek, Michael Shara, Knox S. Long
Monthly Notices of the Royal Astronomical Society, Volume 513, Issue 2, June 2022
DOI: 10.1093/mnras/stac1039, arXiv: 2204.09681 [astro-ph.SR]

A discontinuity in the luminosity-mass relation and fluctuations in the evolutionary tracks of low-mass and low-metallicity stars at the Gaia M-dwarf gap
Santana Mansfield, Pavel Kroupa
Astronomy & Astrophysics, Volume 650, A184, June 2021
DOI: 10.1051/0004-6361/202140536, arXiv: 2104.13951 [astro-ph.SR]

A discontinuity in the luminosity-mass relation and fluctuations in the evolutionary tracks of low-mass and low-metallicity stars at the Gaia M-dwarf gap (Corrigendum)
Santana Mansfield, Pavel Kroupa
Astronomy & Astrophysics, Volume 661, C1, May 2022
DOI: 10.1051/0004-6361/202140536e

The convective kissing instability in low-mass M-dwarf models: convective overshooting, semi-convection, luminosity functions, surface abundances and star cluster age dating
Santana Mansfield, Pavel Kroupa
Monthly Notices of the Royal Astronomical Society, Volume 525, Issue 4, August 2023
DOI: 10.1093/mnras/stad2587, arXiv: 2309.07523 [astro-ph.SR]

Abstract

Stellar exotica are unusual stars or binary systems which are distinctive due to variability in their brightness, or by their emission in the ultraviolet and X-ray wavelengths which indicate high energies. These stars and systems demonstrate some of the most ferocious physics known to astronomy, such as colliding stars, mass accretion and nova explosions. Some stellar exotica form due to the interactions between binary components, for example blue straggler (BS) stars, cataclysmic variables (CVs) and X-ray binaries. Others show fluctuations in their luminosities from instabilities in their interiors, such as RR Lyrae variables and M-dwarf stars undergoing the convective kissing instability (CKI). An understanding of how these stars defy the norm broadens our knowledge of stellar evolution, and the extreme physics taking place deepens our fascination of the profound and diverse universe.

This thesis explores these stars and systems by processing far-ultraviolet (FUV) exposures taken by the *Hubble Space Telescope* of the globular cluster M30, and computing models using Modules for Experiments in Stellar Astrophysics (`MESA`). The sources in M30 are catalogued and provided to the VizieR database at the Centre de Données astronomiques de Strasbourg (CDS). The blue and red sub-populations of the double BS sequence in M30 appear mixed in the ultraviolet, and the radial distribution of BS stars indicates that mass segregation has taken place, confirming that M30 is a core-collapsed cluster. Measuring the magnitudes over time reveal several sources demonstrating variability. One BS star is a known W-UMa contact binary and one of the gap objects is a known CV identified in this work to be experiencing a dwarf nova event. Two variable horizontal branch stars are previously known RR Lyrae variables of types RRab and RRc, and one is potentially a new RRab classification. Assessing stars in colour magnitude diagrams (CMDs) of different wavelengths identifies other interesting sources. Within the FUV field of view are ten known X-ray sources, to which six confident counterparts are made, consisting of two CVs, one RS CVn, one red giant with strong FUV emission and two sources only detected in the FUV.

A recent discovery in the CMD from the *Gaia* datasets has revealed a new type of stellar exotica: M-dwarf stars undergoing the CKI. To investigate this phenomenon, models are calculated with `MESA` using very fine mass increments and a maximum timestep. CKI stars experience repeated merging events of their convective core and envelope resulting in fluctuations in luminosity and temperature. This leads to a discontinuity in the luminosity-mass relation and loops in the evolutionary tracks which explains the low-density region of the M-dwarf gap. The CKI is reduced with increasing amounts of overshooting but sustained with semi-convection. The width of the MS decreases over time along with the difference in MS width between masses higher and lower than the CKI. The parallel offset between the upper and lower MS also change with time, providing a potential age-dating method for single stars and stellar populations.

Contents

Chapter 1

Introduction

1.1 Stellar evolution

In the night sky, we see an array of beautiful, twinkling stars of varying sizes, colours and brightnesses. Many of these stars evolve in a similar way and so when we notice differences between the stars, it is usually because they are in distinct stages of that evolution, with high-mass stars burning hot and fast, and low-mass stars burning slowly and at lower temperatures. We also notice stars which act in a peculiar way, shining very brightly or pulsating in brightness for example. These can usually be explained by binary systems consisting of two stars, where the interactions between them can vastly alter the single-star evolution process and result in exotic systems, such as one star transferring its mass to a compact companion. Other single stars at certain masses experience internal phenomena such as fluctuations which make them distinctive and exotic compared to other stars, although the processes involved do not ultimately deter the star from its evolutionary path. We take an interest in these strange stars as they demonstrate some of the most intense and extreme physics of the known universe. To begin, I will briefly detail the 'standard' single-star evolution and some example paths that may be taken by stars in binary systems. I will then describe the stellar exotica that are explored in this thesis.

1.1.1 Single-star evolution

Stars form from dense clouds of molecular gas that fall inwards due to gravity. As material is drawn in, the temperature rises and the pressure becomes greater, establishing dense balls of hot matter. The high temperatures and pressures at the center of these balls leads to large amounts of kinetic energy for the positively charged hydrogen nuclei, which allows them to move fast enough that they no longer repel one another and they collide. Energy is released as the ionised hydrogen nuclei (protons) fuse together into helium through a process known as the proton-proton I (pp-I) chain:

$$p + p \longrightarrow d + e^{+} + \nu_e \tag{1.1}$$
$$p + d \longrightarrow {}^{3}\mathrm{He} + \gamma \tag{1.2}$$
$${}^{3}\mathrm{He} + {}^{3}\mathrm{He} \longrightarrow {}^{4}\mathrm{He} + 2p \tag{1.3}$$

where two protons (p) combine to make deuterium (d) by releasing a positron (e^{+}) and an electron neutrino (ν_e). A helium (^{4}He) nucleus is formed with the release of a photon (γ) and via two ^{3}He nuclei (Iliadis 2015). Once this nuclear fusion begins, the star joins the main sequence (MS) on the Hertzsprung-Russell diagram (HRD, Fig. 1.1). The star is in a stable equilibrium state where the radiative pressure of the outmoving photons balances the gravitational force of the mass of the star pushing inwards. The star remains on the MS burning all the hydrogen atoms in its core into helium. Once the hydrogen runs out, the nuclear fusion process comes to a halt, the radiative pressure pushing outwards diminishes, and the star begins to collapse inwards under the immense force of gravity. This compresses the core, increasing the temperature and pressure until a shell of hydrogen surrounding the helium core begins to fuse hydrogen into helium (Lamers & Levesque 2017). Due to the increased temperature and pressure, more energy is produced than the previous core hydrogen burning, and so this shell burning can sustain the star again in equilibrium, however the increased outward radiation pressure causes the envelope to expand to satisfy the pressure gradient (Pols 2011). The star grows to a large radius, and since the surface spreads over a much larger area, it cools and the star becomes a red giant. As seen in Fig. 1.1, the star turns off from the MS on the HRD to lower temperatures but to brighter luminosities and travels along the red giant branch (RGB). This is also illustrated in Fig. 1.2 which shows the colour-magnitude diagram (CMD) of the globular cluster M30, demonstrating the evolution in observed data.

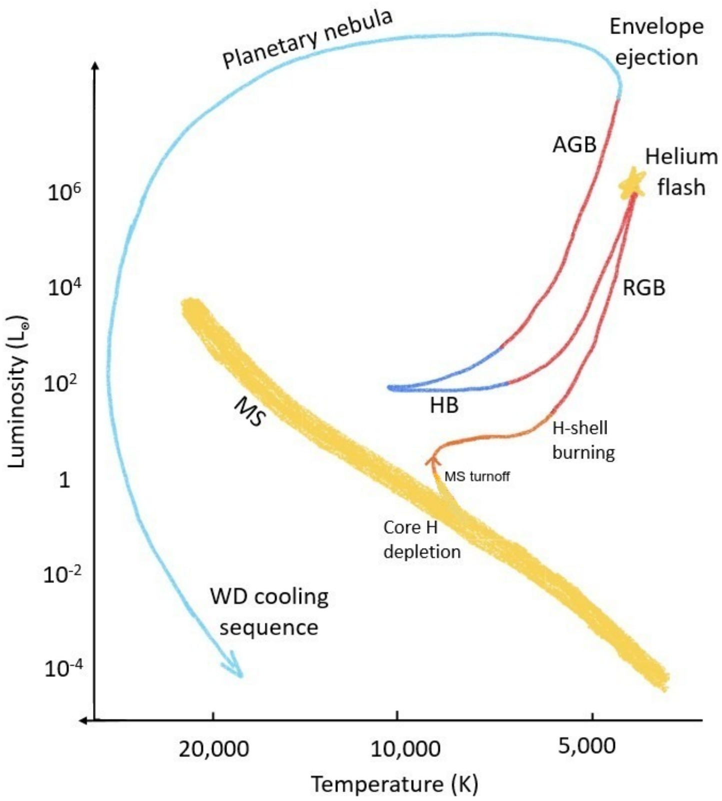

Figure 1.1: Hertzsprung-Russell diagram (HRD) showing an example evolution of a solar-mass single star through the main sequence (MS), red giant branch (RGB), horizontal branch (HB), asymptotic giant branch (AGB), planetary nebula and white dwarf (WD) stages. Note the inverse temperature on the x-axis, the hotter (bluer) stars are to the left and the cooler (redder) stars are to the right. Higher-mass stars are positioned at brighter luminosities and hotter temperatures on the MS (upper left) than lower-mass stars. (Credit: Self-drawn image).

Electrons must obey the Pauli exclusion principle (as they are fermions), meaning that no two electrons can occupy the same state (Pauli 1924). For stars with less mass than around 2.25 $M_\odot$ (Iben 1967), the material of the inert helium core is so dense that the electrons are pushed together until they occupy all the available energy states, known as electron degeneracy. As the higher energy states are filled with increasing temperature and pressure when the core is being crushed down into a smaller volume, the electrons gain large amounts of momentum (Iliadis 2015). This momentum creates an outwards pressure called electron degeneracy pressure which withstands the gravitational

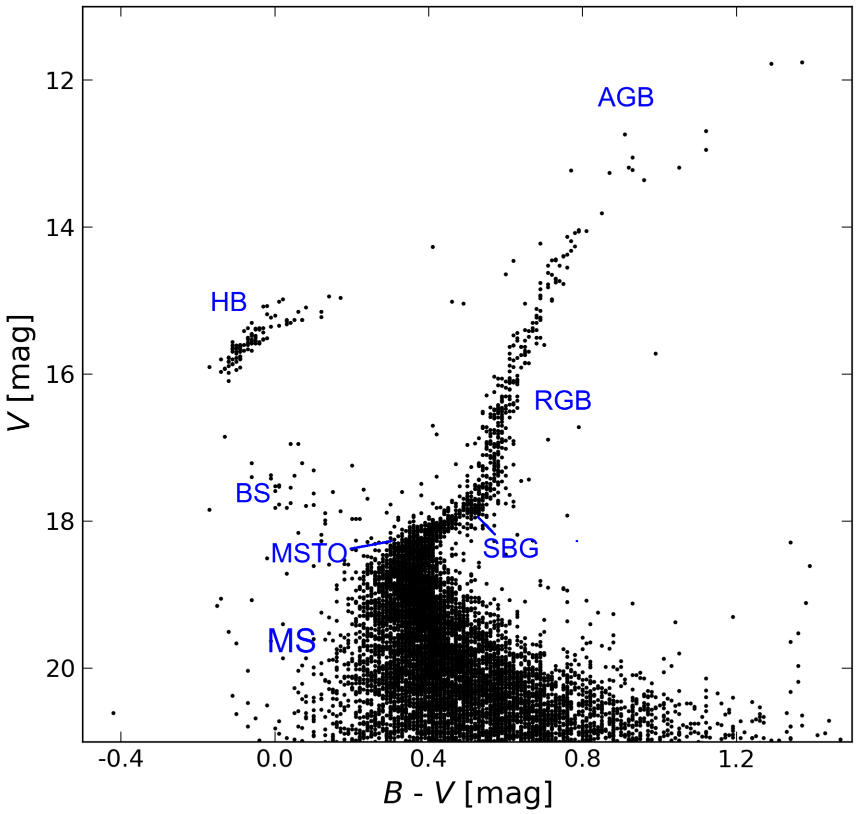

Figure 1.2: Colour-magnitude diagram (CMD) for the globular cluster M30 in the optical, with brightness on the y-axis measured in the visual V-magnitude and colour on the x-axis given as the difference between the B and V magnitudes. The colour represents temperature in the same way as the HRD in Fig. 1.1, with the hotter (blue) stars on the left and cooler (red) stars on the right. In addition to the stages given in Fig. 1.1 are the MS turnoff (TO), blue stragglers (BS) and the sub giant branch (SGB). As the stars in a globular cluster are born at roughly the same time, the CMD of a cluster gives an excellent depiction of the evolutionary steps of stars as we are able to see them as distinct populations. (Image created from the data in Chp. 2).

force. As the star continues hydrogen shell burning, the helium produced falls inward to the core and the increased mass adds to the pressure and temperature until the helium nuclei have enough kinetic energy to fuse into carbon and oxygen through the triple-α process:

$$^{4}\mathrm{He} + ^{4}\mathrm{He} \longrightarrow \; ^{8}\mathrm{Be} \tag{1.4}$$

$$^{8}\mathrm{Be} + ^{4}\mathrm{He} \longrightarrow \; ^{12}\mathrm{C} + 2\gamma \tag{1.5}$$

$$^{12}\mathrm{C} + ^{4}\mathrm{He} \longrightarrow \; ^{16}\mathrm{O} + \gamma \tag{1.6}$$

where two helium nuclei (^{4}He, alpha particles) form into beryllium (^{8}Be). Carbon (^{12}C) is formed with the addition of another helium nucleus and also oxygen (^{16}O) with a forth helium nucleus, whilst releasing photons (γ) (Iliadis 2015). The degenerate matter in the core is isothermal as energy cannot be released by electrons falling into already-occupied lower energy states. As such, once this helium burning begins in one part of the core, it quickly spreads across the entire core in thermonuclear runaway which is known as a helium flash (Schwarzschild & Härm 1962). The temperature in the core from the renewed nuclear fusion allows the core to expand out of its degenerative state, and for the envelope to contract (Iliadis 2015). The temperature of the surface increases due to the smaller surface area and the star moves blueward to higher temperatures in the HRD along the horizontal branch (HB). Stars with masses greater than 2.25 $M_{\odot}$ have a high enough core temperature to ignite helium before the material becomes degenerate and so core helium burning commences without a helium flash (Iben 1974; Iliadis 2015).

The star now continues hydrogen shell burning and core helium burning into carbon and oxygen until the helium in the core is depleted. The core contracts again under the pressure of gravity until it is hot enough to fuse carbon and oxygen nuclei. This requires greater temperatures than helium burning because carbon and oxygen nuclei have more protons which repel one another, and thus much higher temperatures and kinetic energies are needed for the nuclei to collide (Lamers & Levesque 2017). This is only possible however if the star has enough mass for the pressure of gravity to heat the core up to the required amount, which is not the case for our Sun. In this case, the temperatures are large enough to form a helium burning shell around an inert degenerate core which sustains the stars existence for slightly longer, but it also undergoes multiple helium flash phases (Schwarzschild & Härm 1965; Pols 2011). Similar to the red giant phase, the increase of radiation pressure forces the envelope to expand again and the star moves upward in the HRD (Fig. 1.1) to brighter luminosities and cooler surface temperatures along the asymptotic giant branch (AGB). The envelope of the star has reached such a large radius that the outer material has very low density with low surface gravities and can easily begin to be blown away by the radiation pressure coming from within (Iben 1974; Pols 2011). This is escalated by the repeated helium flashes that happen, producing runaway temperatures that cause thermal pulsations, increasing the outward pressure and mass loss (Iliadis 2015). Eventually the outer layers of the star are shed, leaving behind the hot bright remnant of the core which emits in ultraviolet radiation, ionising the surrounding clouds of ejected material and creating a glowing planetary nebula (Paczyński 1971; Iben 1995). This material will only glow for a while before expanding away and dimming so all that remains of our star is the degenerate core, a white dwarf (WD, Iben 1974). As the WD is degenerate, it is isothermal, and therefore cools down very slowly, only releasing heat from its thin outer surface where the material is not degenerate. In the HRD, WDs follow a downward motion towards lower magnitudes as they cool and dim, known as the WD cooling sequence. They can last in this state for billions of years, eventually dimming into hard cold objects.

If a star has enough mass to sufficiently raise the core temperature for each possible burning stage, it will continue until it produces iron. Carbon is burnt to produce oxygen, neon and magnesium. Neon photo-disintegrates (by absorbing a high energy gamma photon) into an oxygen and helium nucleus, the latter of which is captured by another neon nucleus to produce magnesium (Pols 2011). Then oxygen burning into sulphur and silicon, and finally silicon burning into iron. Each burning stage requires a higher core temperature to overcome the binding energy of the elements, which increases with atomic mass. This means that each stage occurs on a shorter timescale than the previous one, as the fuel is burnt more quickly with higher intensity. For example, Woosley et al. (2002) calculated that a 15 $M_{\odot}$ star burns hydrogen on the MS for approximately 11 million years, helium for two million years, carbon for two thousand years, neon for half a year, oxygen for two years (slightly longer than neon burning because of the higher amount of oxygen in a star) and silicon for 18 days. Once iron starts being produced in the star, its end is very near. The temperature and pressure in the core is so great that high-energy gamma photons are absorbed by the iron nuclei which photo-disintegrates into several helium nuclei and neutrinos (Iliadis 2015). This reaction absorbs energy and so reduces the available radiation pressure needed to support the core against collapse. As the core begins to contract, the electron degeneracy pressure pushes back, but it can only withstand mass up to a certain limit, called the Chandrasekhar mass limit of approximately 1.4 $M_{\odot}$ (Chandrasekhar 1961). When the infalling mass of a collapsing massive star becomes greater than this limit at the core, the electrons combine with protons into neutrons in a process called neutronisation, removing the number of electrons needed to sustain the degeneracy pressure (Iliadis 2015). Collapse happens in near free-fall until the density is great enough for neutron degeneracy and the core becomes one large neutron nucleus (Y Potekhin 2010). When the rest of the star comes crashing down onto the core, the neutron degeneracy pressure

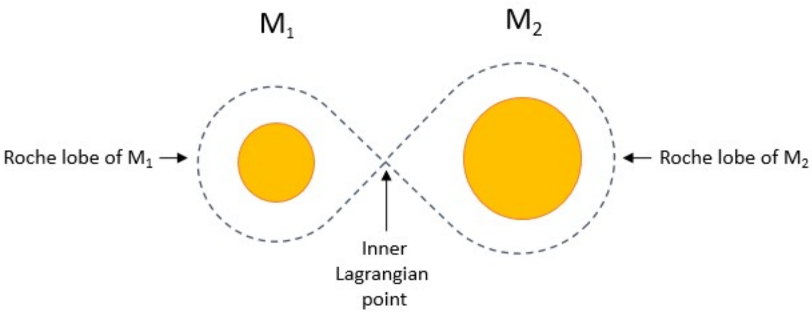

Figure 1.3: A binary system showing the equipotential distance of two stars with masses M_1 and M_2, known as the Roche lobe. (Credit: Self-drawn image)

forces the material to bounce back, sending a shock wave through the stellar material and blasting outwards in a supernova which can outshine the other stars in its host galaxy for months (Pols 2011). Except for the most massive stars, the remnant left behind is a neutron star (NS), where the matter is now extremely dense and the NS exists in a tiny volume. As degeneracy is isothermal, an increase of heat does not increase the pressure, instead it increases only by mass (Iliadis 2015). Thus when more mass is added, the pressure pulls the particles together and so the star becomes more compressed into a tighter volume (Y Potekhin 2010). As such, a NS is much smaller in size than a WD, even though its mass is higher.

Black holes are another possible outcome of a star core collapse, reserved for the most massive of stars. Similarly to how the more massive neutron stars overcome the electron degeneracy to form denser and more compact objects than WDs, if the mass is great enough, the pressure of the infalling material overcomes the neutron degeneracy pressure and crushes the material into an even denser state. Unfortunately, as the escape velocity of this object becomes faster than the speed of light, any information about the state of this matter or object cannot be known to us, and it is called a black hole. We still have yet to determine the nature of these objects, however we could estimate that a similar step occurs that we see from electron to neutron degeneracy, which is due to the higher mass of the initial star and thus the greater pressures and temperatures of the collapsing core. Therefore a black hole is likely to be an unfathomably dense and tightly tiny object of crushed stellar material.

1.1.2 Binary evolution

Outlined above is a basic representation of the 'standard' evolution of a single star, however interactions with a companion star in a binary or multiple system can mean very different final outcomes for their constituents. Illustrated in Fig. 1.4 are example evolutionary paths for a binary system with low or intermediate mass components. Binary systems are common in the Galactic field, with a $\approx 50\%$ binary fraction in the solar neighbourhood (Duquennoy & Mayor 1991; Fischer & Marcy 1992). In high density star clusters such as globular clusters (GCs), the fraction is much less ($\lesssim$10%, Ivanova et al. 2005) due to the dynamical interactions with nearby cluster members.

A binary system is subject to the Roche lobe (named after Edouard Roche 1850), which is the point at which the gravitational potential of each star is equal to the other star (Fig. 1.3). As shown in step B1 in Fig. 1.4, if any material from one star (the donor), which can be the outer radius of the star itself or material in the form of a mass-loss-driven wind, reaches the Roche lobe, it will no longer be bound to that stars gravity, but instead fall towards the other star (the accretor) in Roche lobe overflow (RLOF, De Loore & Doom 1992). This mass transfer can happen gradually and evenly, or it can be volatile, as is the case if the accretor is a compact object such as a WD or NS. Then the transferring

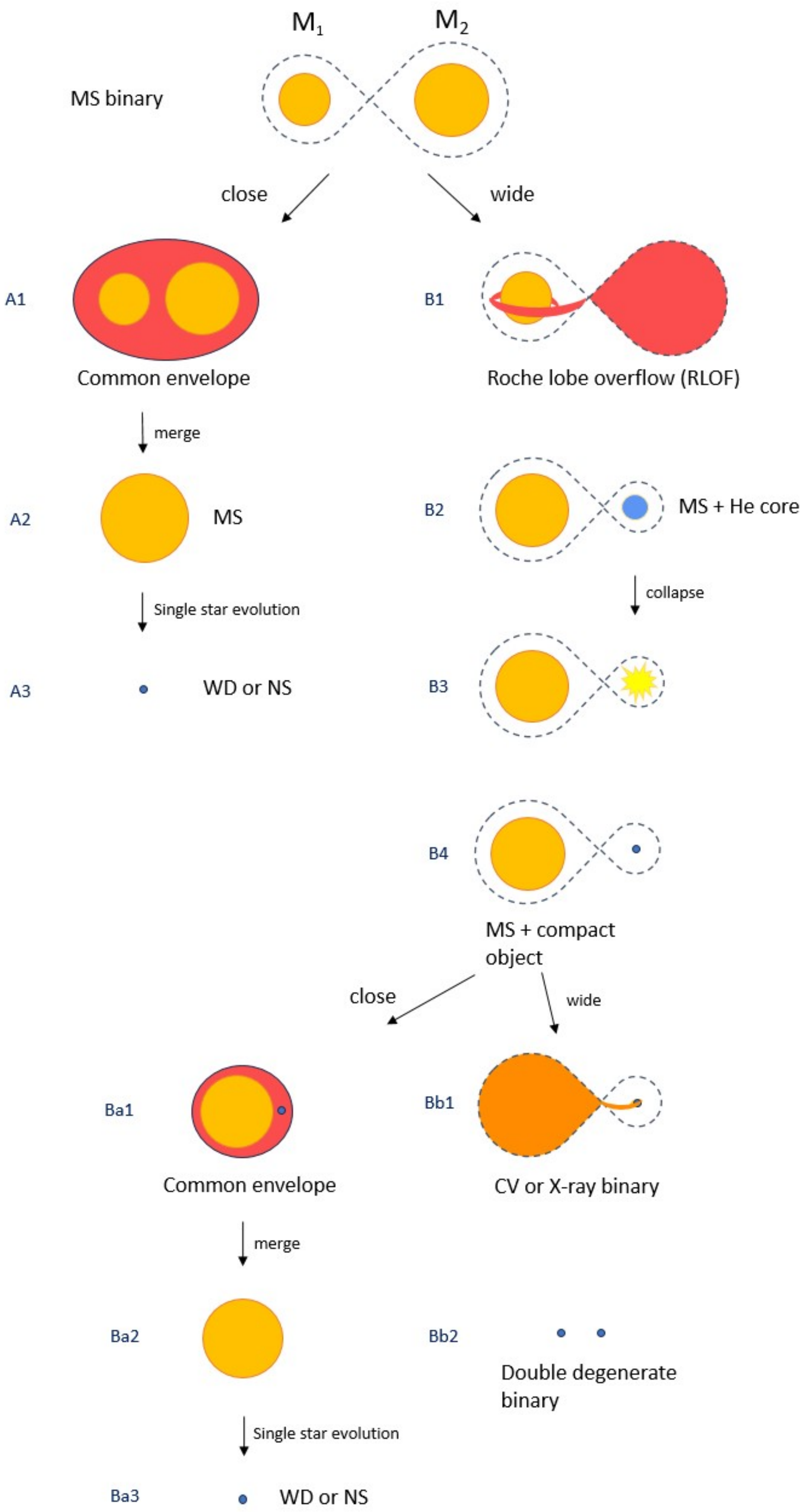

Figure 1.4: Flow chart depicting example evolutionary steps for stars of masses M_1 and M_2, with different paths if the stars orbit closely or have a wide distance. (Credit: Self-drawn image)

material spirals around the compact object in a hot accretion disk, and when it falls onto the surface of the accretor it heats up the point of impact. As the compact object is mostly degenerate matter and the heat cannot escape, thermonuclear runaway can occur and result in nova explosions on the surface of the compact object (Lamers & Levesque 2017). Binary systems with a WD where this is happening are called cataclysmic variables (CVs) and are discussed in Sect. 1.2.3 and depicted in step Bb1 in Fig. 1.4. A CV system may be created from a star capturing a WD in its gravitational pull, or it could have been two MS stars in which the higher mass one evolves faster into a WD, and then the lower mass star evolving to expand its envelope so it fills the Roche lobe, for example (De Loore & Doom 1992). If the compact object is instead a neutron star or a black hole, the binary system is called an X-ray binary as they emit strongly in X-rays, and are discussed in Sect. 1.2.4.

Another interesting binary process is when two stars pull each other close enough that they merge into one star. This may happen quickly in the case of a collision, but also slowly by one star filling its Roche lobe in such close enough proximity to the other star that it engulfs it. Then the cores of both stars continue to orbit one another in a common envelope (Paczynski 1976; Lamers & Levesque 2017) as depicted in step A1 in Fig. 1.4. This can also occur in a binary system with a larger orbital distance if both stars evolve at similar times. Then both stars fill their respective Roche lobes and gravity pulls them together to become a contact binary. Eventually in both cases, the cores will merge together and unless a large portion of the outer common envelope was lost from the system, the result will be a more massive star with renewed fuel for burning at its core (De Loore & Doom 1992). If this happens between two MS stars, then the resulting star appears at a higher position in the CMD, and if it is higher than the MS turnoff of a cluster, then it is called a blue straggler (BS), which is described in Sect. 1.2.1. Contact binaries and binary systems in which one of the stars has reached a higher mass from mass transfer may also appear in the BS region of the CMD.

1.2 Stellar exotica

Stellar exotica are unusual stars or binary systems that exhibit observational phenomena such as magnitude variability, which distinguishes them from stars with similar initial mass and metallicity that follow the 'standard' process of stellar evolution. These exotic objects occur due to particular aspects of their evolution, for example from instabilities in their energy transport processes if they are single stars, or from the influence of interactions with a companion star. These mechanisms affect the luminosities produced by the star or binary pair which allow us to detect them.

Some of the stellar exotica discussed in detail in this thesis that formed from interactions in a binary system are BS stars, CVs, and X-ray binaries. Stellar exotica in the form of single stars that exhibit peculiar processes and variability are RR Lyrae stars, and M-dwarf stars undergoing the convective kissing instability (CKI stars), and will be detailed below. Other stellar exotica briefly mentioned in this thesis are contact binaries and RS Canum Venaticorum (CVn) variables, which are close binary systems where the luminosity fluctuates due to chromospheric activity, resulting in large stellar spots. Stellar exotica could be formed in any part of the Galactic field, but an excellent place to detect them is in star clusters, as these are optimal laboratories for stellar evolution due to the stars forming under the same initial conditions, as seen in Fig. 1.2. In this thesis, I investigate the globular cluster M30 (NGC 7099, Fig. 1.5) and discuss the stellar exotica detected. In this work, this is especially credited to the use of ultraviolet bandpasses, as many of these objects emit at these wavelengths due to the high temperatures that result from mass transfer. As CKI stars are low-mass M-dwarfs, they have yet to be detected in such clusters since they do not experience very high temperatures, and thus are too faint in the ultraviolet to be seen. Instead they have been detected in the solar neighbourhood and in the field in CMDs from the *Gaia* Data Release 2 (Jao et al. 2018) and early Data Release 3 (Gaia

Collaboration, et al. 2021), as described in Sect. 1.2.5. In this thesis, I compute stellar evolution models using Modules for Experiments in Stellar Astrophysics (MESA, Paxton et al. 2011, 2013, 2015, 2018, 2019) to investigate these recently found unusual stars.

The CMD and the parallel HRD are the primary, fundamental and indispensable tools that have been used throughout the history of stellar research and detection. By comparing the relative positions of a source in CMDs of different colours, we can gain insights into their nature, e.g. strong ultraviolet emission indicates a very high temperature, such as material from a donor star falling onto the surface of a companion. Therefore, utilising these diagrams allows us to determine the steps in stellar evolution and also expose objects that seem to defy that evolution, the stellar exotica.

1.2.1 Blue straggler stars

In a star cluster, where stars are born at roughly the same time, the higher mass stars burn through their hydrogen supply at a faster rate in order to withstand their higher inward gravitational forces, and so they evolve away from the MS earlier than the lower mass stars. We see this in the MS turnoff (Fig. 1.2), where the higher mass stars have evolved to later stages and the lower mass ones are still hydrogen burning. Over time, as more stars evolve away from the MS, the turnoff moves downward in the CMD. Blue straggler (BS) stars are detected because they appear higher than the MS turnoff (Fig. 1.2), giving the impression that they were left behind. This is because the BS stars have gained mass either by a collision with another star or after mass transfer from a companion, as described in Sect. 1.1.2. They are still hydrogen burning and so they remain on the MS but at the position of an initially higher mass star, and as such appear above the MS turnoff.

BS stars were first described by Burbidge & Sandage (1958) after they were detected in the CMD of globular clusters M67 and NGC 7789. Our current understanding is that BS stars are present in most, if not all, globular clusters (Davies et al. 2004), many open clusters (Ahumada & Lapasset 1995) and can also be found in the field by comparing to stars in the galactic halo (Casagrande 2020). In M30, BS stars were originally detected by Guhathakurta et al. (1998), and reported by Ferraro et al. (2009) to be in two distinct BS sequences in the $V - I$ CMD, with the blue BS sequence forming from collisions (Sills et al. 2009), and the red BS sequence as a result of mass transfer (Xin et al. 2015).

Since they have additional mass from either mass transfer or collisions, BS stars are the most massive type of star within a GC. Due to the dense neighbourhood within the center of a cluster, the BS stars can play a role in the dynamical evolution of the cluster (Bailyn 1995). Aside from interactions with other stars in the crowded central region, the heaviest members of the cluster (the BS stars) will tend to drift inwards over time. This results in a segregation of mass, with more stellar mass found in the center of the cluster compared to further out. Once this occurs, the cluster is said to be core-collapsed, which typically is seen in very old clusters, where time has allowed this to take place. We can use the radial distribution of BS stars to determine the dynamical state of the cluster by seeing whether they are more centrally located relative to the other populations.

1.2.2 RR Lyrae

RR Lyrae stars were known as 'cluster variables' at the turn of the 19th century, as at the time they were only found in globular clusters (Bailey 1902). After one variable star designated 'RR Lyrae' was detected in the field by Mrs W. Flemming (Pickering 1903) and found to have similar variability to cluster variables, these stars became known as RR Lyrae variables (Smith 1995). Today RR Lyrae variables are well represented throughout the sky in globular clusters, the Galactic field and nearby dwarf galaxies. A total of 270 905 RR Lyrae stars were found in the *Gaia* DR3 dataset, 200 294 of which were already known (Clementini, G. et al. 2023). At the beginning of the investigation for this thesis, seven RR Lyrae variables were previously identified in M30 in the optical and infrared (Pietrukowicz & Kaluzny 2004; Kains, N. et al. 2013).

RR Lyrae variables are single HB stars that radially pulsate due to the κ-mechanism (Good 2003). Compression of stellar material usually results in a rise of temperature, and correspondingly a decrease of opacity, in order to release the thermal energy. However, if the opacity instead increases (which for RR Lyrae stars is due to the ionisation of helium, Maeder 2009), the compression is pushed back by the higher opacity, restraining the additional energy. Then pulsations occur where the thermal energy pushes outward and the compression pushes inward. These repeated pulsations result in fluctuations in the stars luminosity that can be observed by measuring the light curves. Depending on the shape and duration of these light curves, RR Lyrae stars are classified into different types: RRab have steep asymmetrical light curves with typical periods of 12-20 hours, whereas RRc have shorter sinusoidal light curves of 8 - 10 hours (Bailey 1902; Smith 1995).

1.2.3 Cataclysmic variables

A cataclysmic variable (CV) is a binary system composed of a WD that is accreting material from a companion star (Knigge et al. 2011). The material orbits around the WD in an accretion disc which reaches high temperatures and emits in the ultraviolet before falling inwards. As the material crashes down onto the surface of the degenerate WD, even higher temperatures are reached due to thermonuclear runaway at the impact site, resulting in nova explosions that emit strongly in the ultraviolet and in X-rays (Lamers & Levesque 2017). These volatile and erratic dwarf nova events can also observed in the optical, which is how CVs were first detected: as variable sources which undergo fluctuations in a 'cataclysmic' manner.

CVs are difficult to detect in globular clusters in the optical as at these wavelengths they are indistinguishable from the abundant MS stars, unless variability and spectroscopy can be measured. Because of this, CVs in star clusters have only been discovered in the recent years (compared to BS stars which stand out from MS stars in the optical), with the first confirmed CV in the cluster M5 (Margon et al. 1981). Many CVs have since been found in other globular clusters including 47 Tuc (Knigge et al. 2008; Beccari et al. 2013; Rivera Sandoval et al. 2018), NGC 2808 (Servillat, M. et al. 2008), NCG 6397 (Grindlay et al. 1995), NCG 6624 (Deutsch et al. 1999), NGC 6752 (Pooley et al. 2002; Thomson et al. 2012), M15 (Dieball et al. 2007), M71 (Huang et al. 2010), M80 (Dieball et al. 2010), M92 (Lu et al. 2011) and ω Cen (Cool et al. 2013). Spectroscopy can help identify CVs, for example, in the optical, CVs exhibit distinct H Balmer emission lines, particularly Hα and Hβ, due to the hot accretion disc and the infall of material onto the WD surface (Sarty & Wu 2006). Using X-ray wavelengths, Lugger et al. (2007) and Zhao et al. (2020) propose two and seven CV candidates in M30 respectively. In ultraviolet wavelengths, the higher energy emission of the mass transfer pushes CVs bluewards of the MS in the CMD, into the gap between the MS and the WD cooling sequence. Sources located in this region are known as gap objects and many of these are likely to be CVs. Thus observing globular clusters such as M30 using ultraviolet wavelengths will provide a valuable method of efficiently detecting CVs.

1.2.4 X-ray binaries

Another type of exotic binary system that can be found in the gap region of an ultraviolet CMD are X-ray binaries. These are similar to CVs expect that the primary accretor is a neutron star or a black hole. Due to the small size of the compact object, the accreting material and infall onto the surface emits mostly in X-rays. As they can emit high intensity X-ray radiation, X-ray binaries have been known to be present in star clusters since their first detection by Giacconi et al. (1974).

X-ray binaries can be classified into several subgroups (Lewin et al. 1997). A low-mass X-ray binary (LMXB) has a donor star with lower mass than the compact accretor. Due to the low-mass companion, LMXBs are typically very faint in optical wavelengths, emitting most of their radiation as X-rays. One LMXB in a quiescent state (qLMXB) has been detected in M30 (Lugger et al. 2007). X-ray bursters are LMXBs that experience novae explosions at their surface due to the thermonuclear runaway under the infall of material, similar to CVs (Lewin et al. 1997). High-mass X-ray binaries (HMXBs) contain a massive accreting star which is detectable in the optical. For a pulsar, hot accreting material from the companion star is blasted away from a magnetic neutron star by magnetic fields which are strongest at the poles (Y Potekhin 2010). The temperature at the surface of these outflows are great enough to emit in X-rays. As the neutron star rotates, we observe these outflows as repeated pulses of X-ray radiation. If the neutron star spins extremely quickly, which occurs from the infall of material adding to the angular momentum of the compact object, the period of pulses may be as short as milliseconds, making these objects known as millisecond pulsars (MSP). Two MSPs have been detected in M30 (Ransom et al. 2004).

1.2.5 CKI stars

The final type of stellar exotica discussed in this thesis are single M-dwarf stars undergoing the convective kissing instability (CKI). As these stars are a relatively recent discovery, a significant portion of this thesis will concentrate on these stars.

The convective kissing instability occurs at the mass boundary (≈ 0.35 $M_{\odot}$) between fully convective stars and stars with radiative cores and convective envelopes. It was first described by van Saders & Pinsonneault (2012) however it was not seen in observations until recently. Due to the production of helium in the core during the MS and the convection criterion (fully explained in Chapter 5), a convective region grows within the radiative core until it merges with the convective envelope. A moment of full convection occurs, during which the ^{3}He-rich material in the core is mixed throughout the star, luminosity decreases and temperature rises allowing the core material to revert back to a radiative state. The process repeats, continuously merging together the convective core and envelope (hence 'kissing' instability), from a constant unbalancing of the convection criterion. With each merger, less ^{3}He is needed before equilibrium abundance is reached and so the amplitude of the CKI is dampened over time. Eventually, the luminosity of the star is great enough to maintain the star in a fully convective state for the remainder of the MS.

The observational outcome of this phenomenon are fluctuations in the luminosity and temperature of the star. Plotting these in a HRD show that models of these stars undergo loops in their evolutionary tracks, which was not seen before the work presented in this thesis. When there are many stars of slightly different masses and metallicities experiencing these fluctuations, they result in a region of the CMD which contains fewer stars, as the stars are moving around in loops in this region. This lower density region was discovered in the *Gaia* DR2 data by Jao et al. (2018) as the M-dwarf gap, and was later confirmed to also be present in the eDR3 data (Gaia Collaboration, et al. 2021).

The CMD and HRD are once again fundamental and integral tools in first detecting and now investigating these new CKI stars. The movements of stellar models within the CMD, as well as the morphology of the MS of cluster populations of M-dwarfs, will provide significant knowledge that is paramount to our understanding of these exotica.

1.3 This thesis

The work done for this thesis includes the processing of observational ultraviolet data on the globular cluster M30 and reporting on the stellar populations and exotica found within it, including BS stars, RR Lyrae, CVs and probable counterparts to X-ray sources. As M30 is at a great distance from us, CKI stars are too faint to be detected in this dataset, thus for the remainder of this thesis I compute theoretical simulations of M-dwarf stars undergoing the CKI, and consider the consequences that should be seen observationally, including MS morphology and potential age-dating methods for single stars and clusters.

1.3.1 Stellar populations in M30

In chapter 2, we perform the photometry on the ultraviolet *Hubble Space Telescope (HST)* data of M30 (program GO-10561; PI: Dieball). M30 is a metal-poor globular cluster found in the Galactic halo, 8.3 ± 0.2 kpc away from us (Kains, N. et al. 2013). With an estimated age of 13.0 ± 0.1 Gyr, mass segregation has already occurred, establishing M30 as a core-collapsed cluster with a high central density of 10^6 $M_\odot$ pc^{-3} (Lugger et al. 2007). M30 has been studied in the optical, infrared and X-ray wavelengths, but analysis in the ultraviolet, which would enable us to detect any optically-faint hot exotic objects, was lacking.

To achieve this, photometry is performed on far-ultraviolet (FUV) *HST* Advanced Camera for Surveys (ACS) exposures taken with the F150LP filter, and mid-ultraviolet (UV) *HST* Wide Field Planetary Camera 2 (WFPC2) exposures with the F300W filter. A master image is first created for each set of exposures, which realigns the individual images in order to account for the small shifts in position due to guide star re-acquisition and the thermal breathing of the telescope. Sky subtraction, drizzling and cosmic ray removal (for the WFPC2 exposures) are also performed when creating the final combined master image.

The potential sources in the master images are detected by a combination of computational software and also from manually checking the images. Aperture photometry is carried out on the source positions which determines the intensity of the source flux that can then be converted into a magnitude. Once the sources are attained in each wavelength, the coordinates of one set of sources are transferred into the reference frame of the other set. This is because the two sets of exposures were taken with two different cameras and two distinct fields of view. Reference stars that can be identified in both images are used to transform the coordinates. The positions of the sources are compared in the single frame to find objects that are detected in both wavelengths, and then the two magnitudes can be used to create the CMD. The identified sources and their magnitudes are reported in a catalogue to the VizieR database at the Centre de Données astronomiques de Strasbourg (CDS).

We find 1218 MS stars, 185 red giants, 47 BS stars, 41 HB stars and 78 WD/Gap objects. Comparing the positions of the sources in the ultraviolet and visual wavelengths, the WD/Gap objects appear mixed within the MS of the optical CMD. This demonstrates the importance of the CMD in identifying different types of stars using different wavelengths, and also specifically the ability for us to detect sources such as CVs (which are found in the gap region) using the ultraviolet.

A Kolmogorov–Smirnov (KS) test indicates that the BS stars evolved by a different means than the other populations which evolve by single-star evolution, i.e. either from a collision or by mass transfer. We compare the positions in the $FUV - UV$ CMD of the blue and red BS stars of the double BS sequence and find that in the ultraviolet it is difficult to distinguish the two sequences. This is due to the stars on the red BS sequence being binary systems undergoing mass transfer, the high energy of which emits in the far-ultraviolet, resulting in these sources being blue-shifted in the CMD towards the

Figure 1.5: Hubble ACS image of M30, taken Dec 2009, credit NASA/ESA

blue BS stars. The blue BS stars are single stars produced after a merger of two lower-mass MS stars. They shine brighter in the ultraviolet than the MS due to their higher mass, but are not experiencing any mass transfer so their position in the CMD remains in line with the MS.

We also confirm that mass segregation has occurred in the cluster by comparing the radial distributions of the BS stars to the other populations to demonstrate evidence of dynamical evolution. We find that the higher-mass BS stars have a larger central concentration than the other populations, showing that they have fallen inwards over time. We also find a deficiency of HB stars and CVs in the center.

For this publication, I performed the photometry on the exposures under the guidance of Andrea Dieball, produced the catalogue, analysed the data, compared the results to the optical dataset, performed the KS test, prepared the visual plots, interpreted the findings in discussions with all of the co-authors, and wrote the manuscript.

1.3.2 Variables and X-ray counterparts in M30

In chapter 3, we compare the positions of known X-ray sources to the ultraviolet catalogue created in chapter 2, in order to identify any potential counterparts. Currently there are 23 X-ray sources detected in M30 (Lugger et al. 2007; Zhao et al. 2020), with 10 of these residing in the *FUV* field of view, including a milli-second pulsar (MSP). After applying a coordinate transformation using a reference star, several of the ultraviolet sources fall within the positional 95% error radii of the X-ray sources. An examination is then performed on the characteristics of the potential counterparts, including comparisons with their positions in an optical CMD, in order to narrow down the possibility of one of them being the counterpart to the X-ray source. Also taken into account is the number of possible chance coincidences and cluster membership probability.

We also perform a variability study in chapter 3 by identifying the variable sources using the standard deviation of their magnitudes, and producing light curves and periodograms. As these require data over a period of time, photometry is carried out on each of the 64 individual *FUV* exposures taken by the ACS. Since the intensity of the flux is likely to change from each individual exposure to the next due to instrumental effects, even for stars with very little variability, plotting the standard deviation over the mean *FUV* magnitude can distinguish which sources truly show significant variability. Lomb-Scargle periodograms (Lomb 1976; Scargle 1982) can estimate the period from folded light curves which is then used to determine the type of variable object. Several sources are found to be variable in M30: seven BS stars, four HB stars, seven red giants, several MS stars, four gap objects, and three sources only detected in the *FUV* with no *UV* counterparts.

One of the variable BS stars is a known contact W-UMa binary, which as described in Sect. 1.1.2, is where the orbits of two stars have come so close that the envelopes of the stars are touching. The stars will continue to orbit one another, coming close enough to share a common envelope, and eventually their cores will merge, producing a new higher mass star.

The light curves of three of the four variable HB stars indicate that they are RR Lyrae variables, with one being a new RRab identification. The light curve of one of the variable gap objects shows it to be experiencing a dwarf nova event. As described in Sect. 1.2.3, a dwarf nova occurs when hot material falling onto the surface of a WD experiences thermonuclear runaway and detonates. This indicates that this source is a CV, and we are able to show it shining brighter in the exposures that were taken.

Combining the characteristic examinations and the variability study, we are able to confidently identify six counterparts to the X-ray sources, although we did not find a companion to the MSP. The companion to X-ray source A2 has strong *FUV* emission, however appears in the optical CMD as a red giant. This is an interesting CV system with a red giant donor and shows again the value of investigating the CMD in different wavelengths in order to find stellar exotica. Two *FUV* sources which had no *UV* counterparts match to X-ray sources B and 6. The CV dwarf nova event corresponds in position to X-ray source C. Another CV found in the CMD gap region matches to source W15 and a further red giant to source W16. Despite the high relative proportion of MS stars in the central region of the cluster, three out of the ten X-ray sources match to red giants.

For this publication, I performed photometry on the individual exposures, created light curves, computed the periodograms, compared the ultraviolet results to the known X-ray sources by transforming the coordinates, and proposed candidate counterparts considering the chance coincidences, positional error radii and variability. I then prepared the visual plots and interpreted the findings in discussions with the co-authors to determine the confident matches, and wrote the manuscript.

1.3.3 The M-dwarf gap and convective kissing instability

In chapter 4, we investigate the recently discovered M-dwarf gap with the hypothesis that it is caused by the convective kissing instability (CKI) occurring in M-dwarf stars at the boundary ($\approx 0.35\ M_\odot$) where stars with lower masses are fully convective, and stars with higher masses have radiative cores and convective envelopes. In order to achieve this, we calculate stellar evolution models of M-dwarf stars using Modules for Experiments in Stellar Astrophysics (`MESA`, Paxton et al. 2011, 2013, 2015, 2018, 2019). `MESA` is an indispensable tool to simulate stellar evolution and has been continuously updated and advanced to ensure the most accurate representation of stellar physics. Until this work, previous models computed using other stellar evolution codes have found the CKI only occurring four to six times in models (Feiden et al. 2021). By using a small maximum timestep of 50 000 years, and a small mass increment for the models of $0.00025\ M_\odot$, we find the CKI to occur much more frequently in our models using `MESA`, and that the CKI produces loops in the HRD and a discontinuity in the luminosity-mass relation. The CKI was unseen in any `MESA` models previously because for the majority of stars, the MS is rather uneventful. As such, `MESA` is designed to perform calculations using large timesteps during the MS, in order to keep the computational time of a model to a minimum. Without setting a maximum timestep, the CKI is not present in models since the conditions for it are skipped over. Thus by setting a small timestep we are able to produce the CKI in models, even though they require a long computational time. Similarly, there was little reason to calculate models in such small mass increments at this particular mass range until the discovery of the M-dwarf gap. By now performing these models, great detail is found in the HRD with interesting differences between the models in this small mass range that was not seen before. We include sets of models with low metallicities, as the M-dwarf gap is more prominent at the blueward edge of the MS, where lower metallicity stars are found.

The CKI occurs from the delicate balance between temperature and luminosity in the convection criterion. With the production of ^{3}He in the core, the luminosity is increased, which makes the material in the core unstable to convection. As production continues, the core grows and we see the central ^{3}He abundance rise. When the core has grown to meet the convective envelope, they merge and the model becomes fully convective. Material is mixed throughout the model, and we see this as the central abundance fall, and the surface abundance increase, as ^{3}He makes its way to the surface. As ^{3}He is pulled out of the core, the nuclear production halts, luminosity decreases, and the convection criterion means that the material becomes radiative again. Nuclear production resumes and we see the central abundance of ^{3}He begin to rise. This continues until the luminosity becomes large enough to sustain the model in a fully convective state. The changes in surface abundances will be investigated in chapter 5.

As a consequence of the fluctuations in luminosity and temperature, from the models repeatedly switching from a fully convective state to a convective core and envelope separated by a radiative region, we find that loops are produced in the evolutionary tracks of the models in the HRD. The evolutionary track for models with lower masses has smaller loops, which occur earlier in the model lifetime compared to models with higher masses. The higher mass models undergo the instability for longer periods than the lower masses. A movie is included with this publication[1] which shows that as time progresses, the convective kissing instability moves to higher masses. Similarly, for models with lower metallicity, the CKI occurs at a higher mass range and for a longer time period than models with higher metallicity.

The fluctuations in luminosity result in a discontinuity in the luminosity–mass relation at this mass range. This is also shown in the published movie to move to higher masses over time. This discontinuity means that the luminosity-mass relation can no longer be differentiated, which has implications for the stellar mass function and luminosity function which depend on the slope of the luminosity-mass relation. The luminosity function will be addressed in chapter 5.

For this publication, I computed the models, analysed the results, prepared the visual plots and movie, interpreted the findings in discussions with the co-author, and wrote the manuscript.

In preparation for the work in chapter 5, I realised that the helium abundance that had been used in the models was set to $Y = 0.28$ instead of the metallicity-dependant value of $Y = 0.28 + 2Z$. I re-calculated the models and we published the correct mass ranges as a corrigendum. We found that the CKI occurs at slightly higher masses than initially reported and at a higher mass range for lower metallicity. Since $L \propto T^4/\kappa$ (Eq. 4.4), a decrease of opacity leads to an increase of luminosity. As such, low metallicity stars are brighter than high metallicity stars with the same mass (Kroupa & Tout 1997). Then, according to Eq. 4.4, the material at the core would remain convective at higher masses for lower metallicities. Higher temperatures (and therefore masses) are needed to overcome the larger luminosity for the material at the core to become radiative and for the CKI to begin.

1.3.4 Energy transfer in CKI stars and potential age dating methods

In chapter 5, we compute sets of `MESA` models representing CKI stars with varying amounts of overshooting and semi-convection, as these processes should have an influence on the energy transport mechanisms within M-dwarfs, and could effect the CKI and the M-dwarf gap seen in observations. Overshooting is the process where material does not have zero velocity when it reaches the convective boundary, and will continue to move a small distance past the boundary into the radiative region. Semi-convection is the slow mixing of material due to differences in density and molecular weight of the material to its surroundings. We look at both of these because they could alter the way the convective and radiative regions are formed and develop as well as the mixing processes within the models of CKI stars. We find that the intensity and amplitude of the CKI is reduced with increasing amounts of overshooting, but sustained when semi-convection is present. As it is reasonable to assume that stars have both overshooting and semi-convection, this provides a guideline for the amounts of these to use in future stellar modelling.

As seen in chapter 4, the surface abundances of ^{3}He are increased during the merging of the convective core and envelope, when the M-dwarfs are fully convective and mixing ^{3}He out from the core to the surface. In chapter 5, we investigate the surface abundances of various light elements including ^{3}He to see if the changes of these due to the CKI might be observable. We find that a drop in the surface abundances of ^{3}He and ^{4}He (and a rise of ^{1}H) from lower to higher masses occurs, and moves towards higher masses over time. However, the differences in the surface abundances are very small and are not likely to be seen in observations.

[1]https://www.aanda.org/articles/aa/olm/2021/06/aa40536-21/aa40536-21.html

We also compute synthetic populations of M-dwarfs and construct CMDs to see the CKI in the MS. We find that the CKI produces a large indent into the blueward edge of the MS where the models are undergoing the loops caused by the instability, as well as a slight over-density of models at masses just higher than the CKI. This instability region is more sparsely populated for models with higher amounts of overshooting, as for these models the CKI is suppressed. As seen in chapter 4, the mass–magnitude relation (or luminosity–mass relation) contains a discontinuity and is indifferentiable at the mass range of the CKI, which is one method of producing a stellar luminosity function (LF). Instead we can count the number of stars at each magnitude and create the LF. We find a small peak and dip in the LF due to the indent and over-density in the MS. We also compute a synthetic population representing both a globular cluster and Galactic-field populations, and compare the morphology of the MS in the CMD of these populations over time. As the duration of the CKI, and the time at which it begins, depends on mass and metallicity, the MS and the M-dwarf gap within it changes over time. The M-dwarf gap in the MS is much more pronounced in the early few Gyr, and is almost non-existent by 7 Gyr. The width of the MS for Galactic-field populations decreases with time, as well as the difference in width for masses higher and lower than the instability. There is a parallel offset in the direction of the MS, and a difference between the relative angle for globular clusters, for masses higher and lower than the instability, which also changes with time. We see the mass–magnitude relation and its derivative to also be time-dependent. This evolution of the MS provides a potential age-dating method to both star clusters and also single stars, if the metallicity and the location of a star in the CMD can be confidently known.

For this publication, I computed the models, constructed the synthetic population of stars, analysed the results, prepared the visual plots, interpreted the findings in discussions with the co-author, and wrote the manuscript.

Chapter 2

Far-ultraviolet investigation into the galactic globular cluster M30 (NGC 7099): I. Photometry and radial distributions

Santana Mansfield, Andrea Dieball, Pavel Kroupa, Christian Knigge, David R. Zurek, Michael Shara, Knox S. Long

Monthly Notices of the Royal Astronomical Society, Volume 511, Issue 3, April 2022

Abstract We present a far-ultraviolet (*FUV*) study of the globular cluster M30 (NGC 7099). The images were obtained using the Advanced Camera for Surveys (ACS/SBC, F150LP, *FUV*) and the Wide Field Planetary Camera 2 (WFPC2, F300W, *UV*) which were both on board the *Hubble Space Telescope (HST)*. The $FUV - UV$ colour-magnitude diagram (CMD) shows a main sequence (MS) turnoff at $FUV \approx 22$ mag and $FUV - UV \approx 3$ mag. The MS extends 4 mag below the turnoff, and a prominent horizontal branch (HB) and blue straggler (BS) sequence can be seen. A total of 1218 MS stars, 185 red giant branch stars, 47 BS stars and 41 HB stars are identified, along with 78 sources blueward of the MS which consist of white dwarfs (WDs) and objects in the gap between the WDs and the MS that include potential cataclysmic variable (CV) candidates. The radial distribution of the BS population is concentrated towards the cluster centre, indicating that mass segregation has occurred. The blue and red sub-populations of the double BS sequence appear mixed in the ultraviolet CMD, and no significant central concentration of CV candidates is seen in this cluster.

2.1 Introduction

Globular clusters (GCs) in our Milky Way are tightly bound groups of very old (> 10 Gyr) and metal-poor stars. They formed in the early Galaxy and can contain hundreds of thousands of stars, with extremely high stellar densities in the cores. At optical wavelengths, the luminosity of a GC is dominated by the large number of main sequence (MS) stars and evolved stars including red giant branch (RGB) stars and horizontal branch (HB) stars, as well as blue stragglers (BSs). White dwarfs (WDs), binaries such as cataclysmic variables (CVs; consisting of a WD accreting mass from a companion) and low-mass X-ray binaries (containing a neutron star or a black hole accreting material from a low-mass companion) are optically faint and are therefore not easily detected in the cores of GCs in the visual wavebands. The spectral energy distribution of these hot exotic objects usually peaks at far-ultraviolet (*FUV*) wavelengths, where MS stars and RGBs are faint. As a result, the core of a GC appears less crowded in the *FUV* and the exotic sources can be more easily detected and examined. Several cores of Galactic GCs have been studied in the far-ultraviolet, including M2 (Dalessandro et al. 2009), M15 (Dieball et al. 2007), M80 (Dieball et al. 2010; Thomson et al. 2010), NGC 1851 (Parise et al. 1994; Zurek et al. 2009; Maccarone et al. 2010; Zurek et al. 2016; Subramaniam et al. 2017), NGC 2808 (Brown et al. 2001; Dieball et al. 2005), NGC 5466 (Sahu et al. 2019), NGC 6397 (Dieball et al. 2017), NGC 6752 (Thomson et al. 2012), 47 Tuc (Knigge et al. 2000). Also M3, M13 and M79 (Dalessandro et al. 2013a), and the outskirts of GCs have been observed with the *Galaxy Evolution Explorer (GALEX)* survey of GCs (Dalessandro et al. 2012; Schiavon et al. 2012), and the *Swift Gamma-Ray Burst Mission* UVOT survey (Siegel et al. 2014, 2015).

We are able to probe deeper into GCs by detecting stellar populations that shine brightly in specific wavelengths, particularly those populations which formed by dynamical interactions. For example, blue stragglers appear to be on the MS above the turnoff point, although the clusters age indicates that they should have evolved away from the MS to become red giants. These sources likely have mass added by either mass transfer from a companion (McCrea 1964), or resulting from a direct collision (Hills & Day 1976), which adds hydrogen fuel to the core allowing these stars to remain on the MS for longer than they would have otherwise. The high density of stars in the cluster core allows frequent interactions resulting in various exotic sources such as BS stars, CVs, X-ray binaries and millisecond pulsars (MSPs, Shara & Hurley 2006; Hurley et al. 2007; Ivanova et al. 2006; Hong et al. 2016; Kremer et al. 2020). Detailed stellar-dynamical analyses can be found in Leigh et al. (2007, 2011, 2013, 2015); Chatterjee et al. (2010, 2013); Hypki & Giersz (2012); Wang et al. (2016); Belloni et al. (2017, 2018a,b); Belloni et al. (2020) and Rui et al. (2021). Binary systems are important for the dynamical evolution of the cluster (Heggie 1975; Hut et al. 1992), as the binding energy in the binary can be transferred to other stars in dense stellar systems, stabilising the cluster against deep core collapse (Hills 1975; Hurley & Shara 2012; Breen & Heggie 2013; Rodriguez et al. 2016), such that the initial binary population constitutes an essential aspect (Belloni et al. 2017). Thus, the detection of binary systems is important for our understanding of the dynamical state of the cluster.

M30 (NGC 7099) is a metal-poor globular cluster with a metallicity of [Fe/H] = –2.12 (Harris 1996). It is located 8.3 ± 0.2 kpc away from us in the Galactic halo and has an estimated age of 13.0 ± 0.1 Gyr (Kains, N. et al. 2013). M30 has a retrograde orbit with an average orbital eccentricity of $\langle e \rangle = 0.316$, average perigalactic and apogalactic distances of $\langle r_{min} \rangle = 3.94$ kpc and $\langle r_{max} \rangle = 7.58$ kpc respectively, and an average maximum distance from the Galactic plane of $\langle |z|_{max} \rangle = 4.95$ kpc (Allen et al. 2006, based on a nonaxisymmetric (barred) Galactic potential). M30 has a cluster mass of $\approx 1.6 \times 10^5$ $M_\odot$ and is core-collapsed: it has dynamically evolved so that the most massive stars have fallen inward and are concentrated towards the cluster core within a radius of only 1.9″ (0.08 pc, Sosin 1997). M30 has a very high central density ($\approx 10^6$ $M_\odot$ pc^{-3}, Lugger et al. 2007), indicating a high rate of stellar interactions and activity in the core region. This has resulted in a large bluer inward colour gradient,

Table 2.1: Log of the observation dates, the camera and filters used, and the total exposure times.

Camera	Filter	Data Set	Start Date	Exposure Time (s)
ACS/SBC	F150LP	J9HC02011	29 May 2007 16:45:50	5040
ACS/SBC	F150LP	J9HC04011	3 June 2007 11:51:14	5040
ACS/SBC	F150LP	J9HC04021	3 June 2007 15:01:42	2520
ACS/SBC	F150LP	J9HC06011	9 June 2007 02:10:34	7560
WFPC2	F300W	U9HC0301M-U9HC0308M	29 May 2007 19:58:16	4000
WFPC2	F300W	U9HC0501M-U9HC0508M	3 June 2007 16:39:16	4000
WFPC2	F300W	U9HC0701M-U9HC0708M	9 June 2007 07:00:16	4000

where the $B-V$ colour profile has a strong inclination towards bluer magnitudes in the centre, resulting from the infall of BS stars and a depletion of RGs from the core (Howell et al. 2000). Optical studies on M30 have yet to find a significant CV or WD population.

Based on the optical *Hubble Space Telescope (HST)* Wide Field Planetary Camera 2 (WFPC2) data, a significant BS population is observed in M30 (Guhathakurta et al. 1998), and Ferraro et al. (2009) suggest that these stars can be divided into two distinct blue straggler sequences in the $V-I$ colour-magnitude diagram (CMD). The blue BS sequence aligns with the zero-age main sequence (ZAMS) and the red sequence lies at a brighter magnitude of $\Delta V \approx 0.75$ mag. Isochrones from stellar evolution models representing collisions are found to lie along the blue BS sequence (Ferraro et al. 2009; Sills et al. 2009), and the red BSs populate a region that can be reproduced with models which undergo mass transfer (Xin et al. 2015). Portegies Zwart (2019) also produced stellar simulations and show that red BSs form by mass transfer at a constant rate over the cluster lifetime, whereas the blue BSs may have formed by mergers during a short burst of activity when the core of the cluster collapsed roughly 3.2 Gyr ago. The burst of activity would have resulted from the increased likelihood for interactions between stars due to the collapsing cluster core. It remains unknown however why the two sequences are parallel and why the red sequence is ≈ 0.75 mag brighter than the blue one. Double BS sequences have also been detected in NGC 362 (Dalessandro et al. 2013b) and NGC 1261 (Simunovic et al. 2014).

This first work in our study of M30 aims at analysing *HST FUV* and *UV* data using photometry, and providing an ultraviolet CMD and an analysis of the radial distributions of the different stellar populations. The observations and data reduction are described for each filter in Sect. 3.2 and the *FUV* − *UV* CMD is presented in Sect. 5.6. The optical counterpart matching is given in Sect. 2.4, and radial distribution analysis in Sect. 2.5, followed by a summary in Sect. 3.5. A following publication in this study will include potential counterparts to known X-ray sources and an investigation into the variable sources in M30.

2.2 Observations and image processing

2.2.1 The ACS *FUV* data

The FUV data were obtained with the Advanced Camera for Surveys (ACS) on board the *HST*, using the Solar Blind Channel (SBC) and F150LP filter (program GO-10561; PI: Dieball), in 15 orbits distributed over three visits, from the 29th May to the 9th June 2007. The SBC has a field of view of $34.6'' \times 30.8''$ and a pixel scale of $0.034'' \times 0.030''$ pixel^{-1}. Sixty-four images were taken, each with an exposure time of 315 s, resulting in a total exposure time of 20160 s, and are described in Table 2.1. Thermal breathing during the 96 minute day-night cycle of the *HST* for each visit, as well as guide star re-acquisition, can create small shifts between the individual images taken at

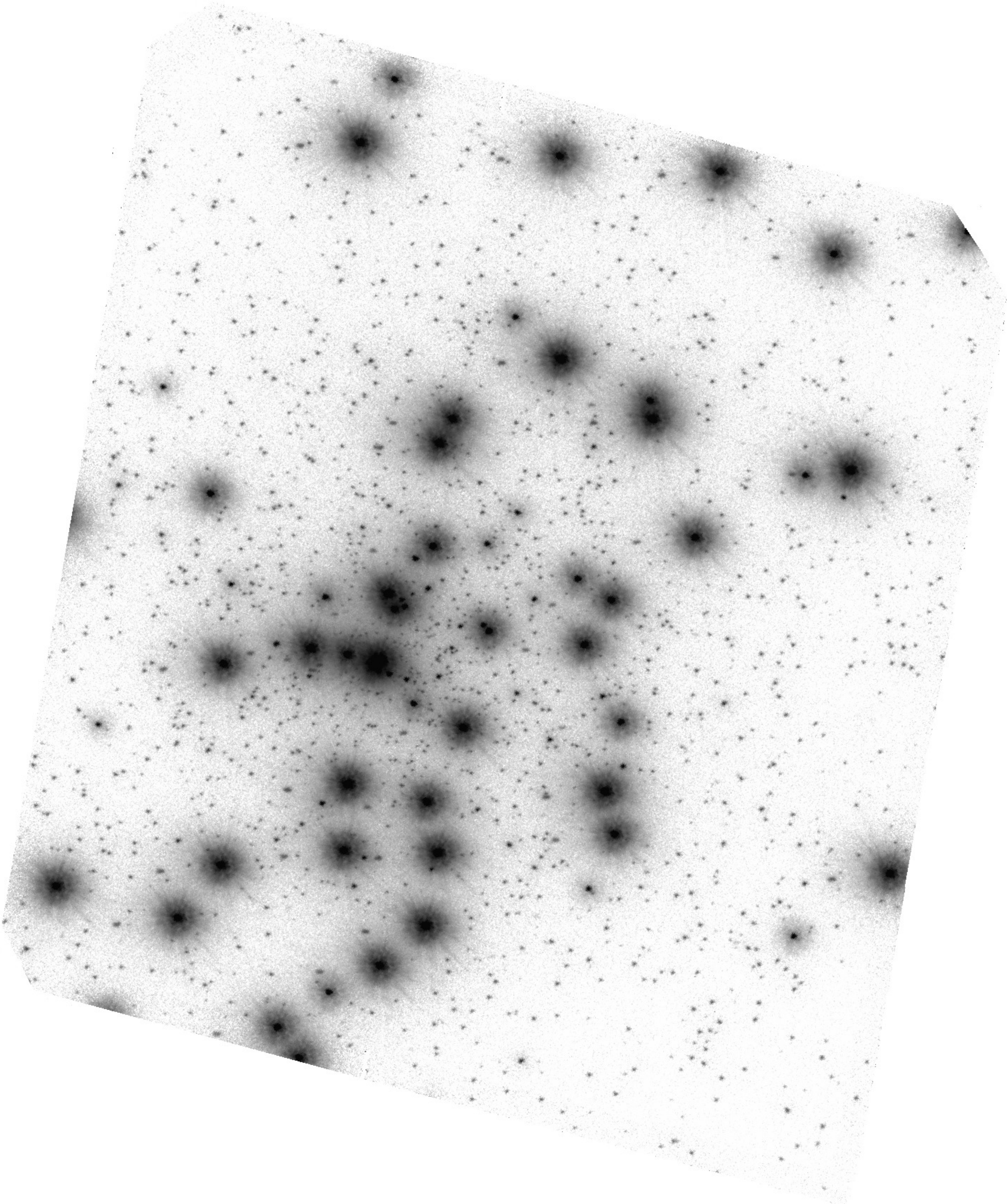

Figure 2.1: Master image of the *FUV* ACS/F150LP exposures of the core of M30, which spans $34.6'' \times 30.8''$ (1.40 pc $\times$ 1.24 pc). North is up and east is to the left.

the same pointing position. As a first step, a master image is created which realigns all individual images using the TWEAKREG task from the DRIZZLEPAC package running under PYRAF (Greenfield & White 2000). This task compares the world coordinate system (WCS) data in the header of each image to a reference image (the first in our list), and calculates the small residual shifts made by the pointing differences. The threshold is adjusted to ensure the rms of the shifts is small and there is no correlation in the residual plots. The images are then combined into a geometrically-corrected master image using the ASTRODRIZZLE task from the DRIZZLEPAC package. This task incorporates the processes of performing sky subtraction, drizzling, creating a median image, cosmic ray removal and final combination into the master image. In this instance, cosmic ray removal is not needed as the SBC is not sensitive to cosmic rays. The *FUV* master image is shown in Fig. 2.1. Although this shows the extremely dense core region of the cluster, the *FUV* image does not suffer from much crowding since the numerous MS stars are faint at these wavelengths.

Object identification

Most of the potential sources are automatically detected using the DAOFIND task in the DAOPHOT package (Stetson 1987), running under PYRAF. This task determines if there is a source in a given pixel by applying a Gaussian profile on the surrounding pixels. A detection is recorded if there is a good fit with a large positive central height of the Gaussian, whereas a negative or minimal height resembles the edge of a star or an empty region of sky (Stetson 1987). A FWHM of 3 and zero readnoise is used for the ACS/SBC. The coordinates of found sources are overplotted onto the master image to be checked by eye. The threshold for DAOFIND needs to be chosen such that it detects as many faint sources as possible without making too many false detections in the vicinity of the brightest stars. These false detections are then removed from the list by hand (along with some false detections at the edge of the image), and any of the faint sources missed by the DAOFIND task are added. The resulting number of objects found in the *FUV* is 1934.

Stellar photometry

Aperture photometry was performed using the task DAOPHOT (Stetson 1987) running under PYRAF. An aperture of 4 pixels was used with a sky annulus of 8-12 pixels. A small aperture is needed for dense stellar systems, however in order to account for the limited percentage of flux contained in the small aperture, an aperture correction, ApCorr, is applied, which is the inverse of the encircled energy. The small sky annulus also contains light from the star itself, and thus a sky correction, SkyCorr, is needed. Assuming that a larger sky annulus of 60-70 pixels contains only background flux, SkyCorr is determined by taking the magnitude ratio of the large sky annulus and the small sky annulus for several chosen isolated stars (see e.g. Dieball et al. 2007). The fluxes are then converted into the magnitude system STMAGs using the formula:

$$\mathrm{STMAG} = -\,2.5 \times \log\,(\mathrm{flux} \times \mathrm{SkyCorr} \times \mathrm{ApCorr} \,/\, \mathrm{ExpTime}) + \mathrm{ZPT}$$

where ZPT = –21.1 mag is the zero point for the STMAG system, and flux = counts × PHOTFLAM, where PHOTFLAM is the inverse sensitivity of the instrument used to convert count rates into fluxes, and can be found in the image header. For the ACS filter F150LP, this is:

$$\mathrm{PHOTFLAM}_{\mathrm{ACS,F150LP}} = 3.246305 \times 10^{-17}\mathrm{erg\ cm^{-2}\ \AA^{-1}\ count^{-1}}$$

For an annulus of 4 pixels, the corrections are ApCorr = 1.7636 (Avila & Chiaberge 2016) and SkyCorr = 1.011.

2.2.2 The WFPC2 F300W data

The *UV* data were obtained using the WFPC2 which was on board the *HST* (program GO-10561; PI: Dieball) with the F300W filter in 15 orbits distributed over three visits, from the 29th May to the 9th June 2007. The WFPC2 consists of four cameras: the three Wide Field Cameras (WFCs), each with a field of view of $50'' \times 50''$, and the Planetary Camera (PC) with a field of view of $34'' \times 34''$ and a pixel scale of $0.046''$ pixel^{-1}. The PC was centred on the cluster core. The exposures from these four chips are placed together into a mosaic image. Twenty-four mosaic images were taken with a total exposure time of 12000 s (Table 2.1).

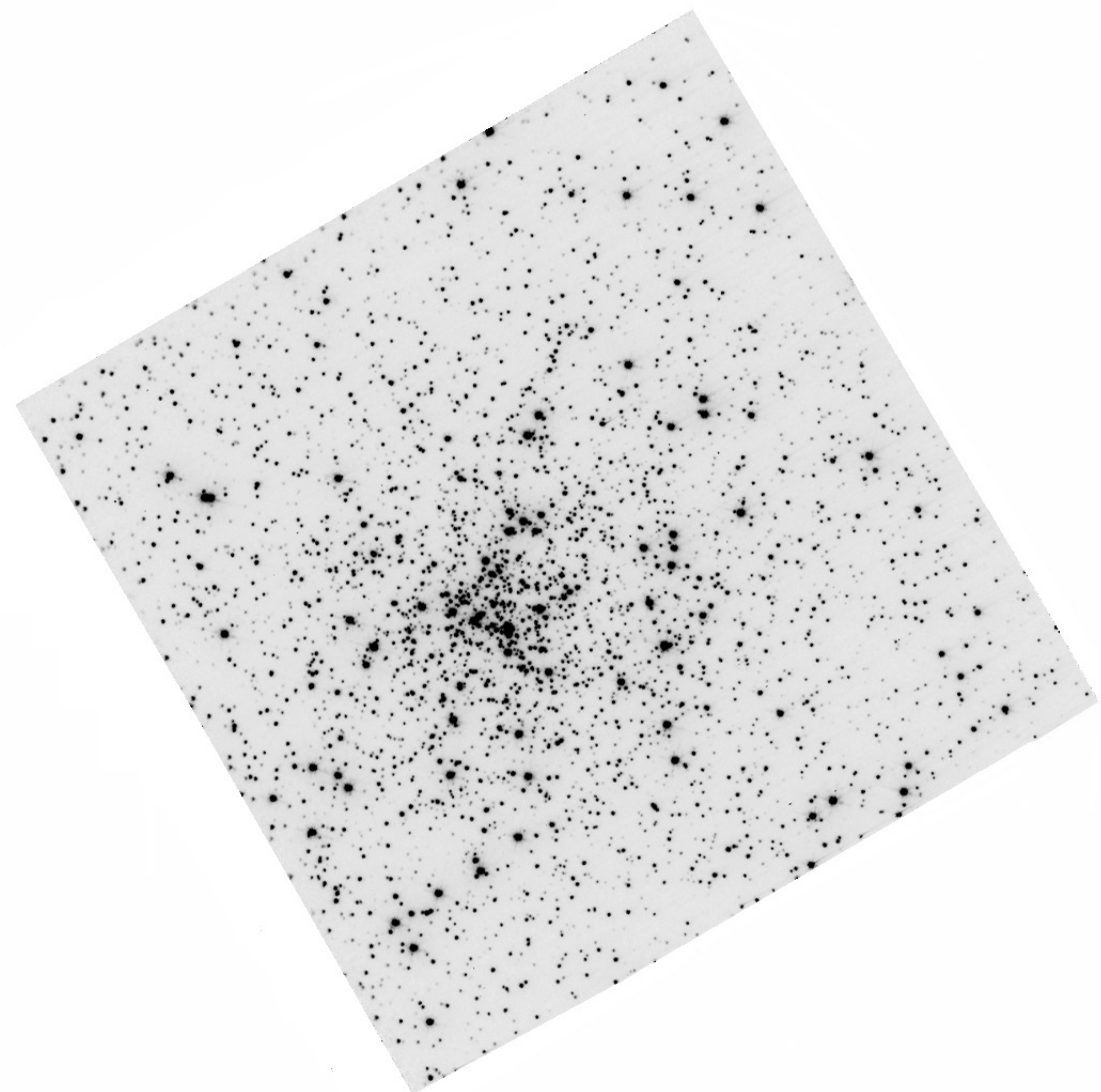

Figure 2.2: F300W master image of the WFPC2/PC exposures of M30, with a field of view of 34×34 (1.37 pc $\times$ 1.37 pc). North is up and east is to the left.

Object identification and stellar photometry

A master image is created using the same method that was used for the *FUV* data, with the `TWEAKREG` and `ASTRODRIZZLE` tasks from the `DRIZZLEPAC` package running under `PYRAF` (Greenfield & White 2000), and is shown in Fig. 2.2. Photometry was performed using the package `DOLPHOT` (Dolphin 2000), running under `IRAF` (Tody 1986; Tody 1993). This program carries out the image alignment with respect to a reference image (our master image), source detection, and photometry directly on the 24 flat-fielded exposures. `DOLPHOT` contains a specific module for the WFPC2 which performs point-spread function (PSF) fitting using a pre-calculated PSF model for the F300W filter[1], and the output magnitudes are already flux corrected. As the ACS/*FUV* field of view is contained within the field of view of the PC, only the data from this chip are needed here. For the photometry, the recommended parameters for the WFPC2 module are first used, then optimised so that as many faint sources were measured as possible[2]. The number of objects found in the PC/F300W data is 10451, with 8836 of these within the *FUV* field of view.

2.2.3 Catalogue matching

In order to find objects that appear in both the *FUV* and *UV* data, the coordinates of the sources found in the *FUV* image are transferred into the *UV* frame. In order to make the conversion, the x and y positions of 30 reference stars easily identified in both images are used as input for the task `GEOMAP` running under `PYRAF`. This computes the spatial transformation which is used by the `GEOXYTRAN` task to transform the coordinates of the *FUV* objects into the *UV* frame. This is checked by overplotting the transformed *FUV* coordinates onto the *UV* image. The two catalogues are then compared for matching stars using the task `TMATCH` which correlates the two lists for sources matching in coordinates within a radius of a given number of pixels. The average matching radius for sources in both frames is 0.35 pixels, and this procedure results in 1569 matching objects. The first 30 entries of the final list of sources are given in Table 2.2.

A number of chance matches are expected, and can be estimated using the numbers of objects in the two wavelengths and the matching radius (Knigge et al. 2003). The estimated number of spurious matches is 74 pairs (4.6% of all matches).

2.3 The *FUV* – *UV* CMD

The *FUV* – *UV* CMD is given in Fig. 2.3. A theoretical ZAMS, zero-age horizontal branch (ZAHB), and WD cooling sequence with marked surface temperatures are included for orientation purposes. These are calculated using the fitting formulae of Tout et al. (1996), the theoretical ZAHB models from Dorman (1992a) and the Wood (1995) grid of WD cooling curves with a grid of synthetic WD spectra by Gänsicke et al. (1995). Kurucz models of stellar atmospheres are used for interpolation and the resulting spectra are then folded with the appropriate filter and detector combinations using `PYSYNPHOT` running under `PYRAF`. The cluster parameters used are a distance of 8.3 kpc, a metallicity of [Fe/H]= −2.12 and a reddening of $E(B-V) = 0.03$ mag.

There is a well-defined main sequence, with turnoff at $FUV \approx 22$ mag and $FUV - UV \approx 3$ mag. Many BS sources are seen along the ZAMS at brighter magnitudes than the turnoff. The RGB

[1] http://americano.dolphinsim.com/dolphot

[2] The optimised parameters are: imgRPSF = 10, RCentroid = 1

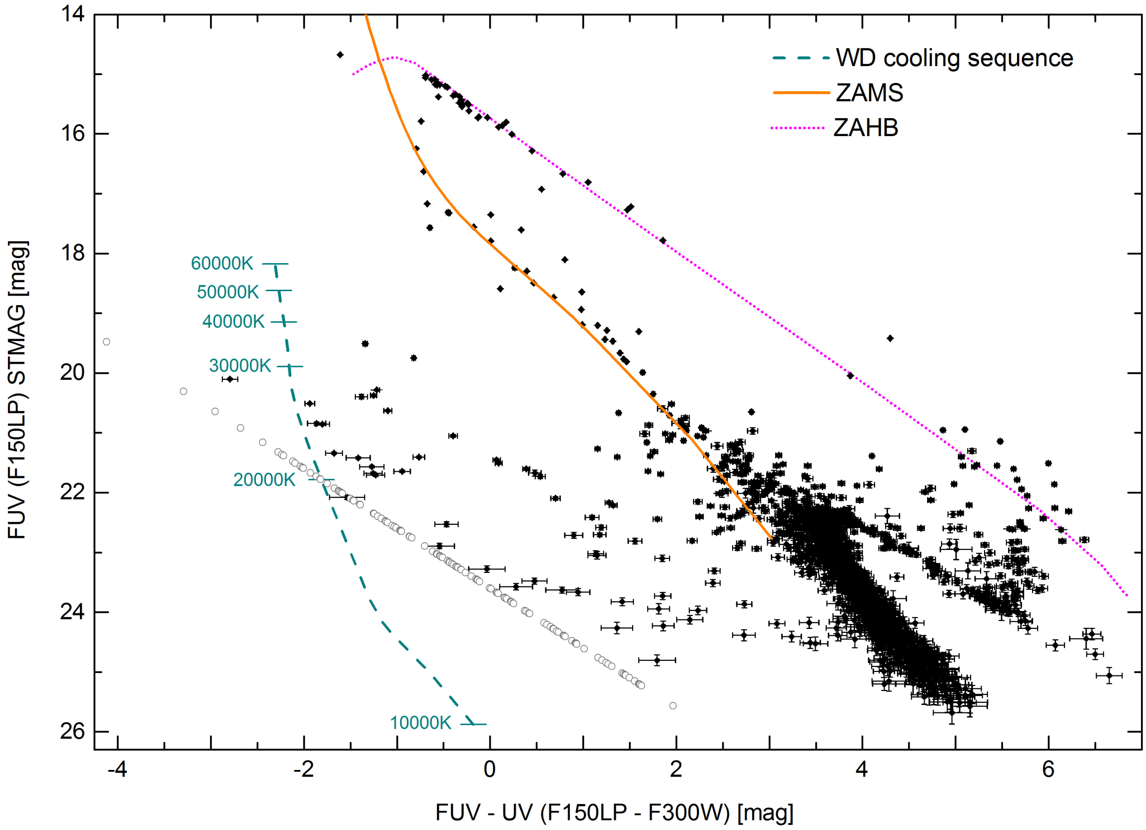

Figure 2.3: *FUV* – *UV* CMD of M30. A theoretical ZAMS (solid orange line), ZAHB (dotted pink line), and a WD cooling sequence (dashed green line) have been added for orientation. The surface temperatures of WDs are also indicated. Additionally shown are sources measured in the *FUV* but with no *UV* counterpart (grey circles), using the detection limit of the *UV* to estimate their position on the CMD, which also represents the location of the detection limit.

lies from the turnoff towards fainter and redder magnitudes. The HB reaches from the RGB up to *FUV* ≈ 15 mag. The sources between the MS and WD cooling sequence are called gap objects and are likely to include CV candidates (Dieball et al. 2007). Also included are 126 sources with *FUV* measurements but no *UV* counterparts. The detection limit of *UV* = 23.6 mag was used to estimate the position of these sources in the CMD, and as such they lie on the line representing this limit.

Figure 2.4 shows 16 of the BSs that are situated in the red BS sequence in Ferraro et al. (2009), and 13 from the blue BS sequence. As the separations in colour are small, they are also plotted in Fig. 2.4 in a verticalized CMD with respect to the theoretical ZAMS curve used in Fig. 2.3. The highest uncertainty in the *FUV* - *UV* position for these sources was 0.024 mag, and 0.004 mag for the *FUV*. Of the two BS sources without counterparts from Ferraro et al. (2009), the source at *FUV* – *UV* ≈ 0 mag (ID27) was just outside of their field of view, and the one at *FUV* – *UV* ≈ – 0.65 mag (ID283) matched within 2 pixels to the position of a source that was between the double BS sequence and the RGB (Ferraro et al. 2009, their source #11002543), and as such was not included. The field of view in our study only included the cluster centre, thus further observations using a larger field of view of this cluster in *FUV* wavelengths is needed to fully explore the BS population, however we find that there is no clear distinction between the two BS sequences in our dataset. The sources that were attributed to the distinct sequences in Ferraro et al. (2009) appear to be well mixed in the ultraviolet, particularly as two of the red BS sources have a large blue excess compared to the blue BSs (Fig. 2.4). As the sources on the red BS sequence are thought to be the result of mass transfer (Xin et al. 2015), the reason the

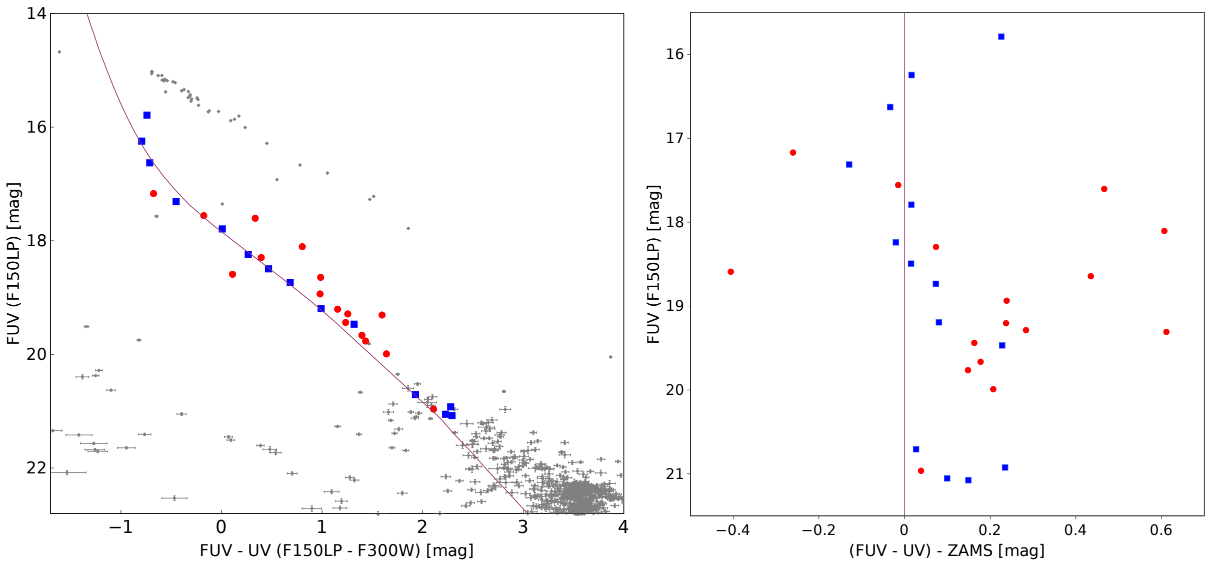

Figure 2.4: The BS sources that are found to be in a double BS sequence in the infrared by Ferraro et al. (2009), marked according to whether they belonged to the blue (squares) or red (circles) BS sequence, on the $FUV - UV$ CMD (left) and their position verticalized along with respect to the ZAMS (right).

two sub-populations appear mixed may be due to the sources on the red sequence being in an active state of mass transfer. Xin et al. (2015) detail a binary model which begins mass transfer at 7.54 Gyr, becomes brighter than the MS turnoff at around 10 Gyr, remains in the BS region for another 3-4 Gyr with mass transfer ceasing at 12.78 Gyr. Systems with active mass transfer emit FUV radiation due to the hot material in the accretion disk which would give these sources a blue excess in the $FUV - UV$ CMD. These active systems would then be shifted bluewards towards (and even beyond) the blue BS sequence in the ultraviolet.

There are around 78 WD/Gap objects blueward of the main sequence. We can make an estimate of the expected number of WDs in M30 by assuming that the number of stars in both of the HB and WD phases is proportional to the lifetime τ of these phases (Richer et al. 1997):

$$\frac{N_{WD}}{N_{HB}} \approx \frac{\tau_{WD}}{\tau_{HB}} \tag{2.1}$$

If we assume that $\tau_{HB} \approx 10^8$ yr (Dorman 1992b), the temperature of the WD cooling curve at the detection limit is 20,000 K $\approx 5 \times 10^7$yr (Althaus & Benvenuto 1998), and using the number of HB sources found in our sample $N_{HB} = 41$, we find that the estimated expected number of WDs is $N_{WD} \approx 20$. This rough estimate is in agreement with the sources on or near the WD cooling curve (Fig. 5.6) which have UV counterparts, and there may also be a few WDs in the 23 sources with $FUV < 22$ but were not detected in the UV.

The other sources in the gap between the WD cooling curve and the MS are expected to include a number of CVs. A GC such as M30 should produce $\approx$ 200 CVs by 13 Gyr (Ivanova et al. 2006), through various formation channels such as primordial CVs in which the binary components are the original two stars, and also dynamical binary exchange encounters and tidal capture. However, in the dense core, interactions with other cluster members mean that the rate of destruction of CVs is greater than the formation rate (Belloni et al. 2018b), and CVs are expected to have shorter lifetimes than their field counterparts by a factor of three (Shara & Hurley 2006). Belloni et al. (2018b) find that around 45% of detectable CVs are within the half-light radius of a GC, which for M30 is 1.03′ (Harris 1996). After scaling down to our field of view, and taking the destruction rate into account, we have a predicted number of detectable CVs in our images of $\approx$ 8. The remaining sources in this

Table 2.2. The first 30 entries from the catalogue of sources in the *FUV* and *UV* field of view. The ID number is given in the first column, the position of the source in Cols. 2 and 3, the radial distance is given in Col. 4, and the pixel position of the source on the *FUV* image is in Cols. 5 and 6. The magnitudes are in Cols. 7 − 9 and the resulting population type of each source (determined from the position in the $FUV - UV$ CMD) is given in Col. 10. Also included in Cols. 11−13 are the corresponding $B - V$ and V magnitudes and ID number from the optical catalogue (Guhathakurta et al. 1998). This table is published in its entirety in the supplementary material (online).

ID	RA	Dec	r^a	x_{FUV}	y_{FUV}	FUV	UV	$FUV-UV$	Type	B−V[b]	V[b]	ID[b] Optical
	[h:m:s]	[°:′:″]	[arcmin]	[pixels]	[pixels]	[mag]	[mag]	[mag]		[mag]	[mag]	
1	21:40:20.94	-23:10:55.71	0.313	479.48	74.20	15.431 ± 0.001	15.742 ± 0.001	-0.311 ± 0.002	HB	-0.09	15.63	755
2	21:40:20.79	-23:10:48.11	0.314	794.64	81.69	22.464 ± 0.030	18.868 ± 0.004	3.596 ± 0.034	MS	0.34	18.69	635
3	21:40:20.87	-23:10:48.48	0.296	767.87	119.88	22.654 ± 0.033	18.908 ± 0.004	3.746 ± 0.037	MS	0.37	18.74	699
4	21:40:20.89	-23:10:47.74	0.291	793.36	137.83	22.550 ± 0.039	18.654 ± 0.004	3.896 ± 0.036	MS	0.39	18.43	714
5	21:40:20.81	-23:10:42.51	0.319	1005.74	157.13	22.583 ± 0.033	18.852 ± 0.004	3.731 ± 0.037	MS	0.36	18.67	665
6	21:40:20.92	-23:10:46.79	0.282	823.92	168.39	22.521 ± 0.031	18.835 ± 0.004	3.686 ± 0.035	MS	0.34	18.69	746
7	21:40:21.19	-23:10:57.86	0.283	358.25	182.20	18.495 ± 0.005	18.027 ± 0.003	0.468 ± 0.008	BS			
8	21:40:21.16	-23:10:56.00	0.270	434.47	187.06	21.511 ± 0.020	15.513 ± 0.002	5.998 ± 0.022	RG	1.12	12.69	1005
9	21:40:21.16	-23:10:54.62	0.256	485.79	207.67	22.478 ± 0.031	18.767 ± 0.004	3.711 ± 0.035	MS	0.44	18.57	1025
10	21:40:20.90	-23:10:42.02	0.301	1010.36	210.87	22.364 ± 0.032	18.781 ± 0.004	3.583 ± 0.036	MS	0.29	18.57	730
11	21:40:21.22	-23:10:56.63	0.264	400.37	213.90	22.314 ± 0.029	16.099 ± 0.001	6.215 ± 0.030	RG	0.72	14.65	1107
12	21:40:21.30	-23:10:58.23	0.266	325.55	240.04	22.390 ± 0.030	18.784 ± 0.004	3.606 ± 0.034	MS			
13	21:40:20.97	-23:10:40.17	0.298	1071.16	266.28	22.401 ± 0.033	18.685 ± 0.004	3.716 ± 0.037	MS	0.33	18.48	796
14	21:40:21.26	-23:10:53.33	0.226	520.49	272.55	21.896 ± 0.023	18.325 ± 0.003	3.571 ± 0.026	MS	0.36	18.16	1163
15	21:40:21.23	-23:10:51.75	0.223	586.04	273.16	22.376 ± 0.029	18.568 ± 0.004	3.808 ± 0.033	MS	0.34	18.29	1120
16	21:40:21.19	-23:10:50.02	0.223	658.10	274.11	22.578 ± 0.032	18.921 ± 0.004	3.657 ± 0.036	MS	0.36	18.82	1070
17	21:40:21.03	-23:10:42.37	0.270	976.93	274.68	19.812 ± 0.009	18.346 ± 0.003	1.466 ± 0.012	BS	0.12	18.18	860
18	21:40:21.01	-23:10:41.41	0.280	1016.38	276.28	15.187 ± 0.001	15.758 ± 0.001	-0.571 ± 0.002	HB	-0.12	15.78	841
19	21:40:21.36	-23:10:54.51	0.216	459.70	312.16	22.301 ± 0.028	18.568 ± 0.004	3.733 ± 0.032	MS	0.57	18.27	1278
20	21:40:21.31	-23:10:52.23	0.207	554.79	311.87	22.431 ± 0.031	16.489 ± 0.001	5.942 ± 0.032	RG	0.69	15.14	1222
21	21:40:21.23	-23:10:37.61	0.267	1127.68	436.35	22.270 ± 0.028	23.859 ± 0.276	-1.589 ± 0.304	Gap	0.30	18.70	1221
22	21:40:21.19	-23:10:45.25	0.222	841.07	327.62	22.445 ± 0.030	18.627 ± 0.004	3.818 ± 0.034	MS	0.37	18.33	1075
23	21:40:21.03	-23:10:37.57	0.307	1161.20	328.22	22.492 ± 0.032	18.604 ± 0.004	3.888 ± 0.036	MS	0.43	18.32	865
24	21:40:21.25	-23:10:47.84	0.205	732.63	329.89	22.497 ± 0.031	18.814 ± 0.004	3.683 ± 0.035	MS	0.32	18.70	1158
25	21:40:21.47	-23:10:57.80	0.235	316.94	331.07	22.390 ± 0.030	18.640 ± 0.004	3.750 ± 0.034	MS	0.40	18.49	1459
26	21:40:21.16	-23:10:43.49	0.235	913.04	333.06	22.618 ± 0.034	18.496 ± 0.003	4.122 ± 0.037	RG	0.37	18.26	1036
27	21:40:21.13	-23:10:41.56	0.254	992.76	335.06	17.353 ± 0.003	17.345 ± 0.002	0.008 ± 0.005	BS	-0.01	17.37	987
28	21:40:21.12	-23:10:40.56	0.262	1031.70	345.38	22.304 ± 0.034	18.767 ± 0.004	3.537 ± 0.038	MS	0.32	18.70	983
29	21:40:21.48	-23:10:56.31	0.213	371.12	357.70	22.529 ± 0.032	18.961 ± 0.004	3.568 ± 0.036	MS	0.35	18.77	1482
30	21:40:21.35	-23:10:49.55	0.185	651.59	362.87	21.075 ± 0.016	18.783 ± 0.004	2.292 ± 0.020	BS	0.18	18.69	1269
⋮												

(a) From the cluster centre at $x = 443.9$, $y = 362.8$ in the UV image, corresponding to RA = 21^h40^m2213, Dec = $-23°10'4740$, determined as the centre of gravity by Ferraro et al. (2009).
(b) Guhathakurta et al. (1998).

region of the CMD that are not CVs or individual WDs are likely to be detached WD-MS binaries, where the hot emission from the WD surface and the cooler radiation from the MS surface places the combined flux of the binary in the region between these two populations. There is also the possibility of chance superpositions, and following the same prescription that was used for the whole dataset in Sect. 2.2.3, the expected number of spurious matches in the WD/Gap population is ≈ 1. Additionally, some sources which lie close to the MS and BS sequence may indeed be MS or BS stars. We stress that the predicted number of CVs is a rough estimate, and a closer investigation into the particular sources that are CV candidates is given in the following publication in this study.

We note that for the remainder of this study, most of the sources discussed have been determined as belonging to certain populations by their location in the $FUV - UV$ CMD. Yet there may be some sources which truly belong to a different group, as mentioned in the preceding paragraph of the gap sources close to the MS and BS sequence. This is especially true for the sources near the MS turnoff that have been included in the BS group for example, but may really be MS stars or gap objects, and vice versa. These initial distinctions allow us to make useful preliminary investigations into the cluster population, however supplementary tools such as spectroscopy and additional multiwavelength observations would enable us to more accurately determine a stars true nature.

2.4 Comparison to optical

Guhathakurta et al. (1998) presented an optical catalogue of 9507 sources for M30, the exposures of which were also taken with the WFPC2 on board the *HST* (program GO-5324, PI: Yanny). Eight exposures were taken on 31st March 1994, two using the F336W filter with an 100 s exposure time, two using the F439W filter and 40 s exposure time and four using the F555W filter with 4 s exposure times. This data was accessed from VizeiR[3], and by taking the well-defined group of HB stars in the optical CMD (Fig. 2.5), and overplotting their coordinates onto the *FUV* image (Fig. 2.1), it is easily seen that they corresponded to the brightest sources in the *FUV* image, albeit with a slight shift. After correcting for the shift, these are then used as reference stars to convert the coordinates of the optical catalogue into our *FUV* frame. The coordinates of the HB stars are given as input for the task `GEOMAP` which computes the transformation. The `GEOXYTRAN` task carries out the transformation of the optical catalogue into the *FUV* frame, and then also into the *UV* frame using the same transformation used in Sect. 2.2.3. The optical coordinates are first converted into the *FUV* frame rather than directly into the *UV* frame, because it was easy to identify stars to use for the transformation, as the HB stars are the brightest objects in the *FUV* and as such are an efficient choice for the reference stars.

The resulting comparison is given in Fig. 2.5. Groups of sources belonging to both catalogues are plotted in colour. There are 1201 matching MS stars (yellow), 178 RGB stars (red), 44 BS sources (blue), all 41 HB stars (purple), and 42 WD/Gap objects (green) which include CV candidates. The comparison illustrates the importance of *FUV* observations in detecting and identifying stellar exotica such as WDs and CVs, as in the optical they are indistinguishable in position from the MS, but their hot emission in the *FUV* shifts their location in the $FUV - UV$ CMD blueward and brighter than the MS. This is also true for a few *FUV*-bright BS candidates that are in the MS region in the optical CMD. These sources appear brighter than the MS turnoff in the *FUV* suggesting that they could have a hot WD companion (Sahu et al. 2019). Additionally, two of our BS sources, ID7 and ID66, do not have an optical counterpart. Source ID7 was just out of the field of view in the optical exposures, and ID66 is close to the MS turnoff in the $FUV - UV$ CMD, and as such it may be a binary system with a hot WD that is bright in the ultraviolet but with an optically faint MS star companion (Knigge et al.

[3]https://cdsarc.cds.unistra.fr/viz-bin/cat/J/AJ/116/1757

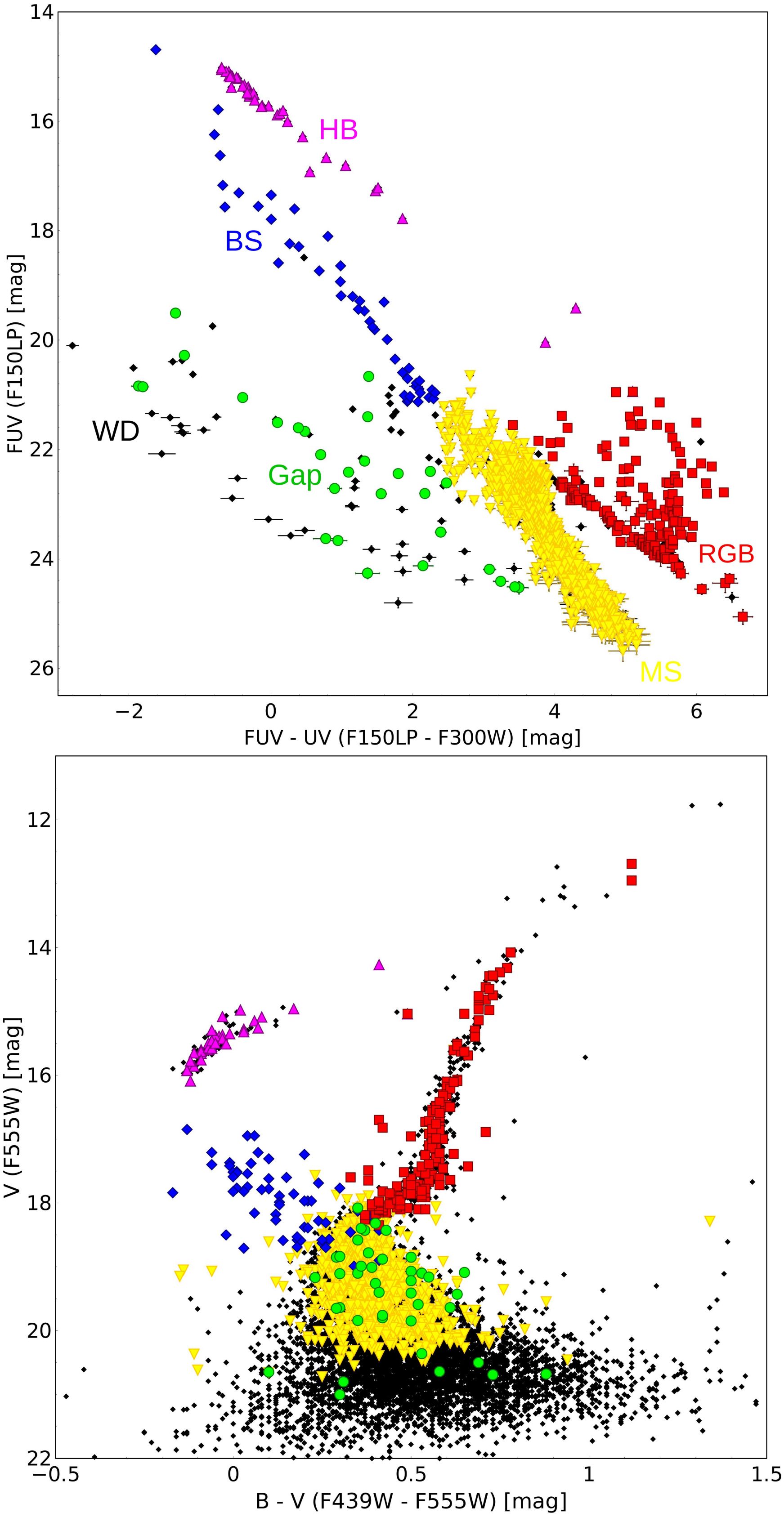

Figure 2.5: Comparison of the various stellar populations in the *FUV – UV* CMD (top) and the optical CMD (bottom, based on the Guhathakurta et al. 1998 catalogue). Only the sources present in both catalogues are marked in colour. Included are MS stars (yellow down triangles), red giants (red squares), HB stars (purple up triangles), BS stars (blue diamonds), and gap objects (which include CV candidates, green circles).

2000). If this is the case, it would really be a Gap object rather than a BS star, as discussed at the end of Sect. 5.6.

Several sources at the top of the optical RGB do not have *FUV* counterparts as they are located outside the *FUV* field of view. Additionally, there were 76 sources in the *FUV* that are undetected in the optical, including nearly half of the WD/Gap objects. This is expected for the sources in the WD cooling region as WDs are optically very faint. The reason for the Gap objects not having optical counterparts may be due to them being CVs with very low-mass MS companions, as their radial distributions suggest (Sect. 2.5), and as such were too faint to be detected in the optical. The MS stars given in the optical catalogue fainter than V $\approx$ 20.5 mag are too faint to be detected in the *FUV*. The matched optical counterparts are identified in Table 2.2.

2.5 Radial distribution

Figure 2.6 shows the cumulative radial distributions of the stellar populations found in both the *FUV* and *UV* images within a radius of 15.5″ from the cluster centre. The centre of the cluster used was $\alpha = 21^h40^m2213$, $\delta = -23°10'4740$ (Ferraro et al. 2009) which corresponds to pixel coordinates $x = 443.9$, $y = 362.8$ in the *UV* frame and $x = 612.1$, $y = 800.1$ in the *FUV*. The numbers for each stellar population in the $FUV - UV$ catalogue and those within 15.5″ radius of the cluster centre are given in Table 2.3. Included in the group WD/Gap sources are all sources blueward of the MS/BS sequence and $FUV > 19$ mag.

The most prominent result in the radial distributions is the strong concentration of BS stars towards the centre, compared to the other populations. M30 is a core-collapsed cluster, meaning that over time the more massive stars have concentrated inward towards the centre (mass segregation). BS stars are the most massive stars out of these stellar populations, having gained mass by either mass transfer from a companion or by the merger of two stars (McCrea 1964; Hills & Day 1976), and as they are still hydrogen burning they have not yet undergone the mass loss observed in the later stages of evolution. They are also likely to form in the cluster centre due to the high number of stellar interactions in this dense region. Thus, the BS concentration towards the centre is expected evidence of the dynamical history of the core, and is also representative of the bluer inward colour gradient observed in M30 (Howell et al. 2000).

The colour gradient also results from the central deficiency of RGB stars (Howell et al. 2000), which corresponds to the lack of central concentration of this population shown in Fig. 2.6. This may be due to the mass that stars typically lose during the RGB phase which could allow these stars to drift outwards. This may also be the case for the least centrally concentrated population, the HB stars, which evolve from the RGB stage. The HB stars are even absent within the inner core region of 1.9″ (0.08 pc), so whilst the high concentration of BS stars in the centre may add to the bluer inward colour gradient of M30, it seems that the numerous HB stars, which are similar to BS in colour magnitude, do not contribute to this gradient.

The group WD/Gap sources includes $\approx$ 20 sources that are likely isolated WD stars that are located near the WD cooling curve (Fig. 2.3), an estimated number of $\approx$ 8 CVs, and detached WD-MS binaries. Overall, the sources in this group are only slightly more centrally located than MS stars in M30, which is unexpected at first glance, since a central concentration was seen in other GCs such as NGC 2808 (Dieball et al. 2005) and M15 (Dieball et al. 2007), and as CVs can form from two-body interactions that are frequent in the high density centre of the cluster. CVs are binary systems, which along with the non-interacting WD-MS binaries, means a higher combined mass than the individual stars alone. Similarly to BS stars, these higher mass sources should concentrate towards the cluster centre over time. However, the segregation of WD/Gap sources towards the centre is not observed, and a possible

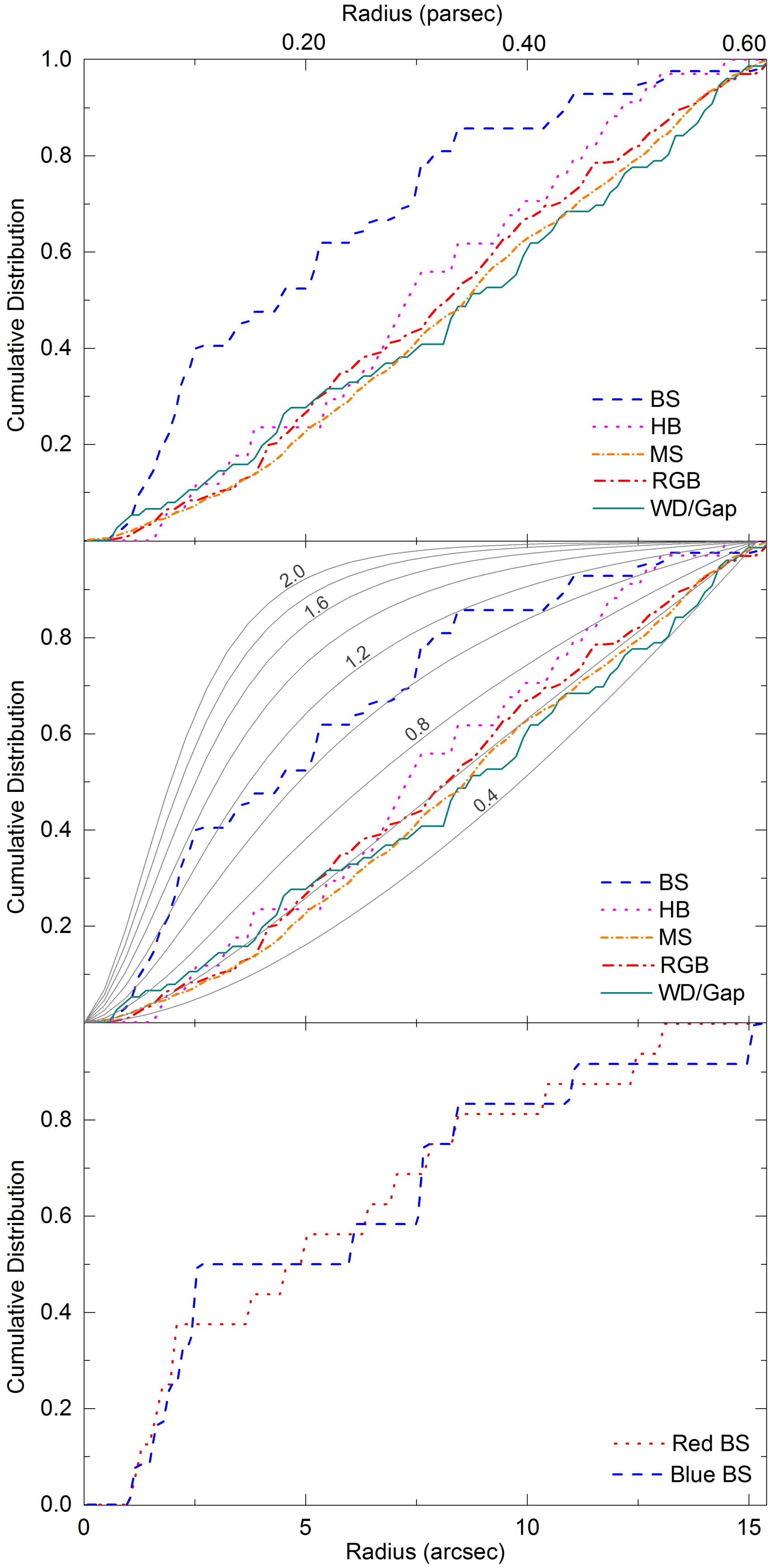

Figure 2.6: Cumulative radial distributions of the various stellar populations (top), with mass estimate models ranging from 0.4 $M_\odot$ – 2.0 $M_\odot$ (middle), and the sources on the red and blue BS sequences (bottom) found by Ferraro et al. (2009), within a radius of 15.5″ from the centre of M30.

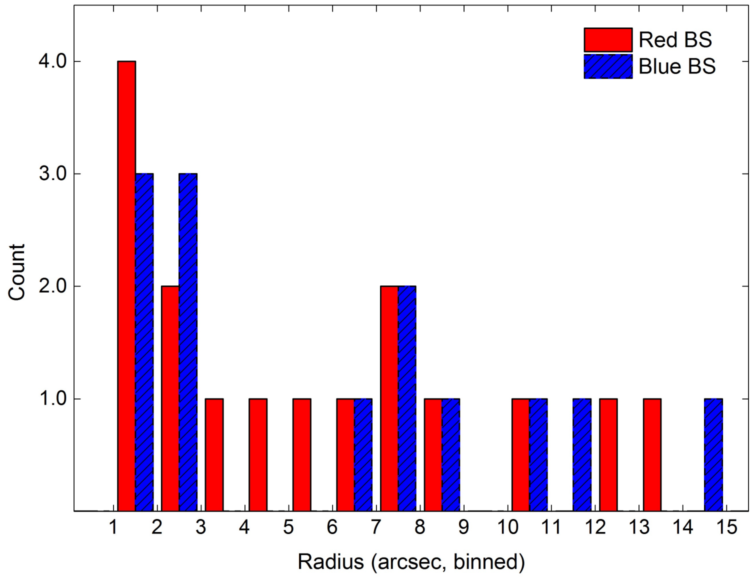

Figure 2.7: Discrete radial distribution of the red and blue BS sources. The radius is split into 1 arcsec-sized bins, where any red (blue) BS sources appear on the left (right) side of each bin.

Table 2.3. Numbers of sources for the stellar populations in the *FUV – UV* catalogue and within a radius of 15.5″ of the cluster centre of gravity, along with their estimated masses.

Population	Catalogue	15.5″ radius	Mass
MS	1218	1030	0.5 - 0.6 $M_\odot$
BS	47	42	1.0 - 1.2 $M_\odot$
RG	185	169	0.6 - 0.7 $M_\odot$
HB	41	34	0.6 - 0.8 $M_\odot$
WD/Gap	78	70	0.5 - 0.6 $M_\odot$

explanation for this might be that the combined mass of these binary systems is actually relatively low. This is true for old ($\approx$ 10 Gyr) CVs where the WD has devoured almost all of the mass from their companion, leaving behind as little as $\approx$ 0.1 $M_\odot$, a negligible mass relative to the WD (Hillman et al. 2020), and also mass is lost from the system over time due to wind and outbursts from the accretion disc (Tout & Hall 1991). Additionally, as the destruction rate of CVs is higher than the formation rate in the dense cores of GCs (Belloni et al. 2018b), a number of the detached WD-MS binaries may also have undergone mass transfer in the past. Even if we also detect younger systems, it is likely that the MS companion has a low mass, as otherwise the flux from the MS star would be higher in the UV wavelength, which is not the case for our Gap sources. As there is no central concentration seen in M30, this suggests that a large proportion of the Gap sources are binary systems with low combined masses.

The average masses of the various stellar populations can be estimated from the radial distributions by assuming the spatial distribution of a typical star is described by King (1966) models. Following the method by Heinke et al. (2003), we compare our radial distributions using a maximum-likelihood fitting to generalised theoretical King models, with the radial profile of the source surface density:

$$S(r) = \int \left(1 + \left(\frac{r}{r_{c\star}}\right)^2\right)^{\frac{1-3q}{2}} dr \tag{2.2}$$

Table 2.4. Probabilities that two populations of stars are from the same parent population.

Population Comparison	Probabilities %
MS–BS	0.001
MS–HB	47.996
MS–RG	40.998
MS–WD/Gap	62.156
BS–HB	0.5416
BS–RG	0.0452
BS–WD/Gap	0.0201
HB–RG	78.936
HB–WD/Gap	36.181
RG–WD/Gap	53.490

where $q = M_X/M_\star$, with M_X being the mass of the source population we wish to find, and $M_\star$ is the mass of the population within the core radius $r_{c\star} = 1.9''$ (Sosin 1997). After applying a correction to the distribution to cover the non-circular field of view of the images as a function of radius, models with masses 0.4 – 2.0 $M_\odot$ in steps of 0.2 $M_\odot$ are calculated and shown in Fig. 2.6. The estimated masses for each stellar population are given in Table 2.3. The average mass of the BS stars is estimated to be 1.0 – 1.2 $M_\odot$, and the mass of the WD/Gap sources is 0.5 – 0.6 $M_\odot$. Whilst only a slight overall concentration of WD/Gap sources towards the centre was seen, the sources near to the core are estimated to be more massive than those further out.

The radial distribution of the red and blue BS sources identified as two distinct sequences in Ferraro et al. (2009) is also shown in Fig. 2.6 which reveals no significant distinction in radial spread for the two BS sequences; both populations are centrally concentrated. Ferraro et al. (2009) show a slightly higher central concentration of red BS in M30, although they use a different cumulative radial range. Therefore we also give the discrete red and blue BS radial distributions in Fig. 2.7, again displaying no significant difference between the two sub-populations. From the other two clusters known to have a double BS sequence, Dalessandro et al. (2013b) find a higher central concentration of red BSs in NGC 362 and contrastingly, Simunovic et al. (2014) find a higher central concentration of blue BS stars in NGC 1261.

The similarity of the radial distributions of the various stellar populations is investigated using a Kolmogorov–Smirnov (KS) test. The KS test compares two populations and returns a probability that the two distributions are drawn from the same parent population. The higher the returned probability, the more likely the distributions are from the same population. The BS sources are comparable to the other stellar populations with KS probabilities of 0.54% (BS to HB), 0.05% (BS to RG), and 0.02% (BS to WD/Gap sources), suggesting that the BS sources formed through a different process to the HB and RG stars, i.e. from mergers or mass transfer rather than single star evolution. The results for all population comparisons are given in Table 2.4.

2.6 Summary

Far-ultraviolet (*FUV*, ACS/SBC/F150LP) and mid-ultraviolet (*UV*, WFPC2/F300W) exposures of the GC M30 were photometrically analysed. A total of 1934 sources are detected in the *FUV* image and 10451 sources in the *UV* image. Out of these, 1569 matching sources were found. Different stellar populations are well distinguished in the resulting $FUV - UV$ CMD. The MS turnoff lies at $FUV \approx 22$ mag and $FUV - UV \approx 3$ mag. The horizontal branch consists of 41 sources, all of which have an optical counterpart from the catalogue by Guhathakurta et al. (1998). The RGB extends towards fainter and redder magnitudes, with 185 RGB sources, 178 of which are also found in the optical. A sequence of 47 BS stars is observed, 44 of these having optical counterparts. Seventy-eight WD/Gap objects are identified, 42 of which were in the optical catalogue. The $FUV - UV$ CMD allows us to easily distinguish the WD/Gap sources from MS stars.

The double BS sequence suggested by Ferraro et al. (2009) in the $V - I$ CMD is not seen in the $FUV - UV$ CMD. The two sets of BS sources are mixed in the ultraviolet which may be a result of the sources on the red BS sequence experiencing active mass transfer and emitting FUV radiation, shifting these sources blueward in the ultraviolet CMD.

The radial distributions of the stellar populations show a strong concentration of BS sources towards the centre of the cluster, implying that mass segregation has taken place. There is a deficiency of HB stars in the very centre of the cluster and no central concentration of CV candidates is found, which may be due to these being old systems with low-mass MS companions.

The *HST* data for this project is sensitive enough to detect a previously unseen, significant population of WD/Gap objects, providing new insight into M30 in the ultraviolet. Investigations in the FUV continue to provide detailed detections and identifications of stellar populations.

Chapter 3

Far-ultraviolet investigation into the galactic globular cluster M30 (NGC 7099): II. Potential X-ray counterparts and variable sources

Santana Mansfield, Andrea Dieball, Pavel Kroupa, Christian Knigge, David R. Zurek, Michael Shara, Knox S. Long

Monthly Notices of the Royal Astronomical Society, Volume 513, Issue 2, June 2022

Abstract We present a far-ultraviolet (*FUV*) study of the globular cluster M30 (NGC 7099). The images were obtained using the Advanced Camera for Surveys (ACS/SBC, F150LP, *FUV*) and the Wide Field Planetary Camera 2 (WFPC2, F300W, *UV*) on board the *Hubble Space Telescope (HST)*. We compare the catalogue of *FUV* objects to 10 known X-ray sources and find six confident matches of two cataclysmic variables (CVs), one RS CVn, one red giant with strong *FUV* emission and two sources only detected in the *FUV*. We also searched for variable sources in our dataset and found a total of seven blue stragglers (BSs), four horizontal branch (HB) stars, five red giant branch stars, 28 main sequence stars and four gap objects that demonstrated variability. One BS star is a known W-UMa contact binary, one of the gap objects is a known CV identified in this work to be a dwarf nova, and the three other gap sources are weak variables. The periods and positions of two of the variable HB stars match them to two previously known RR Lyrae variables of types RRab and RRc.

3.1 Introduction

The high density of stars in the cores of globular clusters allows frequent interactions which produces various exotic sources, such as blue straggler (BS) stars that are located at brighter magnitudes in the colour-magnitude diagram (CMD) than the main sequence (MS) turnoff. BS stars are typically thought to have higher masses than MS stars, by gaining mass from a companion (McCrea 1964), or from a direct collision (Hills & Day 1976), in order to remain in the location of the zero-age main sequence (ZAMS), while single MS stars of similar masses have turned off to become red giants. Other exotic sources include binary systems such as cataclysmic variables (CVs; a white dwarf (WD) star accreting mass from a companion), X-ray binaries and millisecond pulsars (MSPs, Shara & Hurley 2006; Ivanova et al. 2006; Hong et al. 2016), as well as individual WDs.

CVs and low-mass X-ray binaries (LMXBs; a neutron star or black hole accreting material from a low-mass companion), are faint at optical wavelengths and not easily detectable in globular clusters as they are surpassed by the large number of MS stars that shine brightly in the optical. Instead, we search for these exotic sources in the ultraviolet and X-ray wavelengths. Since the accretion of material in these binary systems results in very hot temperatures in the accretion disk, as well as when material falls onto the surface of the compact object, the spectral energy distribution of this hot emission peaks in the far-ultraviolet (FUV) or X-ray wavelengths. Since the surfaces of the numerous MS and red giant branch (RGB) stars in globular clusters do not reach such high temperatures, they are faint at these wavelengths and the cluster core appears much less crowded. By taking observations in the ultraviolet, we can more easily detect and identify such exotic sources.

For the first part of this investigation (Mansfield et al. 2022a, hereafter Paper I), we performed the photometry of ultraviolet observations of the globular cluster M30 (NGC 7099) and presented a $FUV - UV$ CMD and an analysis of the radial distributions of the different stellar populations. A more detailed overview of M30 and the previous studies on this cluster can be found in Paper I. We also presented an ultraviolet catalogue of sources[1]. We note that, along with the strong central concentration of BS stars, the radial distributions given in Paper I also show that a dominant stellar population in the central region is the WD/Gap sources, which has recently been theorised to be the case for core-collapsed globular clusters (Kremer et al. 2020, 2021). In this present work, we continue our investigation into the properties of M30 and compare the positions of the sources detected in the ultraviolet to the locations of the known X-ray sources in M30. In this work, we also perform a variability study using the FUV exposures to find active binary systems in M30, including those in the vicinity of the X-ray sources.

Stars can exhibit brightness variability due to the orbit of a binary (or multiple) system, structural processes within single stars which generate pulsations, or from interactions between binary members such as mass transfer. For example, the emission from a hot accretion disk in a CV system, as well as the fall of material onto the surface of the WD, can produce strong variability which helps to distinguish CVs from isolated WDs. Investigating brightness fluctuations allows for precise stellar identification within the population groups. For instance, within M30, seven RR Lyrae variables have been observed on the horizontal branch (HB) in the optical and infrared (Pietrukowicz & Kaluzny 2004; Kains, N. et al. 2013), and since Zurek et al. (2016) saw brightness variability on the HB in the FUV for NGC 1851, a variability study of M30 in the FUV will be valuable to find other potential RR Lyrae stars on the horizontal branch of M30, as well as possible CV candidates.

M30 also contains a number of X-ray sources which indicate exotic binary systems. Lugger et al. (2007) detected 13 X-ray sources that were also found by Zhao et al. (2020), who discovered an additional 10 sources, based on observations with *Chandra* ACIS-S. Some of these sources are

[1]http://vizier.u-strasbg.fr/viz-bin/VizieR?-source=J/MNRAS/511/3785

thought to be CVs, and one is likely a quiescent low-mass X-ray binary (qLMXB). Two milli-second pulsars were also found in M30 by Ransom et al. (2004).

The observations and coordinate transformations used for this investigation are described in Sect. 3.2. The potential ultraviolet counterparts to the X-ray sources and their locations in the $FUV - UV$ CMD are described in Sect. 3.3. The variable sources are described in Sect. 3.4, followed by a summary in Sect. 3.5.

3.2 Data processing

3.2.1 Photometry

The FUV data were obtained with the Advanced Camera for Surveys (ACS) on board the *HST*, using the Solar Blind Channel (SBC) and the F150LP filter. The UV data were acquired using the Wide Field Planetary Camera 2 (WFPC2) and the F300W filter, which was also on board the *HST*. These were both part of the program GO-10561 (PI: Dieball) and were taken using 15 orbits distributed over three visits, from the 29th May to the 9th June 2007. The SBC has a field of view of $34.6'' \times 30.8''$ and a pixel scale of $0.034'' \times 0.030''$ pixel^{-1}. Sixty-four images were taken, each with an exposure time of 315 s, resulting in a total exposure time of 20160 s. The WFPC2 consists of four cameras, the three Wide Field Cameras (WFCs) each with a field of view of $50'' \times 50''$, and the Planetary Camera (PC) with a field of view of $34'' \times 34''$, and a pixel scale of $0.046''$ pixel^{-1}. As the PC was centred on the cluster core and the region observed for the FUV imaging, only the exposures from this camera are used in this work. Twenty-four images were taken with a total exposure time of 12000 s. The observations, image processing and data reduction are described in detail in Paper I. Out of 1934 sources detected in the FUV, 1569 have UV counterparts, including 1218 MS stars, 41 HB stars, 47 blue stragglers (BS), 185 RGB stars and 78 WD/Gap objects (sources blueward of the MS and with $FUV \gtrsim 19$ mag).

The optical data used in this work is the catalogue from Guhathakurta et al. (1998), the exposures of which were also taken with the WFPC2 on board the *HST* (program GO-5324, PI: Yanny). Eight exposures were taken on 31st March 1994, two using the F336W filter with 100 s exposure time, two using the F439W filter and 40 s exposure time, and four using the F555W filter with 4 s exposure times. The data was accessed from VizeiR[2].

3.2.2 X-ray coordinate transformation

Lugger et al. (2007) found 13 X-ray sources within the half-mass radius of M30 ($1.15'$, Harris 1996) using *Chandra* ACIS-S. In order to check the positions of these sources against our ultraviolet dataset, we use the astrometric reference star adopted by Guhathakurta et al. (1998), a red giant (their source #3611), which in our catalogue is ID366. From our dataset, the position of this star is:

$$\alpha = 21^h40^m2231, \quad \delta = -23^\circ10'4013 \quad \text{(J2000.0)} \tag{3.1}$$

which has a shift of $\Delta\alpha = +0.02''$, $\Delta\delta = +0.53''$ from the position of $\alpha = 21^h40^m2229$, $\delta = -23^\circ10'3960$ given by Lugger et al. (2007) (and also a relatively small shift of $\Delta\alpha = -0.004''$, $\Delta\delta = +0.03''$ to the position of $\alpha = 21^h40^m22314$, $\delta = -23^\circ10'4010$ reported by Ransom et al. (2004)). This is within

[2]https://vizier.cds.unistra.fr/viz-bin/VizieR?-source=J/AJ/116/1757

Table 3.1. The positions and distances of the potential counterparts to the X-ray sources and their ultraviolet photometric quantities as found in this study. The radius r in Column 2 is the distance of the X-ray source from the centre of the cluster, and the distance of the potential counterpart to the X-ray source is given in Column 7. The X-ray sources A1–6 are from Lugger et al. (2007), sources W15–W17 are from Zhao et al. (2020), and the MSP from Ransom et al. (2004).

ID_{X-ray}	r [arcsec]	P^{a}_{err} [arcsec]	ID_{FUV}	RA [h:m:s]	Dec [°:′:″]	Distance [arcsec]	Err^{b}	Type	FUV [mag]	$FUV-UV$ [mag]
A1	1.312	0.24	ID272	21:40:22.16	-23:10:45.85	0.238	0.992	BS	17.170 ± 0.004	-0.676 ± 0.006
A2	1.064	0.24	ID283	21:40:22.22	-23:10:47.65	0.078	0.325	BS/RG	17.570 ± 0.013	-0.646 ± 0.016
			ID290	21:40:22.23	-23:10:47.71	0.224	0.933	BS	14.676 ± 0.001	-1.612 ± 0.002
A3	1.599	0.42	ID181	21:40:22.03	-23:10:47.85	0.134	0.319	RG	23.195 ± 0.066	5.677 ± 0.068
			ID187	21:40:22.03	-23:10:47.46	0.289	0.688	RG	22.129 ± 0.034	3.971 ± 0.037
			ID191	21:40:22.04	-23:10:47.51	0.336	0.800	RG	21.549 ± 0.023	5.444 ± 0.024
			ID806	21:40:22.00	-23:10:47.88	0.405	0.964	MS	23.050 ± 0.054	3.801 ± 0.059
B	4.904	0.24	ID1647	21:40:22.18	-23:10:52.17	0.005	0.021	–	21.582 ± 0.026	–
C	11.483	0.24	ID456	21:40:22.96	-23:10:49.74	0.038	0.158	WD/Gap	19.748 ± 0.009	-0.821 ± 0.019
6	11.718	0.41	ID1700	21:40:21.51	-23:10:55.15	0.090	0.220	–	23.256 ± 0.048	–
W15	9.559	0.43	ID449	21:40:22.81	-23:10:47.61	0.292	0.679	MS	22.298 ± 0.029	3.464 ± 0.033
			ID452	21:40:22.83	-23:10:47.88	0.364	0.847	MS	22.453 ± 0.031	3.483 ± 0.035
			ID912	21:40:22.83	-23:10:47.63	0.109	0.253	WD/Gap	23.971 ± 0.071	2.233 ± 0.093
W16	16.672	0.44	ID1029	21:40:20.97	-23:10:43.43	0.108	0.245	RG	23.692 ± 0.060	4.929 ± 0.064
W17	3.843	0.46	ID1681	21:40:22.18	-23:10:43.83	0.297	0.646	–	22.648 ± 0.060	–
MSP A	3.870	0.43	ID1217	21:40:22.39	-23:10:48.35	0.399	0.928	RG	22.272 ± 0.054	3.859 ± 0.057

a) 95% error circle.

b) Characteristic uncertainty, Err = Distance/P_{err}.

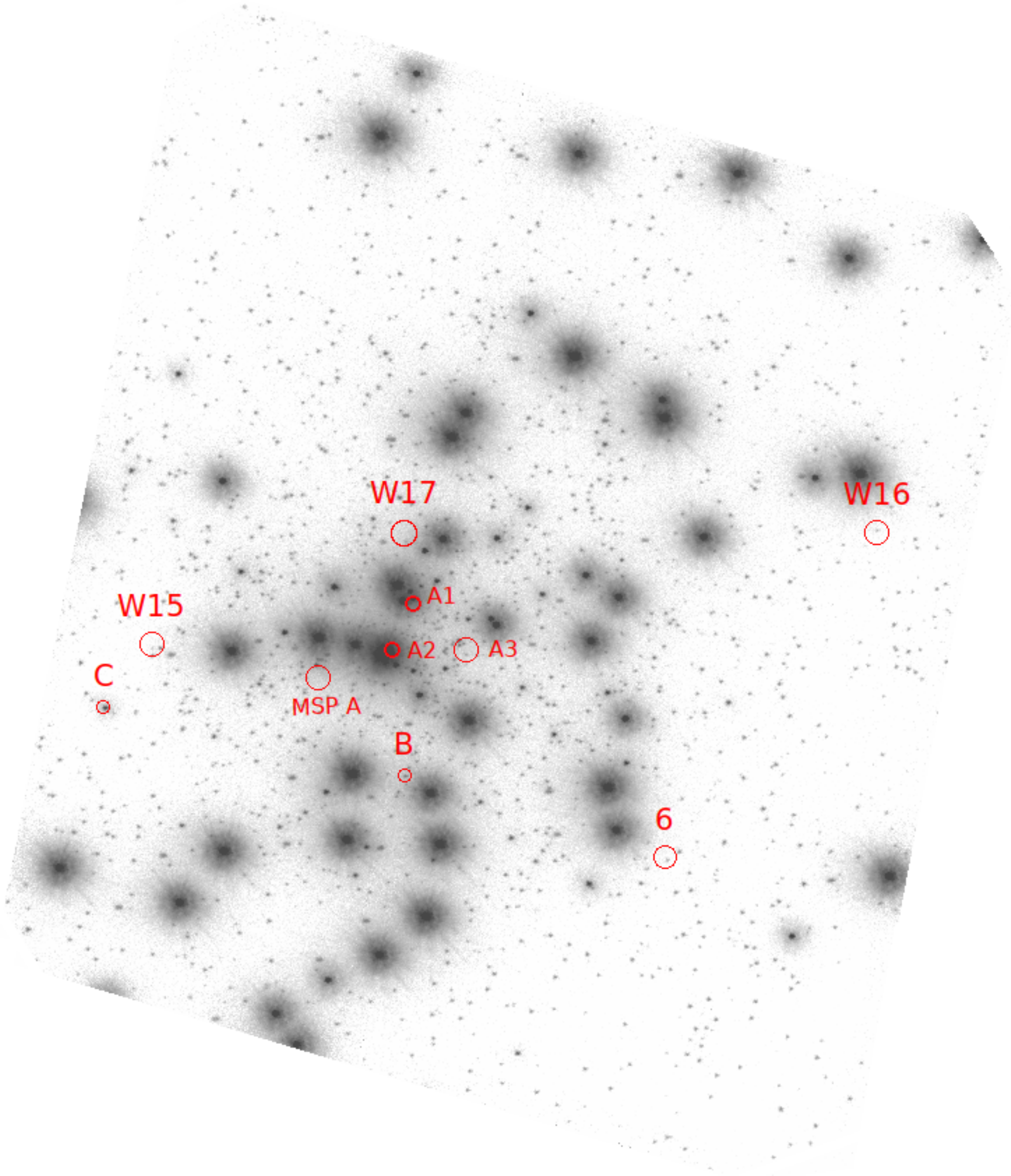

Figure 3.1: Positions of the 10 X-ray sources listed in Table 3.1, seen as red circles with sizes proportional to their positional uncertainties, superimposed onto the FUV master image of M30. North is up, east is to the left and the image spans $34.6'' \times 30.8''$.

the uncertainties of $0.70''$ in the world coordinate system (WCS) for both *HST* and *Chandra*. This positional shift is then applied to the Lugger et al. (2007) X-ray sources in order to match to our dataset. These 13 sources were also detected by Zhao et al. (2020), as well as an additional 10 sources within the updated half mass radius of $1.03'$ (Harris 2010). By comparing the coordinates given for the 13 sources discovered by Lugger et al. (2007) to those of Zhao et al. (2020), an additional shift can be applied to the new 10 sources to match them to our dataset. Out of the 23 total sources, 10 are within the FUV field of view and are marked in Fig. 3.1. After comparing the datasets, we find six confident matches: ID283 to A2, ID1647 to B, ID456 to C, ID1700 to 6, ID912 to W15 and ID1029 to W16 (described in detail in Sect. 3.3). The average distance of these six sources to their X-ray counterparts was $0.148''$, which is then used as an additional boresight correction to shift the X-ray catalogue into the FUV frame. After this shift the confident matches have an average positional offset of $0.071''$.

3.2.3 Brightness variability

For the variability study, the magnitudes of the individual 64 FUV exposures are measured using the DAOPHOT task (Stetson 1987), running under PYRAF (Greenfield & White 2000). As the individual images are slightly shifted with respect to one another, a specific coordinate list of the sources is first created for each exposure, using the coordinate list of the drizzled master image from Paper I. This list is transformed into individual coordinate lists using the task WCSCTRAN which takes the WCS information from each exposure. Then the DAOPHOT task performs aperture photometry on each exposure using the specific coordinate list. This task was performed without recentering which would measure the magnitude of a nearby bright star if the flux at the target coordinate is faint. Aperture and sky corrections to the measured fluxes are applied using the same method described in Paper I (Sect. 2.2.1).

3.3 X-ray source matching

3.3.1 Positional error radii

The X-ray sources are given in Table 3.1 along with their potential counterparts. The positional 95% error radii P_{err} is included for each X-ray source and is shown in Figs. 3.1, 3.3 and 3.4 as red circles. For the bright sources (> 100 counts, i.e. sources A1, A2, B and C), we calculate P_{err} using the positional uncertainties of the six confident matches and the formula:

$$\sigma_r^2 = \sigma_{RA}^2 + \sigma_{Dec}^2 \tag{3.2}$$

After applying the shifted boresight correction, the rms errors in RA and Dec are 0.076″ and 0.063″ respectively, correlating to 1σ in each of the two directions. A 95% error radii corresponds to 2.45σ and as such the resulting P_{err} for the bright sources is 0.243″.

For the fainter sources, we take the 95% error radii for *Chandra* ACIS-S given by Zhao et al. (2020) and calculated from the individual source count and offset (Hong et al. 2005). Then all the FUV sources within P_{err} are marked with blue circles in Figs. 3.3 & 3.4.

3.3.2 Chance coincidences

In the dense core of the cluster, there may be stars within the positional error radii that are chance coincidences. To estimate the number of chance coincidences of each stellar population within these radii, we follow the method of Zhao et al. (2020), and split the cluster into concentric annuli, with 1 arcsec thicknesses over the 15 arcsec radius contained in our field of view. Assuming the populations are evenly distributed within each annulus, we can then calculate the number of chance coincidences, N_C, using the number of stars in each population in each annulus, N_{tot}, the area of each annulus, A_{ann}, and the area of the 95% positional error radii, A_{err}, in the formula:

$$N_C = N_{tot} \times \frac{A_{err}}{A_{ann}} \tag{3.3}$$

which we have applied to the bright and faint X-ray sources separately, using the value $A_{err} = 0.18$ arcsec^2 for the bright sources and the average value $A_{err} = 0.58$ arcsec^2 for the faint sources. The number of chance coincidences found within the error circle for either a bright or a faint X-ray source

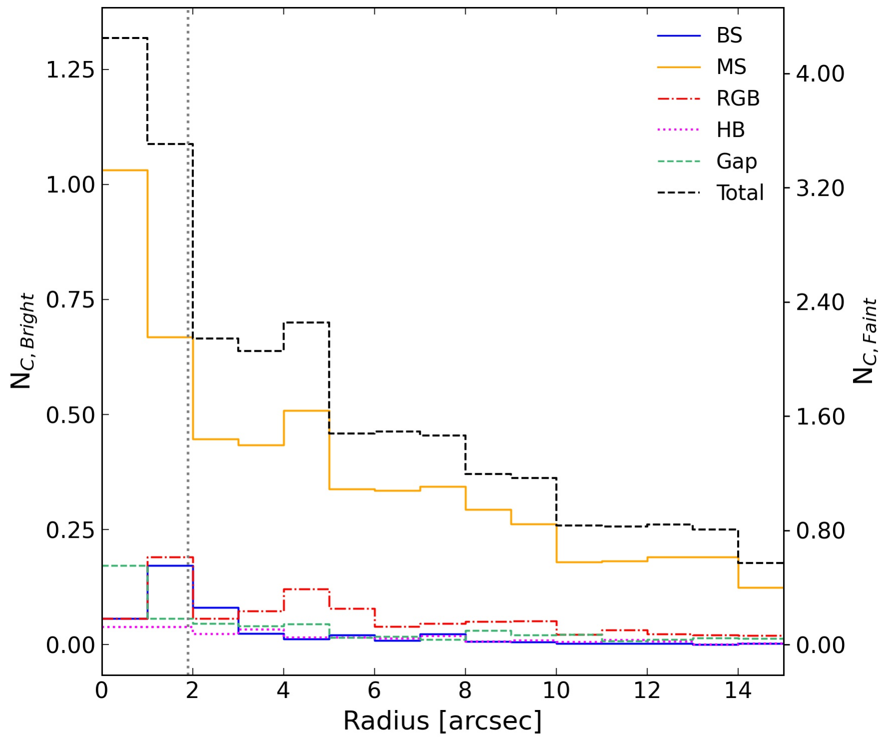

Figure 3.2: Number of chance coincidences within the error circle for either a bright or a faint X-ray source, plotted as a function of radial distance from the centre of the cluster. For a bright source the error radius $A_{err} = 0.18$ arcsec^2 is used and for a faint source $A_{err} = 0.58$ arcsec^2 is used. The dotted vertical line indicates the cluster core region. The group Total gives the chance of finding any coincidental star in the error radii.

is shown in Fig. 3.2 for each population, as well as the total chance of finding any type of star. As the area of the 95% positional error is slightly more than three times as large for the fainter X-ray sources, the number of chance coincidences within these radii are also slightly more than triple. Within the very core of the cluster, the number of a chance coincidence of any type of star is 1.32 in the area around a bright X-ray source, but drops to an average of 0.52 over the rest of the *FUV* field of view. The average number of chance coincidences within a faint X-ray error circle is 1.66.

3.3.3 Cluster membership probability

Some of the ultraviolet sources discussed in this section, and also in Sect. 3.4, have cluster membership probabilities calculated from their proper motions derived from the *Hubble Space Telescope UV Legacy Survey of Galactic Globular Clusters* (HUGS) catalogue (Piotto et al. 2015; Nardiello et al. 2018). The values for these sources are given in Table 3.2.

3.3.4 Potential X-ray counterparts

A total of 16 *FUV* sources are located within the 10 X-ray positional error radii. In order to see if we can already identify a number of these sources as confident matches based on their positions alone, we count the number of *FUV* sources within the error radii at several small and increasing offsets. Due to the crowding in the centre of the cluster, the total number of *FUV* sources within all 10 error radii remained roughly the same at different offset positions. This indicates that a detailed examination

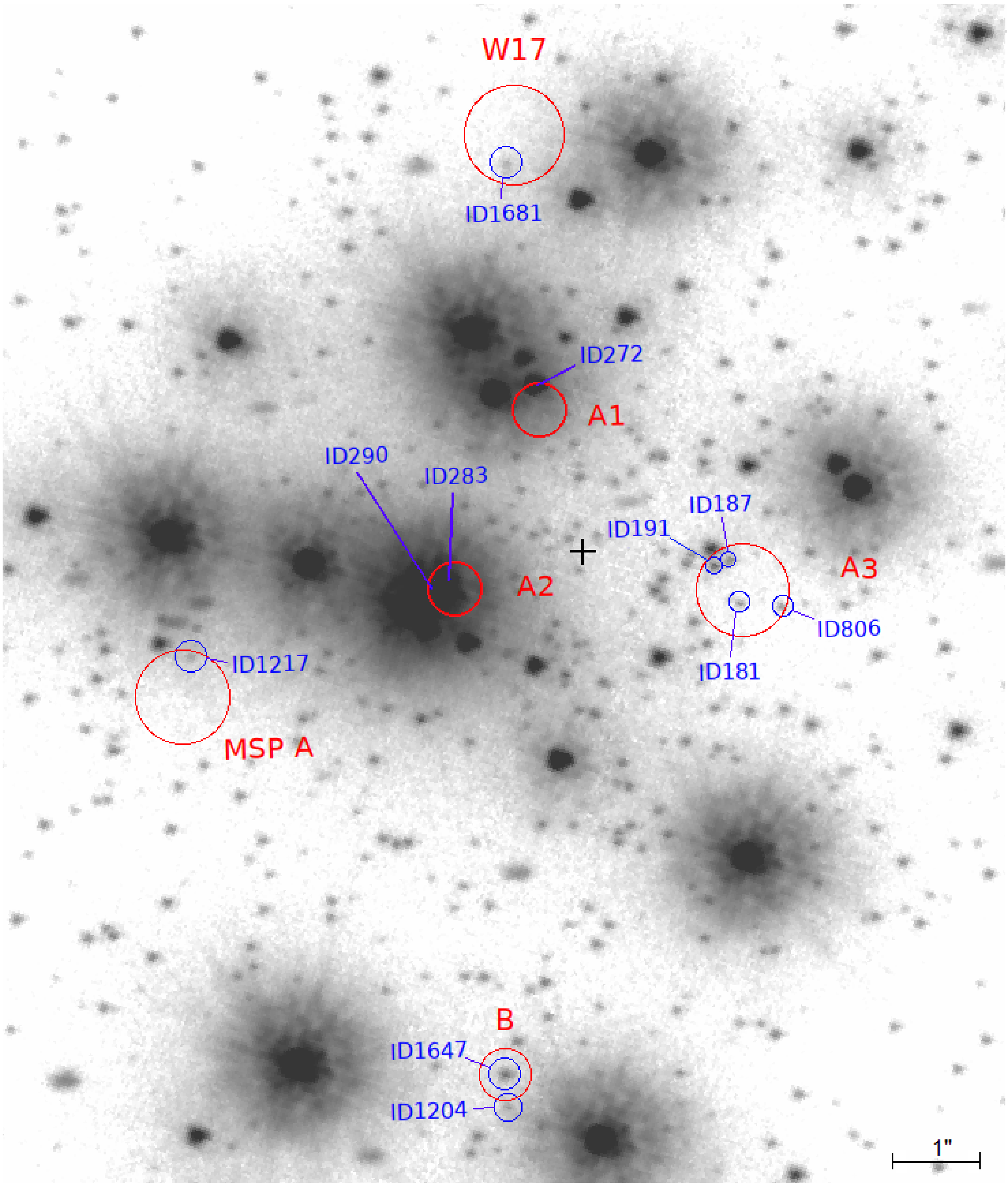

Figure 3.3: Position of X-ray sources with 95% error radii, marked with red circles. The potential counterparts are given in blue. The black cross indicates the centre of the cluster.

into the characteristics of each potential X-ray counterpart is needed to evaluate the likelihood of associating it with the X-ray source. This examination will include an analysis of the photometric properties in both optical and ultraviolet wavelengths. The locations of these sources in the $FUV - UV$ CMD are marked in Fig. 3.5, which includes their optical counterpart locations in the $B - V$ CMD from the Guhathakurta et al. (1998) catalogue. The coordinate transformation to the optical catalogue was described in Paper I. The examination will also include a consideration of any variability which is discussed in Sect. 3.4 (Figs. 3.6, 3.7 and 3.8).

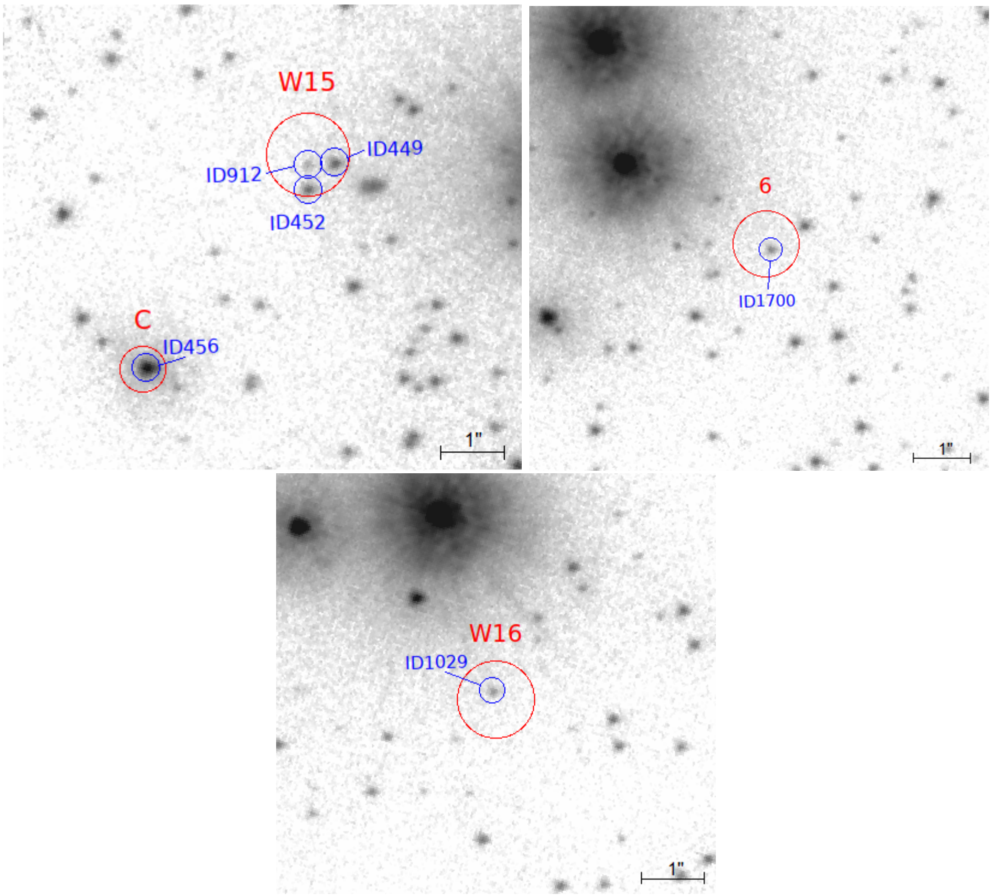

Figure 3.4: Same as Fig. 3.3.

Source A1

The X-ray source A1 (Lugger et al. 2007) is thought to be a qLMXB with a neutron star that has either a He atmosphere or a H atmosphere with significant hotspots (Echiburú et al. 2020). As LMXBs in a quiescent state have very reduced or no accretion, they are generally faint at ultraviolet and other wavelengths. Zhao et al. (2020) note that the donor star should be a He WD if the neutron star has a He atmosphere, and it could be a MS star if the neutron star has hotspots which distort the spectrum. Lugger et al. (2007) suggest two MS stars that lie close to the MS turnoff in the optical CMD as possible companions, however they note that the area in the vicinity of A1 is severely crowded. As A1 lies within 2″ of the cluster centre, the number of coincidental stars within the error radii at this radius is 1.09. From our dataset, there is only one potential counterpart that lies on the edge of the error circle for A1, a BS star ID272 with a bright FUV magnitude (≈ 17.2 mag), making it one of the brightest BS sources, and it it also relatively bright in the optical, with $V = 18.16$ mag (Guhathakurta et al. (1998), their source #3115). As ID272 is a bright BS star and neither a WD or MS star, it is likely that ID272 is a chance superposition in this dense region of the cluster core, and the true counterpart is too faint to be seen in the FUV.

Source A2

Lugger et al. (2007) consider the brightest FUV source (#3327 in Guhathakurta et al. 1998, ID290 in this work) as a possible companion to the X-ray source A2 as it sits within 0.50″ of it. However they note that the crowding in this central region of the cluster (Fig. 3.3, $N_{C,Bright} = 1.09$) may mean that a different star may be the companion. From our dataset, the error circle for A2 includes source

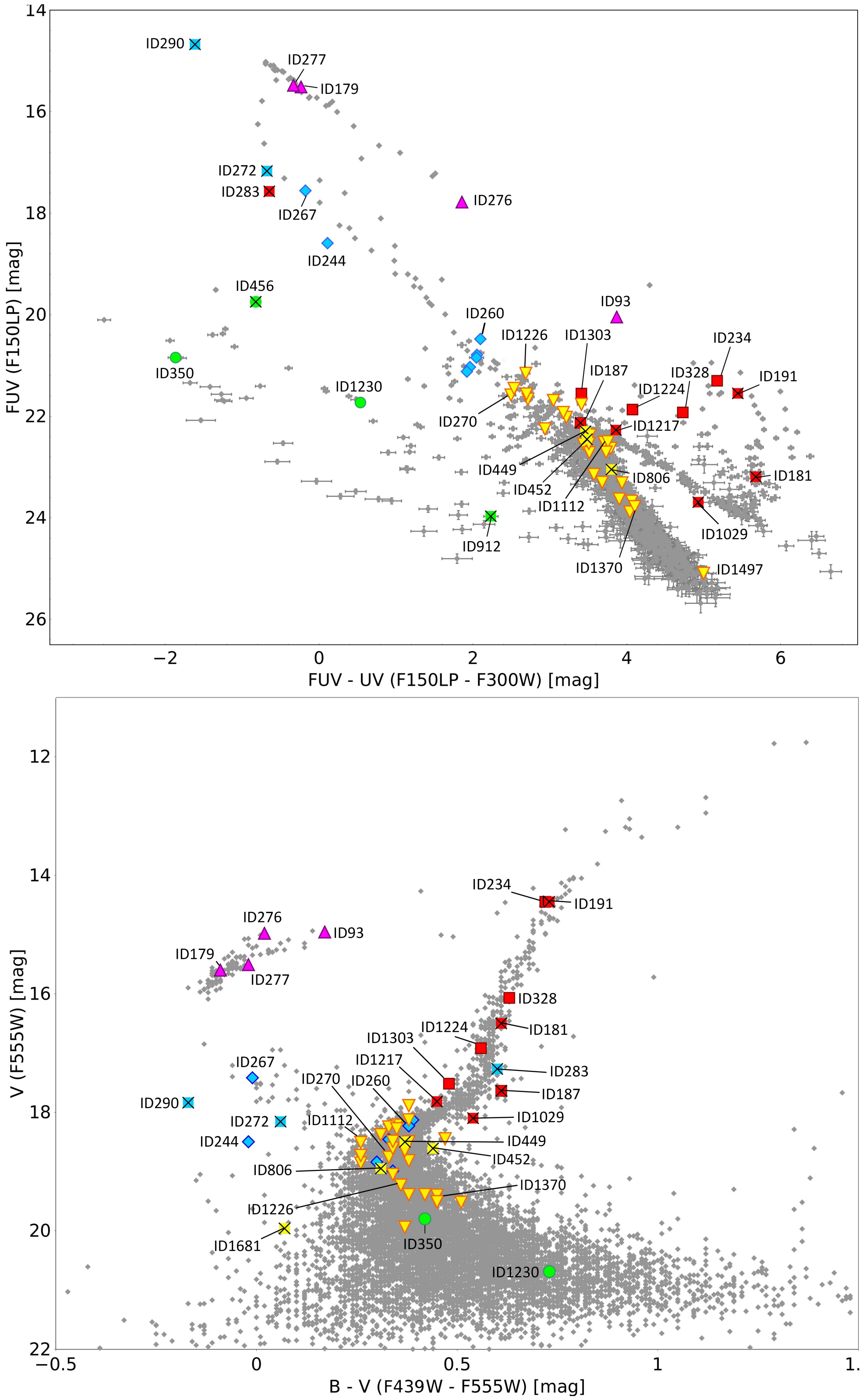

Figure 3.5: *FUV* − *UV* (top) and optical (Guhathakurta et al. 1998, bottom) CMDs with the positions of the variable BS (blue diamonds), HB (purple up triangles), MS (yellow down triangles), RGB (red squares) and WD/Gap (green circles) sources marked. The colours and shapes in one CMD are given based on the source location in the other CMD. Those mentioned in the text are numbered and their properties are in Table 3.3. Additionally, the potential counterparts to the X-ray sources (Lugger et al. 2007; Zhao et al. 2020) are marked with crosses and are numbered. The reason that source ID283 is marked differently in the two CMDs is discussed in the text.

ID290 at a distance of 0.224″ which is located in the BS region in the optical CMD (Fig. 3.5), but has the brightest *FUV* magnitude in this work. Lugger et al. (2007) conclude that this source is likely to be a sub-dwarf B star (sdB) with a WD companion. Yet, as noted by Lugger et al. (2007), not many sdB binaries are known to emit X-ray emission and thus its proximity to A2 could be a chance superposition. There is one other source within the error circle: ID283 at a distance of 0.078″ from A2. This is an interesting counterpart candidate as in the $FUV - UV$ CMD it has the position of a bright BS star, however in the optical CMD it is located on the red giant branch. This likely represents a binary system in which the RGB star has overfilled its Roche Lobe and is transferring mass to a compact companion resulting in strong *FUV* emission. CVs undergoing substantial mass transfer appear considerably bluer in the ultraviolet relative to their optical colours. These objects are rare although have been found in other globular clusters (eg. Edmonds et al. 2003). Thus, it is likely then that ID283 is the counterpart to the X-ray source A2 and is a CV system with a red giant donor star.

Source A3

The source A3 was a faint X-ray detection with no optical counterparts proposed by Lugger et al. (2007). In our work, there are four sources within the error circle of A3, all with optical counterparts. One MS star lies on the edge of the error circle, ID806, which is located in the MS in both optical and ultraviolet CMDs. As this source does not show significant variability (Sect. 3.4), this is unlikely to be the counterpart to A3. The number of chance coincidences within the faint X-ray source error radii at this distance from the centre is 1.60 for a MS star and 0.25 for a red giant (Fig. 3.2). Three RGB stars are also in the error circle, making one of these likely to be the correct counterpart. The closest to the X-ray source is ID181 at a distance of 0.134″, and the other two ID187 and ID191 are at distances of 0.289″ and 0.336″ respectively. ID191 shows no variability, however ID181 and ID187 are interesting possibilities as counterparts to A3 as they are both slightly variable stars which could result from instabilities in accretion if they are binary systems. As seen later in Sect. 3.4, ID187 has a larger standard deviation relative to sources of similar *FUV* magnitude than ID181, and it appears bluer in the ultraviolet CMD relative to the other red giants than in the optical CMD. Thus, the most likely counterpart to A3 is the variable RGB star ID187, with the closer RGB star ID181 also a possibility.

Source B

Lugger et al. (2007) suggest a faint companion to X-ray source B that lies in the halo of a RGB star and is located on the MS in their infrared CMD, but has blue excess in the ultraviolet, and concluded that source B is a potential CV. However, no MS star was detected at the location of source B in this present work, and the RGB star ID1204 is located just outside of the error circle for B, at a distance of 0.288″ and did not show any significant variability. Only one source is located within the error circle for source B, ID1647, which is only detected in the *FUV* and has no *UV* counterpart. At a distance of 0.005″ from source B, this is the likely counterpart to B and the source which showed blue excess in Lugger et al. (2007). Piotto et al. (2015) and Nardiello et al. (2018) also find a source at this position with a cluster membership probability of 90.5%. The light curve for ID1647 is given in Fig. 3.8 which shows little variability, and as the detection limit is $UV = 23.6$ (Paper I), it is likely that the companion to source B is a faint MS star, as suggested by Lugger et al. (2007).

Source C

One ultraviolet source is detected within the error circle of X-ray source C (Fig. 3.4), a WD/Gap object ID456 at a distance of 0.038″. This source was found by Lugger et al. (2007) to be a CV as it was fainter in the year 1999 by 1 mag than in 1994. ID456 is shown as a variable WD/Gap object in Sect.

Table 3.2. Cluster membership probabilities of some of the sources discussed in the text, from the HUGS catalogue (Piotto et al. 2015; Nardiello et al. 2018)

ID	P_{μ}(%)
93	92.6
179	44.2
181	90.2
187	88.5
191	88.5
268	97.5
272	97.1
276	98.0
277	96.9
350	85.1
456	94.3
912	96.7
1029	97.5
1217	95.6
1226	96.7
1230	96.7
1647	90.5
1681	90.5

3.4, where its magnitude in the first observing epoch was ≈ 1.5 mag brighter than in the latter two epochs (Fig. 3.12). We agree then that ID456 is a CV that is experiencing a dwarf nova event. ID456 is one of the brightest Gap sources, with $FUV \approx 19.7$ mag, however as no source was detected in the optical at this location, and the optical detection limit is $V \approx 22$, this suggests a very faint low-mass MS companion. Göttgens et al. (2019) also classify this source (ACS ID 23423) as a CV due to its broad Hα and Hβ emission detected with the Multi Unit Spectroscopic Explorer (MUSE, Bacon et al. 2017)

Source 6

One source, ID1700, lies at a distance of 0.090″ from X-ray source 6 from Lugger et al. (2007) and is detected in the FUV but is not seen in the UV. Due to the detection limit of $UV = 23.6$ (Paper I), the companion is likely a very faint MS star.

Source W15

Of the 10 additional X-ray sources detected by Zhao et al. (2020), three are in our FUV field of view: W15, W16 and W17. Three ultraviolet sources are found within the error circle of W15: two MS stars, ID449 and ID452, and a gap source, ID912. The number of chance coincidences of MS stars in the error radius for W15 is 0.845 but for a gap source is only 0.068, meaning that the gap source is the more likely true counterpart. The gap object is also the closest to W15 at a distance of 0.109″, and corresponds in position to the optical counterpart for W15 proposed by Zhao et al. (2020), who confirmed that it is a cluster member with a probability of 96.7% (Piotto et al. 2015; Nardiello et al. 2018), and that this source has a blue excess in ultraviolet to infrared wavelengths, thus concluding that W15 is a CV. This source was not in the Guhathakurta et al. (1998) catalogue, but due to its location blueward of the MS in the $FUV - UV$ CMD and its proximity to W15, we agree that ID912 is most likely a CV.

Source W16

Zhao et al. (2020) suggest a subgiant as a companion to W16 which correlates to the position of ID1029, a source that is located just below the red giant branch in both the $FUV - UV$ and optical CMDs in this work. At a distance of 0.108″ from W16, it is the only source detected in the FUV to be within the error circle of X-ray source W16. As Göttgens et al. (2019) find variable Hα emission from this source using MUSE, Zhao et al. (2020) propose that this is an RS CVn type of AB. The FUV light curve for ID1029 illustrated in Sect. 3.4 shows that it is not more variable relative to other sources with similar FUV magnitudes (Fig. 3.6).

Source W17

Only one source was found within the error circle for W17, ID1681, another source with an FUV detection but no counterpart in the UV, however it does have a counterpart from the optical catalogue (Guhathakurta et al. 1998, their source #3175); a star located blueward of the MS in the optical CMD. Piotto et al. (2015) and Nardiello et al. (2018) also find a source at this position with a cluster membership probability of 98.1%. Zhao et al. (2020) proposed two potential counterparts to W17, both MS stars which exhibit brightness variability, neither of which match to the position of ID1681. The light curve for ID1681 is shown in Fig. 3.8, which only shows a slight variation in magnitude.

MSP A

Two MSPs were found in M30 by Ransom et al. (2004) using radio pulsar timing, one of which (PSR J2140–2310A, MSP A) was also faintly observed in X-ray wavelengths by Ransom et al. (2004) and is detected again by Zhao et al. (2020), who measure a higher number of X-ray counts for MSP A. Ransom et al. (2004) suggest a MS star companion within 0.09″ of this pulsar that was seen in V_{555} images but not U_{336} or I_{814} images. This companion is not seen in our ultraviolet exposures, instead the only source within the error circle is a red giant, ID1217, located just off the MS turnoff, and at 0.399″ away from the position of MSP A, is likely to be a chance superposition.

3.4 Variable FUV sources

In order to find objects in the FUV dataset that exhibit significant variability, we plot the standard deviation, σ_{mean}, of the FUV magnitude over the mean FUV magnitude for each star (Fig. 3.6). Variable sources have a larger deviation than other sources with the same magnitude, and the red line in the figure indicates twenty percent above the binned average σ_{mean} as a rough criterion for variability. From this, seven BS, four HB, five RGB and one WD/Gap source are identified as variable, and their light curves are plotted in Fig. 3.7. The two WD/Gap sources ID350 and ID1230 are also included as they are close to the variability criterion. Also included in Figs. 3.6 & 3.7 are the gap source ID912 and the RGB stars ID181 and ID1029, as these are potential X-ray counterparts. The light curves for the three sources within X-ray source error circles that are detected in the FUV but with no UV counterparts are given in Fig. 3.8. The light curves for 28 MS stars are shown in Fig. 3.9. The other sources above the variability criterion that are not identified were unremarkable in their light curves. The cluster membership probabilities for some of the sources discussed are given in Table 3.2 (Piotto et al. 2015; Nardiello et al. 2018).

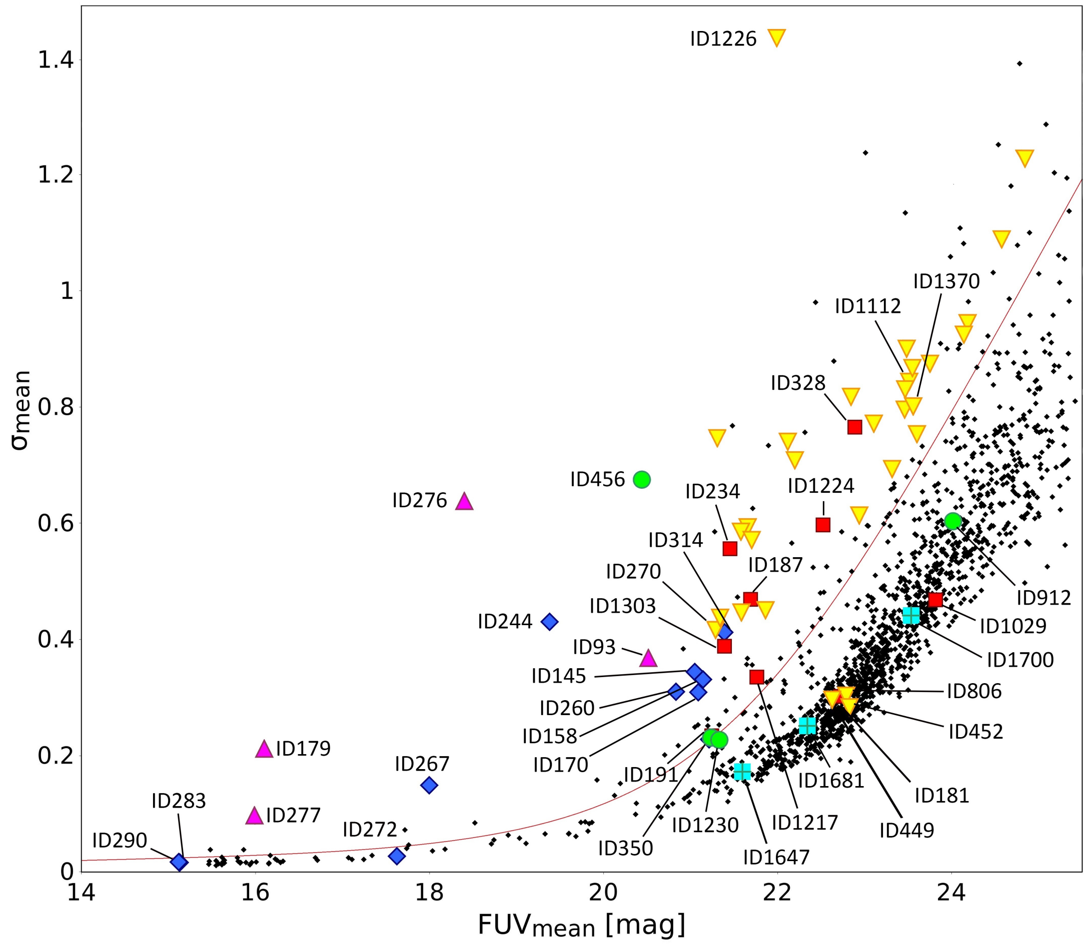

Figure 3.6: The standard deviation over time, plotted against the mean *FUV* magnitude. Marked are the variable BS sources (blue diamonds), HB stars (purple up triangles), RGB stars (red squares), MS (orange down triangles), WD/Gap objects (green circles), and sources without *UV* measurements (blue squares). The light curves for these sources are presented in Figs. 3.7 and 3.9. The faint red line indicates twenty percent above the binned average σ_{mean}.

The periods of variable objects can be estimated by producing Lomb–Scargle periodograms (Lomb 1976; Scargle 1982), which performs a Fourier transform of the light curve data points. In order to check for discrepancies in the data due to the observing window used, the window function is also calculated from a Lomb–Scargle periodogram with a non-floating mean model and without centering the data (VanderPlas 2018). The window function is plotted over the periodograms in Fig. 3.11. The accuracy of this period is checked by comparing to the folded light curves. Four of our variable sources have periods measured and these are then used to plot sine curves representing this periodicity onto the light curves. The photometric properties and any found periods are given in Table 3.3 for all variable sources. The uncertainties in the FUV_{mean} magnitudes are larger than those for the $FUV-UV$ measurements since they are taken from the individual flat-fielded exposures rather than the cleaner drizzled master image.

3.4.1 Blue stragglers

The light curves of the BS stars are shown in Fig. 3.7. The source ID267 corresponds within 0.07″ to the position of the variable M30_5, identified as a W UMa-type contact binary by Pietrukowicz &

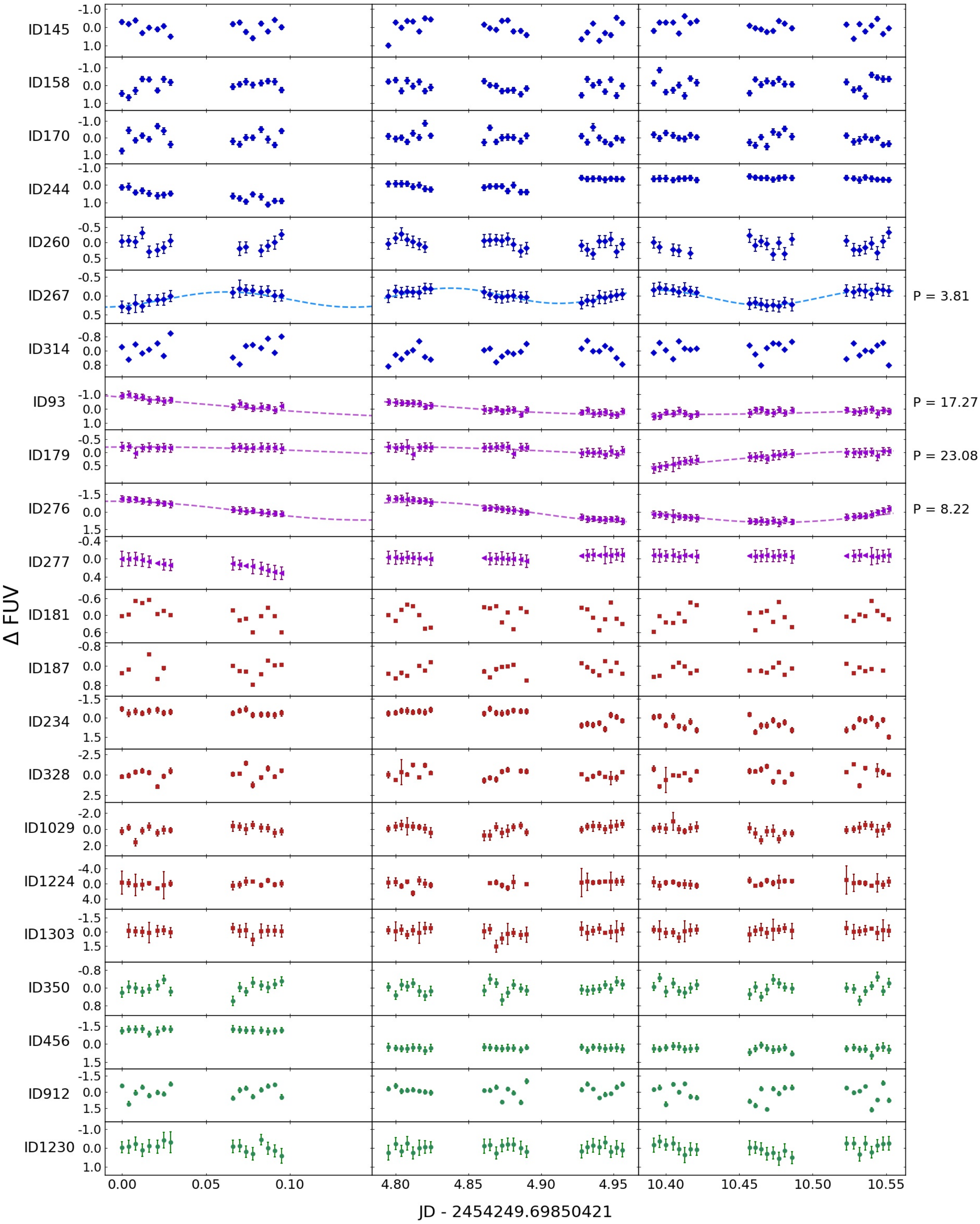

Figure 3.7: *FUV* mean-subtracted magnitudes ($\Delta FUV = FUV - FUV_{mean}$) are plotted over time for seven variable BS sources (blue diamonds), four HB stars (ID93 - ID277, purple triangles), seven RGB stars (red squares) and four gap objects (green circles). The sine curves represent the periods which are found for several sources, and the period in hours is given. The measured period of 3.81 hours for ID267 is half of the true period for this contact binary (see text).

Table 3.3. Photometric and variability parameters of all variable sources whose light curves are shown in this work.

ID	Type	FUV - UV [mag]	FUV_{mean} [mag]	σ_{mean}	Period [hours]
93	HB	3.870 ± 0.011	20.518 ± 0.099	0.368	17.27
145	BS	1.961 ± 0.030	21.050 ± 0.152	0.344	
158	BS	1.923 ± 0.037	21.146 ± 0.161	0.331	
170	BS	2.054 ± 0.034	21.091 ± 0.158	0.309	
179	HB	0.234 ± 0.002	16.103 ± 0.013	0.212	23.08
181	RG	5.677 ± 0.068	22.726 ± 0.274	0.302	
187	RG	3.971 ± 0.037	21.690 ± 0.172	0.469	
223	MS	3.215 ± 0.091	21.658 ± 0.226	0.593	
234	RG	5.176 ± 0.044	21.455 ± 0.196	0.556	
242	MS	2.688 ± 0.052	21.340 ± 0.181	0.437	
251	MS	2.715 ± 0.058	21.581 ± 0.221	0.585	
260	BS	2.098 ± 0.043	20.835 ± 0.162	0.310	
267	BS	0.176 ± 0.007	17.999 ± 0.034	0.149	3.81
268	MS	3.175 ± 0.050	21.703 ± 0.229	0.571	
270	MS	2.495 ± 0.062	21.288 ± 0.170	0.416	
276	HB	1.857 ± 0.005	18.401 ± 0.038	0.638	8.22
277	HB	0.332 ± 0.002	15.989 ± 0.012	0.097	
282	MS	2.536 ± 0.032	21.862 ± 0.278	0.450	
293	MS	2.697 ± 0.046	21.585 ± 0.205	0.446	
311	MS	3.413 ± 0.056	22.200 ± 0.403	0.708	
314	BS	2.046 ± 0.092	21.390 ± 0.373	0.412	
343	MS	3.048 ± 0.066	22.120 ± 0.357	0.740	
350	Gap	-1.864 ± 0.098	21.238 ± 0.169	0.231	
380	MS	3.522 ± 0.038	23.109 ± 0.346	0.771	
448	MS	3.438 ± 0.038	23.462 ± 0.409	0.795	
455	MS	3.793 ± 0.038	23.552 ± 0.433	0.867	
456	Gap	0.821 ± 0.019	20.443 ± 0.099	0.675	
458	MS	3.706 ± 0.037	23.317 ± 0.377	0.693	
471	MS	3.513 ± 0.041	23.603 ± 0.430	0.753	
806	MS	3.801 ± 0.059	22.792 ± 0.282	0.303	
912	Gap	2.233 ± 0.093	24.019 ± 0.512	0.603	
1029	RG	3.929 ± 0.064	23.817 ± 0.429	0.468	
1081	MS	3.507 ± 0.041	23.753 ± 0.473	0.874	
1099	MS	4.067 ± 0.064	24.187 ± 0.486	0.944	
1112	MS	3.756 ± 0.036	23.513 ± 0.423	0.843	
1126	MS	3.732 ± 0.047	23.469 ± 0.412	0.830	
1206	MS	2.937 ± 0.049	21.309 ± 0.149	0.746	
1224	RG	4.074 ± 0.057	22.524 ± 0.471	0.597	
1226	MS	2.491 ± 0.064	21.992 ± 0.556	1.437	
1230	Gap	0.539 ± 0.054	21.333 ± 0.147	0.227	
1235	MS	3.682 ± 0.055	24.143 ± 0.570	0.924	
1240	MS	4.041 ± 0.065	24.577 ± 0.712	1.088	
1260	MS	3.903 ± 0.065	22.847 ± 0.312	0.817	
1303	RG	3.412 ± 0.036	21.391 ± 0.176	0.388	
1334	MS	3.937 ± 0.053	23.484 ± 0.422	0.900	
1370	MS	4.104 ± 0.070	23.560 ± 0.433	0.801	
1473	MS	3.573 ± 0.051	22.942 ± 0.314	0.613	

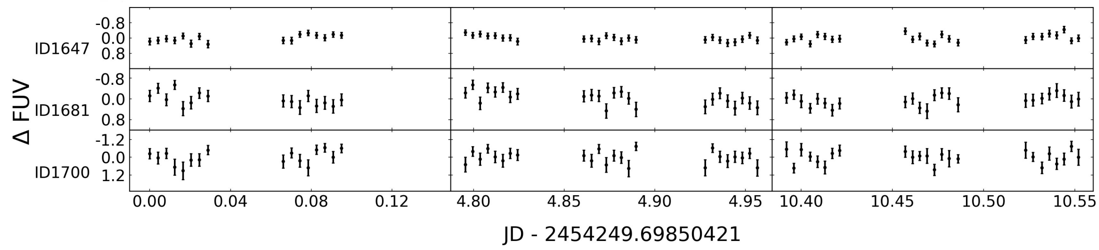

Figure 3.8: *FUV* light curves for the three potential X-ray counterparts that have no matching *UV* measurement. The mean-subtracted magnitude is plotted over time.

Kaluzny (2004) who measure a period of 7.61 hours. Due to the symmetry of such a system, the light curve would show a double-peak, and in our dataset we measure the half-period of 3.81 hours (Figs. 3.7 & 3.11), however 7.61 hours would be the true period for this system. Pietrukowicz & Kaluzny (2004) measured a maximum V magnitude for this star of 17.28 mag, which also agrees well to the value of 17.42 mag of the matched optical counterpart to ID267 from the Guhathakurta et al. (1998) catalogue (their source #3238).

3.4.2 Horizontal branch stars - RR Lyrae

RR Lyrae are variable giant stars with spectral class A−F and are generally found on the horizontal branch in globular clusters. The sub-group RRab have steep and asymmetrical light curves with periods in the range of 12−20 hours, whereas the light curves for the sub-group RRc are more sinusoidal with shorter periods of 8−10 hours (Bailey 1902; Smith 1995). Four HB stars in our dataset were found to be variable, two of which have periods of 8.22 and 17.27 hours, indicating that these are RR Lyrae variables. ID93 matches in position within 0.12″ of M30_2, identified by Pietrukowicz & Kaluzny (2004) as an RRab variable. Our period of 17.27 hours agrees well to the period of 16.54 hours found for M30_2 (Pietrukowicz & Kaluzny 2004). These authors found a maximum V magnitude for this star of 15.21 mag, which also agrees well to the value of 14.96 mag of the matched optical counterpart to ID93 from Guhathakurta et al. (1998) (their source #2105). ID93 also correlates in position to V15 from Kains, N. et al. (2013), who find a period of 16.23 hours and V = 15.07, as well as V15 from Göttgens et al. (2019), who find that it exhibits variable Hα emission which is typical for RR Lyrae stars.

The other HB star, ID276, found in this work to have a period of 8.22 hours, matches within 0.15″ to M30_3, an RR Lyrae variable of type RRc which has a period of 8.18 hours (Pietrukowicz & Kaluzny 2004). These authors measured V_{max} = 15.08 mag, in agreement to the optical counterpart #3009 from Guhathakurta et al. (1998) which had V = 14.98 mag. ID276 also corresponds to V19 from Kains, N. et al. (2013) who find a period of 8.24 hours. Our period of 8.22 hours was found by taking the second highest peak from the periodogram (Fig. 3.11), which was double the frequency of the highest peak. This was done as the frequency of the highest peak did not produce a reasonable folded light curve and because the second highest peak corresponds well to the literature period values.

One of the other variable HB stars, ID179, is potentially a new RRab identification although it has a slightly long estimated period of 23.08 hours and also a low cluster member probability of 44.2% (Piotto et al. 2015; Nardiello et al. 2018). No period was found for the other variable HB star ID277 but it is a cluster member with probability of 96.9% (Piotto et al. 2015; Nardiello et al. 2018). These sources are located on the HB in the *FUV* – *UV* CMD in Fig 3.5, with *FUV* = 15.51 for ID179 and *FUV* = 15.48 for ID277. ID179 is found at the position $\alpha = 21^h40^m2225, \delta = -23^\circ10'5851$ and ID277 at $\alpha = 21^h40^m2203,\ \delta = -23^\circ10'3925$.

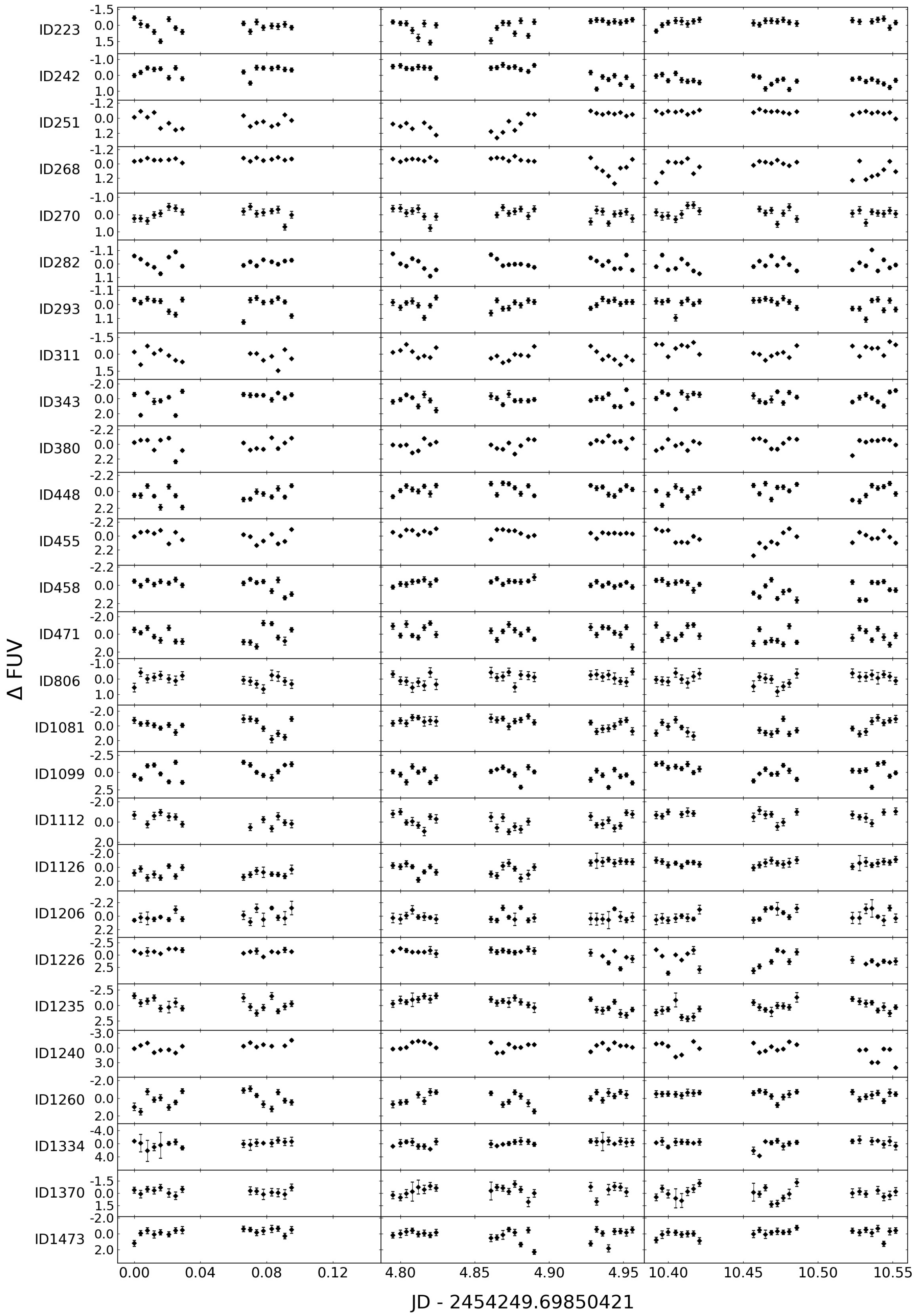

Figure 3.9: Light curves for the 28 MS stars which showed variability.

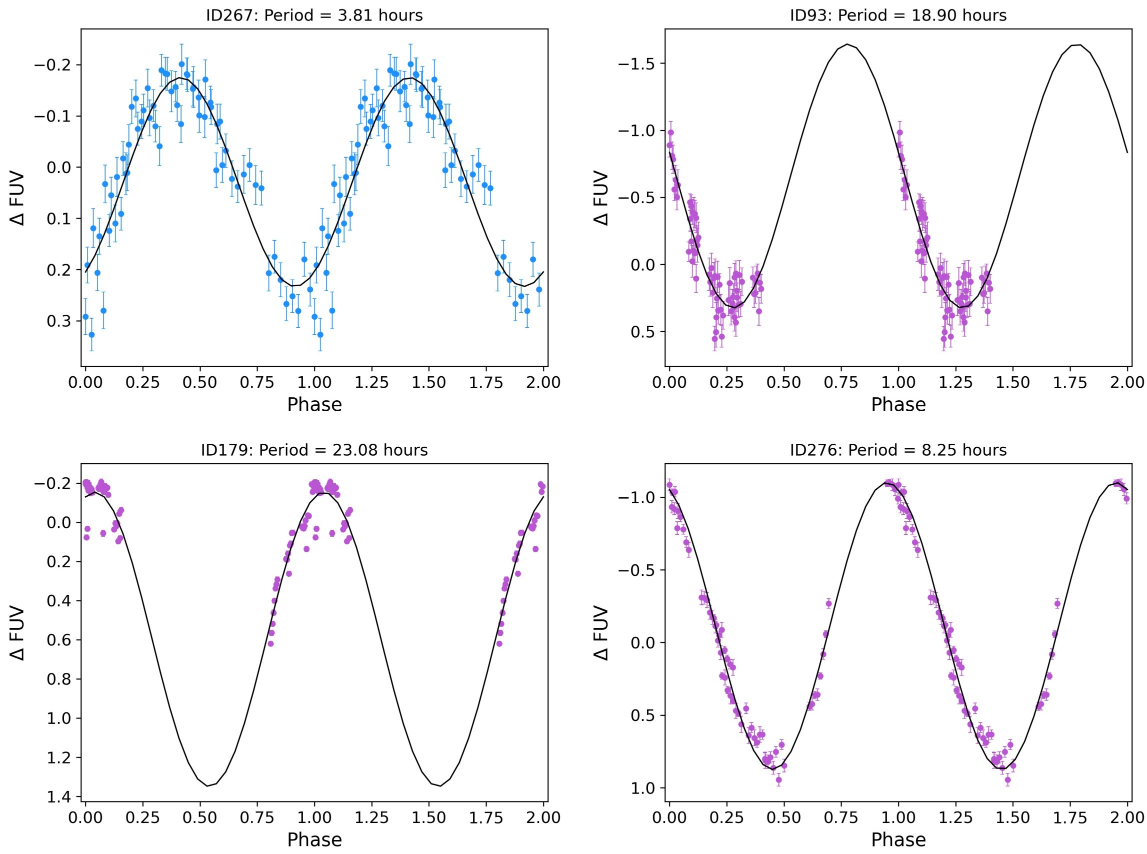

Figure 3.10: Folded light curves for the BS and HB stars with estimated periods shown in Fig. 3.7. The measured period of 3.81 hours for ID267 is half of the true period for this contact binary (see text).

3.4.3 Red giant branch stars

As mentioned in Sect. 3.3, sources ID181 and ID187 are located at a distance of 0.134″ and 0.289″ of the X-ray source A3 (Lugger et al. 2007) respectively. As ID187 has a larger σ_{mean} relative to sources of similar *FUV* magnitudes, and ID181 only shows variations comparable to other stars at the same magnitude, this suggests that ID187 may have overfilled its Roche Lobe and is transferring mass to a low-mass compact companion which results in X-ray and variable ultraviolet emission.

The RGB star ID234 is located at the tip of the red giant branch and shows stability in magnitude for the first and most of the second observing epochs but exhibits fluctuations in magnitude during the last epoch. This behaviour is also seen in MS stars ID268 and ID1226 in Sect. 3.4.5, the cause of which is unknown. The sub-subgiant ID1029 was included in Fig. 3.7 as it was the only source within the error circle of X-ray source W16, however as seen in Fig. 3.6, it is no more variable in the ultraviolet than other sources of similar magnitudes.

3.4.4 WD/Gap sources

The *FUV* light curves for four of the WD/Gap sources are shown in Fig 3.7. Source ID456 is, as indicated in Sect. 3.3, 0.038″ from the X-ray source C, and was proposed by Lugger et al. (2007) to be a CV, as it had decreased in the *UV* by 1 mag from 1994 to 1999. In the present work, ID456 decreases by roughly 1.5 mag in the *FUV* from the first observing epoch to the second, which is representative of a dwarf nova and is pictured in Fig. 3.12. Göttgens et al. (2019) finds that this source exhibits broad

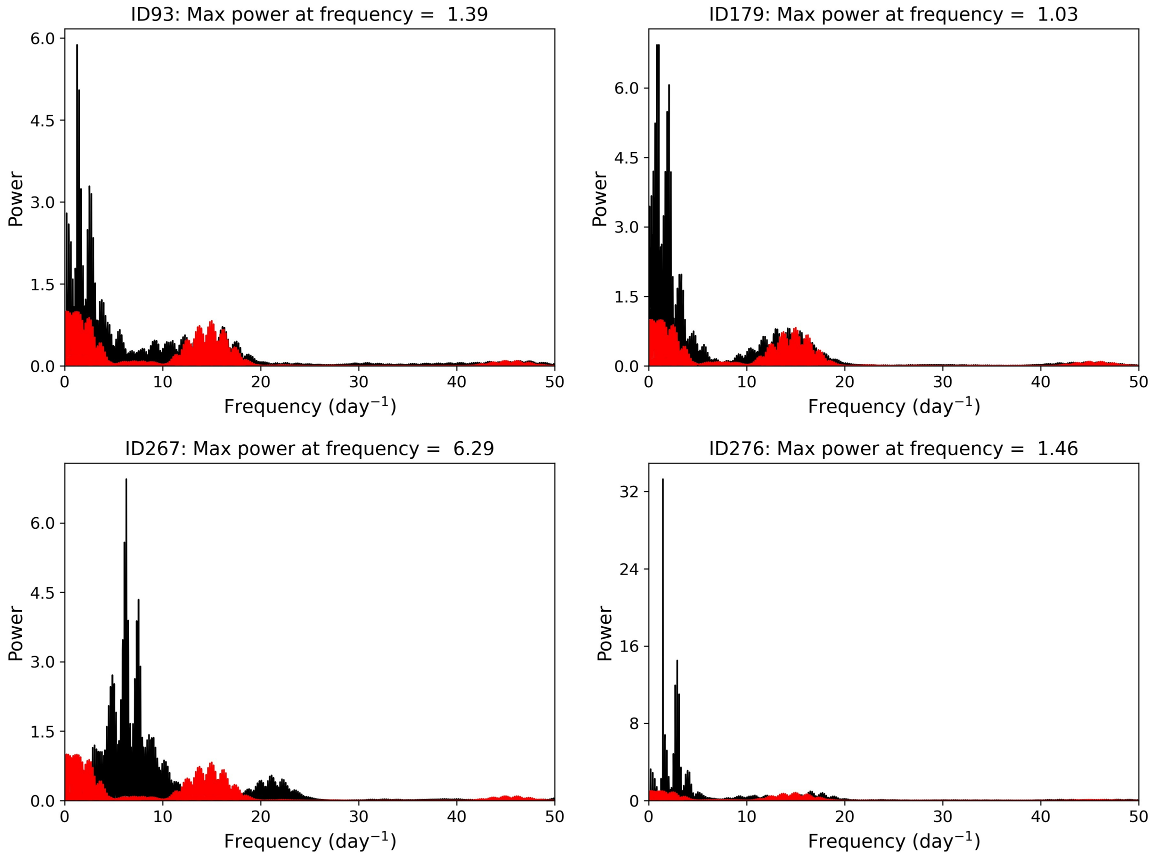

Figure 3.11: Lomb–Scargle periodograms (black) of the sources with periods measured along with the window function plotted in red.

Hα and Hβ emissions representative of accretion and it is thus very likely that this long-period CV candidate is the counterpart to the X-ray source C.

ID912 is the likely counterpart to X-ray source W15 making this source a potential CV, which was found by Zhao et al. (2020) to have a blue excess, however the σ_{mean} for ID912 is not much larger than other sources of similar magnitudes.

Sources ID350 and ID1230 lie close to the variability criterion (Fig. 3.6), but their light curves only show slight variations. As such, these two sources can be considered weak variables.

3.4.5 Main sequence stars

The light curves for the MS stars which exhibit variability are given in Fig. 3.9. The fluctuations of many of the MS stars seem more erratic than for the other populations which may indicate starspot activity (Brown et al. 2011). Some stars show little variance in magnitude over the course of one observing day, and then have large variations on another day, for example sources ID268 and ID1226 (this behaviour was also seen in the RGB star ID234). ID1226 has one of the highest σ_{mean} values and remains stable for almost two observing epochs and then exhibits a period of large variability before settling into a stable period again.

Source ID806 is on the edge of the error circle for X-ray source A3, and whilst it shows slight fluctuations in *FUV* magnitude, its σ_{mean} is no larger than sources of similar magnitude, and it remains likely that one of the RGB stars is the likely counterpart to A3.

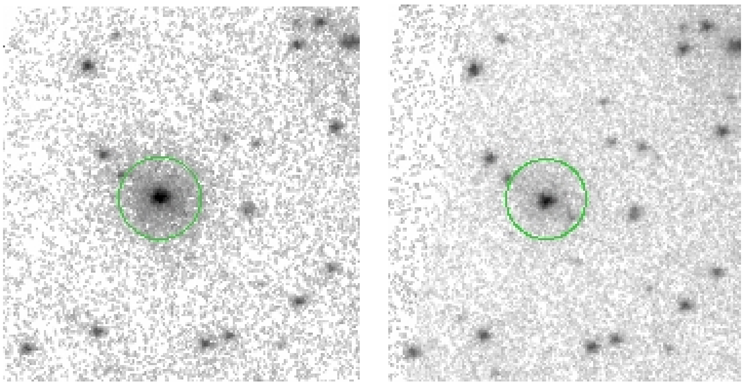

Figure 3.12: *FUV* image of the CV candidate ID456 during dwarf nova outburst (left) and quiescence (right).

3.5 Summary

We performed a comparison of the positions of the sources detected in the far-ultraviolet to known X-ray sources and possible companions or counterparts to these were discussed. The crowding in the center of the cluster makes it difficult to determine the exact counterparts, and in this work all those that are within the 95% error radii of the X-ray source are considered. Out of the ten X-ray sources within our field of view, six confident counterparts are: the RGB star with strong *FUV* emission ID283 to X-ray source A2, the gap source ID456 to source C, agreeing with Lugger et al. (2007) that this is a CV, gap source ID912 to X-ray source W15, agreeing with Zhao et al. (2020) that this is also a CV, RGB star ID1029 to W16 which was proposed by Zhao et al. (2020) to be a RS CVn, and the two sources detected in the *FUV* but with no matching *UV* counterparts: ID1647 to X-ray source B and ID1700 to source 6. Although MS stars are much more numerous in the core region of globular clusters, if we include ID187 as the possible counterpart to A3, then three of the counterparts to the ten X-ray sources are red giants.

Light curves were shown for *FUV*-variable objects and we found periods for four of these sources. Several of these variables were considered as potential X-ray counterparts. Out of the seven variable BS stars, the half-period is measured for one of them that is a known W UMa-type contact binary. Four HB stars show variability, two are known RR Lyrae variables and one (ID179) is potentially a new RR Lyrae (RRab) classification, however it may be a field star. One gap source, ID456, a previously identified CV, shows a dwarf nova event and two other gap sources have weak variability. Twenty-eight MS stars also exhibit fluctuations.

Observations into the far-ultraviolet allow us to detect and identify exotic stellar systems such as CVs which are less easily observed at optical wavelengths amongst the numerous optically-bright MS stars. Studies using ultraviolet wavelengths and multiwavelength comparisons continue to provide valuable insights into the different populations in dense stellar systems.

Chapter 4

A discontinuity in the luminosity-mass relation and fluctuations in the evolutionary tracks of low-mass and low-metallicity stars at the Gaia M-dwarf gap

Santana Mansfield, Pavel Kroupa
Astronomy & Astrophysics, Volume 650, A184, June 2021

Abstract The Gaia M-dwarf gap is a recently discovered feature in the colour-magnitude diagram that shows a deficiency of low-mass and low-metallicity stars at the lower end of the main sequence. We aim at performing theoretical stellar modelling at low metallicities using a fine mass increment and a fine timestep, looking specifically for the transition of models from partially to fully convective, since the convective kissing instability that occurs at this transition is believed to be the cause of the gap. Stellar evolution models with metallicities of Z = 0.01, Z = 0.001 and Z = 0.0001 are performed using `MESA`, with a mass step of 0.00025 $M_{\odot}$ and a timestep of 50,000 years. The small timestep produced models that experience loops in their evolutionary tracks in the Hertzsprung-Russell (HR) diagram. The fluctuations in effective temperature and luminosity correspond to repeated events in which the bottom of the convective envelope merges with the top of the convective core, transporting ^{3}He from the core to the surface. In addition to the episodes of switching from partially to fully convective, several near-merger events that produced low amplitude fluctuations were also found. Low-metallicity models undergo the convective kissing instability for longer portions of their lifetime and with higher fluctuation amplitudes than models with higher metallicities. The small mass step used in the models revealed a discontinuity in the luminosity-mass relation at all three metallicities. The repeated merging of the convective core and envelope, along with several near-merger events, removes an abundance of ^{3}He from the core and temporarily reduces nuclear burning. This results in fluctuations in the star's luminosity and effective temperature, causing loops in the evolutionary track in the HR diagram and leading to the deficiency of stars at the M-dwarf gap, as well as a discontinuity in the luminosity-mass relation.

4.1 Introduction

Stars are formed from the gravitational infall of material in molecular clouds, which produces many stars with masses lower than the mass of the Sun. A substantially greater amount of material is needed for stars with masses higher than the Sun, and so these stars are formed in much fewer numbers. Stars undergo nuclear reactions in their cores for masses $m \gtrsim 0.08$ M$_\odot$, and thus the majority of all stars have masses from this lower limit up to the solar mass.

The stellar luminosity function and the stellar mass function are used to make comparisons across all types of stars, and these functions depend sensitively on the luminosity-mass relation. This relation has long been considered a smooth and differentiable function that exhibits structure correlating to the features of the stellar luminosity function (Kroupa et al. 1990). For example, an inflection in the luminosity-mass relation at ≈ 0.30 M$_\odot$ was first discussed by Copeland et al. (1970) as the H_2 dissociation zone having a lower adiabatic gradient. The minimum in the first derivative of the luminosity-mass relation, dm/dM_{bol}, at this mass was found to correspond to the maximum of the observed luminosity function of low-mass stars (Kroupa et al. 1990; Kroupa & Tout 1997), due to H_2 formation as well as stars becoming fully convective at this mass. Thus, all mono-age and mono-metallicity stellar populations show a pronounced and sharp maximum in the stellar luminosity function at a visual absolute magnitude of $M_{\rm V} \approx 12$ (Kroupa 2002; Kroupa et al. 2013). The luminosity-mass relation has also long been known to be metallicity dependant (Elson et al. 1995; Kroupa & Tout 1997).

A recently discovered and related feature, called the *Gaia* M-dwarf gap, or Jao gap, was found in the observational *Gaia* Data Release 2 (DR2) data (Jao et al. 2018), and coincides with the same stellar mass of the inflection in the luminosity-mass relation at ≈ 0.30 M$_\odot$. This feature lies at the lower end of the main sequence (MS) in the G$_{BP}$−G$_{RP}$, M$_G$ colour-magnitude diagram (CMD), and represents a deficiency in the density of stars (and subsequently a dip in the luminosity function). This gap was recently confirmed in the *Gaia* Early Data Release 3 (EDR3) data (Gaia Collaboration, et al. 2021) at *Gaia* magnitudes $2.2 < \mathrm{G}_{BP} - \mathrm{G}_{RP} < 2.8$ and $10.0 < \mathrm{M}_G < 10.3$, and portrays a drop in density by $17 \pm 6\%$ (Jao et al. 2018). It is postulated that this occurs due to M-dwarf stars with masses around $\approx 0.30 - 0.35$ M$_\odot$ at which there is a transition from being partially to fully convective (Jao et al. 2018; Baraffe & Chabrier 2018).

The thermonuclear process for low-mass stars is governed by the proton-proton I (ppI) chain:

$$p + p \longrightarrow d + e^+ + \nu_e \tag{4.1}$$
$$p + d \longrightarrow {}^3He + \gamma \tag{4.2}$$
$${}^3He + {}^3He \longrightarrow {}^4He + 2p \tag{4.3}$$

where two protons (p) combine to make deuterium (d) by releasing a positron (e^+) and an electron neutrino (ν_e), and ultimately synthesise a ^{4}He nucleus with the release of a photon (γ) and via two ^{3}He nuclei. Equation 4.3 becomes important once the central temperature is T $\gtrsim 7\times10^6$ K (Dearborn et al. 1986), that is, $m \gtrsim 0.26$ M$_\odot$. Without this reaction, the energy produced by the other two reactions (Eqs. 4.1 and 4.2) is not great enough for the material in the core to become unstable to convection (Baraffe & Chabrier 2018), which occurs when the radiative temperature gradient is larger than the adiabatic gradient, $\nabla_{rad} > \nabla_{ad}$, where

$$\nabla_{rad} \propto L\kappa/T^4 \tag{4.4}$$

with L being luminosity and κ the opacity.

When the reaction given by Eq. (4.2) dominates, the ^{3}He abundance grows, and at a temperature T $\gtrsim 7 \times 10^6$ K, Eq. (4.3) produces enough energy in the core for the centre to become convective (Chabrier & Baraffe 1997). Then, for example, as a 0.30 $M_\odot$ star approaches the MS, it has a radiative core, but the temperature increase due to the pre-MS contraction means that the production and destruction of ^{3}He by Eqs. (4.2) and (4.3) releases enough energy for the material in the core to become unstable to convection. As such, the star reaches the MS with a convective core and envelope, which are separated by a thin radiative layer (Ezer & Cameron 1967).

Before the discovery of the M-dwarf gap, van Saders & Pinsonneault (2012) theorised that at the mass directly above the convective boundary, stars undergo the 'convective kissing instability'. As ^{3}He is destroyed at a slower rate by Eq. (4.3) than is produced by Eq. (4.2) at these low-mass temperatures (Baraffe & Chabrier 2018), it cannot reach equilibrium abundance. The abundance of ^{3}He increases, and the core grows in size until it comes into contact with the convective envelope, resulting in periods of full convection (van Saders & Pinsonneault 2012). The mixing during these periods carries ^{3}He out towards the surface, nuclear reactions in the core subside, and the core contracts and becomes separated again from the envelope (van Saders & Pinsonneault 2012). This continues periodically, with variations in the stars luminosity and effective temperature, until the abundance of ^{3}He is high enough throughout the star that it remains fully convective for the remainder of its lifetime. The variations from this convective kissing instability are thought to result in the M-dwarf gap as the lower density of observed stars seen at these temperatures and luminosities. Baraffe & Chabrier (2018) produced models in steps of 0.01 $M_\odot$ and note the merging of the core and envelope in their 0.34 $M_\odot$ and 0.36 $M_\odot$ models, along with a decrease in central ^{3}He abundance and a change in the slope of the luminosity-mass relation at these masses. MacDonald & Gizis (2018) also find this relation and a dip in the luminosity function for their 0.33 – 0.35 $M_\odot$ models. Feiden et al. (2021) reproduced the M-dwarf gap in a CMD made from population synthesis models and also find periodic pulsations in luminosity, radius, and core temperature due to the ^{3}He instability.

The *Gaia* M-dwarf gap is prominent across the blueward edge of the MS, where lower metallicity stars are found. Feiden et al. (2021) show that their models with low metallicity ([Fe/H] = – 0.7) encounter this instability at lower masses (and thus cooler core temperatures) than models with higher metallicities; from this they conclude that the dependence of temperature on stellar mass is one of the critical factors for this instability. At low temperatures, the opacity dependence of the radiative temperature gradient (Eq. 4.4) becomes important. For lower metallicity, the opacity is decreased and the central temperature needed for the energy transport in the core to occur by radiative transport is lower (Chabrier & Baraffe 1997), and thus requires less mass. As such, the convective kissing instability is expected to happen at lower masses for lower metallicities, since the higher-mass models have the temperatures necessary for radiative cores. This work aims to investigate the dependence of the M-dwarf gap on the very low metallicities found in old globular clusters. Based on this, we suggest that the M-dwarf gap should be well represented in metal-poor globular cluster CMDs, although the low stellar masses at which this effect is found will be difficult to detect in clusters at great distances.

This work uses stellar evolution models to reproduce the convection-mass transition and investigate a fine grid of masses and very low metallicities with a short-scale timestep. These models are described in Sect. 4.2, the results are presented in Sect. 4.3, and we conclude with a discussion in Sect. 4.4.

4.2 Stellar models

The 1D stellar evolution code Modules for Experiments in Stellar Astrophysics (`MESA`, version 15140) was used (Paxton et al. 2011, Paxton et al. 2013, Paxton et al. 2015, Paxton et al. 2018, Paxton et al. 2019). The equations of state (EOSs) used in `MESA` are a combination of the SCVH (Saumon et al.

1995), OPAL (Rogers & Nayfonov 2002), HELM (Timmes & Swesty 2000), FreeEOS (Irwin 2004), and PC (Potekhin & Chabrier 2010) EOSs. The opacity tables relevant to this work are given by Grevesse & Sauval (1998) and OPAL (Iglesias & Rogers 1993, Iglesias & Rogers 1996); additionally, the electron conduction opacities are from Cassisi et al. (2007) and the opacity tables for the low temperatures of M-dwarf atmospheres in which molecules and dust grains are able to form are from Ferguson et al. (2005). For the outer boundary conditions, we adopted the prescriptions provided by the Hauschildt et al. (1999) model atmosphere tables, taken at $\tau = 100$ (Paxton et al. 2011; Chabrier & Baraffe 1997). The nuclear reaction rates are from Cyburt et al. (2010), and we included additional weak reaction rates (Fuller et al. 1985; Oda et al. 1994; Langanke & Martínez-Pinedo 2000). Screening was included via the prescription of Chugunov et al. (2007). Thermal neutrino loss rates are from Itoh et al. (1996). The initial helium abundance is Y = 0.24 + 2Z by mass fraction. Material becomes unstable to convection under the Schwarzschild criterion, and convective energy transport is described using mixing length theory.

Three initial metallicities were chosen (Z = 0.01, Z = 0.001, and Z = 0.0001) in order to investigate the M-dwarf gap on the blue edge of the MS and investigate the low metallicities found in globular clusters. An initial set of models for each metallicity was computed using a mass step of 0.01 $M_\odot$ to determine at which mass the models begin to have radiative cores. Once found, model sets were then produced using a smaller mass step of 0.00025 $M_\odot$. The models were calculated from the zero-age main sequence (ZAMS) up to 10 Gyr with a maximum timestep of 50,000 years. One final model with an initial mass of 0.28 $M_\odot$ and Z = 0.0001 was computed up to 1 Gyr using a maximum timestep of 1,000 years.

4.3 Results

The low-mass MS models slowly undergo nuclear burning via the ppI chain (Eqs. 4.1 - 4.3). By the time they reach an age of 10 Gyr, the hydrogen abundance in the core has only just begun to deplete. The Hertzsprung-Russell (HR) diagrams in Fig. 4.1 (and also later in Fig. 4.4) show the models experiencing a period of fluctuations that appear as loops along their evolutionary tracks during the MS. The age of the model at which this occurs increases with increasing mass. The mass range for this instability occurs at a higher mass for a higher metallicity, and the range of masses is larger for the higher-metallicity models. For the masses below the convective boundary, the models are fully convective throughout their lifetimes. Between a certain mass range for each metallicity (given in Table 4.1), the models begin their lives with a convective core, a thin radiative layer, and a convective envelope. They then undergo a period whereby they repeatedly switch from this structure to one of full convection and then relax into a fully convective state for the remainder of their lifetimes. This is illustrated in Fig. 4.2, which shows the mass coordinates of the convective and radiative regions of the Z = 0.001 models over time. At 1 Gyr, the models with mass $m < 0.28600\ M_\odot$ are fully convective, models with mass $0.28600\ M_\odot \leq m \geq 0.29845\ M_\odot$ have begun the convective kissing instability, and the models with higher masses have a stable convective core and radiative region. The 0.28550 $M_\odot$, 0.28900 $M_\odot$, and 0.29450 $M_\odot$ models are also fully convective at 1 Gyr, having undergone a merger of the convective core and envelope. At 3 Gyr, models with mass $m < 29275\ M_\odot$ and the 0.29550 $M_\odot$ model that has merged are fully convective. At 5 Gyr, the models with mass $m < 0.29500\ M_\odot$ along with the 0.29525 $M_\odot$ and 0.29550 $M_\odot$ models that are merged at this time are fully convective. By 9 Gyr, models with mass $m < 0.29775\ M_\odot$ are fully convective, and models with mass $m > 0.31150\ M_\odot$ have a radiative core.

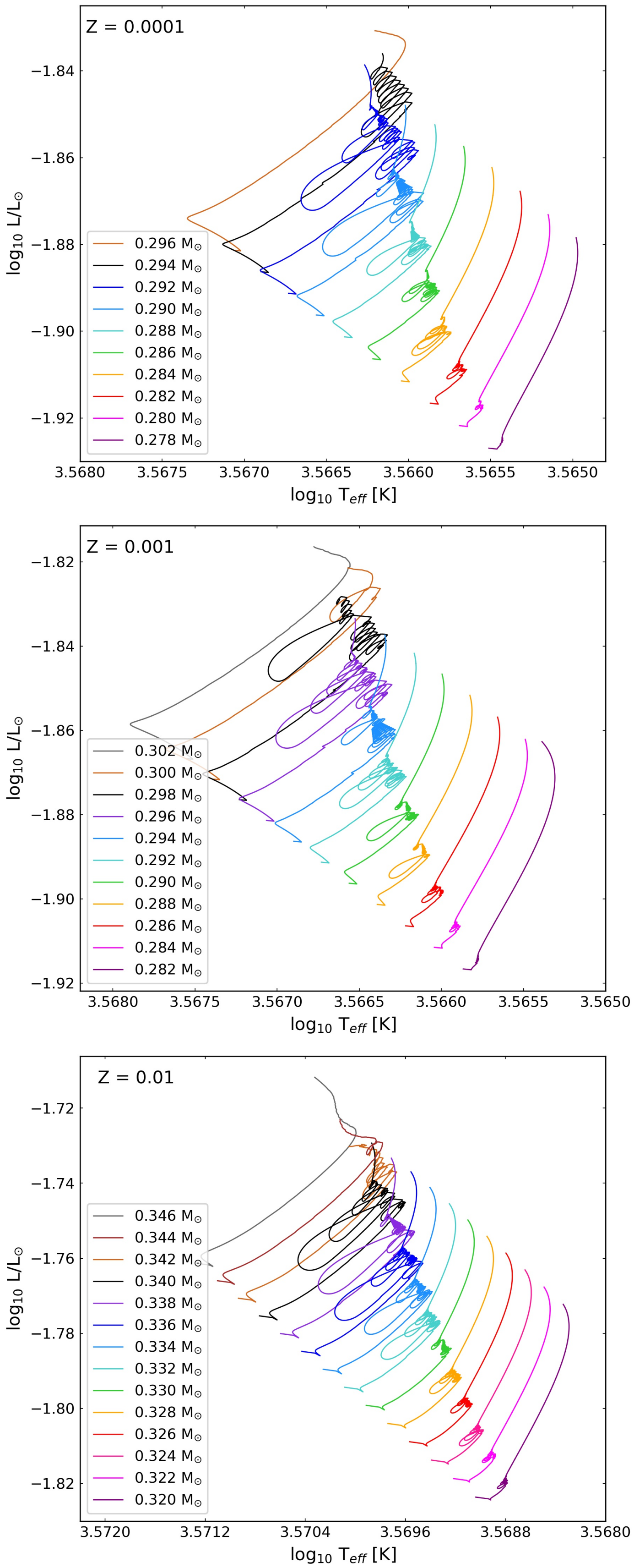

Figure 4.1: Evolutionary tracks shown in the HR diagram for three sets of stellar models with metallicities Z = 0.0001 (top), Z = 0.001 (middle), and Z = 0.01 (bottom). The models begin their evolution on the left and move upwards along the tracks to reach the final points at 10 Gyr. The stars are on the MS throughout this evolution.

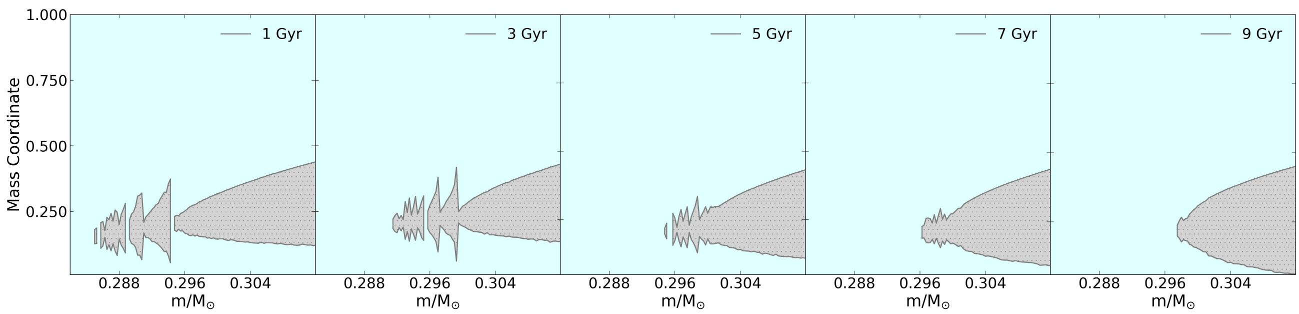

Figure 4.2: Mass coordinates of the convective (blue) and radiative (grey dotted) regions within the Z = 0.001 models over 1, 3, 5, 7, and 9 Gyr. The models that experience a merger of the convective core and envelope at these snapshots can be seen as gaps in the radiative region. A movie with the full time lapse is available online (https://www.aanda.org/articles/aa/olm/2021/06/aa40536-21/aa40536-21.html).

4.3.1 Convective kissing instability

The luminosity, effective temperature, and central ^{3}He abundance over time are displayed in Fig. 4.3 for several models with a metallicity of Z = 0.001. For the sake of clarity, some models are not shown. At this metallicity, the models up to 0.30025 $M_\odot$ undergo fluctuations in luminosity and temperature, some over the course of several billion years, which correlate to the increase and decrease of ^{3}He in the core. There is a clear correlation between the dips in central ^{3}He abundance and both the peaks in luminosity and the troughs in temperature. The amplitude of the fluctuations generally decreases over time until the models settle into a fully convective state; however, the models also exhibit large changes in luminosity and temperature, corresponding to the larger loops seen in the HR diagrams in Fig. 4.1. Figure 4.4 shows the convective kissing instability for the 0.296 $M_\odot$, Z = 0.001 model. The top panel shows the HR diagram, with each point representing 50,000 years, illustrating that the loops occur over a long period of time. The next panels down in the figure give the temperature, luminosity, radius, and ^{3}He abundance profiles over time, along with the mass coordinate positions of the top of the convective core and the bottom of the convective envelope; the region in between is radiative. Again, the correlation between these properties is clear. When the bottom of the convective envelope reaches down and merges with the core, the central ^{3}He abundance drops as the material is carried out towards the surface, and correspondingly the surface ^{3}He abundance rises. This results in a decrease in luminosity as the nuclear production is reduced. The temperature rises due to the now fully convective model contracting to compensate for the loss in nuclear energy output, which is represented by the drop in radius. Once the temperature is high enough to resume ^{3}He production, the abundance of ^{3}He in the core begins to rise along with the luminosity, and the model can increase again in radius. As the radius increases, the surface temperature drops. This repeated process, which results in fluctuations in temperature and luminosity, produces the loops seen in the HR diagrams in Fig. 4.1. After the luminosity is large enough to sustain the material in a convective state (Eg. 4.4), the fluctuations subside and the models remain fully convective. The time period during which the models undergo the convective kissing instability, as well as the amplitude in luminosity and temperature fluctuations, increases with increasing mass. The 1,000 year time step model showed that the smallest pulsations took place on timescales of a few thousand years.

The models additionally exhibit several events where the bottom of the convective envelope reaches down towards the core but remains disconnected from it. These near-merger events correspond to small drops in central ^{3}He abundance and increases in surface ^{3}He, and they occur over a period of $\approx$ 1 Myr.

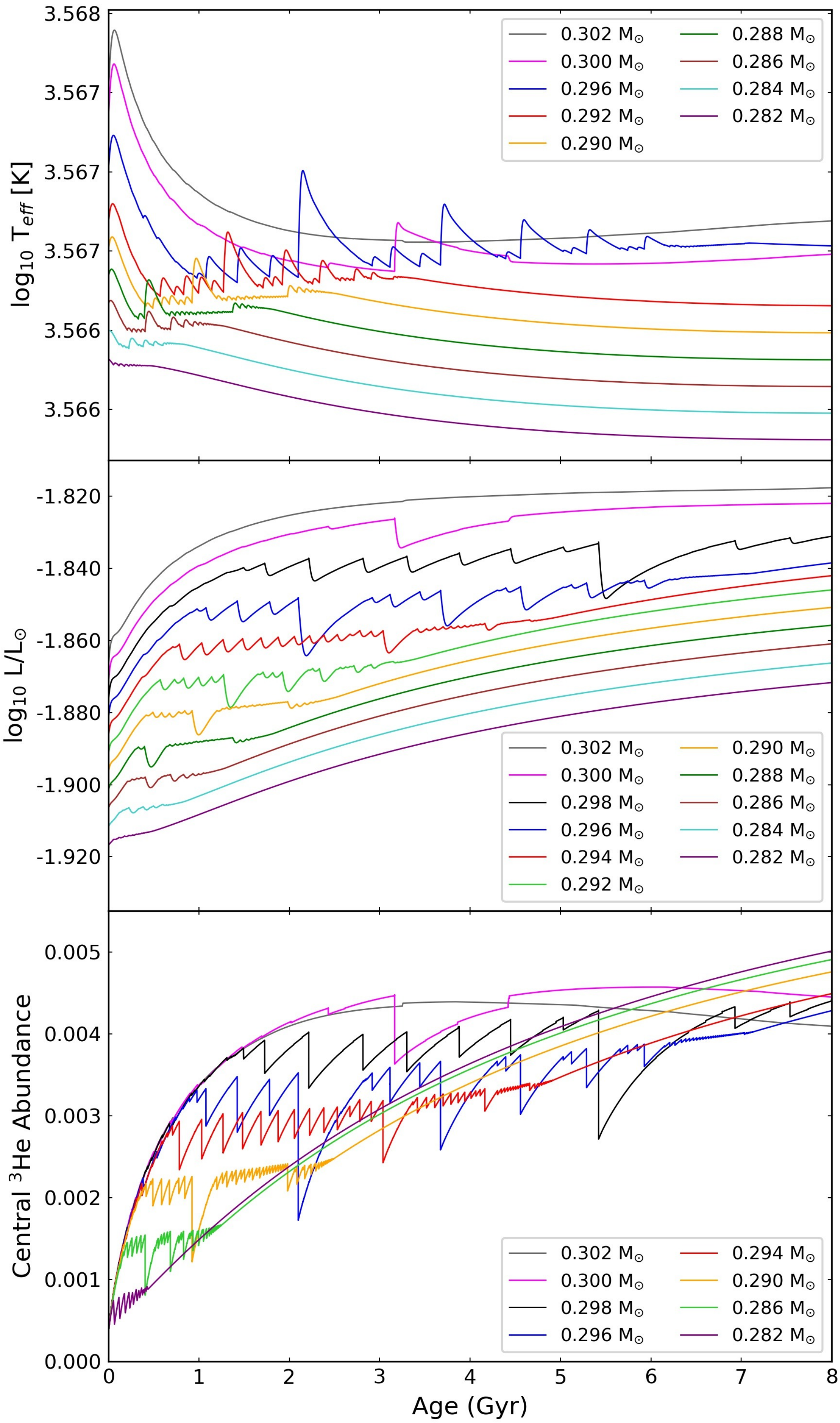

Figure 4.3: Temperature (top) luminosity (middle), and central ^{3}He abundance (by mass fraction; bottom) over time for models with a metallicity of Z = 0.001. The fluctuations occur for several billion years for the higher-mass models.

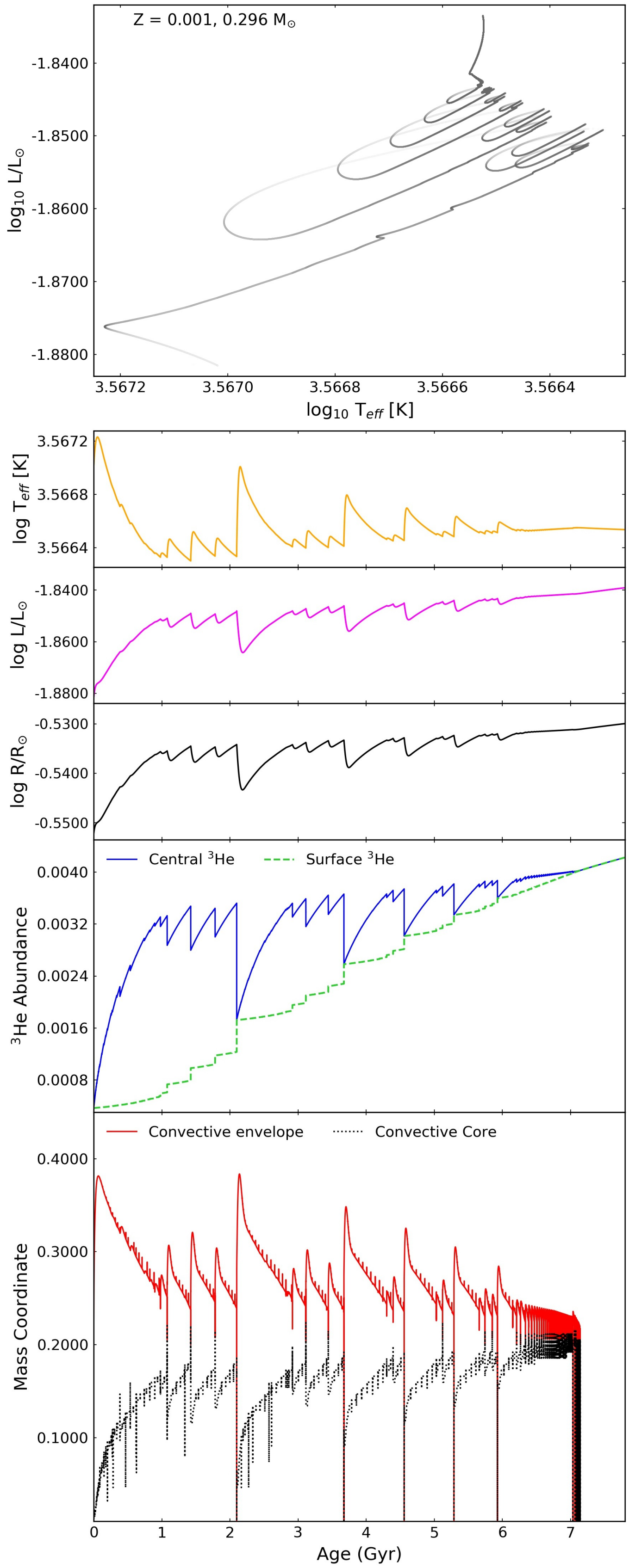

Figure 4.4: HR diagram (top) for the 0.296 M$_\odot$, Z = 0.001 model, where each point represents 50,000 years. Also displayed are: the temperature, luminosity, and radius profiles for the same model (middle); and the centre and surface ^{3}He abundances (by mass fraction), along with the mass coordinate of the bottom of the convective envelope and the top of the convective core (bottom). A radiative region is found in between. After about 7 Gyr, this model has evolved to be fully convective.

Table 4.1. Model mass ranges for the convective kissing instability.

Age [Gyr]	Z = 0.01	Z = 0.001	Z = 0.0001
1	0.32650 – 0.33875 $M_\odot$	0.28600 – 0.29485 $M_\odot$	0.28275 – 0.29000 $M_\odot$
3	0.33450 – 0.34325 $M_\odot$	0.29275 – 0.29925 $M_\odot$	0.28850 – 0.29450 $M_\odot$
5	0.34025 – 0.34325 $M_\odot$	0.29500 – 0.30125 $M_\odot$	0.29050 – 0.29500 $M_\odot$
7	0.34175 – 0.34325 $M_\odot$	0.29575 – 0.30150 $M_\odot$	0.29175 – 0.29450 $M_\odot$
9	0.34150 – 0.34350 $M_\odot$	0.29775 – 0.30025 $M_\odot$	0.29250 – 0.29525 $M_\odot$

4.3.2 Metallicity dependence

The main effect due to metallicity is the convective kissing instability occurring at larger masses for models with higher metallicity. Correspondingly, the effective temperature is also higher for models with increased metallicity. Figure 4.5 shows the effect of metallicity for one chosen model with mass $m = 0.290\ M_\odot$. This figure includes the HR diagrams along with the temperature, luminosity, radius, and central ^{3}He abundance over time for metallicities of Z = 0.001 and Z = 0.0001. A comparison to Z = 0.01 could not be made here as the lowest mass to undergo the convective kissing instability for this metallicity is 0.32650 $M_\odot$. The higher-Z model begins the instability at an earlier age, around 0.3 Gyr, relative to the low-Z model, which begins at around 0.8 Gyr. The fluctuation period subsides and the higher-Z model becomes fully convective by 2.5 Gyr, compared to 5.5 Gyr for the low-Z model (more than twice as long). The amplitude of the fluctuations found in the luminosity, temperature, radius, and central ^{3}He abundance are much higher for the low-Z model.

4.3.3 Luminosity-mass relation

Figure 4.6 shows the luminosity-mass relation for the three metallicities investigated, at the model ages of 1, 3, 5, 7, and 9 Gyr. A discontinuity is seen at all metallicities. The discontinuity is present over many billions of years and is more prominent at the lower age. The mass ranges in which the discontinuity occurs are given in Table 4.1. By 9 Gyr, the lower-mass models that underwent the convective kissing instability at 1 Gyr have settled into a fully convective state, and as such the discontinuity shifts to higher masses and higher luminosities over time. Additionally, the discontinuity occurs at higher masses and luminosities for higher metallicities. Interestingly, the discontinuity is greatly reduced at 7 Gyr for Z = 0.01 to little more than a dip in the luminosity-mass relation, but then appears again at 9 Gyr. Also for Z = 0.01, the highest-mass model to undergo the instability remains 0.34325 $M_\odot$ at 3, 5, and 7 Gyr, whereas for the other metallicities the highest mass increases over time.

4.4 Discussion

The models in this work undergo luminosity, temperature, and radial fluctuations due to the convective kissing instability that was predicted by van Saders & Pinsonneault (2012), and found in models by Baraffe & Chabrier (2018) and Feiden et al. (2021) to be responsible for the *Gaia* M-dwarf gap. This work finds these fluctuations in the form of loops in the evolutionary tracks in the HR diagrams for models with metallicities down to Z = 0.0001, and our results agree with the conclusion that low-mass

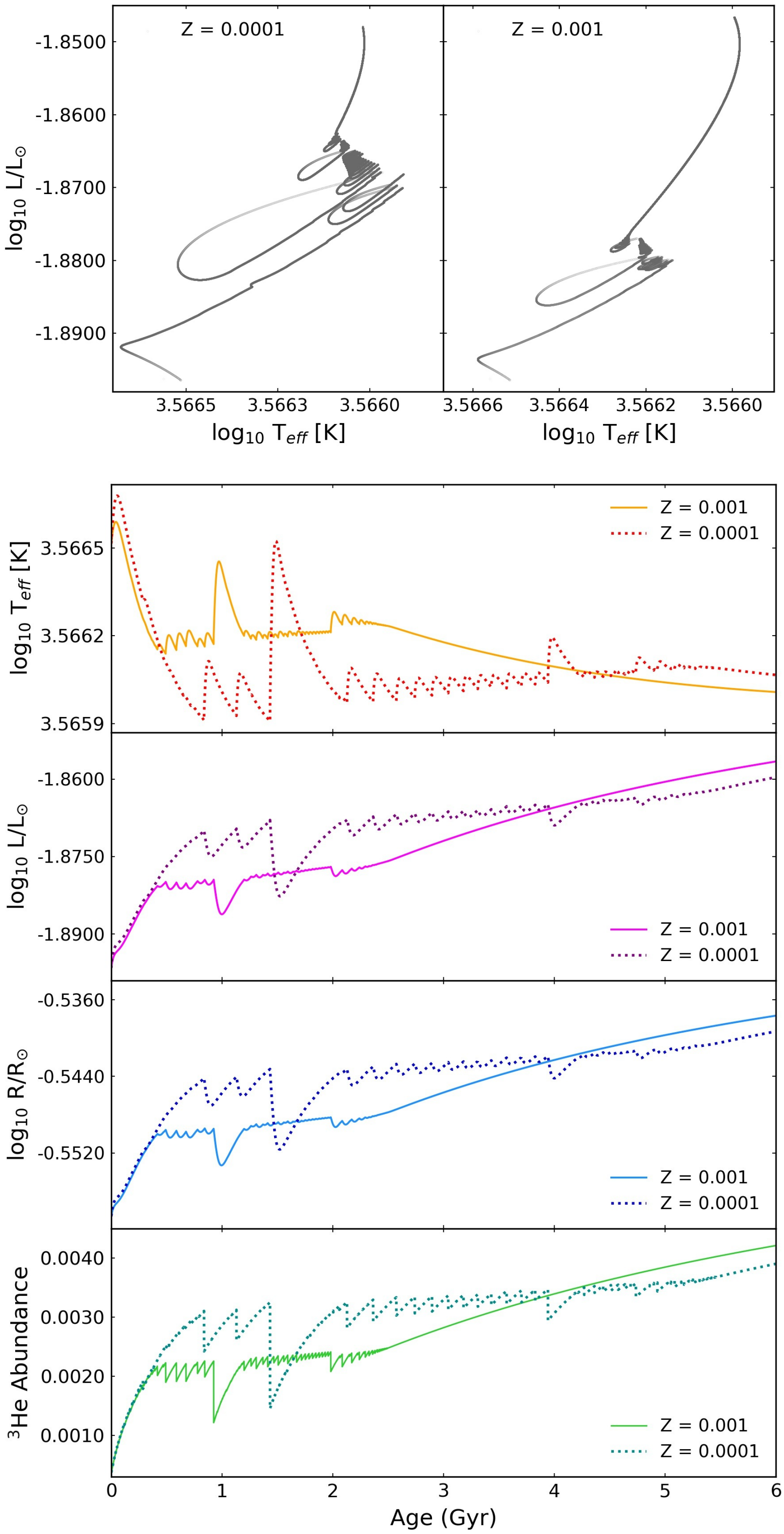

Figure 4.5: HR diagrams for the 0.290 $M_\odot$ model with Z = 0.0001 (top left) and Z = 0.001 (top right). Each point represents 50,000 years. Also shown are the temperature, luminosity, radius, and central ^{3}He abundance profiles (bottom grid) for the two models.

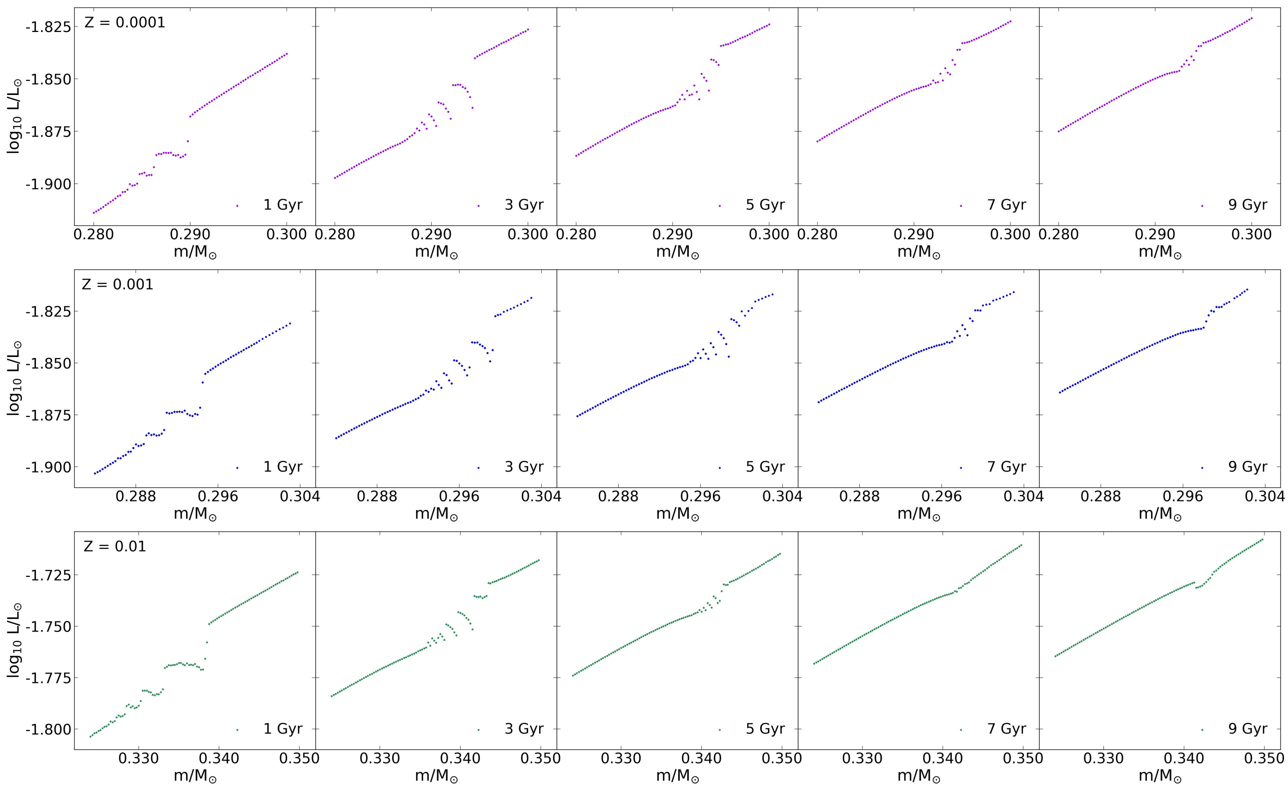

Figure 4.6: Luminosity-mass relation for metallicities Z = 0.0001 (top), Z = 0.001 (middle), and Z = 0.01 (bottom) at model ages 1, 3, 5, 7, and 9 Gyr. A movie of the full time lapse is available online for the Z = 0.001 model set (`https://www.aanda.org/articles/aa/olm/2021/06/aa40536-21/aa40536-21.html`).

stars undergo these periods of fluctuations due to ^{3}He production and transport.

A dip in the luminosity-mass relation was found by MacDonald & Gizis (2018), and by using smaller mass steps, this work finds that there is in fact a discontinuity. We find that the discontinuity occurs at lower masses and luminosities for the lower-metallicity models, as a direct consequence of the convective kissing instability developing at higher masses for higher metallicities. The discontinuity is a result of the merging of the convective envelope and core with the production of ^{3}He, and of the model subsequently and periodically switching between partially and fully convective states. This affects the nuclear energy output, which results in the disruption in the luminosity-mass relation as well as the *Gaia* M-dwarf gap. This discontinuity, which is present over many billions of years, has a great impact on stellar physics as the luminosity-mass relation is no longer differentiable at these masses. For example, in order to constrain the stellar mass function, the slope of the luminosity-mass relation is used (Kroupa et al. 1990, Kroupa et al. 2013). This stellar mass function provides information on the nature of low-mass star formation and the contribution of low-mass stars to the dark matter problem (Kroupa et al. 1990).

The extra model with a maximum timestep of 1,000 years that ran up to 1 Gyr was calculated in order to check if the 50,000 year timestep was able to provide an acceptable resolution for the computational time taken. The 1,000 year timestep model did reveal that the smallest pulsations took place on timescales of a few thousand years. However, the HR diagram as well as the luminosity and temperature profiles of the 1,000 year model were visually comparable to the 50,000 year timestep model. As the 1,000 year model took 82 hours to complete, the computationally quicker 50,000 year timestep is adequate for our purposes.

Feiden et al. (2021) find that the merger events between the convective core and envelope happen four to six times before their models settle into a fully convective state; however, the small timestep used in this work reveals a much higher number of merger events. Additionally, some models experience several near-merger events during which the convective envelope reaches down into the radiative layer but not all the way to the core. These mixing events transport ^{3}He-rich material into the radiative region, into which the convective envelope reaches and pulls ^{3}He outwards to the surface. Whilst the core and envelope do not merge during these events, there exists a million-year-long instability between the two that results in small fluctuations in the ^{3}He abundance, as well as in the surface temperature and luminosity. Further investigation is needed to fully resolve and determine the processes occurring during these near-merger events which was beyond the scope of this work.

The convective kissing instability occurs at higher masses for higher metallicities. This was expected due to the increased opacity for higher metallicities. Convection occurs when the radiative temperature gradient is higher than the adiabatic gradient, and by increasing the opacity, a higher temperature (and thus mass) is needed for the growth of a radiative core than for a lower opacity. For lower metallicities, the central temperature required for radiative transport is lower (Chabrier & Baraffe 1997), and thus the low-Z models have a radiative core at lower masses than the models with high metallicities. For a given mass, the convective kissing instability occurs earlier in the model lifetime for a higher metallicity since the evolution of the central temperature occurs earlier (see Chabrier & Baraffe (1997), Fig. 10a). Additionally, the convective kissing instability occurs for longer portions of the model lifetime for lower metallicities (Fig. 4.5), in agreement with Feiden et al. (2021) and Jao et al. (2018), who note that the observational M-dwarf gap is more prominent at the blue edge of the MS in the HR diagram that represents stars of low metallicities. The instability is found in models with metallicities down to Z = 0.0001, which would be well represented in old globular clusters; this is especially true since the instability period was found to be almost twice as long for the Z = 0.0001 models relative to the Z = 0.001 models. It would be of great importance to find the M-dwarf gap in the observations of these star clusters, although the great distances of the clusters create difficulties in finding these faint low-mass stars. Infrared observations of the nearest globular clusters may be able to achieve this.

4.5 Summary

Stellar evolution models were computed using three different metallicities over a range of masses in order to reproduce the M-dwarf gap observed in the lower region of the MS. The models used a mass step of 0.00025 $M_\odot$ and a timestep of 50,000 years and ran until 10 Gyr. A final model used a 1,000 year timestep up to 1 Gyr; however, this was computationally time consuming, and the timestep of 50,000 years was adequate for the purposes of this investigation. A discontinuity is found in the luminosity-mass relation for masses 0.32650 – 0.34350 $M_\odot$ for the metallicity Z = 0.01, masses 0.28600 – 0.30025 $M_\odot$ for Z = 0.001, and masses 0.28275 – 0.29525 $M_\odot$ for Z = 0.0001. The HR diagrams for these models show loops during the MS, which results in fluctuations in luminosity and effective temperature. The lower-metallicity models undergo the convective kissing instability at lower masses than the higher-metallicity models, due to the lower opacity and thus the lower temperature (and mass) required for radiative transport in the core. The instability occurs for a longer portion of the models lifetime for a given mass with decreasing metallicity.

Comparing the central and surface ^{3}He abundances, as well as the mass coordinates of the convective core and envelope, the loops and pulsations correspond to the merging of the core and envelope, resulting in the switching of the model from a partially to fully convective state and the transport of ^{3}He from the core to the surface. These loops lead to the deficiency of stars in the *Gaia* M-dwarf gap and are due to the production and mixing of ^{3}He throughout the star from the merging of the convective core and envelope.

4.6 Corrigendum

Santana Mansfield and Pavel Kroupa, Astronomy & Astrophysics, Volume 661, C1, May 2022

The initial helium abundance used in the models was Y = 0.28, and not the stated metallicity-dependent value of Y = 0.24 + 2Z. The mass ranges for models which undergo the convective kissing instability with this initial helium abundance are: $0.33000\,M_{\odot} \leq m \leq 0.37100\,M_{\odot}$ for Z = 0.01, $0.34300\,M_{\odot} \leq m \leq 0.36900\,M_{\odot}$ for Z = 0.001, and $0.35600\,M_{\odot} \leq m \leq 0.39033\,M_{\odot}$ for Z = 0.0001. All conclusions remain accurate except that the instability here occurs at a higher mass range for lower metallicity.

Chapter 5

The convective kissing instability in low-mass M-dwarf models: convective overshooting, semi-convection, luminosity functions, surface abundances and star cluster age dating

Santana Mansfield, Pavel Kroupa

Monthly Notices of the Royal Astronomical Society, Volume 525, Issue 4, August 2023

Abstract Low-mass models of M-dwarfs that undergo the convective kissing instability fluctuate in luminosity and temperature resulting in a gap in the main sequence that is observed in the *Gaia* data. During this instability, the models have repeated periods of full convection where the material is mixed throughout the model. Stellar evolution models are performed using `MESA` with varying amounts of convective overshooting and semi-convection. We find that the amplitude and intensity of the instability is reduced with increasing amounts of overshooting but sustained when semi-convection is present. This is reflected in the loops in the evolutionary tracks in the Hertzsprung-Russell diagram. The surface abundances of ^{1}H, ^{3}He, ^{4}He, ^{12}C, ^{14}N and ^{16}O increase or decrease over time due to the convective boundary, however the relative abundance changes are very small and not likely observable. The mass and magnitude values from the models are assigned to a synthetic population of stars from the mass-magnitude relation to create colour-magnitude diagrams, which reproduce the M-dwarf gap as a large indent into the blueward edge of the main sequence (MS). This is featured in the luminosity function as a small peak and dip. The width of the MS decreases over time along with the difference in width between the MS at masses higher and lower than the instability. The parallel offset and relative angle between the upper and lower parts of the MS also change with time along with the mass-magnitude relation. Potential age-dating methods for single stars and stellar populations are described.

5.1 Introduction

The M-dwarf gap is a recently discovered deficiency of stars at the lower end of the main sequence (MS) in the *Gaia* Data Release 2 (DR2) data (Jao et al. 2018), and the early *Gaia* Data Release 3 (eDR3) dataset (Gaia Collaboration, et al. 2021). The drop in density of stars at this location is understood to be due to the stars undergoing the convective kissing instability at the boundary between less-massive stars that are fully convective and slightly higher-mass ones with radiative cores and convective envelopes (van Saders & Pinsonneault 2012; Baraffe & Chabrier 2018; Feiden et al. 2021; Mansfield & Kroupa 2021; Boudreaux & Chaboyer 2023).

This phenomenon is a consequence of a delicate balance between temperature and luminosity in the criteria for convection, which leads to a convective region growing at the centre of a star, and also the unequal abundance of hydrogen and helium throughout the star due to the radiative region between the convective core region and convective envelope (illustrated in Fig. 5.1). According to the Schwarzschild criterion (Schwarzschild & Härm 1958), convection occurs in stellar material when the radiative temperature gradient is larger than the adiabatic gradient, $\nabla_{rad} > \nabla_{ad}$, where

$$\nabla_{rad} \propto \frac{L\kappa}{T^4}. \tag{5.1}$$

where L is the luminosity, κ is the opacity and T is the temperature. Simplified, if the term on the right side of Eq. (5.1) is small then the material is radiative, and if it is large then it is convective. Within the small mass range at which stars undergo the convective kissing instability, the luminosity and temperature compete to dominate Eq. (5.1), such that there is a persistent unbalancing of the equation, leading to the material at the very centre of the star repeatedly switching between a convective and radiative state. As described in Mansfield & Kroupa (2021), the pp-I chain is the primary thermonuclear process for M-dwarf stars

$$p + p \longrightarrow d + e^+ + \nu_e \tag{5.2}$$
$$p + d \longrightarrow {}^3He + \gamma \tag{5.3}$$
$${}^3He + {}^3He \longrightarrow {}^4He + 2p \tag{5.4}$$

where Eq. (5.3) dominates. At around 0.35 $M_\odot$, a star begins on the zero-age main sequence (ZAMS) with sufficient central temperature (Eq. 5.1) to have a radiative core. Then with the onset of nuclear burning, which primarily produces ^{3}He in Eq. (5.3), enough luminosity is produced in the core that a convective region forms within the radiative one (Eq. 5.1). The abundance of ^{3}He rises in the convective core but is unable to reach equilibrium abundance with the rest of the star due to the radiative region. As nuclear production proceeds, greater amounts of the material in the core region becomes convective until it finally merges with the convective envelope. The star undergoes a short ($\approx$ 1 Myr) period of full convection, resulting in a mixing of the stellar material. As ^{3}He and ^{4}He are pulled out of the core, the pp-I chain is disrupted and the nuclear productivity, and thus luminosity, subsides. A reduction in nuclear generation means the star contracts and the temperature increases. With the decrease in luminosity and rise in temperature, the material in the central region becomes radiative again according to Eq. (5.1). Once the central temperature becomes high enough to produce sufficient ^{3}He, which is now no longer being transported out towards the surface due to convection, Eq. (5.4) can resume and the pp-I chain is restored. Then the luminosity is sufficient again to once more begin growing an inner convective region as per Eq. (5.1). The fluctuations in luminosity and temperature result in loops in the Hertzsprung–Russell (HR) diagram of stellar evolution models (Mansfield & Kroupa 2021), and is understood to produce the M-dwarf gap.

The process of the convective kissing instability occurs repeatedly over time but is also dampened with time due to the equilibrium abundances. Each time there is a merging of core and envelope, the

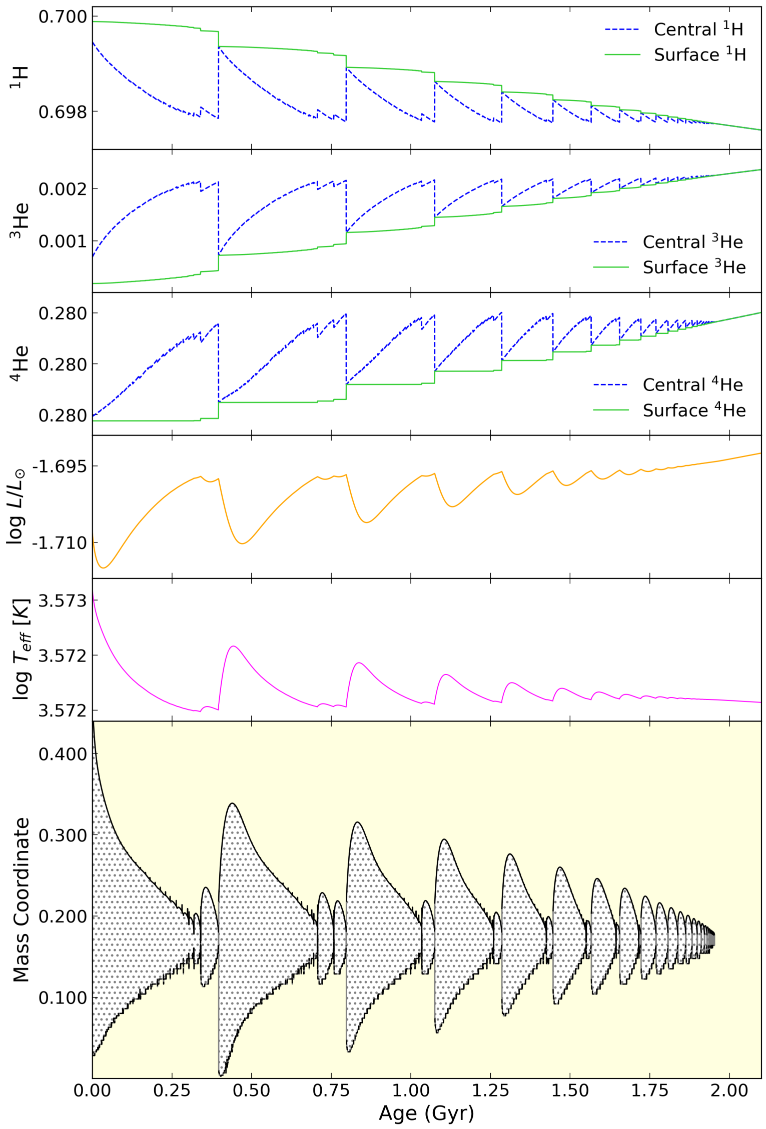

Figure 5.1: The top five plots give the surface and central abundances by mass fraction of hydrogen and helium, luminosity, and effective temperature over time for a 0.37 $M_\odot$, Z = 0.02 model, without overshooting or semi-convection. The bottom plot shows the convective (solid yellow) and radiative (dotted grey) regions for the same model in which the convective kissing instability can be seen.

helium abundance drops in the centre and rises at the surface, as helium becomes distributed throughout the star. When the nuclear production resumes, the central helium abundance rises but only to a certain 'critical' amount before falling again at the next merging event. At this time, because the surface abundance of helium is higher than that of the previous merging event, the decrease of central helium abundance is less before it reaches equilibrium. And so, with each moment of full convection, the time it takes to reach equilibrium abundance becomes increasingly less, and correspondingly the time at which the nuclear production is diminished is lower. Accordingly then, the amount by which the luminosity drops is also reduced, resulting in a smaller region of the stellar material becoming radiative. This is what we see in Fig. 5.1 with the radiative region becoming smaller over time. Once the surface abundance reaches the critical central abundance, true equilibrium is attained and the pp-I chain can finally run without disruption. Now that luminosity is steadily produced, it is high enough (Eq. 5.1) to retain the stellar material in a prevailing fully convective state.

Whilst it is now understood that the convective kissing instability is a possible cause of the M-dwarf gap, some questions about the nature of the instability remain, namely how certain convective and mixing processes may alter and affect the intensity and duration of the convective kissing instability, due to the blurring of boundaries between convective and radiative regions, and the added mixing of material towards equilibrium abundance. These processes are primarily convective overshooting and semi-convection. The effects of these processes will be investigated in this publication along with the consequences of the instability on the surface abundances and the stellar luminosity function.

Convective overshooting occurs when the material in a convective cell has a non-zero velocity when it reaches the boundary of the cell and so continues to move a small distance past it, mixing the material into the radiative region. The extent of overshooting is mass dependent (Claret 2007), and so for low-mass stars, only a small amount of overshooting will be present. Yet for even small numbers, the ability for material to be mixed across the boundary will alter the distribution of helium abundance and likewise the amplitude of the convective kissing instability.

Semi-convection is a diffusive process in a material that occurs in a region which is unstable to convection as per the Schwarzschild criterion, but stable according to the Ledoux criterion (Ledoux 1947). This happens when:

$$\nabla_{ad} < \nabla_{rad} < \nabla_L, \tag{5.5}$$

with the Ledoux temperature gradient:

$$\nabla_L = \nabla_{ad} + \frac{\varphi}{\delta}\nabla_\mu, \tag{5.6}$$

and

$$\varphi = \left(\frac{\delta \ln \rho}{\delta \ln \mu}\right)_{P,T}, \delta = \left(\frac{\delta \ln \rho}{\delta \ln T}\right)_{P,\mu}, \nabla_\mu = \left(\frac{\delta \ln \mu}{\delta \ln P}\right), \tag{5.7}$$

where ρ is the density, μ is the mean molecular weight, P is the pressure and T is the temperature. When a non-homogeneous composition of material remains after a convective region shrinks, a discontinuity of density and molecular weight results in a slow mixing of material called semi-convection. This process would happen in M-dwarf stars undergoing the convective kissing instability due to the convective regions repeatedly growing and shrinking.

This work will also look at the changes in surface abundances of the models, as the abundance of ^{3}He is seen to increase each time the core and envelope merges (Mansfield & Kroupa 2021). Until now only the effects of the instability on ^{3}He have been previously investigated. We will look to see if the convective kissing instability influences the surface abundances of other light elements, particularly ^{1}H, ^{12}C and ^{16}O, as these affect the spectra of M-dwarfs. The cool temperatures of M-dwarf atmospheres allow for the formation of molecules and dust particles, which leads to considerable molecular absorption in their spectra (Allard & Hauschildt 1995). The main molecules responsible for the opacity of M-dwarf atmospheres are those which contain either C, O or H, namely TiO and VO that dominates the optical spectrum (Allard et al. 1997), and H_2O and CO that prevails in the infrared (Veyette et al. 2016; Rajpurohit et al. 2013). Changes in the surface abundances may result in alterations of the atmosphere properties. For example, a reduction of carbon and oxygen would lead to less TiO, CO and H_2O forming, and thus a different configuration of the surface material for stars of lower masses. This would then affect the properties and structure of M-dwarf atmospheres, which are sensitive to these abundances. For example, Allard et al. (1997) found that a reduction in H_2O and TiO in models results in a cooling of the atmosphere.

Additionally, we will explore the consequence of the convective kissing instability on the stellar

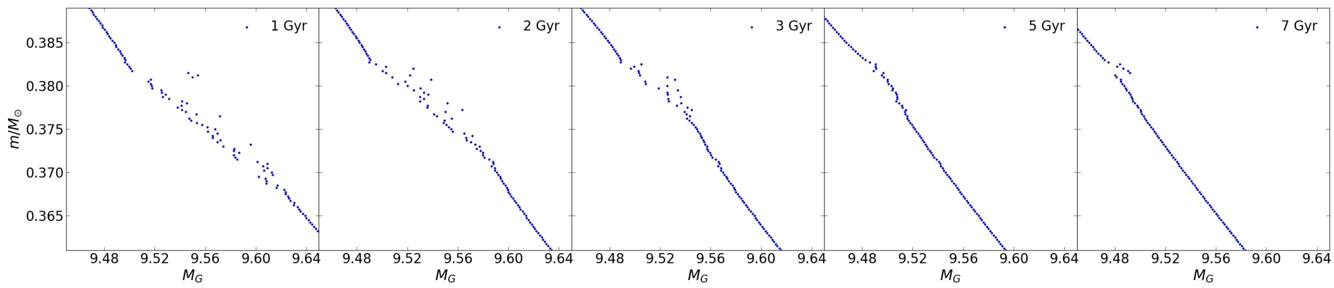

Figure 5.2: Mass–magnitude relation in the photometric $G-$band, for models with $Z = 0.02$, without overshooting or semi-convection, at five time intervals of 1, 2, 3, 5 and 7 Gyr. The fluctuations in magnitude caused by the convective kissing instability create a discontinuity in the relation.

luminosity function (LF), which is given by:

$$\phi_p = \frac{dN}{dM_p} = -\frac{dN}{dm}\frac{dm}{dM_p} = -\xi\frac{dm}{dM_p}, \tag{5.8}$$

where N is the number of stars per cubic parsec, M_p is the absolute magnitude in photometric pass band p, m is the stellar mass, and $\xi(m)dm$ is the number of stars per cubic parsec with masses between m and $m + dm$. Specific features are present in the stellar LF which are due to the internal material of stars at certain masses. For solar metallicity stars, the LF has a minimum at $M_V \approx 7$ called the Wielen dip (Wielen 1974), due to H^- becoming a more important source of opacity for decreasing mass. Once it becomes the primary source, there is a flattening of the luminosity–mass relation and the dip in the luminosity function (Kroupa et al. 1990). The stellar LF also has a maximum at $M_V \approx 11 - 12$ due to the onset of H_2 formation in a thin outer shell (Kroupa et al. 1990). For lower metallicities, these features become shifted to brighter magnitudes (Kroupa & Tout 1997). Upon discovering the M-dwarf gap, Jao et al. (2018) predict that there should be a dip in the LF at around $M_V \approx 10.5 - 11.5$ for solar metallicities.

The fluctuations in luminosity during the convective kissing instability causes a discontinuity in the luminosity–mass relation (Mansfield & Kroupa 2021). The LF depends on the slope of the luminosity–mass relation, and as such, the discontinuity means that the relation is indifferentiable and thus the slope, dm/dM_p, cannot be calculated at the mass range of the convective kissing instability. In this work we will use an alternative method to determine the LF by creating a synthetic population of stars with properties that are assigned using the results from the stellar evolution models. As the LF represents the number of stars per magnitude bin, we can recreate the LF from a count of the number of stars within the magnitude bins. We also consider the mass-magnitude relation and its derivative, as well as potential age-dating methods for single stars and populations such as star clusters.

This investigation uses stellar evolution models which are detailed in Sect. 5.2. The setup for a synthetic population of stars using the results of these models is described in Sect. 5.3. The results are presented in Sect. 5.4, a discussion is given in Sect. 5.5, followed by a summary in Sect. 5.6.

5.2 Stellar Models

The 1D stellar evolution code Modules for Experiments in Stellar Astrophysics (`MESA`, version r22.11.1) is utilised (Paxton et al. 2011, 2013, 2015, 2018, 2019). The equations of state (EOSs) applied in `MESA` are a combination of the SCVH (Saumon et al. 1995), HELM (Timmes & Swesty 2000), OPAL (Rogers & Nayfonov 2002), FreeEOS (Irwin 2004), and PC (Potekhin & Chabrier 2010) EOSs.

Molecules and dust grains are able to form in the low temperatures of M-dwarf atmospheres and the opacity tables for these temperatures are from Ferguson et al. (2005). The nuclear reaction rates are from Cyburt et al. (2010), with additional weak reaction rates (Fuller et al. 1985; Oda et al. 1994; Langanke & Martínez-Pinedo 2000). The opacity tables are those given by OPAL (Iglesias & Rogers 1993, Iglesias & Rogers 1996) and Grevesse & Sauval (1998), as well as electron conduction opacities from Cassisi et al. (2007). Thermal neutrino loss rates are from Itoh et al. (1996). Screening was included using the prescription of Chugunov et al. (2007). For the outer boundary conditions of M-dwarfs, the Hauschildt et al. (1999) model atmosphere tables were used, taken at $\tau = 100$ (Paxton et al. 2011; Chabrier & Baraffe 1997). The initial helium abundance is Y = 0.24 + 2Z by mass fraction. Convective mixing is described using mixing length theory (mixing length parameter $\alpha_{MLT} = 2$), with the convective premixing scheme (CPM, Paxton et al. 2019), which iterates over each cell and instantaneously applies mixing to the cells which are found to be convective (Ostrowski et al. 2020). Sets of models are calculated at solar metallicity ($Z = 0.020$), and a lower metallicity of $Z = 0.001$ to represent a globular cluster (GC). They begin at the ZAMS and run until 9 Gyr. A maximum time step of 2×10^5 years is used in order to slow the code down during the MS where the convective kissing instability occurs. Similarly to that described in Mansfield & Kroupa (2021), this timestep is small enough to see the instability with sufficient resolution, but large enough that the computational time is reasonable. Binary systems were considered but not applied here for simplicity. The conclusions drawn should be similar for binary systems as the convective kissing instability affects the stars individually.

Convective overshooting is administered by an exponentially decaying, time-dependent diffusive process past the convective boundary given by

$$D_{ov} = D_0 \exp\left(-\frac{2r}{f_{ov} H_p}\right), \tag{5.9}$$

where D_0 is the diffusion coefficient inside the boundary, r is the radial distance past the boundary, f_{ov} is the free overshooting parameter, and H_p is the pressure scale height (Herwig 2000; Paxton et al. 2011). The amount of convective core overshooting is strongly dependent on mass for $m \lesssim 2\,\mathrm{M}_\odot$ with f_{ov} increasing sharply up to $f_{ov} \approx 0.0160$ where it stays constant for masses higher than $2\,\mathrm{M}_\odot$ (see Claret 2007, Fig. 10). As such, M-dwarf stars of this mass range will have a very small amount of overshooting. We used $0.0005 \le f_{ov} \le 0.0060$ in this work to see the effect on the models, but note that it is likely that $f_{ov} \ll 0.0050$.

For semi-convection to be implemented, the Ledoux criterion for convection is used (Eqs. 5.5 - 5.7). Mixing in regions satisfying Eq. 5.5 is via a time-dependent diffusive process with diffusion coefficient

$$D_{sc} = \alpha_{sc} \left(\frac{\kappa_r}{6 c_p \rho}\right) \frac{\nabla_{rad} - \nabla_{ad}}{\nabla_L - \nabla_{rad}}, \tag{5.10}$$

where κ_r is the radiative conductivity and c_p is the specific heat at constant pressure. The values applied in this work for the dimensionless semiconvection parameter, α_{sc}, are 0.1 and 1.

The models do not include thermohaline mixing as it is not an important mixing process for M-dwarfs on the MS. This is because, for thermohaline mixing to occur, the mean molecular weight decreases inwards, which can occur in low-mass stars after the first dredge up (Charbonnel & Zahn 2007; Cantiello & Langer 2010), but is not present during the early MS at which the convective kissing instability occurs.

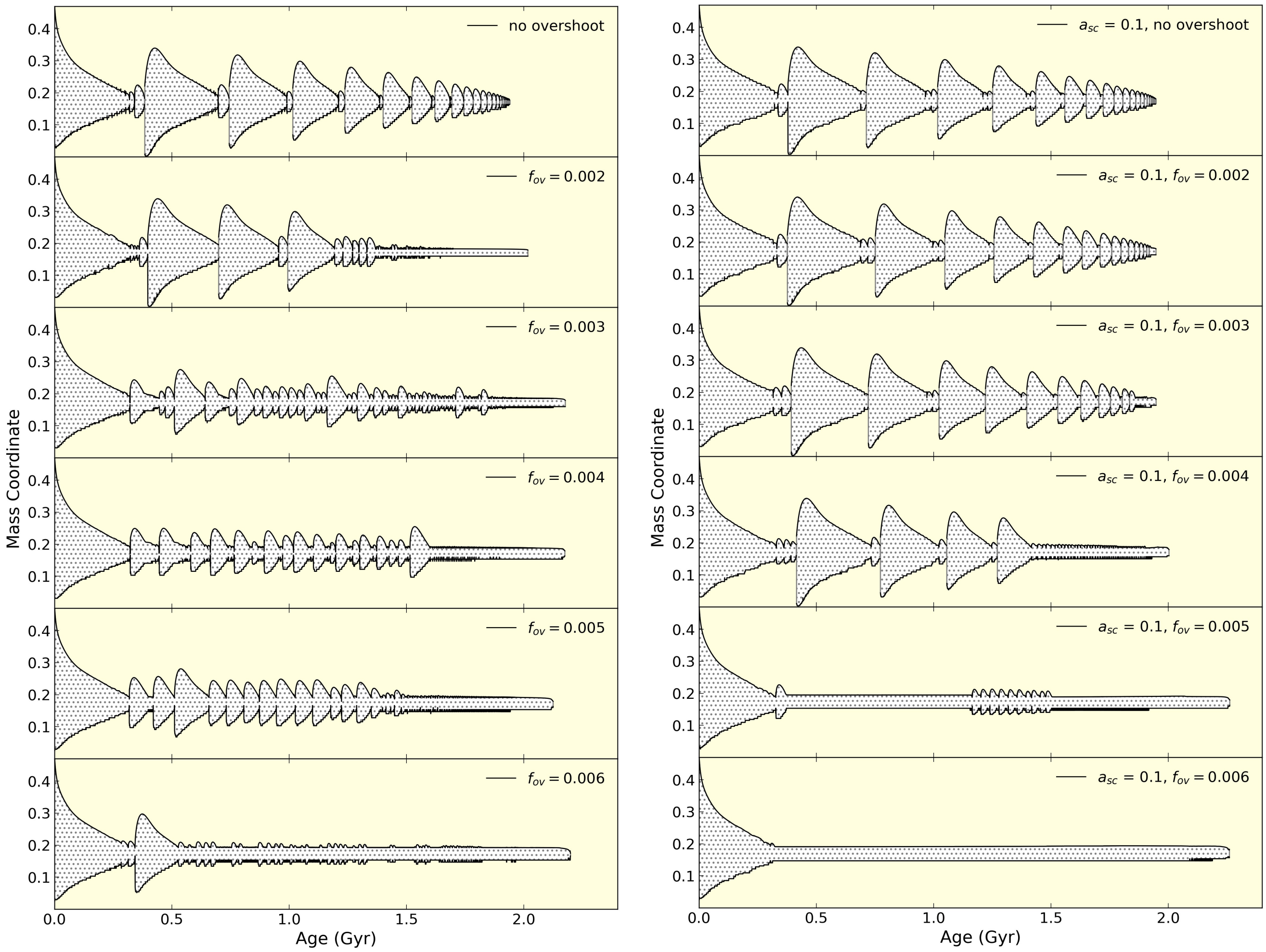

Figure 5.3: Mass coordinate of the convective (yellow solid) and radiative (grey dotted) regions plotted over time for a $0.37\mathrm{M}_\odot$, $Z = 0.02$ model. The models on the left use the Schwarzschild criterion for convection with no semi-convection but increasing overshooting parameter f_{ov}, and the models on the right use the Ledoux criterion with semi-convection parameter $\alpha_{sc} = 0.1$, and also increasing f_{ov}.

5.3 Population synthesis

To construct colour-magnitude diagrams (CMDs) and the luminosity function, three sets of 100 000 stars are given masses ranging from 0.08 $\mathrm{M}_\odot$ to 0.60 $\mathrm{M}_\odot$, according to the canonical initial mass function (IMF) $\xi(m) \propto m^{-\alpha}$, with $\alpha = 1.3$ for $m \leq 0.50\ \mathrm{M}_\odot$ and $\alpha = 2.3$ for $m > 0.50\ \mathrm{M}_\odot$ (Kroupa 2001; Kroupa et al. 2013). These are then assigned an age and corresponding magnitude value due to the mass–magnitude relation determined from the `MESA` models which is shown in Fig. 5.2, where there is a discontinuity due to the fluctuations in luminosity. The slope of the mass–magnitude relation differs at masses lower than and larger than the discontinuity, and changes over time. Thus in order to assign magnitude values to masses higher and lower than the discontinuity, the equation of the line is determined at each point in time. For the masses within the instability range, the magnitude is taken directly from the corresponding `MESA` models. This method is applied because the slope, dm/dM_p, within the instability range cannot be determined, as the relation is indifferentiable across the discontinuity.

Following Paxton et al. (2018), the absolute magnitude of a star in a photometric pass band p is

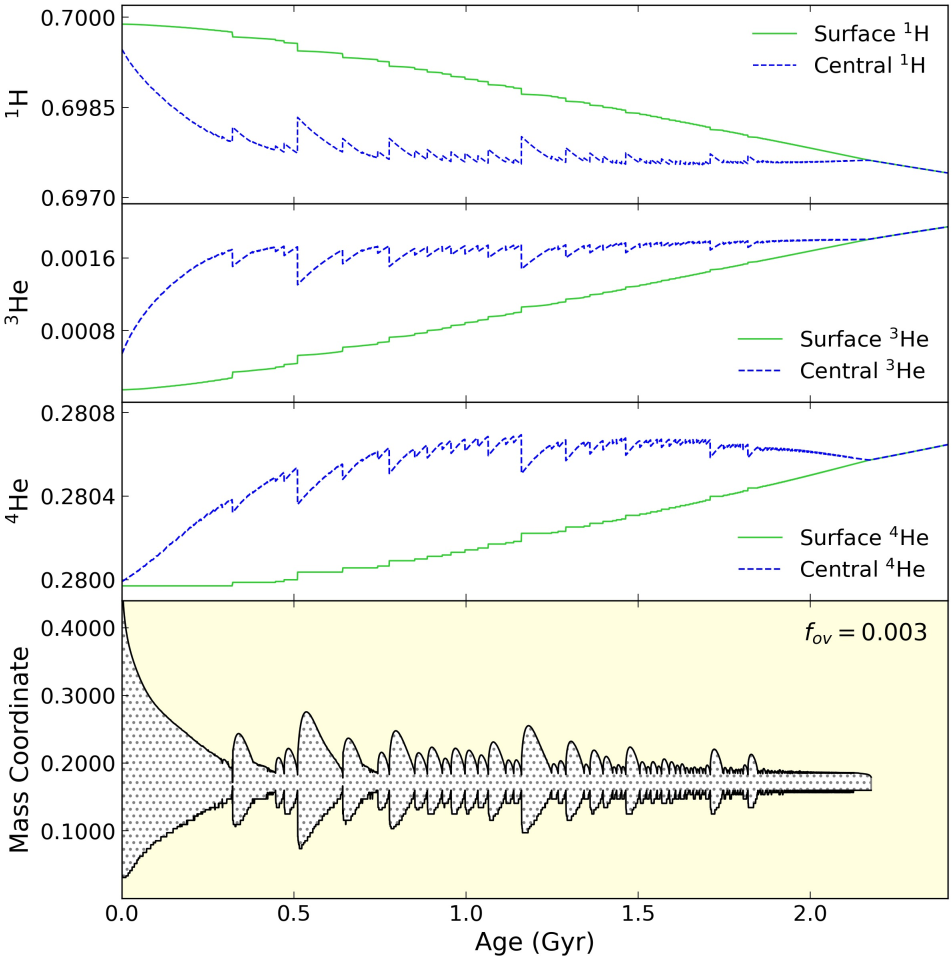

Figure 5.4: Central and surface abundances by mass fraction for the 0.37 $M_\odot$, $Z = 0.02$ model with overshooting parameter $f_{ov} = 0.003$, along with the mass coordinate of the radiative (grey dotted) and convective (yellow solid) regions over time.

determined by

$$M_p = M_{bol} - BC_p, \tag{5.11}$$

with the absolute bolometric magnitude

$$M_{bol} = -2.5 \log_{10}(L/L_\odot) + M_{bol,\odot}, \tag{5.12}$$

where $M_{bol,\odot} = 4.74$ is the absolute bolometric magnitude of the Sun. The bolometric corrections BC_p are taken from a pre-processed set of tables provided within MESA that are described in Paxton et al. (2018) as computed from atmosphere models, and defined as functions of the stellar photosphere including the effective temperature T_{eff} (Code et al. 1976; Houdashelt et al. 2000). The conversion to the *Gaia* G-band magnitudes follows Jordi, C. et al. (2010).

The first set has a metallicity of $Z = 0.020$ to represent stars in the local neighbourhood, and the second set uses a metallicity of $Z = 0.001$ to represent stars in a globular cluster. Both of these sets have no overshooting or semi-convection applied. The third set is calculated using semi-convection with an efficiency of $\alpha_{sc} = 0.1$, and an overshooting parameter of $f_{ov} = 0.006$, with a metallicity of $Z = 0.020$. All other parameters of the sets remain the same.

5.4 Results

Models with masses 0.3440 $M_\odot$ − 0.3825 $M_\odot$ undergo the convective kissing instability for Z = 0.020.

5.4.1 Convective overshooting and semi-convection

Figure 5.3 illustrates the effects of overshooting up to f_{ov} = 0.006 and semi-convection with efficiency α_{sc} = 0.1 for a 0.37 $M_\odot$ model. As f_{ov} increases, the amplitude of the convective kissing instability is lessened, and there are fewer mergers of the core and envelope into a fully convective state. Instead, the core and envelope come close enough together that the remaining distance is small enough for material to cross the radiative region due to overshooting. As the abundance of helium is able to gradually increase throughout the model by passing through the radiative region (as seen by the steady increase of surface ^{3}He abundance in Fig. 5.4), there is no longer the dampening of the convective kissing instability over time that was seen when no overshooting is present (Fig. 5.1). The results here are shown up to f_{ov} = 0.006, however we again note that real M-dwarfs are likely to have a very low amount of overshooting (Claret 2007).

Figure 5.5 shows that the loops in the evolutionary tracks of the models in the HR diagrams become much smaller for an increasing amount of overshooting. Whilst overshooting reduces the convective instability, adding semi-convection to the models can retain it. For example, the f_{ov} = 0.003 model on the left hand side of Fig. 5.3 does not fully merge at any point, yet when semi-convection is present, the results become comparable to the model without any overshooting. The radiative region gradually shrinks until the model is fully convective, then a large portion of the material becomes radiative again. With semi-convection, the loops in the HR diagrams are prominent once more, as seen in Fig. 5.5. The same is true for a more efficient semi-convection with parameter α_{sc} = 1 which is not shown here.

A comparison of the colour-magnitdue diagrams created by the population synthesis for models with no semiconvection or overshooting, and for models with a_{sc} = 0.1 and f_{ov} = 0.006 is given in Fig. 5.6. The indent into the blueward edge of the MS represents the instability region, where the luminosity and temperature of the models fluctuate (as indicated by the loops in Fig. 5.5). This instability region is more sparsely populated for the models with high amounts of overshooting, as expected, however it is still distinguishable, meaning that if M-dwarfs were to have high amounts of overshooting, the M-dwarf gap would still be present in the observational CMD. The 0.37 $M_\odot$ model is marked in Fig. 5.6 which shows a reduction (from top panel to bottom panel) in the area of the instability region over which the model proceeds.

5.4.2 Surface abundances

An illustration of the changes to the central and surface ^{1}H, ^{3}He and ^{4}He abundances over time is given in Fig. 5.1. For a model without overshooting, the rise and drops in the abundances occur when the model becomes fully convective and mixes the stellar material throughout the model. When overshooting is applied (Fig. 5.4) the material is mixed without the model being fully convective. In either case, the surface abundance of helium continuously rises (and hydrogen decreases) until it is equal to the central abundance.

If we view the surface abundances across the mass range, we can see the difference between the models which are fully convective and those that are not. Figure 5.7 shows the surface abundances of ^{1}H, ^{3}He and ^{4}He by mass fraction, plotted against the mass range, given at time intervals of 1, 4

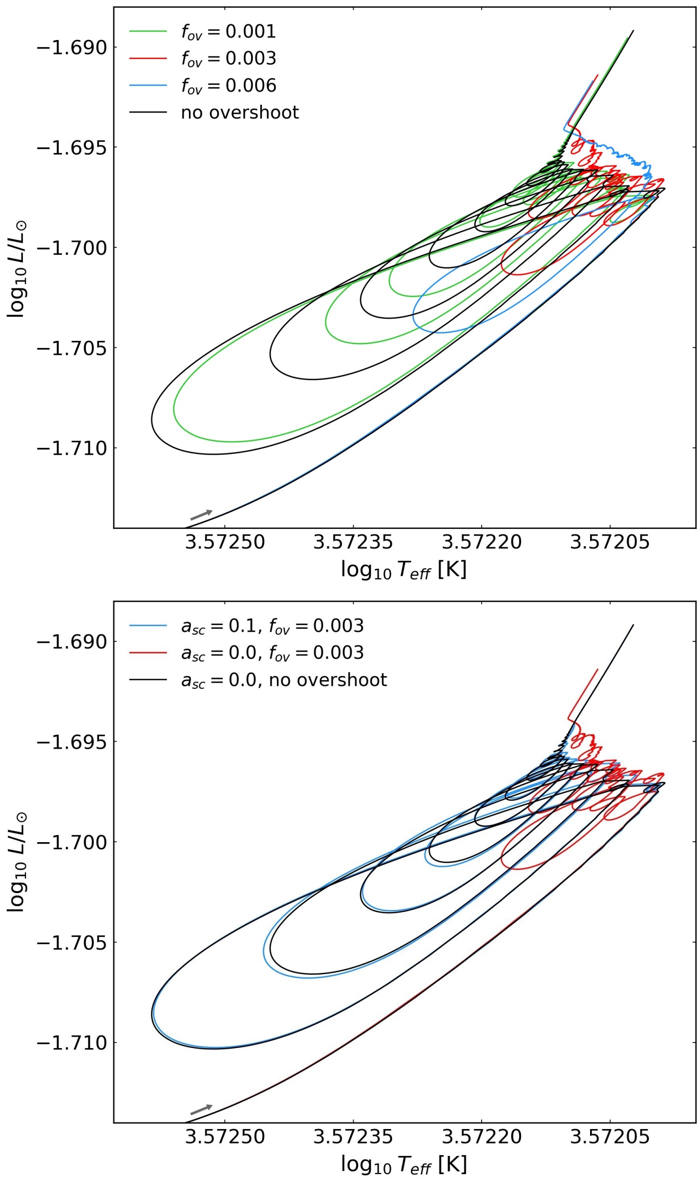

Figure 5.5: HR diagram showing the evolutionary track of the 0.37 $M_\odot$, Z = 0.02 model with varying amounts of overshooting (*top*), where increasing the overshooting diminishes the loops. The models evolve from the lower left as indicated by the arrow. The bottom plot shows the tracks with no overshooting or semi-convection (black), with overshooting added (red), and with both overshooting and semi-convection (blue) which sustains the loops.

and 7 Gyr. As the models age, a drop forms within the model sets, which represents the convective boundary. The models with masses higher than the drop are those with radiative cores and convective envelopes, and as such the surface abundances of these do not vary significantly over time. The models with masses lower than the drop are fully convective, and so the surface abundances of ^{3}He and ^{4}He steadily increase with time as these are produced in the core and carried outward to the surface by convection. Conversely, the surface abundance of ^{1}H decreases over time for the fully convective models, as ^{1}H is mixed downward re-fuelling the core.

The drop illustrated in Fig. 5.7 moves to higher masses with time. This was seen in Mansfield & Kroupa (2021) as the lower mass models undergo the instability at an earlier point in their lifetimes than the higher mass models, and once the instability ceases, the models remain fully convective. This drop would still be present in the absence of the convective kissing instability, however it would likely

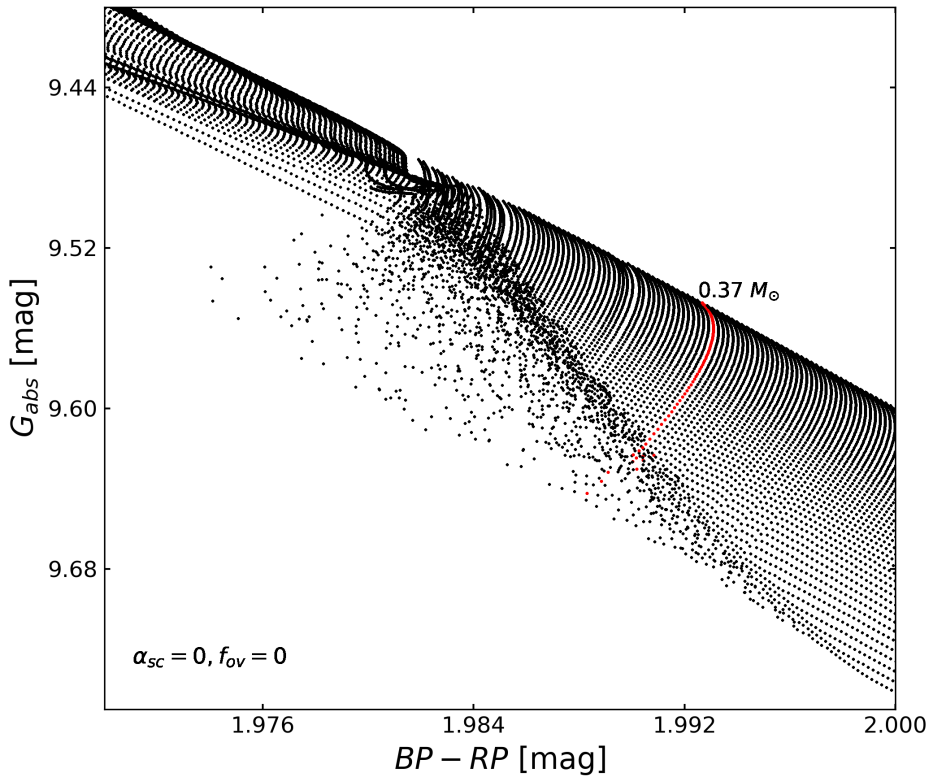

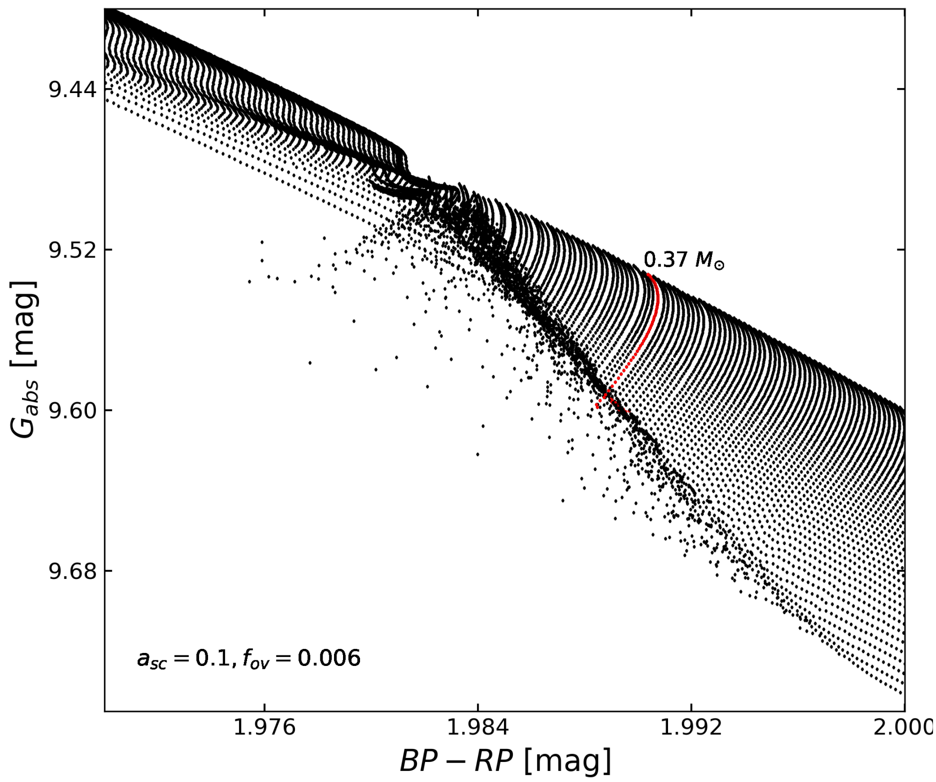

Figure 5.6: Colour-magnitude diagram showing the main sequence for $Z = 0.02$ across all ages, for no overshooting or semi-convection (*top*), and for $a_{sc} = 0.1$ and $f_{ov} = 0.006$ (*bottom*). The convective kissing instability causes an indent into the blueward edge of the MS. This instability region is more sparsely populated for models with high amounts of overshooting, however it is still present. Marked in red is the 0.37 $M_\odot$ model.

be a sudden discontinuity which would not change with time.

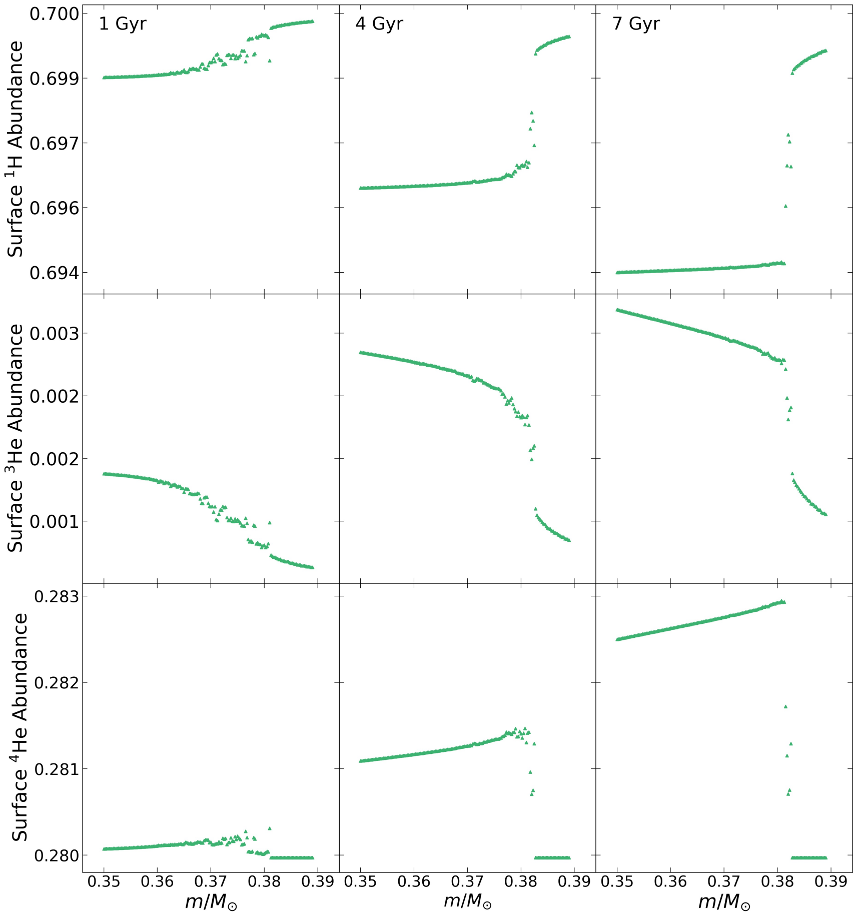

Figure 5.7: Surface abundances by mass fraction of ^{1}H, ^{3}He and ^{4}He, taken at time intervals of 1, 4 and 7 Gyr, plotted against the mass range for $Z = 0.02$, with no overshooting or semi-convection applied.

The average relative changes in surface abundance by the end of the model lifetime is approximately a 1.0% decrease for ^{1}H and a 1.2 % increase of ^{4}He and as such are unlikely to be detected over observational noise. The surface abundance of ^{3}He has quadrupled although it still remains a small fraction of the overall stellar material.

Similarly to hydrogen and helium, once the lower mass models have undergone the convective kissing instability and remain fully convective, the surface ^{12}C and ^{16}O values decrease, and ^{14}N increases, however these abundances change by less than 0.2% during the total model evolution. As the differences are so small, they are not shown here.

5.4.3 The width of the MS: the Solar neighbourhood

As seen in Sect. 5.4.1, the convective kissing instability presents as an indent into the blueward edge of the MS (Fig. 5.6) in the CMD from our population synthesis. The width of the MS varies significantly across this region. Figure 5.8 shows the CMD at increasing population age, representing composite Galactic-field populations, where the overall width of the MS decreases over time. Additionally, the width of the MS is larger for stars with masses lower than the instability than for masses higher, and with time the difference between these two widths also becomes smaller.

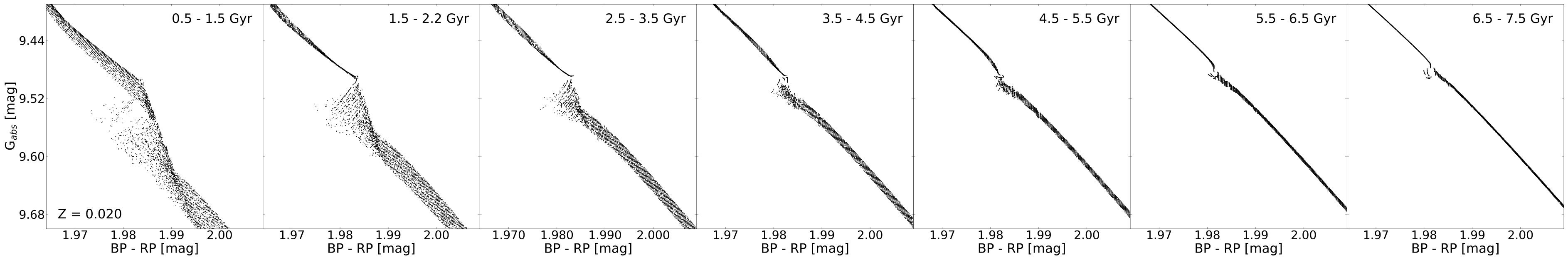

Figure 5.8: Composite Galactic-field populations grouped into age bins spanning 1 Gyr at increasing population age, showing that the width of the MS decreases with time. Here no overshooting or semi-convection is used.

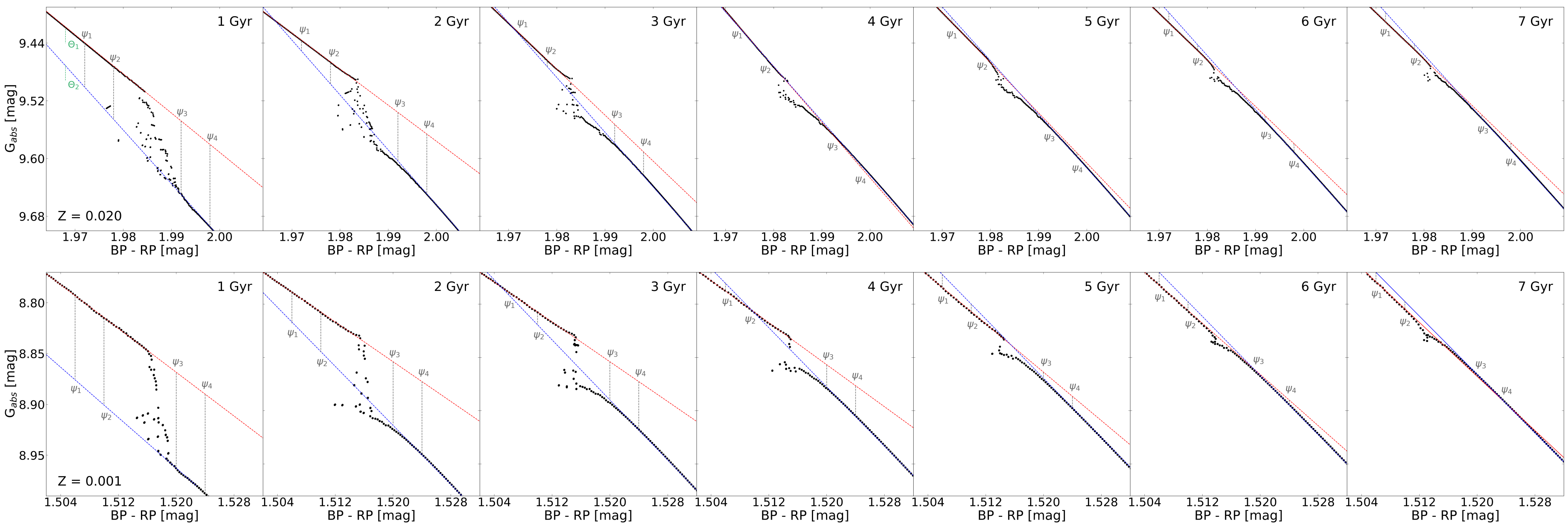

Figure 5.9: A set of solar metallicity stars (*top*) and with $Z = 0.001$ (*bottom*) are given, where the stars have the same age and no overshooting or semi-convection is used. The changes in width can no longer be seen without any age distribution, but the parallel offset of the MS and the kink due to the convective kissing instability remain. The offsets, Ψ_i, and the relative angle, $\theta = \theta_1 - \theta_2$, of the upper and lower parts of the MS are detailed in Fig. 5.10.

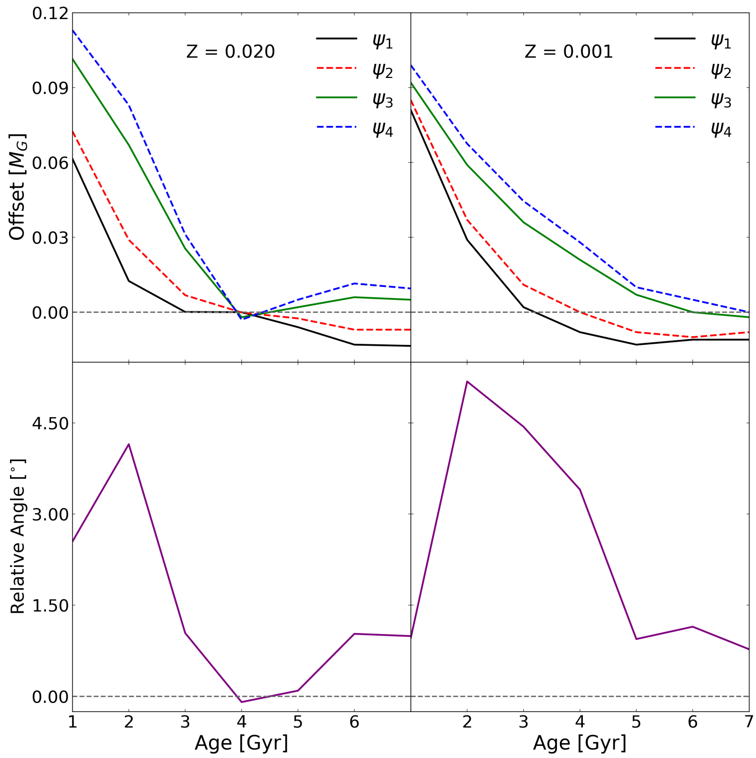

Figure 5.10: The offsets Ψ_i (*top*), and the relative angle (*bottom*) between the upper and lower parts of the MS shown in Fig. 5.9.

5.4.4 Age dating: star clusters

Figure 5.9 gives a set of CMDs for $Z = 0.020$ and a lower metallicity of $Z = 0.001$ with stars of the same age, representing a Solar neighbourhood open cluster and a Galactic halo globular cluster respectively. Although the absence of an age spread does not show the development in MS width in this case, we can still see the change in parallel offset between the upper and lower parts of the MS, as well as the large kink due to the convective kissing instability. The offsets Ψ_i measured at four points ($BP - RP = 1.972, 1.978, 1.992$ and 1.998 for $Z = 0.020$, and $BP - RP = 1.506, 1.510, 1.520$ and 1.524 for $Z = 0.001$) are quantified in Tables 5.1 & 5.2 and illustrated in Fig. 5.10, along with the relative angle from vertical, $\theta = \theta_1 - \theta_2$, between the upper and lower MS. For $Z = 0.020$, the directions of the MS at masses higher (upper MS) and lower (lower MS) than the convective kissing instability are considerably divergent by 2 Gyr and then become more in line with each other as the models evolve, except for at 4 Gyr when the sign of the relative angle becomes reversed. Similarly for $Z = 0.001$, the MS is roughly parallel at the beginning of the evolution, the upper and lower parts of the MS diverge by 2 Gyr, then become increasingly more aligned until 7 Gyr when they are nearly parallel again. By measuring the parallel offset and the relative angle between the upper and lower MS, the age of a star cluster could be estimated.

5.4.5 Age dating: single M-dwarf stars

A method for potential age dating of an M-dwarf star with known distance, metallicity and mass is by the stars position in the CMD, if the mass is lower than the convective kissing instability. This is illustrated in Fig. 5.11 where the time-dependent location in the CMD of a single mass model is

Table 5.1. The parallel offsets and relative angle between the upper and lower parts of the MS as shown in Fig. 5.9, for $Z = 0.02$

Age [Gyr]	Ψ_1 $[M_G]$	Ψ_2 $[M_G]$	Ψ_3 $[M_G]$	Ψ_4 $[M_G]$	θ [°]
1	0.062	0.073	0.102	0.113	2.551
2	0.013	0.029	0.067	0.083	4.155
3	0.001	0.007	0.026	0.031	1.042
4	0.000	-0.001	-0.002	-0.003	-0.094
5	-0.006	-0.003	0.002	0.005	0.094
6	-0.013	-0.007	0.006	0.115	1.029
7	-0.014	-0.007	0.005	0.010	0.992

Table 5.2. Same as Table 5.1 but for $Z = 0.001$

Age [Gyr]	Ψ_1 $[M_G]$	Ψ_2 $[M_G]$	Ψ_3 $[M_G]$	Ψ_4 $[M_G]$	θ [°]
1	0.081	0.085	0.092	0.099	0.960
2	0.029	0.037	0.059	0.068	5.181
3	0.002	0.011	0.036	0.045	4.437
4	-0.008	0.000	0.021	0.028	3.403
5	-0.013	-0.008	0.007	0.010	0.943
6	-0.011	-0.010	0.000	0.005	1.146
7	-0.011	-0.008	-0.002	0.000	0.775

given. As the model evolves, it moves redward and towards higher luminosities, but only up to a point, meaning that this method could only be used to estimate the age of a star up until around 7 Gyr.

5.4.6 Mass-magnitude relation and the luminosity function

Figure 5.12 shows the mass-magnitude relation and its derivative, dm/dM_V, with the convective kissing instability shown in the inset plot. The gap in the peak of the derivative at $M_V = 10.20$ is due to the discontinuity being indifferentiable. Just as the width of the MS in the CMD is wider for models with masses below the instability when viewed over time, the mass-magnitude relation and its derivative also exhibits a time dependence for these masses.

Figure 5.13 shows the stellar luminosity function in different wavebands. At the magnitude where the convective kissing instability occurs, there is a small peak and dip in the number of stars at $M_V = 10.20$ and $M_K = 6.63$. The inset plots give a closer view of this feature. The dip corresponds to the indent into the blueward edge of the MS, and the small peak that is brighter in magnitude indicates a slight over-density which can be seen in Fig. 5.6 as the wave-like overlapping of models just above the gap. This peak is likely to correlate to the same slight over-abundance of stars seen close to the gap in observations (Jao & Feiden 2020).

5.5 Discussion

The convective kissing instability is reduced with increasing amounts of overshooting. The loops in the evolutionary tracks of the models in the HR diagram also become suppressed when increasing

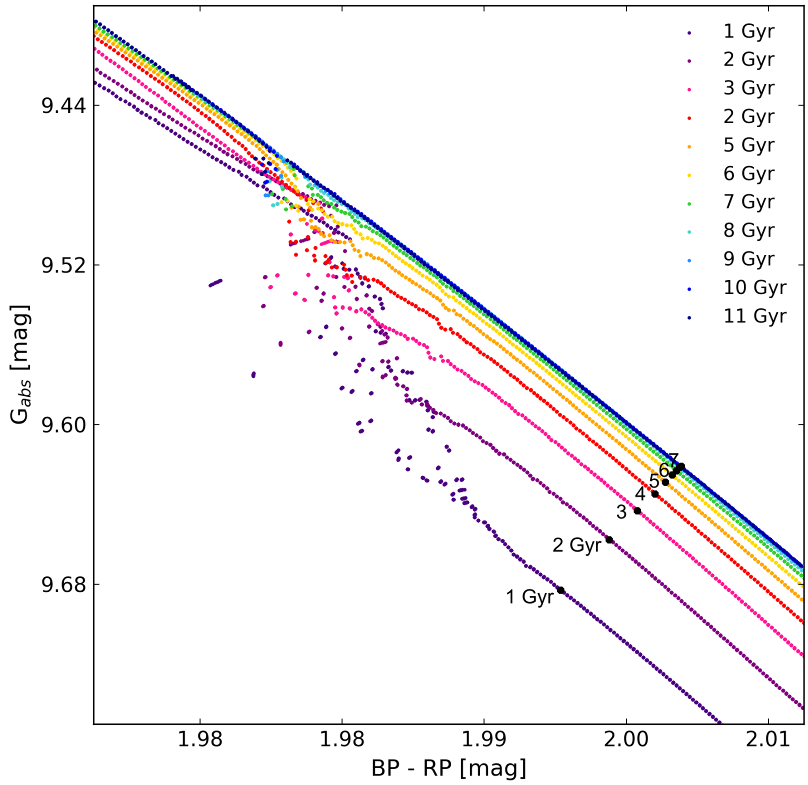

Figure 5.11: A CMD showing the MS of M-dwarf stars at different snapshots in time, without overshooting or semi-convection applied, and a metallicity of $Z = 0.02$. Marked on the diagram is a single model at different ages. If the position in the CMD of a star can be accurately known, along with its metallicity, then the age of the star could be determined, until around 7 Gyr.

overshooting. This brings into question whether M-dwarf stars undergoing the convective kissing instability with overshooting can still be responsible for the M-dwarf gap. The CMD created from the population synthesis (Fig. 5.6) using a relatively high amount of overshooting indicates that there are fewer models within the instability region, yet it does remain. If the amount of overshooting is low, and semi-convection is also present, then the loops in the HR diagram are sustained (Fig. 5.5). Therefore, in order to reproduce sufficient fluctuations in luminosity and temperature to cause the observed M-dwarf gap, stars at this mass range may have overshooting, with less overshooting being preferable (we suggest an upper limit of $f_{ov,max} = 0.004$), and semi-convection should also be present.

The indent that lies in the blueward edge of the MS is more pronounced for the younger models, similar to the larger kinks found in lower-age isochrones given by Baraffe & Chabrier 2018 (their fig. 6). This is due to the models settling into a fully convective state after several gigayear (Mansfield & Kroupa 2021), and the cessation of the fluctuations in luminosity and temperature. From our models we see that there is a reduction in the width of the MS over time for composite Galactic-field populations, and a difference in width of the MS at masses lower than the instability compared with masses higher (Fig. 5.8). For star clusters, which can be assumed to have members of all the same age, the parallel offset and relative angle between the upper and lower MS changes with time (Figs. 5.9 & 5.10). This is detected in a recently observed CMD of the Hyades cluster, which finds a difference in MS direction for stars higher and lower than 0.35 $M_\odot$ (for a super-solar metallicity of [Fe/H] = +0.25, Brandner et al. 2022, their fig. 1). These findings then have the potential to be used as an age estimator of stellar populations. The width of the MS may also be used to estimate the age of single M-dwarf stars if the precise metallicity and mass are known (Fig. 5.11).

The stellar luminosity function shows a small feature located at around $M_V \approx 10.20$ (Fig. 5.13),

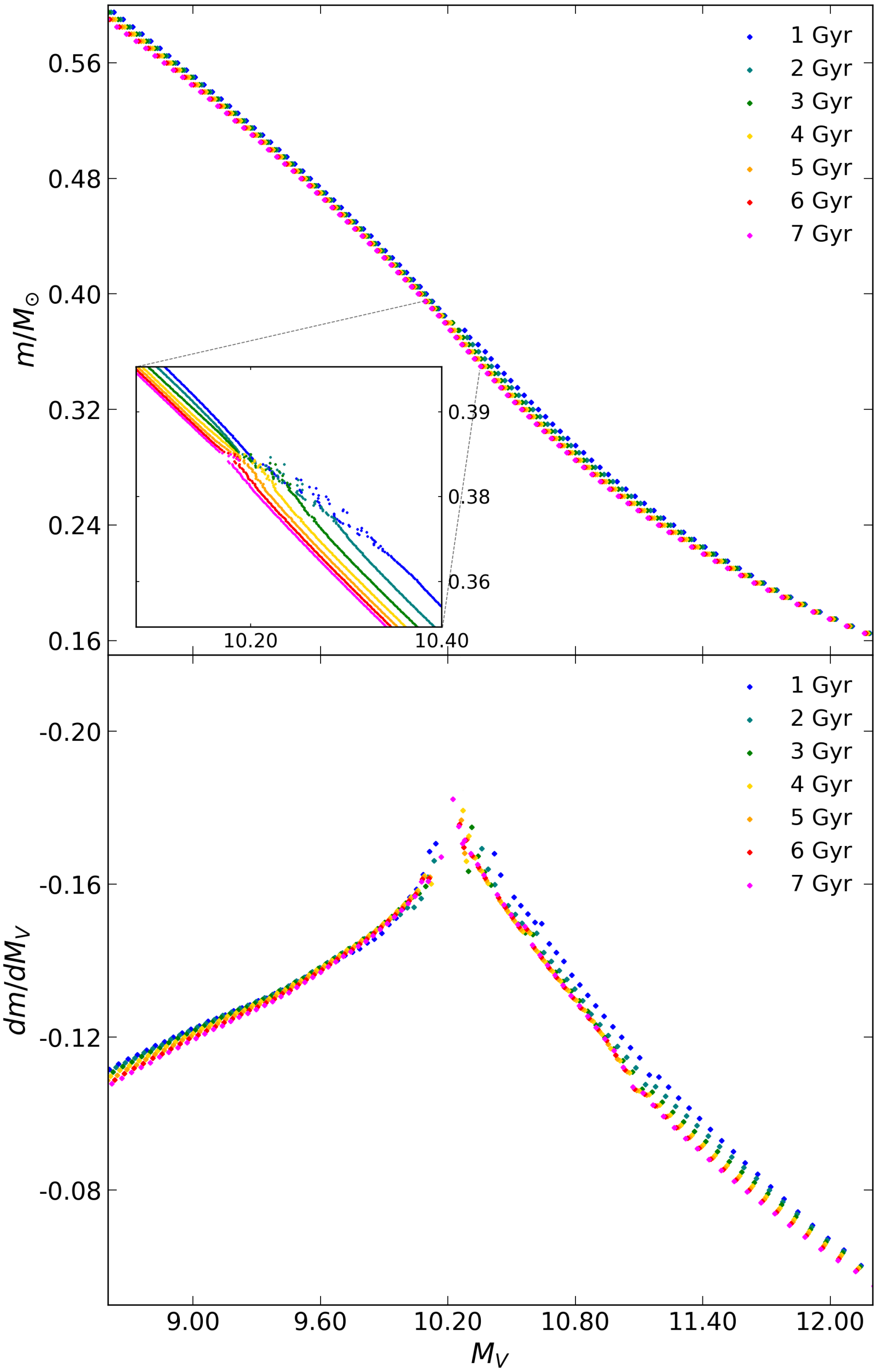

Figure 5.12: Mass – M_V relation (*top*) and its derivative (*bottom*) for solar metallicity and no overshooting or semi-convection applied, showing a slight dependence in time for the models with masses lower than the convective kissing instability. Inset is a zoomed in region of the instability, showing the discontinuity.

which is at a slightly brighter magnitude than the prediction by Jao et al. (2018) of finding a gap in the stellar luminosity function at around $M_V \approx 10.5 - 11.5$. A dip in the luminosity function at $M_K = 6.71$ is also predicted by MacDonald & Gizis (2018), which is in agreement to the dip seen in Fig. 5.13 at $M_K \approx 6.63$. MacDonald & Gizis 2018 propose an alternative theory to explain the M-dwarf gap, in which convective mixing is treated as a diffusive process, resulting in their models undergoing a single merger event rather than the convective kissing instability. However, they report that the central ^{3}He abundance is increased during this merger from the mixing of ^{3}He from the envelope, yet we find

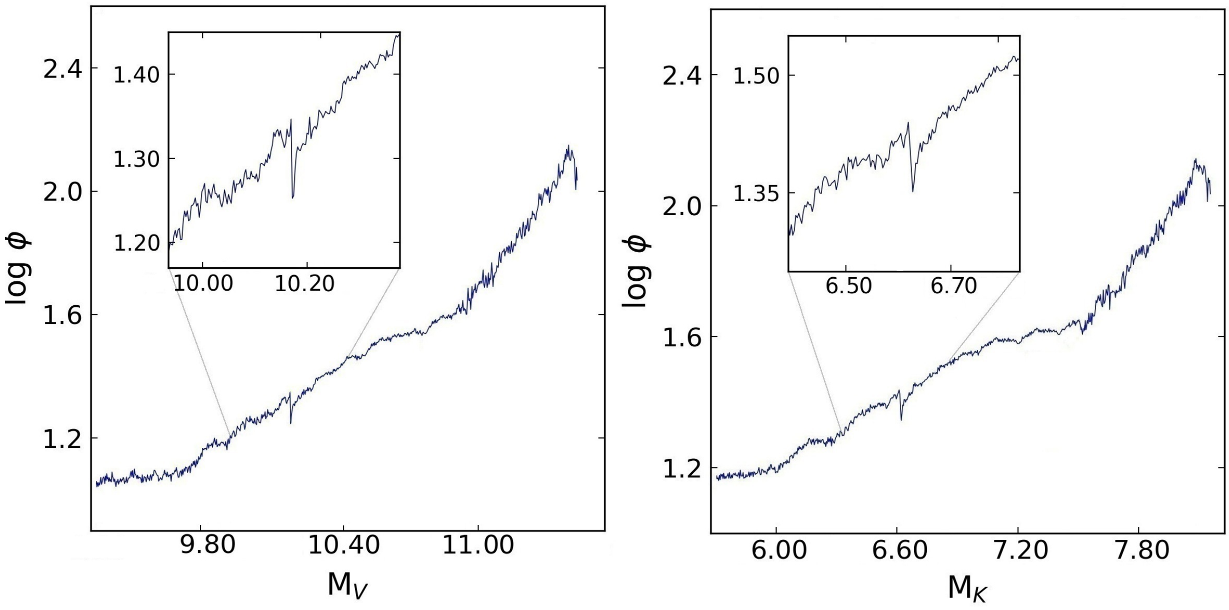

Figure 5.13: Stellar luminosity function in the V and K wavebands for $Z = 0.02$, all ages and no overshooting or semi-convection applied, showing a peak and dip due to the convective kissing instability.

the opposite relation in our models. The central ^{3}He abundance is reduced when the model becomes fully convective and material is mixed throughout the star (Fig. 5.1).

The convective kissing instability effects the surface abundance values of ^{1}H, ^{3}He, ^{4}He, ^{12}C, ^{14}N and ^{16}O through the core and envelope merger events, when the models are fully convective and material is transported throughout the model. The instability effects higher mass models over time and the lower masses settle into a fully convective state. This can be seen as the relative changes in abundance values move to higher masses over time. If the abundance values of a star could be measured and the metallicity is also known, this could be used to estimate the age and mass of the star. However, the relative changes for all elements and isotopes studied are very small and likely will not be larger than observational noise, as well as being within the normal variations of abundances due to stars being formed at different locations and times. Thus, whilst interesting from the evolutionary model standpoint, the predicted changes in surface abundances will be challenging to detect in observations.

5.6 Summary

The amplitude and intensity of the convective kissing instability is reduced with increasing amounts of overshooting but sustained when semi-convection is also present. This effect is seen to modify the loops in the evolutionary tracks in the HR diagram.

The surface abundance values of M-dwarf models are altered by moments of full convection as well as once the models settle into a fully convective state. However the relative changes are small and unlikely to be detected significantly enough to be separated from observational noise or natural variation.

The merging of the convective core and convective envelope produces a discontinuity in the mass-magnitude relation, and we are able to take the magnitudes from the models at multiple moments in time to create the stellar luminosity function. This synthetic population of stars shows the M-dwarf gap as an indent into the blueward edge of the MS, as well as an over-abundance of stars at slightly brighter magnitudes where the models overlap. This results in a feature consisting of a small peak and dip in the luminosity function near $M_V \approx 10.20$.

The width of the MS for a Galactic-field composite population decreases over time, as well as the difference in width of the MS from stars with masses higher and lower than the instability. The parallel offset and relative angle between the upper and lower MS for a single-age star cluster changes with time. This may be used to estimate the ages of stellar populations. Due to the large width of the lower MS, the position of a star in the CMD with known metallicity and mass may also be used to estimate the age of the star if the mass is close to but lower than the convective kissing instability. Furthermore, the width of the lower MS also correlates to a time dependence in the mass-magnitude relation and its derivative.

Finally, a consideration for future study is to investigate different mixing lengths and rotation. Rotation can drive strong mixing of material within stars, and M-dwarfs have been observed to rotate quickly at young ages, and thus an investigation into rotation would also be beneficial for further study.

Chapter 6

Summary

In this thesis, I explore stellar evolution and present instances of the unusual stars and systems that stand out or defy that evolution. These stellar exotica either experience instabilities in their interiors in the case of single stars, or interactions with a companion including mass transfer and collisions, in the case of binary systems. We are able to spot these distinctive stellar objects because these processes result in changes and fluctuations in the luminosities that set them apart from 'standard' stars. The primary and fundamental tools for discovery are the colour-magnitude diagram (CMD) and the parallel Hertzsprung-Russell diagram (HRD). The locations in the CMD of some stellar exotica can easily identify them, such as the position of blue straggler (BS) stars above the main sequence (MS) turnoff. We can also compare CMDs in different wavelengths to infer the existence of other exotica, such as stars which appear to be in the MS or on the red giant branch (RGB) at optical wavelengths, but are located blueward of these in an ultraviolet CMD, such as cataclysmic variable (CV) candidates in the gap between the MS and white dwarf (WD) cooling sequence. We can also find stellar exotica by plotting the evolution of a star in the CMD over time. Additionally, models of stars provide the ability to determine what properties of a star will result in the star encountering internal instabilities, and what effect of this we might see in observations, such as the convective kissing instability (CKI) happening for stars of a certain mass range and metallicity. For this we use Modules for Experiments in Stellar Astrophysics (`MESA`) which is one of the leading stellar evolution codes at the present time, mainly due to its continual progression and the perpetual advancement of the code by numerous researchers globally. `MESA` has been an essential and invaluable tool for this thesis to create simulations of M-dwarfs in order to explore and explain the M-dwarf gap seen in observations.

Until the work in this thesis, the globular cluster M30 has previously been explored using optical, infrared and X-ray wavelengths, but analysis in the ultraviolet was needed. By processing the far-ultraviolet (FUV) and mid-ultraviolet (UV) exposures taken in 2009, we find 1218 MS stars, 185 red giants, 47 BS stars, 41 horizontal branch (HB) stars and 78 WD/Gap objects. These are provided to the the VizieR database at the Centre de Données astronomiques de Strasbourg (CDS)[1]. Within this dataset we find many fascinating stellar exotica because the observations made in the ultraviolet allow us to be able to identify sources which are indistinguishable from MS stars in the optical, such as WDs and gap sources which include potential CV candidates. The temperatures resulting from the infall of material during mass transfer in binary systems such as CVs mean they are blue-shifted in the ultraviolet compared to optical wavelengths, and so they stand apart from the MS. The high surface temperatures of WDs also emit in the far-ultraviolet, and push these sources blueward.

By comparing the sources found in the ultraviolet to the optical and X-ray wavelengths, and by looking for magnitude variability, we find additional exotica. One interesting source is the variable BS source ID267, whose light curve confirmed it is a contact binary. The added mass and increased temperature and luminosity of this ongoing collision has pushed this source to bright magnitudes (in both the $FUV - UV$ and optical $B - V$ CMDs). The periods and positions of two of the variable HB

[1] https://cdsarc.cds.unistra.fr/viz-bin/cat/J/MNRAS/511/3785

stars (ID93) and (ID276) match them to two previously known RR Lyrae variables of types RRab and RRc, for which we now have ultraviolet magnitudes measured. Another a HB star (ID179), is potentially a new RR Lyrae star of classification RRab. Additionally, one of the more noteworthy objects found in this investigation is ID283, which is a BS in our $FUV - UV$ CMD, a red giant in the optical $B - V$ CMD, and is also in the vicinity of the X-ray source A2. This is possibly then a red giant star that is transferring mass to a compact WD companion, making it a bright CV system with a red giant donor that appeared in the BS region in the ultraviolet due to the high temperatures of the mass transfer, and also emits at X-ray wavelengths. Including this CV, we also confirm five further confident matches to the X-ray sources. Two are CVs, ID912 to X-ray source W15, and ID456 to source C, which is seen to be experiencing a dwarf nova event. We also find two sources in the far-ultraviolet that match in position to X-ray sources B and 6 but have no ultraviolet counterparts, ID1647 and ID1700 respectively. The other match is another red giant, ID1029, to X-ray source W16. Interestingly, if we include ID187 as a possible counterpart to X-ray source A3, then three counterparts to the ten X-ray sources are red giants, despite the high numbers of MS stars in the core region of the globular cluster.

The radial distributions of BS stars in M30 are used to confirm the clusters core-collapsed nature. This is where over time the dynamical interactions between the stars results in mass segregation, in which the heavier stars fall inward and the lighter ones drift outward. A core-collapsed cluster has a dense core in a relatively small radius. We find that 40% of detected BS stars (the heaviest of our sample due to their additional mass) are within 5” of the center. A long distinctive BS sequence is observed in the CMD of M30, however the red and blue BSs from the double BS sequence identified in the infrared by Ferraro et al. (2009), is not seen in the ultraviolet. The reason for this is because the red BS stars are believed to be undergoing mass transfer from a companion, as opposed to the blue BSs which are the product of a collision. If mass transfer was occurring as the time of the observations, the infall of material onto the stellar surface would result in high temperatures that emit in ultraviolet wavelengths. This means that, similarly to CVs that appear blueward of the MS in the ultraviolet CMD, the stars that appear on the red BS sequence in the $V - I$ CMD are now shifted blueward in the $FUV - UV$ CMD, and align more with the blue BS stars. This was an interesting consequence/disadvantage of the ultraviolet observations, that we could no longer distinguish the sub-populations of BS stars.

The M-dwarf gap was recently detected in the CMD from the *Gaia* DR2, highlighting again the importance of this invaluable diagram for discovering new stellar exotica. It was theorised by Jao et al. (2018) that the gap is due to M-dwarf stars at the convective boundary undergoing the convective kissing instability (CKI). In order to investigate these stars, we calculate `MESA` models evolving M-dwarf stars at masses around the convective boundary (≈ 0.35 $M_{\odot}$). Until the work performed in this thesis, the CKI had not been seen in any `MESA` models and was only just beginning to be explored using other stellar evolution codes. The evolution of the CKI in the CMD and HRD, its impact on the luminosity–mass relation and stellar luminosity function, and the internal stellar mechanics such as convection in M-dwarfs, had not been explored in any way and we are able to achieve these in this thesis using `MESA`. This has lead to detailed insights into the masses and metallicities of M-dwarfs undergoing the CKI, the duration and intensity of the CKI, the effects on energy transport mechanisms, and possible observational effects including potential age-dating methods. To obtain all these results, setting the maximum timestep and mass increment to be used by `MESA` was essential, as without them the conditions for the CKI are unmet, which is why it went unnoticed in `MESA` models until now. However, once the exact mass range had been found, and by limiting the timestep, the models experience the CKI without the need for any complicated setup, demonstrating the proficiency of `MESA` and the physics that it is built on. The CKI was always there within the abilities of `MESA`, we just had to know where to look for it.

The CKI produces fluctuations in the luminosity and temperature and we find that these result in loops in the HRD which confirms the hypothesis that the CKI is responsible for the M-dwarf gap seen in observations. The CKI occurs at higher masses for higher metallicities and lasts for a longer period of time for higher masses but lower metallicities. Models with increasing amounts of overshooting reduce the effects of the CKI, which are then sustained if semi-convection is also present. This gives a guideline of the amounts of both of these to use when computing stellar models, in order to better represent true stars. The next step in increasing model accuracy is to include and investigate the effects of rotation and also magnetism on the CKI stars.

A discontinuity is found in the luminosity–mass (or mass–magnitude) relation due to the fluctuations in luminosity produced by the CKI. This has implications for the stellar luminosity function (LF), which depends on the slope of the luminosity-mass relation. This is seen to manifest as a small peak and dip in the LF. The mass–magnitude relation and its derivative show a time-dependency in correlation with the width of the MS which decreases in time along with the difference in width between the MS at masses higher and lower than the CKI. The offset in angle between this upper and lower MS also changes with time. These may be used to estimate the ages of stellar populations such as globular clusters. The age of a single star could also be estimated if its position in the CMD and the metallicity are accurately known. Despite the M-dwarf gap only being discovered a few years ago, by utilising a powerful stellar evolution code such as `MESA`, we have gained results which have vastly increased our understanding of these exotic M-dwarf stars.

Stellar exotica have always interested astronomers since they are the weird and wonderful stars which defy the norm, and give us a glimpse into the more extreme and volatile physics in the known universe. We see systems where mass is ripped from one star to another by the immense force of gravity, and can become so hot that nova explosions which could disrupt the structure of the star shine brightly in different wavelengths. We see signs of compact objects such as white dwarfs and neutron stars, and we can detect stars in the process of slowly colliding into each other. And we can even deduce the unstable processes happening within a star which result in repetitive fluctuations and instabilities. In this thesis I have covered some of the impressive stars and systems seen in the globular cluster M30, and the mechanisms that can be applied to M-dwarf stars in the field, however no two stellar exotica are the same. The universe is vast and extremely diverse, and the complicated physics, properties and processes involved can yield fantastically different stars and systems that are still yet to be discovered.

Data availability

The ultraviolet data for M30 are available in the Mikulski Archive for Space Telescopes (MAST): https://archive.stsci.edu. The datasets are derived from images in the public domain: https://archive.stsci.edu/proposal_search.php?mission=hst&id=10561. The catalogue of sources is available at CDS via anonymous ftp to cdsarc.u-strasbg.fr (130.79.128.5) or via https://cdsarc.unistra.fr/viz-bin/cat/J/MNRAS. This research also made use of the optical data available at CDS: https://cdsarc.cds.unistra.fr/viz-bin/cat/J/AJ/116/1757.

For the M-dwarf stars, the datasets were derived using MESA which is in the public domain: https://docs.mesastar.org/.

Bibliography

Ahumada J., Lapasset E., 1995, A&As, 109, 375
Allard F., Hauschildt P. H., 1995, ApJ, 445, 433
Allard F., et al., 1997, ARAA, 35, 137
Allen C., Moreno E., Pichardo B., 2006, ApJ, 652, 1150
Althaus L. G., Benvenuto O. G., 1998, MNRAS, 296, 206
Avila R. J., Chiaberge M., 2016, STScI Instrument Science Report, ACS 2016-5
Bacon R., et al., 2017, A&A, 608, A1
Bailey S., 1902, Annals of Harvard College Observatory, 38, 1
Bailyn C. D., 1995, ARA&A, 33, 133
Baraffe I., Chabrier G., 2018, A&A, 619, A177
Beccari G., et al., 2013, MNRAS, 437, 2621
Belloni D., et al., 2017, MNRAS, 468, 2429
Belloni D., et al., 2018a, MNRAS, 478, 5626
Belloni D., et al., 2018b, MNRAS, 483, 315
Belloni D., et al., 2020, Proc. IAU, 351, 404
Boudreaux T. M., Chaboyer B. C., 2023, ApJ, 944, 129
Brandner W., Calissendorff P., Kopytova T., 2022, MNRAS, 518, 662
Breen P. G., Heggie D. C., 2013, MNRAS, 436, 584
Brown T. M., et al., 2001, ApJ, 562, 368
Brown A., et al., 2011, Proc IAU, 273, 78
Burbidge E. M., Sandage A., 1958, ApJ, 128, 174
Cantiello M., Langer N., 2010, A&A, 521, A9
Casagrande L., 2020, ApJ, 896, 26
Cassisi S., et al., 2007, ApJ, 661, 1094
Chabrier G., Baraffe I., 1997, A&A, 327, 1039
Chandrasekhar S., 1961, *Hydrodynamic and hydromagnetic stability*. Oxford: Clarendon, UK
Charbonnel C., Zahn J.-P., 2007, A&A, 467, L15
Chatterjee S., et al., 2010, ApJ, 719, 915
Chatterjee S., et al., 2013, ApJ, 777, 106
Chugunov A. I., Dewitt H. E., Yakovlev D. G., 2007, Phys. Rev. D, 76, 025028
Claret A., 2007, A&A, 475, 1019
Clementini, G. et al., 2023, A&A, 674, A18
Code A. D., et al., 1976, ApJ, 203, 417
Cool A. M., et al., 2013, ApJ, 763, 126
Copeland H., Jensen J. O., Jorgensen H. E., 1970, A&A, 5, 12
Cyburt R. H., et al., 2010, ApJs, 189, 240
Dalessandro E., et al., 2009, ApJs, 182, 509
Dalessandro E., et al., 2012, ApJ, 144, 126
Dalessandro E., et al., 2013a, MNRAS, 430, 459
Dalessandro E., et al., 2013b, ApJ, 778, 135
Davies M. B., Piotto G., Angeli F. D., 2004, MNRAS, 349, 129

De Loore C. W. H., Doom C., 1992, *Structure and evolution of single and binary stars*. Vol. 179, Kluwer Academic Publishers, Boston, USA

Dearborn D., Schramm D., Steigman G., 1986, ApJ, 302, 35

Deutsch E. W., et al., 1999, ApJ, 118, 2888

Dieball A., et al., 2005, ApJ, 625, 156

Dieball A., et al., 2007, ApJ, 670, 379

Dieball A., et al., 2010, ApJ, 710, 332

Dieball A., et al., 2017, MNRAS, 469, 267

Dolphin A. E., 2000, PASP, 112, 1383

Dorman B., 1992a, ApJs, 80, 701

Dorman B., 1992b, ApJs, 81, 221

Duquennoy A., Mayor M., 1991, A&A, 248, 485

Echiburú C. S., et al., 2020, MNRAS, 495, 4508

Edmonds P. D., et al., 2003, ApJ, 596, 1177

Elson R. A. W., et al., 1995, AJ, 110, 682

Ezer D., Cameron A. G. W., 1967, Can. J. Phys., 45, 3461

Feiden G. A., Skidmore K., Jao W.-C., 2021, ApJ, 907, 53

Ferguson J. W., et al., 2005, ApJ, 623, 585

Ferraro F., et al., 2009, Nature, 462, 1028

Fischer D. A., Marcy G. W., 1992, ApJ, 396, 178

Fuller G. M., Fowler W. A., Newman M. J., 1985, ApJ, 293, 1

Gaia Collaboration, Smart, R. L. et al., 2021, A&A, 649, A6

Gänsicke B. T., Beuermann K., de Martino D., 1995, A&A, 303, 127

Giacconi R., et al., 1974, ApJs, 27, 37

Good G. A., 2003, Pulsating Variable Stars, *Observing Variable Stars*. Springer London UK, p. 57

Göttgens F., et al., 2019, A&A, 631, A118

Greenfield P., White R. L., 2000, ASPCS, 216, 59

Grevesse N., Sauval A. J., 1998, Space Sci. Rev., 85, 161

Grindlay J. E., et al., 1995, ApJ, 455, L47

Guhathakurta P., et al., 1998, AJ, 116, 1757

Harris W. E., 1996, AJ, 112, 1487

Harris W. E., 2010, A New Catalog of Globular Clusters in the Milky Way (arXiv:1012.3224)

Hauschildt P. H., Allard F., Baron E., 1999, ApJ, 512, 377

Heggie D. C., 1975, MNRAS, 173, 729

Heinke C. O., et al., 2003, ApJ, 598, 516

Herwig F., 2000, A&A, 360, 952

Hillman Y., et al., 2020, Nat. Astron., 4, 886–892

Hills J. G., 1975, AJ, 80, 809

Hills J. G., Day C. A., 1976, Astrophys. Lett., 17, 87

Hong J., et al., 2005, ApJ, 635, 907

Hong J., et al., 2016, MNRAS, 464, 2511

Houdashelt M. L., Bell R. A., Sweigart A. V., 2000, ApJ, 119, 1448

Howell J. H., Guhathakurta P., Tan A., 2000, AJ, 119, 1259

Huang R. H. H., et al., 2010, A&A, 513, A16

Hurley J. R., Shara M. M., 2012, MNRAS, 425, 2872

Hurley J. R., Aarseth S. J., Shara M. M., 2007, ApJ, 665, 707

Hut P., et al., 1992, PASP, 104, 981
Hypki A., Giersz M., 2012, MNRAS, 429, 1221
Iben I., 1967, ARA&A, 5, 571
Iben I., 1974, ARA&A, 12, 215
Iben I., 1995, Phys. Rep., 250, 1
Iglesias C. A., Rogers F. J., 1993, ApJ, 412, 752
Iglesias C. A., Rogers F. J., 1996, ApJ, 464, 943
Iliadis C., 2015, *Nuclear physics of stars,*. Wiley-VCH, Weinheim, Germany
Irwin A., 2004, `http://freeeos.sourceforge.net/`
Itoh N., et al., 1996, ApJs, 102, 411
Ivanova N., et al., 2005, MNRAS, 358, 572
Ivanova N., et al., 2006, MNRAS, 372, 1043
Jao W.-C., Feiden G. A., 2020, ApJ, 160, 102
Jao W.-C., et al., 2018, ApJ, 861, L11
Jordi, C. et al., 2010, A&A, 523, A48
Kains, N. et al., 2013, A&A, 555, A36
King I. R., 1966, AJ, 71, 64
Knigge C., et al., 2000, A Far-Ultraviolet Spectroscopic Survey of the Globular Cluster 47 Tuc, *Stellar Collisions, Mergers, and their Consequences*. ASP Conference Series, Vol 263, p. 137 (`arXiv:astro-ph/0012187`)
Knigge C., et al., 2003, ApJ, 599, 1320
Knigge C., et al., 2008, ApJ, 683, 1006
Knigge C., Baraffe I., Patterson J., 2011, ApJs, 194, 28
Kremer K., et al., 2020, ApJs, 247, 48
Kremer K., et al., 2021, ApJ, 917, 28
Kroupa P., 2001, MNRAS, 322, 231
Kroupa P., 2002, Science, 295, 82
Kroupa P., Tout C. A., 1997, MNRAS, 287, 402
Kroupa P., Tout C. A., Gilmore G., 1990, MNRAS, 244, 76
Kroupa P., et al., 2013, The Stellar and Sub-Stellar Initial Mass Function of Simple and Composite Populations, *Planets, Stars and Stellar Systems. Volume 5: Galactic Structure and Stellar Populations,*. Springer, Dordrecht, Netherlands, p. 115
Lamers H. J. G. L. M., Levesque E. M., 2017, *Understanding Stellar Evolution,*. OP Publishing, Bristol, UK
Langanke K., Martínez-Pinedo G., 2000, Nucl. Phys. A, 673, 481
Ledoux P., 1947, ApJ, 105, 305
Leigh N., Sills A., Knigge C., 2007, ApJ, 661, 210
Leigh N., Sills A., Knigge C., 2011, MNRAS, 415, 3771
Leigh N., et al., 2013, MNRAS, 428, 897
Leigh N. W. C., et al., 2015, MNRAS, 446, 226
Lewin W. H. G., van Paradijs J., van den Heuvel E. P. J., 1997, *X-ray Binaries,*. Cambridge University Press, Cambridge, UK
Lomb N. R., 1976, Ap&SS, 39, 447
Lu T.-N., et al., 2011, ApJ, 736, 158
Lugger P. M., et al., 2007, ApJ, 657, 286
MacDonald J., Gizis J., 2018, MNRAS, 480, 1711
Maccarone T. J., et al., 2010, MNRAS, 406, 2087

Maeder A., 2009, *Physics, Formation and Evolution of Rotating Stars,*. Springer Berlin, Heidelberg, Germany

Mansfield S., Kroupa P., 2021, A&A, 650, A184

Mansfield S., Kroupa P., 2023, MNRAS, 525, 6005

Mansfield S., et al., 2022a, MNRAS, 511, 3785

Mansfield S., et al., 2022b, MNRAS, 513, 3022

Margon B., Downes R. A., Gunn J. E., 1981, ApJl, 247, L89

McCrea W. H., 1964, MNRAS, 128, 147

Nardiello D., et al., 2018, MNRAS, 481, 3382

Oda T., et al., 1994, At. Data Nucl. Data Tables, 56, 231

Ostrowski J., et al., 2020, MNRAS, 503, 4646

Paczyński B., 1971, Acta Astron., 21, 417

Paczynski B., 1976, Common Envelope Binaries, *Structure and Evolution of Close Binary Systems,*. Proc. Symp., Cambridge UK, p. 75

Parise R. A., et al., 1994, ApJ, 423, 305

Pauli W., 1924, Naturwissenschaften, 12, 741

Paxton B., et al., 2011, ApJs, 192, 3

Paxton B., et al., 2013, ApJs, 208, 4

Paxton B., et al., 2015, ApJs, 220, 15

Paxton B., et al., 2018, ApJs, 234, 34

Paxton B., et al., 2019, ApJs, 243, 10

Pickering E. C., 1903, Annals of Harvard College Observatory, 48, 91

Pietrukowicz P., Kaluzny J., 2004, Acta Astron., 54, 19

Piotto G., et al., 2015, AJ, 149, 91

Pols O., 2011, *Stellar Structure and Evolution: Lecture Notes,*. Astronomical Institute Utrecht, Netherlands

Pooley D., et al., 2002, ApJ, 569, 405

Portegies Zwart S., 2019, A&A, 621, L10

Potekhin A. Y., Chabrier G., 2010, Contrib. to Plasma Phys, 50, 82

Rajpurohit A. S., et al., 2013, A&A, 556, A15

Ransom S. M., et al., 2004, ApJ, 604, 328

Richer H. B., et al., 1997, ApJ, 484, 741

Rivera Sandoval L. E., et al., 2018, MNRAS, 475, 4841

Roche E., 1850, *Mémoires de la section des sciences,*. Académie des sciences et lettres de Montpellier, France

Rodriguez C. L., et al., 2016, MNRAS, 463, 2109

Rogers F. J., Nayfonov A., 2002, ApJ, 576, 1064

Rui N. Z., et al., 2021, ApJ, 912, 102

Sahu S., et al., 2019, ApJ, 876, 34

Sarty G. E., Wu K., 2006, PASA, 23, 106

Saumon D., Chabrier G., van Horn H. M., 1995, ApJs, 99, 713

Scargle J. D., 1982, ApJ, 263, 835

Schiavon R. P., et al., 2012, ApJ, 143, 121

Schwarzschild M., Härm R., 1958, ApJ, 128, 348

Schwarzschild M., Härm R., 1962, ApJ, 136, 158

Schwarzschild M., Härm R., 1965, ApJ, 142, 855

Servillat, M. et al., 2008, A&A, 490, 641

Shara M. M., Hurley J. R., 2006, ApJ, 646, 464
Siegel M. H., et al., 2014, ApJ, 148, 131
Siegel M. H., et al., 2015, ApJ, 150, 129
Sills A., Karakas A., Lattanzio J., 2009, ApJ, 692, 1411
Simunovic M., Puzia T. H., Sills A., 2014, ApJ, 795, L10
Smith H., 1995, *RR Lyrae Stars*. Cambridge University Press, Cambridge UK
Sosin C., 1997, AJ, 114, 1517
Stetson P. B., 1987, PASP, 99, 191
Subramaniam A., et al., 2017, ApJ, 154, 233
Thomson G. S., et al., 2010, MNRAS, 406, 1084
Thomson G. S., et al., 2012, MNRAS, 423, 2901
Timmes F. X., Swesty F. D., 2000, ApJs, 126, 501
Tody D., 1986, SPIE, 0627, 733
Tody D., 1993, ASPCS, 52, 173
Tout C. A., Hall D. S., 1991, MNRAS, 253, 9
Tout C. A., et al., 1996, MNRAS, 281, 257
VanderPlas J. T., 2018, ApJS, 236, 16
Veyette M. J., et al., 2016, ApJ, 828, 95
Wang L., et al., 2016, MNRAS, 458, 1450
Wielen R., 1974, Highlights of Astronomy, 3, 395
Wood M., 1995, Theoretical white dwarf luminosity functions: DA models, *White Dwarfs*. Springer Berlin Heidelberg, p. 41
Woosley S. E., Heger A., Weaver T. A., 2002, Rev Mod Phys, 74, 1015
Xin Y., et al., 2015, ApJ, 801, 67
Y Potekhin A., 2010, Physics Uspekhi, 53, 1235
Zhao Y., et al., 2020, MNRAS, 499, 3338
Zurek D. R., et al., 2009, ApJ, 699, 1113
Zurek D. R., et al., 2016, MNRAS, 460, 3660
van Saders J., Pinsonneault M., 2012, ApJ, 751, 98

Acknowledgements

First and foremost, the person who deserves my full appreciation and gratitude is Pavel Kroupa for his guidance, support and invaluable advice. His enthusiasm and passion are unbeatable driving forces. His constant encouragement gives me confidence, motivation and the belief in myself that I will succeed. His kindness goes a long way and is greatly appreciated and I thank him deeply.

I would also like to thank Andrea Dieball for taking the time to teach me all the tools I needed to perform the photometry, I learned a great deal from her and truly appreciate it. I also thank the other co-authors on the M30 papers for their support and thoughtful comments throughout the process.

I also humbly thank my best friend and husband William Mansfield without whom I would not be here today. His constant support, love and endless patience throughout my scientific education in Germany has given me the opportunity and ability to succeed in this thesis. And finally, of course, a special mention to my precious four-legged furry companion Luna who has been constantly by my side, bringing everlasting happiness and laughter into our lives.

Appendix A

Far-ultraviolet investigation into the galactic globular cluster M30 (NGC 7099): I. Photometry and radial distributions

The paper **Mansfield et al., MNRAS, Volume 511, Issue 3, April 2022, DOI: 10.1093/mnras/stac242** is provided below in its published form.

Monthly Notices of the ROYAL ASTRONOMICAL SOCIETY

MNRAS **511,** 3785–3794 (2022)
Advance Access publication 2022 January 29

https://doi.org/10.1093/mnras/stac242

Far-ultraviolet investigation into the galactic globular cluster M30 (NGC 7099): I. Photometry and radial distributions

Santana Mansfield [1]★ Andrea Dieball,[1] Pavel Kroupa [1,2] Christian Knigge,[3] David R. Zurek,[4] Michael Shara [4] and Knox S. Long[5]

[1] *Helmholtz-Institut für Strahlen- und Kernphysik (HISKP), Universität Bonn, Nußallee 14-16, D-53115 Bonn, Germany*
[2] *Astronomical Institute, Faculty of Mathematics and Physics, Charles University in Prague, V Holešovičkách 2, CZ-18000 Praha, Czech Republic*
[3] *School of Physics and Astronomy, University of Southampton, Highfield, Southampton SO17 1BJ, UK*
[4] *Department of Astrophysics, American Museum of Natural History, New York, NY 10024, USA*
[5] *Space Telescope Science Institute, 3700 San Martin Drive, Baltimore, MD 21218, USA*

Accepted 2022 January 20. Received 2022 January 20; in original form 2021 October 26

ABSTRACT

We present a far-ultraviolet (FUV) study of the globular cluster M30 (NGC 7099). The images were obtained using the Advanced Camera for Surveys (ACS/SBC, F150LP, FUV) and the Wide Field Planetary Camera 2 (WFPC2, F300W, UV) which were both onboard the *Hubble Space Telescope*. The $FUV - UV$ colour–magnitude diagram (CMD) shows a main sequence (MS) turnoff at $FUV \approx 22$ mag and $FUV - UV \approx 3$ mag. The MS extends 4 mag below the turnoff, and a prominent horizontal branch (HB) and blue straggler (BS) sequence can be seen. A total of 1218 MS stars, 185 red giant branch stars, 47 BS stars, and 41 HB stars are identified, along with 78 sources blueward of the MS which consist of white dwarfs (WDs) and objects in the gap between the WDs and the MS that include potential cataclysmic variable (CV) candidates. The radial distribution of the BS population is concentrated towards the cluster centre, indicating that mass segregation has occurred. The blue and red sub-populations of the double BS sequence appear mixed in the ultraviolet CMD, and no significant central concentration of CV candidates is seen in this cluster.

Key words: techniques: image processing – techniques: photometric – globular clusters: individual: M30 NGC 7099 – blue stragglers – Hertzsprung–Russell and colour–magnitude diagrams – ultraviolet: stars.

1 INTRODUCTION

Globular clusters (GCs) in our Milky Way are tightly bound groups of very old (>10 Gyr) and metal-poor stars. They formed in the early Galaxy and can contain hundreds of thousands of stars, with extremely high stellar densities in the cores. At optical wavelengths, the luminosity of a GC is dominated by the large number of main sequence (MS) stars and evolved stars including red giant branch (RGB) stars and horizontal branch (HB) stars, as well as blue stragglers (BSs). Stellar exotica such as white dwarfs (WDs), binaries such as cataclysmic variables (CVs; consisting of a WD accreting mass from a companion) and low-mass X-ray binaries (containing a neutron star or a black hole accreting material from a low-mass companion) are optically faint and are therefore not easily detected in the cores of GCs in the visual wavebands. The spectral energy distribution of these hot exotic objects usually peaks at far-ultraviolet (FUV) wavelengths, where MS stars and RGBs are faint. As a result, the core of a GC appears less crowded in the FUV and the exotic sources can be more easily detected and examined. Several cores of Galactic GCs have been studied in the FUV, including M2 (Dalessandro et al. 2009), M15 (Dieball et al. 2007), M80 (Dieball et al. 2010; Thomson et al. 2010), NGC 1851 (Parise et al. 1994; Zurek et al. 2009; Maccarone et al. 2010; Zurek et al. 2016; Subramaniam et al. 2017), NGC 2808 (Brown et al. 2001; Dieball et al. 2005), NGC 5466 (Sahu et al. 2019), NGC 6397 (Dieball et al. 2017), NGC 6752 (Thomson et al. 2012), and 47 Tuc (Knigge et al. 2000). Also M3, M13, and M79 (Dalessandro et al. 2013a), and the outskirts of GCs have been observed with the *Galaxy Evolution Explorer* survey of GCs (Dalessandro et al. 2012; Schiavon et al. 2012), and the *Swift Gamma-Ray Burst Mission* UVOT survey (Siegel et al. 2014, 2015).

We are able to probe deeper into GCs by detecting stellar populations that shine brightly in specific wavelengths, particularly those populations which formed by dynamical interactions. For example, BSs appear to be on the MS above the turnoff point, although the cluster's age indicates that they should have evolved away from the MS to become red giants. These sources likely have mass added by either mass transfer from a companion (McCrea 1964), or resulting from a direct collision (Hills & Day 1976), which adds hydrogen fuel to the core allowing these stars to remain on the MS for longer than they would have otherwise. The high density of stars in the cluster core allows frequent interactions resulting in various exotic sources such as BS stars, CVs, X-ray binaries, and millisecond pulsars (Ivanova et al. 2006; Shara & Hurley 2006; Hurley, Aarseth & Shara 2007; Hong et al. 2016; Kremer et al. 2020). Detailed stellar-dynamical analyses can be found in Leigh, Sills & Knigge (2007, 2011), Leigh et al. (2013, 2015), Chatterjee et al.

★ E-mail: smansfield@astro.uni-bonn.de

(2010, 2013), Hypki & Giersz (2012), Wang et al. (2016), Belloni et al. (2017, 2018a, 2018b, 2020), and Rui et al. (2021). Binary systems are important for the dynamical evolution of the cluster (Heggie 1975; Hut et al. 1992), as the binding energy in the binary can be transferred to other stars in dense stellar systems, stabilizing the cluster against deep core collapse (Hills 1975; Hurley & Shara 2012; Breen & Heggie 2013; Rodriguez et al. 2016), such that the initial binary population constitutes an essential aspect (Belloni et al. 2017). Thus, the detection of binary systems is important for our understanding of the dynamical state of the cluster.

M30 (NGC 7099) is a metal-poor GC with a metallicity of [Fe/H] = –2.12 (Harris 1996). It is located 8.3 ± 0.2 kpc away from us in the Galactic halo and has an estimated age of 13.0 ± 0.1 Gyr (Kains et al. 2013). M30 has a retrograde orbit with an average orbital eccentricity of $\langle e \rangle = 0.316$, average perigalactic and apogalactic distances of $\langle r_{\rm min} \rangle = 3.94$ kpc and $\langle r_{\rm max} \rangle = 7.58$ kpc, respectively, and an average maximum distance from the Galactic plane of $\langle |z|_{\rm max} \rangle = 4.95$ kpc [Allen, Moreno & Pichardo 2006, based on a non-axisymmetric (barred) Galactic potential]. M30 has a cluster mass of $\approx 1.6 \times 10^5\,{\rm M}_\odot$ and is core-collapsed: it has dynamically evolved so that the most massive stars have fallen inward and are concentrated towards the cluster core within a radius of only 1.9 arcsec (0.08 pc, Sosin 1997). M30 has a very high central density ($\approx 10^6\,{\rm M}_\odot\,{\rm pc}^{-3}$; Lugger et al. 2007), indicating a high rate of stellar interactions and activity in the core region. This has resulted in a large bluer inward colour gradient, where the $B-V$ colour profile has a strong inclination towards bluer magnitudes in the centre, resulting from the infall of BS stars and a depletion of RGs from the core (Howell, Guhathakurta & Tan 2000). Optical studies on M30 have yet to find a significant CV or WD population.

Based on the optical *Hubble Space Telescope* (*HST*) Wide Field Planetary Camera 2 (WFPC2) data, a significant BS population is observed in M30 (Guhathakurta et al. 1998), and Ferraro et al. (2009) suggest that these stars can be divided into two distinct BS sequences in the $V-I$ colour–magnitude diagram (CMD). The blue BS sequence aligns with the zero-age main sequence (ZAMS) and the red sequence lies at a brighter magnitude of $\Delta V \approx 0.75$ mag. Isochrones from stellar evolution models representing collisions are found to lie along the blue BS sequence (Ferraro et al. 2009; Sills, Karakas & Lattanzio 2009), and the red BSs populate a region that can be reproduced with models which undergo mass transfer (Xin et al. 2015). Portegies Zwart (2019) also produced stellar simulations and show that red BSs form by mass transfer at a constant rate over the cluster lifetime, whereas the blue BSs may have formed by mergers during a short burst of activity when the core of the cluster collapsed roughly 3.2 Gyr ago. The burst of activity would have resulted from the increased likelihood for interactions between stars due to the collapsing cluster core. It remains unknown, however, why the two sequences are parallel and why the red sequence is ≈ 0.75 mag brighter than the blue one. Double BS sequences have also been detected in NGC 362 (Dalessandro et al. 2013b) and NGC 1261 (Simunovic, Puzia & Sills 2014).

This first work in our study of M30 aims at analysing *HST* FUV and UV data using photometry and providing an ultraviolet CMD and an analysis of the radial distributions of the different stellar populations. The observations and data reduction are described for each filter in Section 2 and the $FUV-UV$ CMD is presented in Section 3. The optical counterpart matching is given in Section 4, and radial distribution analysis in Section 5, followed by a summary in Section 6. A following publication in this study will include potential counterparts to known X-ray sources and an investigation into the variable sources in M30.

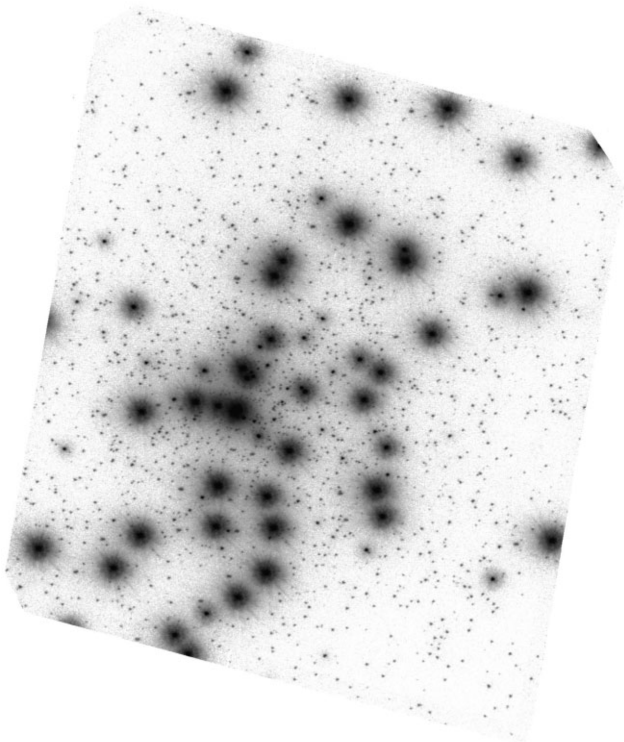

Figure 1. Master image of the FUV ACS/F150LP exposures of the core of M30, which spans 34.6 arcsec × 30.8 arcsec (1.40 pc × 1.24 pc). North is up and east is to the left.

2 OBSERVATIONS AND IMAGE PROCESSING

2.1 The ACS FUV data

The FUV data were obtained with the Advanced Camera for Surveys (ACS) onboard the *HST*, using the Solar Blind Channel (SBC) and F150LP filter (program GO-10561; PI: Dieball), in 15 orbits distributed over three visits, from the 2007 May 29 to June 9. The SBC has a field of view of 34.6 arcsec × 30.8 arcsec and a pixel scale of 0.034 arcsec × 0.030 arcsec pixel^{-1}. Sixty-four images were taken, each with an exposure time of 315 s, resulting in a total exposure time of 20 160 s, and are described in Table 1. Thermal breathing during the 96 min day-night cycle of the *HST* for each visit, as well as guide star re-acquisition, can create small shifts between the individual images taken at the same pointing position. As a first step, a master image is created which realigns all individual images using the TWEAKREG task from the DRIZZLEPAC package running under PYRAF (Greenfield & White 2000). This task compares the world coordinate system data in the header of each image to a reference image (the first in our list) and calculates the small residual shifts made by the pointing differences. The threshold is adjusted to ensure the rms of the shifts is small and there is no correlation in the residual plots. The images are then combined into a geometrically corrected master image using the ASTRODRIZZLE task from the DRIZZLEPAC package. This task incorporates the processes of performing sky subtraction, drizzling, creating a median image, cosmic ray removal, and final combination into the master image. In this instance, cosmic ray removal is not needed as the SBC is not sensitive to cosmic rays. The FUV master image is shown in Fig. 1. Although this shows the extremely dense core region of the cluster, the FUV image does not suffer from

Table 1. Log of the observation dates, the camera and filters used, and the total exposure times.

Camera	Filter	Data set	Start date	Exposure time (s)
ACS/SBC	F150LP	J9HC02011	29 May 2007 16:45:50	5040
ACS/SBC	F150LP	J9HC04011	3 June 2007 11:51:14	5040
ACS/SBC	F150LP	J9HC04021	3 June 2007 15:01:42	2520
ACS/SBC	F150LP	J9HC06011	9 June 2007 02:10:34	7560
WFPC2	F300W	U9HC0301M-U9HC0308M	29 May 2007 19:58:16	4000
WFPC2	F300W	U9HC0501M-U9HC0508M	3 June 2007 16:39:16	4000
WFPC2	F300W	U9HC0701M-U9HC0708M	9 June 2007 07:00:16	4000

much crowding since the numerous MS stars are faint at these wavelengths.

2.1.1 *Object identification*

Most of the potential sources are automatically detected using the DAOFIND task in the DAOPHOT package (Stetson 1987), running under PYRAF. This task determines if there is a source in a given pixel by applying a Gaussian profile on the surrounding pixels. A detection is recorded if there is a good fit with a large positive central height of the Gaussian, whereas a negative or minimal height resembles the edge of a star or an empty region of sky (Stetson 1987). An FWHM of 3 and zero readnoise is used for the ACS/SBC. The coordinates of found sources are overplotted onto the master image to be checked by eye. The threshold for DAOFIND needs to be chosen such that it detects as many faint sources as possible without making too many false detections in the vicinity of the brightest stars. These false detections are then removed from the list by hand (along with some false detections at the edge of the image), and any of the faint sources missed by the DAOFIND task are added. The resulting number of objects found in the FUV is 1934.

2.1.2 *Stellar photometry*

Aperture photometry was performed using the task DAOPHOT (Stetson 1987) running under PYRAF. An aperture of 4 pixels was used with a sky annulus of 8–12 pixels. A small aperture is needed for dense stellar systems, however, in order to account for the limited percentage of flux contained in the small aperture, an aperture correction, ApCorr, is applied, which is the inverse of the encircled energy. The small sky annulus also contains light from the star itself, and thus a sky correction, SkyCorr, is needed. Assuming that a larger sky annulus of 60–70 pixels contains only background flux, SkyCorr is determined by taking the magnitude ratio of the large sky annulus and the small sky annulus for several chosen isolated stars (see e.g. Dieball et al. 2007). The fluxes are then converted into STMAGs using the formula:

$$\mathrm{STMAG} = -2.5 \times \log(\mathrm{flux} \times \mathrm{SkyCorr} \times \mathrm{ApCorr} / \mathrm{ExpTime}) + \mathrm{ZPT},$$

where ZPT = –21.1 mag is the zero-point for the STMAG system, and flux = counts × PHOTFLAM, where PHOTFLAM is the inverse sensitivity of the instrument used to convert count rates into fluxes, and can be found in the image header. For the ACS filter F150LP, this is:

$$\mathrm{PHOTFLAM}_{\mathrm{ACS,F150LP}} = 3.246305 \times 10^{-17} \mathrm{erg\ cm^{-2}\ \AA^{-1}\ count^{-1}}.$$

For an annulus of 4 pixels, the corrections are ApCorr = 1.7636 (Avila & Chiaberge 2016) and SkyCorr = 1.011.

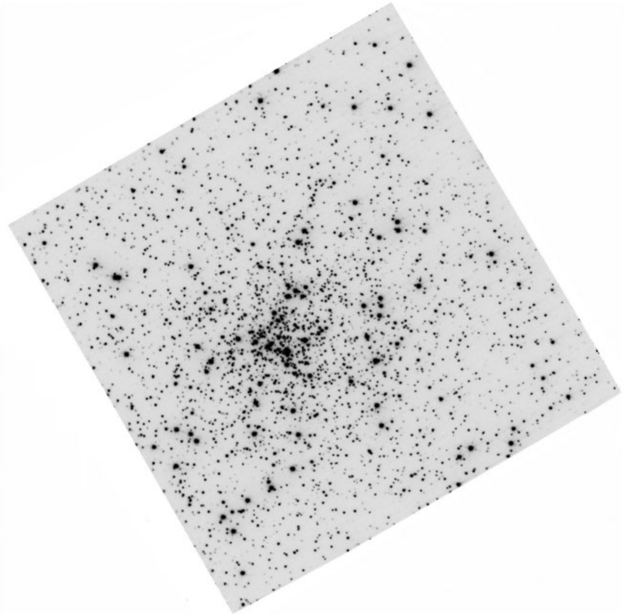

Figure 2. F300W master image of the WFPC2/PC exposures of M30, with a field of view of 34 arcsec × 34 arcsec (1.37 pc × 1.37 pc). North is up and east is to the left.

2.2 The WFPC2 F300W data

The UV data were obtained using the WFPC2 which was onboard the *HST* (program GO-10561; PI: Dieball) with the F300W filter in 15 orbits distributed over three visits, from 2007 May 29 to June 9. The WFPC2 consists of four cameras, the three Wide Field Cameras (WFCs) each with a field of view of 50 arcsec × 50 arcsec, and the Planetary Camera (PC) with a field of view of 34 arcsec × 34 arcsec, and a pixel scale of 0.046 arcsec pixel^{-1}. The PC was centred on the cluster core. The exposures from these four chips are placed together into a mosaic image. Twenty-four mosaic images were taken with a total exposure time of 12 000 s (Table 1).

2.2.1 *Object identification and stellar photometry*

A master image is created using the same method that was used for the FUV data, with the TWEAKREG and ASTRODRIZZLE tasks from the DRIZZLEPAC package running under PYRAF (Greenfield & White 2000), and is shown in Fig. 2. Photometry was performed using the package DOLPHOT (Dolphin 2000), running under IRAF (Tody 1986, 1993). This program carries out the image alignment with respect to a reference image (our master image), source detection and photometry directly on the 24 flat-fielded exposures. DOLPHOT contains a specific module for the WFPC2 which performs PSF-

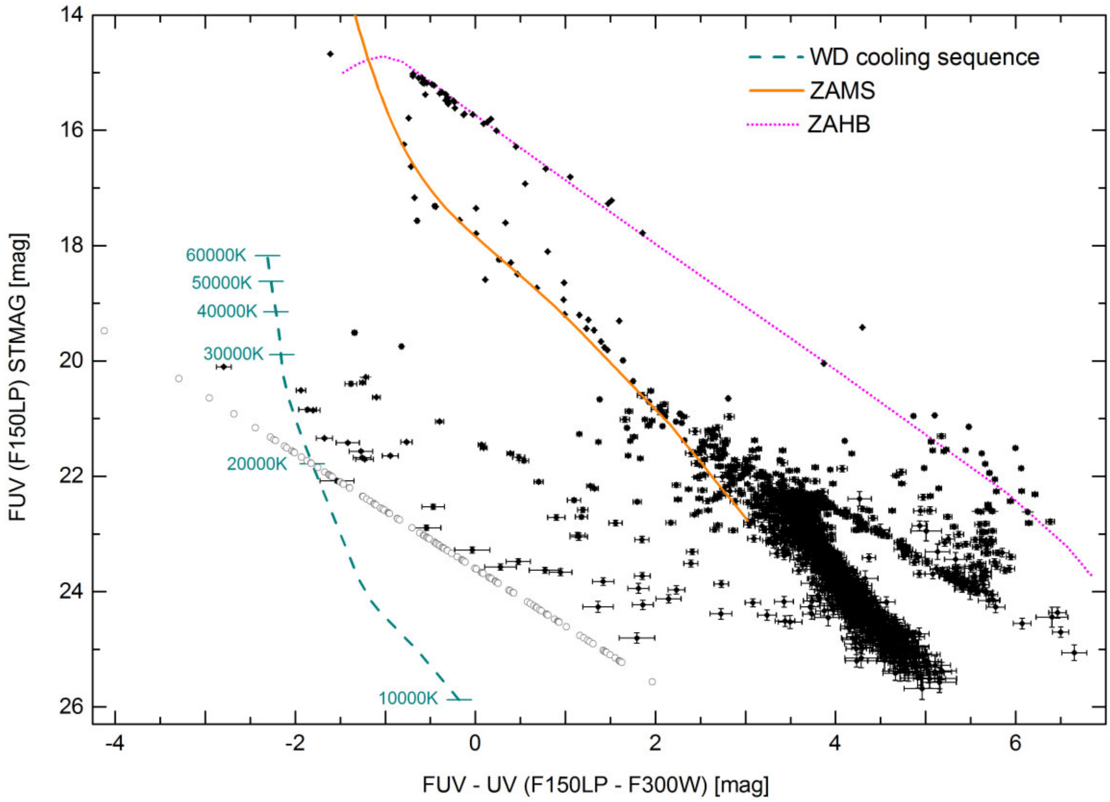

Figure 3. *FUV – UV* CMD of M30. A theoretical ZAMS (solid orange line), ZAHB (dotted pink line), and a CO WD cooling sequence (dashed green line) have been added for orientation. The surface temperatures of WDs are also indicated. Additionally shown are sources measured in the FUV but with no UV counterpart (grey circles), using the detection limit of the UV to estimate their position on the CMD, which also represents the location of the detection limit.

fitting using a pre-calculated PSF model for the F300W filter,[1] and the output magnitudes are already flux corrected. As the ACS/FUV field of view is contained within the field of view of the PC, only the data from this chip are needed here. For the photometry, the recommended parameters for the WFPC2 module are first used, then optimized so that as many faint sources were measured as possible.[2] The number of objects found in the PC/F300W data is 10451, with 8836 of these within the FUV field of view.

2.3 Catalogue matching

In order to find objects that appear in both the FUV and UV data, the coordinates of the sources found in the FUV image are transferred into the UV frame. In order to make the conversion, the x and y positions of 30 reference stars easily identified in both images are used as input for the task GEOMAP running under PYRAF. This computes the spatial transformation which is used by the GEOXYTRAN task to transform the coordinates of the FUV objects into the UV frame. This is checked by overplotting the transformed FUV coordinates onto the UV image. The two catalogues are then compared for matching stars using the task TMATCH which correlates the two lists for sources matching in coordinates within a radius of a given number of pixels. The average matching radius for sources in both frames is 0.35 pixels, and this procedure results in 1569 matching objects. The first 30 entries of the final list of sources are given in Table 2.

[1] http://americano.dolphinsim.com/dolphot

[2] The optimized parameters are: imgRPSF = 10, RCentroid = 1.

A number of chance matches are expected, and can be estimated using the numbers of objects in the two wavelengths and the matching radius (Knigge et al. 2003). The estimated number of spurious matches is 74 pairs (4.6 per cent of all matches).

3 THE *FUV – UV* CMD

The *FUV – UV* CMD is given in Fig. 3. A theoretical ZAMS, zero-age horizontal branch (ZAHB), and WD cooling sequence with marked surface temperatures are included for orientation purposes. These are calculated using the fitting formulae of Tout et al. (1996), the theoretical ZAHB models from Dorman (1992a) and the Wood (1995) grid of WD cooling curves with a grid of synthetic WD spectra by Gänsicke, Beuermann & de Martino (1995). Kurucz models of stellar atmospheres are used for interpolation and the resulting spectra are then folded with the appropriate filter and detector combinations using PYSYNPHOT running under PYRAF. The cluster parameters used are a distance of 8.3 kpc, a metallicity of [Fe/H] $= -2.12$ and a reddening of $E(B-V) = 0.03$ mag.

There is a well-defined MS, with turnoff at $FUV \approx 22$ mag and $FUV - UV \approx 3$ mag. Many BS sources are seen along the ZAMS at brighter magnitudes than the turnoff. The RGB lies from the turnoff towards fainter and redder magnitudes. The HB reaches from the RGB up to $FUV \approx 15$ mag. The sources between the MS and WD cooling sequence are called gap objects and are likely to include CV candidates (Dieball et al. 2007). Also included are 126 sources present in both FUV and UV fields of view with FUV measurements but no UV counterparts. The detection limit of $UV = 23.6$ mag was

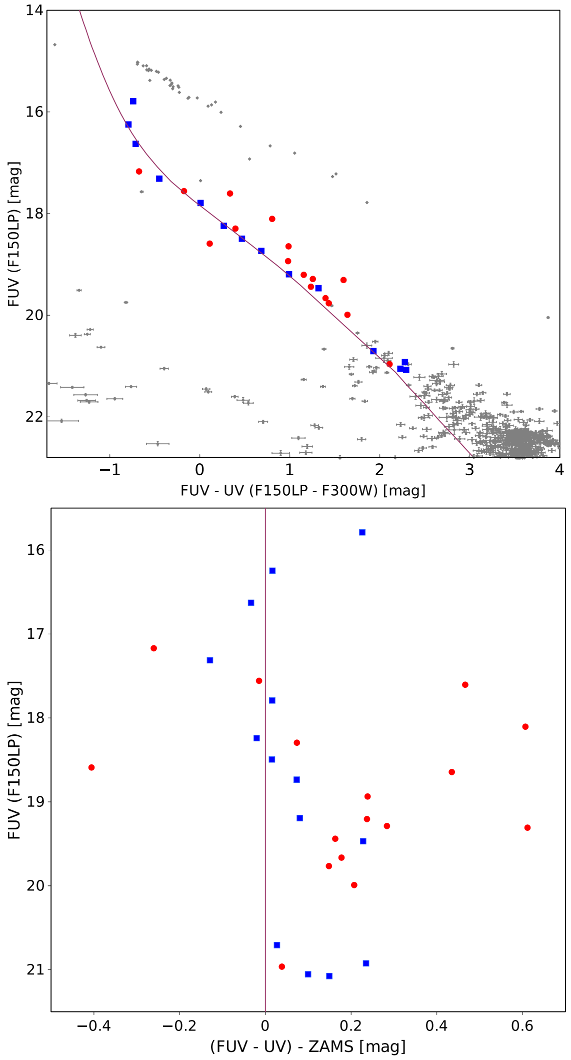

Figure 4. The BS sources that are found to be in a double BS sequence in the infrared by Ferraro et al. (2009), marked according to whether they belonged to the blue (squares) or red (circles) BS sequence, on the $FUV - UV$ CMD (top) and their position verticalized along with respect to the ZAMS (bottom).

used to estimate the position of these sources in the CMD, and as such they lie on the line representing this limit.

Fig. 4 shows 16 of the BSs that are situated in the red BS sequence in Ferraro et al. (2009), and 13 from the blue BS sequence. As the separations in colour are small, they are also plotted in Fig. 4 in a verticalized CMD with respect to the theoretical ZAMS curve used in Fig. 3. The highest uncertainty in the $FUV - UV$ position for these sources was 0.024 mag, and 0.004 mag for the FUV. Of the two BS sources without counterparts from Ferraro et al. (2009), the source at $FUV - UV \approx 0$ mag (ID27) was just outside of their field of view, and the one at $FUV - UV \approx -0.65$ mag (ID283) matched within 2 pixels to the position of a source that was between the double BS sequence and the RGB (Ferraro et al. 2009, their source #11002543), and as such was not included. The field of view in our study only included the cluster centre, thus further observations using a larger field of view of this cluster in FUV wavelengths are needed to fully explore the BS population; however, we find that there is no clear distinction between the two BS sequences in our data set. The sources that were attributed to the distinct sequences in Ferraro et al. (2009) appear to be well mixed in the ultraviolet, particularly as two of the red BS sources have a large blue excess compared to the other BSs (Fig. 4). As the sources on the red BS sequence are thought to be the result of mass transfer (Xin et al. 2015), the reason the two sub-populations appear mixed may be due to the sources on the red sequence being in an active state of mass transfer. Xin et al. (2015) detail a binary model that begins mass transfer at 7.54 Gyr, becomes brighter than the MS turnoff at around 10 Gyr, remains in the BS region for another 3–4 Gyr with mass transfer ceasing at 12.78 Gyr. Systems with active mass transfer emit FUV radiation due to the hot material in the accretion disc which would give these sources a blue excess in the $FUV - UV$ CMD. These active systems would then be shifted bluewards towards (and even beyond) the blue BS sequence in the ultraviolet.

There are around 78 WD/Gap objects blueward of the MS. We can make an estimate of the expected number of WDs in M30 by assuming that the number of stars in both of the HB and WD phases is proportional to the lifetime of these phases (Richer et al. 1997):

$$\frac{N_{\rm WD}}{N_{\rm HB}} \approx \frac{\tau_{\rm WD}}{\tau_{\rm HB}}. \tag{1}$$

If we assume that $\tau_{\rm HB} \approx 10^8$ yr (Dorman 1992b), the temperature of the WD cooling curve at the detection limit is 20 000 K $\approx 5 \times 10^7$yr (Althaus & Benvenuto 1998), and using the number of HB sources found in our sample $N_{\rm HB} = 41$, we find that the estimated expected number of WDs is $N_{\rm WD} \approx 20$. This rough estimate is in agreement with the sources on or near the WD cooling curve (Fig. 3) which have UV counterparts, and there may also be a few WDs in the 23 sources with $FUV < 22$ but were not detected in the UV.

The other sources in the gap between the WD cooling curve and the MS are expected to include a number of CVs. A GC such as M30 should produce $\approx$ 200 CVs by 13 Gyr (Ivanova et al. 2006), through various formation channels such as primordial CVs in which the binary components are the original two stars, and also dynamical binary exchange encounters and tidal capture. However, in the dense core, interactions with other cluster members mean that the rate of destruction of CVs is greater than the formation rate (Belloni et al. 2018b), and CVs are expected to have shorter lifetimes than their field counterparts by a factor of 3 (Shara & Hurley 2006). Belloni et al. (2018b) find that around 45 per cent of detectable CVs are within the half-light radius of a GC, which for M30 is 1.03 arcmin (Harris 1996). After scaling down to our field of view, and taking the destruction rate into account, we have a predicted number of detectable CVs in our images of $\approx$ 8. The remaining sources in this region of the CMD that are not CVs or individual WDs are likely to be detached WD–MS binaries, where the hot emission from the WD surface and the cooler radiation from the MS surface places the combined flux of the binary in the region between these two populations. There is also the possibility of chance superpositions, and following the same prescription that was used for the whole data set in Section 2.3, the expected number of spurious matches in the WD/Gap population is $\approx$ 1. Additionally, some sources which lie close to the MS and BS sequence may indeed be MS or BS stars. We stress that the predicted number of CVs is a rough estimate, and a closer investigation into the particular sources that are CV candidates is given in the following publication in this study.

We note that for the remainder of this study, most of the sources discussed have been determined as belonging to certain populations by their location in the $FUV - UV$ CMD. Yet there may be some sources which truly belong to a different group, as mentioned in the preceding paragraph of the gap sources close to the MS and BS sequence. This is especially true for the sources near the MS turnoff that have been included in the BS group for example, but may really

Table 2. The first 30 entries from the catalogue of sources in the FUV and UV field of view. The ID number is given in the first column, the position of the source in Columns 2 and 3, the radial distance is given in Column 4, and the pixel position of the source on the FUV image is in Columns 5 and 6. The magnitudes are in Columns 7–9 and the resulting population type of each source (determined from the position in the *FUV* – *UV* CMD) is given in Column 10. Also included in Columns 11–13 are the corresponding $B - V$ and V magnitudes and ID number from the optical catalogue (Guhathakurta et al. 1998). This table is published in its entirety in the supplementary material (online).

ID	RA [h:m:s]	Dec. [°:′:″]	r^a [arcmin]	x_{FUV} [pixels]	y_{FUV} [pixels]	FUV [mag]	UV [mag]	$FUV - UV$ [mag]	Type	B−V^b [mag]	V^b [mag]	ID$^b_{\mathrm{Optical}}$
1	21:40:20.94	−23:10:55.71	0.313	479.48	74.20	15.431 ± 0.001	15.742 ± 0.001	− 0.311 ± 0.002	HB	−0.09	15.63	755
2	21:40:20.79	−23:10:48.11	0.314	794.64	81.69	22.464 ± 0.030	18.868 ± 0.004	3.596 ± 0.034	MS	0.34	18.69	635
3	21:40:20.87	−23:10:48.48	0.296	767.87	119.88	22.654 ± 0.033	18.908 ± 0.004	3.746 ± 0.037	MS	0.37	18.74	699
4	21:40:20.89	−23:10:47.74	0.291	793.36	137.83	22.550 ± 0.039	18.654 ± 0.004	3.896 ± 0.036	MS	0.39	18.43	714
5	21:40:20.81	−23:10:42.51	0.319	1005.74	157.13	22.583 ± 0.033	18.852 ± 0.004	3.731 ± 0.037	MS	0.36	18.67	665
6	21:40:20.92	−23:10:46.79	0.282	823.92	168.39	22.521 ± 0.031	18.835 ± 0.004	3.686 ± 0.035	MS	0.34	18.69	746
7	21:40:21.19	−23:10:57.86	0.283	358.25	182.20	18.495 ± 0.005	18.027 ± 0.003	0.468 ± 0.008	BS			
8	21:40:21.16	−23:10:56.00	0.270	434.47	187.06	21.511 ± 0.020	15.513 ± 0.002	5.998 ± 0.022	RG	1.12	12.69	1005
9	21:40:21.16	−23:10:54.62	0.256	485.79	207.67	22.478 ± 0.031	18.767 ± 0.004	3.711 ± 0.035	MS	0.44	18.57	1025
10	21:40:20.90	−23:10:42.02	0.301	1010.36	210.87	22.364 ± 0.032	18.781 ± 0.004	3.583 ± 0.036	MS	0.29	18.57	730
11	21:40:21.22	−23:10:56.63	0.264	400.37	213.90	22.314 ± 0.029	16.099 ± 0.001	6.215 ± 0.030	RG	0.72	14.65	1107
12	21:40:21.30	−23:10:58.23	0.266	325.55	240.04	22.390 ± 0.030	18.784 ± 0.004	3.606 ± 0.034	MS			
13	21:40:20.97	−23:10:40.17	0.298	1071.16	266.28	22.401 ± 0.033	18.685 ± 0.004	3.716 ± 0.037	MS	0.33	18.48	796
14	21:40:21.26	−23:10:53.33	0.226	520.49	272.55	21.896 ± 0.023	18.325 ± 0.003	3.571 ± 0.026	MS	0.36	18.16	1163
15	21:40:21.23	−23:10:51.75	0.223	586.04	273.16	22.376 ± 0.029	18.568 ± 0.004	3.808 ± 0.033	MS	0.34	18.29	1120
16	21:40:21.19	−23:10:50.02	0.223	658.10	274.11	22.578 ± 0.032	18.921 ± 0.004	3.657 ± 0.036	MS	0.36	18.82	1070
17	21:40:21.03	−23:10:42.37	0.270	976.93	274.68	19.812 ± 0.009	18.346 ± 0.003	1.466 ± 0.012	BS	0.12	18.18	860
18	21:40:21.01	−23:10:41.41	0.280	1016.38	276.28	15.187 ± 0.001	15.758 ± 0.001	− 0.571 ± 0.002	HB	−0.12	15.78	841
19	21:40:21.36	−23:10:54.51	0.216	459.70	312.16	22.301 ± 0.028	18.568 ± 0.004	3.733 ± 0.032	MS	0.57	18.27	1278
20	21:40:21.31	−23:10:52.23	0.207	554.79	311.87	22.431 ± 0.031	16.489 ± 0.001	5.942 ± 0.032	RG	0.69	15.14	1222
21	21:40:21.23	−23:10:37.61	0.267	1127.68	436.35	22.270 ± 0.028	23.859 ± 0.276	− 1.589 ± 0.304	Gap	0.30	18.70	1221
22	21:40:21.19	−23:10:45.25	0.222	841.07	327.62	22.445 ± 0.030	18.627 ± 0.004	3.818 ± 0.034	MS	0.37	18.33	1075
23	21:40:21.03	−23:10:37.57	0.307	1161.20	328.22	22.492 ± 0.032	18.604 ± 0.004	3.888 ± 0.036	MS	0.43	18.32	865
24	21:40:21.25	−23:10:47.84	0.205	732.63	329.89	22.497 ± 0.031	18.814 ± 0.004	3.683 ± 0.035	MS	0.32	18.70	1158
25	21:40:21.47	−23:10:57.80	0.235	316.94	331.07	22.390 ± 0.030	18.640 ± 0.004	3.750 ± 0.034	MS	0.40	18.49	1459
26	21:40:21.16	−23:10:43.49	0.235	913.04	333.06	22.618 ± 0.034	18.496 ± 0.003	4.122 ± 0.037	RG	0.37	18.26	1036
27	21:40:21.13	−23:10:41.56	0.254	992.76	335.06	17.353 ± 0.003	17.345 ± 0.002	0.008 ± 0.005	BS	−0.01	17.37	987
28	21:40:21.12	−23:10:40.56	0.262	1031.70	345.38	22.304 ± 0.034	18.767 ± 0.004	3.537 ± 0.038	MS	0.32	18.70	983
29	21:40:21.48	−23:10:56.31	0.213	371.12	357.70	22.529 ± 0.032	18.961 ± 0.004	3.568 ± 0.036	MS	0.35	18.77	1482
30	21:40:21.35	−23:10:49.55	0.185	651.59	362.87	21.075 ± 0.016	18.783 ± 0.004	2.292 ± 0.020	BS	0.18	18.69	1269
:												

Notes. (a) From the cluster centre at $x = 443.9$, $y = 362.8$ in the UV image, corresponding to RA = $21^{\mathrm{h}}40^{\mathrm{m}}22\overset{\mathrm{s}}{.}13$, Dec. = $-23^{\circ}10^{'}47\overset{''}{.}40$, determined as the centre of gravity by Ferraro et al. (2009).
(b) Guhathakurta et al. (1998).

be MS stars or gap objects, and vice versa. These initial distinctions allow us to make useful preliminary investigations into the cluster population; however, supplementary tools such as spectroscopy and additional multiwavelength observations would enable us to more accurately determine a star's true nature.

4 COMPARISON TO OPTICAL

Guhathakurta et al. (1998) presented an optical catalogue of 9507 sources for M30, the exposures of which were also taken with the WFPC2 onboard the *HST* (program GO-5324, PI: Yanny). Eight exposures were taken on 1994 March 31, two using the F336W filter with a 100 s exposure time, two using the F439W filter and 40 s exposure time and four using the F555W filter with 4 s exposure times. The data were accessed from VizeiR,[3] and by taking the well-defined group of HB stars in the optical CMD (Fig. 5), and overplotting their coordinates onto the FUV image, it is easily seen that they corresponded to the brightest sources in the FUV image, albeit with a slight shift. After correcting for the shift, these are then used as reference stars to convert the coordinates of the optical catalogue into our FUV frame. The coordinates of the HB stars are given as input for the task GEOMAP which computes the transformation. The GEOXYTRAN task carries out the transformation of the optical catalogue into the FUV frame, and then also into the UV frame using the same transformation used in Section 2.3. The optical coordinates are first converted into the FUV frame rather than directly into the UV frame, because it was easy to identify stars to use for the transformation, as the HB stars are the brightest objects in the FUV and as such are an efficient choice for the reference stars.

The resulting comparison is given in Fig. 5. Groups of sources belonging to both catalogues are plotted in colour. There are 1201 matching MS stars (yellow), 178 RGB stars (red), 44 BS sources (blue), all 41 HB stars (purple), and 42 WD/Gap objects (green) that include CV candidates. The comparison illustrates the importance of FUV observations in detecting and identifying stellar exotica such as WDs and CVs, as in the optical they are indistinguishable in position from the MS, but their hot emission in the FUV shifts their location in the $FUV - UV$ CMD blueward and brighter than the MS. This is also true for a few FUV-bright BS candidates that are in the MS region in the optical CMD. These sources appear brighter than the MS turnoff in the FUV suggesting that they could have a hot WD companion (Sahu et al. 2019). Additionally, two of our BS sources, ID7 and ID66, do not have an optical counterpart. Source ID7 was just out of the field of view in the optical exposures, and ID66 is close to the MS turnoff in the $FUV - UV$ CMD, and as such it may be a binary system with a hot WD that is bright in the ultraviolet but with an optically faint MS star companion (Knigge et al. 2000). If this is the case, it would really be a Gap object rather than a BS star, as discussed at the end of Section 3.

Several sources at the top of the optical RGB do not have FUV counterparts as they are located outside the FUV field of view. Additionally, there were 76 sources in the FUV that are undetected in the optical, including nearly half of the WD/Gap objects. This is expected for the sources in the WD cooling region as WDs are optically very faint. The reason for the Gap objects not having optical counterparts may be due to them being CVs with very low-mass MS companions, as their radial distributions suggest (Section 5), and as such were too faint to be detected in the optical. The MS stars given in the optical catalogue fainter than $V \approx 20.5$ mag are too faint to be detected in the FUV. The matched optical counterparts are identified in Table 2.

[3]https://cdsarc.cds.unistra.fr/viz-bin/cat/J/AJ/116/1757

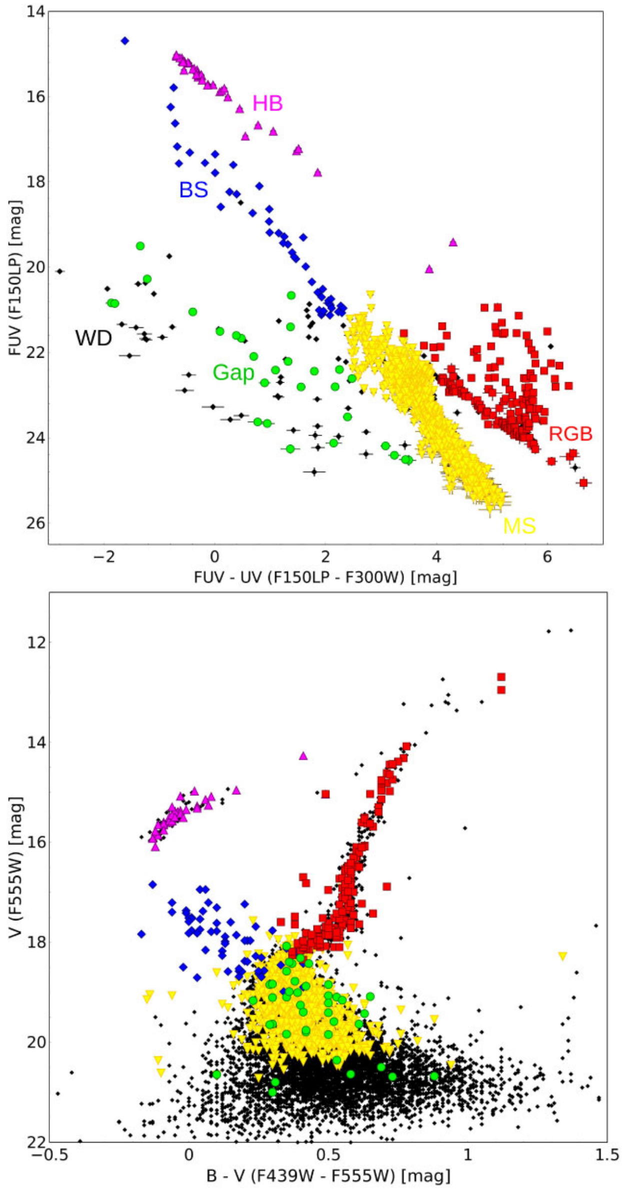

Figure 5. Comparison of the various stellar populations in the $FUV - UV$ CMD (top) and the optical CMD (bottom, based on the Guhathakurta et al. 1998 catalogue). Only the sources present in both catalogues are marked in colour. Included are MS stars (yellow down triangles), red giants (red squares), HB stars (purple up triangles), BS stars (blue diamonds), and gap objects (which include CV candidates, green circles).

5 RADIAL DISTRIBUTION

Fig. 6 shows the cumulative radial distributions of the stellar populations found in both the FUV and UV images within a radius of 15.5 arcsec from the cluster centre. The centre of the cluster used was $\alpha = 21^{\mathrm{h}}40^{\mathrm{m}}22\overset{\mathrm{s}}{.}13$, $\delta = -23^{\circ}10'47\overset{''}{.}40$ (Ferraro et al. 2009) which corresponds to pixel coordinates $x = 443.9$, $y = 362.8$ in the *UV* frame and $x = 612.1$, $y = 800.1$ in the FUV. The numbers for each stellar population in the $FUV - UV$ catalogue and those within 15.5 arcsec radius of the cluster centre are given in Table 3. Included in

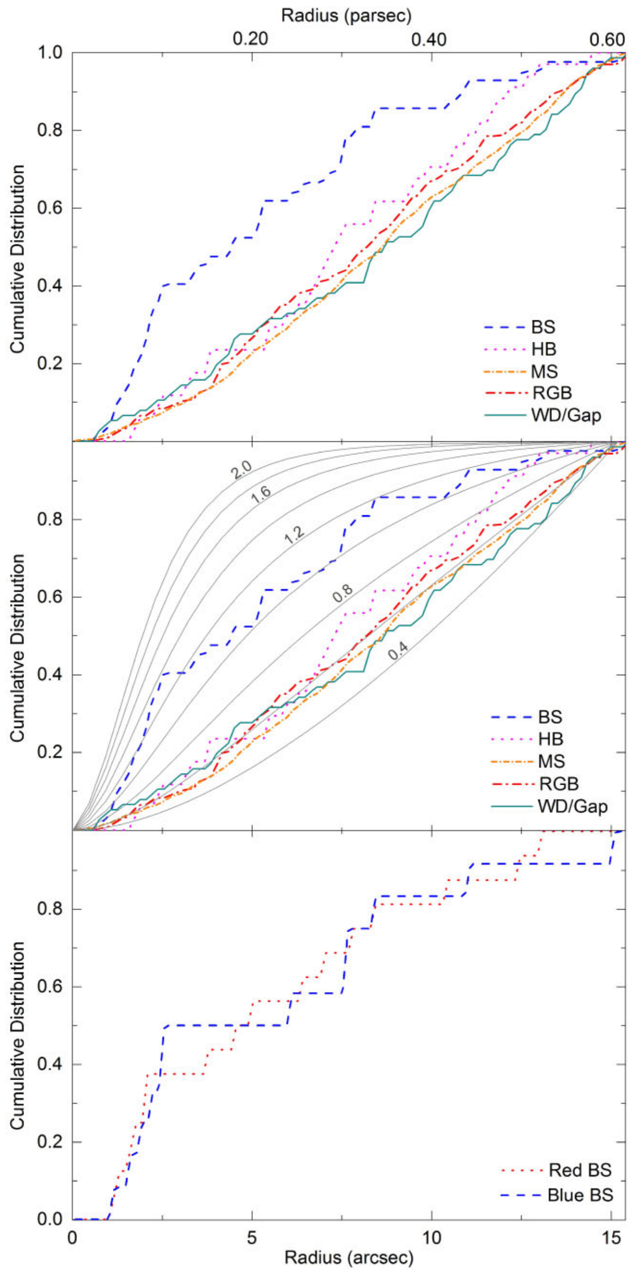

Figure 6. Cumulative radial distributions of the various stellar populations (top) with mass estimate models ranging from 0.4 to 2.0 $M_\odot$ (middle), and the sources on the red and blue BS sequences (bottom) found by Ferraro et al. (2009), within a radius of 15.5 arcsec from the centre of M30.

the group WD/Gap sources are all sources blueward of the MS/BS sequence and $FUV > 19$ mag.

The most prominent result in the radial distributions is the strong concentration of BS stars towards the centre, compared to the other populations. M30 is a core-collapsed cluster, meaning that over time the more massive stars have concentrated inward towards the centre (mass segregation). BS stars are the most massive stars out of these stellar populations, having gained mass by either mass transfer from a companion or by the merger of two stars (McCrea 1964; Hills & Day 1976), and as they are still hydrogen burning they have not yet undergone the mass-loss observed in the later stages of evolution. They are also likely to form in the cluster centre due to the high number of stellar interactions in this dense region. Thus, the BS concentration towards the centre is expected evidence of the dynamical history of the core, and is also representative of the bluer inward colour gradient observed in M30 (Howell et al. 2000).

The colour gradient also results from the central deficiency of RGB stars (Howell et al. 2000), which corresponds to the lack of central concentration of this population shown in Fig. 6. This may be due to the mass that stars typically lose during the RGB phase which could allow these stars to drift outwards. This may also be the case for the least centrally concentrated population, the HB stars, which evolve from the RGB stage. The HB stars are even absent within the inner core region of 1.9 arcsec (0.08 pc), so while the high concentration of BS stars in the centre may add to the bluer inward colour gradient of M30, it seems that the numerous HB stars, which are similar to BS in colour magnitude, do not contribute to this gradient.

The group WD/Gap sources include ≈ 20 sources that are likely isolated WD stars located near the WD cooling curve (Fig. 3), an estimated number of ≈ 8 CVs, and detached WD–MS binaries. Overall, the sources in this group are only slightly more centrally located than MS stars in M30, which is unexpected at first glance, since a central concentration was seen in other GCs such as NGC 2808 (Dieball et al. 2005) and M15 (Dieball et al. 2007), and as CVs can form from two-body interactions that are frequent in the high density centre of the cluster. CVs are binary systems, which along with the non-interacting WD–MS binaries, mean a higher combined mass than the individual stars alone. Similarly to BS stars, these higher mass sources should concentrate towards the cluster centre over time. However, the segregation of WD/Gap sources towards the centre is not observed, and a possible explanation for this might be that the combined mass of these binary systems is actually relatively low. This is true for old (≈ 10 Gyr) CVs where the WD has devoured almost all of the mass from their companion, leaving behind as little as $\approx 0.1\,M_\odot$, a negligible mass relative to the WD (Hillman et al. 2020), and also mass is lost from the system over time due to wind and outbursts from the accretion disc (Tout & Hall 1991). Additionally, as the destruction rate of CVs is higher than the formation rate in the dense cores of GCs (Belloni et al. 2018b), a number of the detached WD–MS binaries may also have undergone mass transfer in the past. Even if we also detect younger systems, it is likely that the MS companion has a low mass as otherwise the flux from the MS star would be high at the UV wavelength which is not the case for our Gap sources. As there is no central concentration seen in M30, this suggests that a large proportion of the Gap sources are binary systems with low combined masses.

The average masses of the various stellar populations can be estimated from the radial distributions by assuming the spatial distribution of a typical star is described by King (1966) models. Following the method by Heinke et al. (2003), we compare our radial distributions using a maximum-likelihood fitting to generalized theoretical King models, with the radial profile of the source surface density:

$$S(r) = \int \left(1 + \left(\frac{r}{r_{c\star}}\right)^2\right)^{\frac{1-3q}{2}} dr, \qquad (2)$$

where $q = M_X/M_\star$, with M_X being the mass of the source population we wish to find and $M_\star$ is the mass of the population within the core radius $r_{c\star} = 1.9$ arcsec (Sosin 1997). After applying a correction to the distribution to cover the non-circular field of view of the images as a function of radius, models with masses 0.4–2.0 $M_\odot$ in steps of 0.2 $M_\odot$ are calculated and shown in Fig. 6. The estimated masses for each stellar population are given in Table 3. The average mass of the

Table 3. Numbers of sources for the stellar populations in the *FUV – UV* catalogue and within a radius of 15.5 arcsec of the cluster centre of gravity, along with their estimated masses.

Population	Catalogue	15.5 arcsec radius	Mass
MS	1218	1030	0.5–0.6 $M_{\odot}$
BS	47	42	1.0–1.2 $M_{\odot}$
RG	185	169	0.6–0.7 $M_{\odot}$
HB	41	34	0.6–0.8 $M_{\odot}$
WD/Gap	78	70	0.5–0.6 $M_{\odot}$

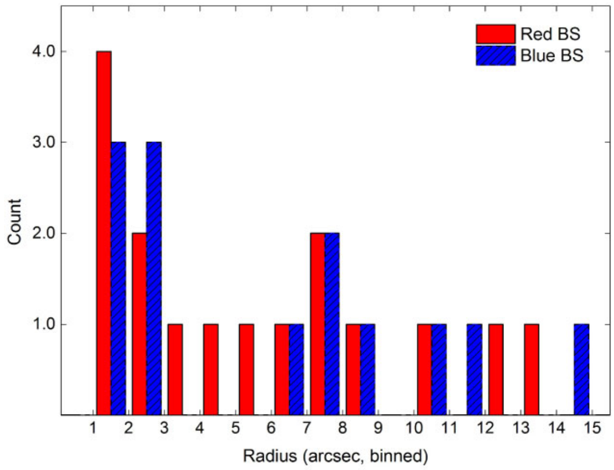

Figure 7. Discrete radial distribution of the red and blue BS sources. The radius is split into 1 arcsec-sized bins, where any red (blue) BS sources appear on the left (right) side of each bin.

BS stars is estimated to be 1.0–1.2 $M_{\odot}$ and the mass of the WD/Gap sources is 0.5–0.6 $M_{\odot}$. While only a slight overall concentration of WD/Gap sources towards the centre was seen, the sources near to the core are estimated to be more massive than those further out.

The radial distribution of the red and blue BS sources identified as two distinct sequences in Ferraro et al. (2009) is also shown in Fig. 6 which reveals no significant distinction in radial spread for the two BS sequences; both populations are centrally concentrated. Ferraro et al. (2009) show a slightly higher central concentration of red BSs in M30, although they use a different cumulative radial range, therefore we also give the discrete red and blue BS radial distributions in Fig. 7, again displaying no significant difference between the two sub-populations. From the other two clusters known to have a double BS sequence, Dalessandro et al. (2013b) find a higher central concentration of red BSs in NGC 362 and contrastingly, Simunovic et al. (2014) find a higher central concentration of blue BS stars in NGC 1261.

The similarity of the radial distributions of the various stellar populations is investigated using a Kolmogorov–Smirnov (KS) test. The KS test compares two populations and returns a probability that the two distributions are drawn from the same parent population. The higher the returned probability, the more likely the distributions are from the same population. The BS sources are comparable to the other stellar populations with KS probabilities of 0.54 per cent (BS to HB), 0.05 per cent (BS to RG), and 0.02 per cent (BS to WD/Gap sources), suggesting that the BS sources formed through a different process to the HB and RG stars, i.e. from mergers or mass transfer rather than single star evolution. The results for all population comparisons are given in Table 4.

Table 4. Probabilities that two populations of stars are from the same parent population.

Population Comparison	Probabilities per cent
MS–BS	0.001
MS–HB	47.996
MS–RG	40.998
MS–WD/Gap	62.156
BS–HB	0.5416
BS–RG	0.0452
BS–WD/Gap	0.0201
HB–RG	78.936
HB–WD/Gap	36.181
RG–WD/Gap	53.490

6 SUMMARY

Far-ultraviolet (FUV, ACS/SBC/F150LP) and mid-ultraviolet (UV, WFPC2/F300W) exposures of the GC M30 were photometrically analysed. A total of 1934 sources are detected in the FUV image and 10451 sources in the UV image. Out of these, 1569 matching sources were found. Different stellar populations are well distinguished in the resulting $FUV - UV$ CMD. The MS turnoff lies at $FUV \approx 22$ mag and $FUV - UV \approx 3$ mag. The HB consists of 41 sources, all of which have an optical counterpart from the catalogue by Guhathakurta et al. (1998). The RGB extends towards fainter and redder magnitudes, with 185 RGB sources, 178 of which are also found in the optical. A sequence of 47 BS stars is observed, 44 of these having optical counterparts. Seventy-eight WD/Gap objects are identified, 42 of which were in the optical catalogue. The $FUV - UV$ CMD allows us to easily distinguish the WD/Gap sources from MS stars.

The double BS sequence suggested by Ferraro et al. (2009) in the $V - I$ CMD is not seen in the $FUV - UV$ CMD. The two sets of BS sources are mixed in the ultraviolet which may be a result of the sources on the red BS sequence experiencing active mass transfer and emitting FUV radiation, shifting these sources blueward in the ultraviolet CMD.

The radial distributions of the stellar populations show a strong concentration of BS sources towards the centre of the cluster, implying that mass segregation has taken place. There is a deficiency of HB stars in the very centre of the cluster and no central concentration of CV candidates is found which may be due to these being old systems with low-mass MS companions.

The *HST* data for this project are sensitive enough to detect a previously unseen, significant population of WD/Gap objects, providing new insight into M30 in the ultraviolet. Investigations in the FUV continue to provide detailed detections and identifications of their stellar populations.

ACKNOWLEDGEMENTS

PK acknowledges support from the Grant Agency of the Czech Republic under grant number 20-21855S.

DATA AVAILABILITY

The data underlying this article are available in the Mikulski Archive for Space Telescopes (MAST): https://archive.stsci.edu. The data sets are derived from images in the public domain: https://archive.stsci.edu/proposal_search.php?mission=hst&id=10561. The catalogue of sources is available at CDS via anonymous ftp to cdsarc.u-strasbg.fr (130.79.128.5) or via https://cdsarc.unistra.fr/viz-bin/cat/J/MNRAS. This research also made use of the optical data available at CDS: https://cdsarc.cds.unistra.fr/viz-bin/cat/J/AJ/116/1757.

REFERENCES

Allen C., Moreno E., Pichardo B., 2006, ApJ, 652, 1150
Althaus L. G., Benvenuto O. G., 1998, MNRAS, 296, 206
Avila R. J., Chiaberge M., 2016, STScI Instrument Science Report ACS 2016-5
Belloni D., Zorotovic M., Schreiber M. R., Leigh N. W. C., Giersz M., Askar A., 2017, MNRAS, 468, 2429
Belloni D., Schreiber M. R., Zorotovic M., Ilkiewicz K., Hurley J. R., Giersz M., Lagos F., 2018a, MNRAS, 478, 5626
Belloni D., Giersz M., Rivera Sandoval L. E., Askar A., Ciecielag P., 2018, MNRAS, 483, 315
Belloni D., Giersz M., Sandoval L. E. R., Askar A., Ciecielag P., 2020, Proc. IAU Symp. 351, Star Clusters: From the Milky Way to the Early Universe. Cambridge University Press, Cambridge, p. 404
Breen P. G., Heggie D. C., 2013, MNRAS, 436, 584
Brown T. M., Sweigart A. V., Lanz T., Landsman W. B., Hubeny I., 2001, ApJ, 562, 368
Chatterjee S., Fregeau J. M., Umbreit S., Rasio F. A., 2010, ApJ, 719, 915
Chatterjee S., Rasio F. A., Sills A., Glebbeek E., 2013, ApJ, 777, 106
Dalessandro E., Beccari G., Lanzoni B., Ferraro F. R., Schiavon R., Rood R. T., 2009, ApJS, 182, 509
Dalessandro E., Schiavon R. P., Rood R. T., Ferraro F. R., Sohn S. T., Lanzoni B., O'Connell R. W., 2012, ApJ, 144, 126
Dalessandro E., Salaris M., Ferraro F. R., Mucciarelli A., Cassisi S., 2013a, MNRAS, 430, 459
Dalessandro E. et al., 2013b, ApJ, 778, 135
Dieball A., Knigge C., Zurek D. R., Shara M. M., Long K. S., 2005, ApJ, 625, 156
Dieball A., Knigge C., Zurek D. R., Shara M. M., Long K. S., Charles P. A., Hannikainen D., 2007, ApJ, 670, 379
Dieball A., Long K. S., Knigge C., Thomson G. S., Zurek D. R., 2010, ApJ, 710, 332
Dieball A., Rasekh A., Knigge C., Shara M., Zurek D., 2017, MNRAS, 469, 267
Dolphin A. E., 2000, PASP, 112, 1383
Dorman B., 1992a, ApJS, 80, 701
Dorman B., 1992b, ApJS, 81, 221
Ferraro F. et al., 2009, Nature, 462, 1028
Gänsicke B. T., Beuermann K., de Martino D., 1995, A&A, 303, 127
Greenfield P., White R. L., 2000, in Manset N., Veillet C., Crabtree D., eds, ASP Conf. Ser. Vol. 216, Astronomical Data Analysis Software and Systems IX. Astron. Soc. Pac., San Francisco, p. 59
Guhathakurta P., Webster Z. T., Yanny B., Schneider D. P., Bahcall J. N., 1998, AJ, 116, 1757
Harris W. E., 1996, AJ, 112, 1487
Heggie D. C., 1975, MNRAS, 173, 729
Heinke C. O., Grindlay J. E., Edmonds P. D., Lloyd D. A., Murray S. S., Cohn H. N., Lugger P. M., 2003, ApJ, 598, 516
Hillman Y., Shara M. M., Prialnik D., Kovetz A., 2020, Nat. Astron., 4, 886
Hills J. G., 1975, AJ, 80, 809
Hills J. G., Day C. A., 1976, Astrophys. Lett., 17, 87
Hong J., Vesperini E., Belloni D., Giersz M., 2016, MNRAS, 464, 2511
Howell J. H., Guhathakurta P., Tan A., 2000, AJ, 119, 1259
Hurley J. R., Shara M. M., 2012, MNRAS, 425, 2872
Hurley J. R., Aarseth S. J., Shara M. M., 2007, ApJ, 665, 707
Hut P. et al., 1992, PASP, 104, 981
Hypki A., Giersz M., 2012, MNRAS, 429, 1221
Ivanova N., Heinke C. O., Rasio F. A., Taam R. E., Belczynski K., Fregeau J., 2006, MNRAS, 372, 1043
Kains N. et al., 2013, A&A, 555, A36
King I. R., 1966, AJ, 71, 64
Knigge C., Shara M. M., Zurek D. R., Long K. S., Gilliland R. L., 2000, in Shara M. M., ed., ASP Conference Series, Stellar Collisions, Mergers, and their Consequences, ASP, Utah USA
Knigge C., Zurek D. R., Shara M. M., Long K. S., Gilliland R. L., 2003, ApJ, 599, 1320
Kremer K. et al., 2020, ApJS, 247, 48
Leigh N., Sills A., Knigge C., 2007, ApJ, 661, 210
Leigh N., Sills A., Knigge C., 2011, MNRAS, 415, 3771
Leigh N., Knigge C., Sills A., Perets H. B., Sarajedini A., Glebbeek E., 2013, MNRAS, 428, 897
Leigh N. W. C., Giersz M., Marks M., Webb J. J., Hypki A., Heinke C. O., Kroupa P., Sills A., 2015, MNRAS, 446, 226
Lugger P. M., Cohn H. N., Heinke C. O., Grindlay J. E., Edmonds P. D., 2007, ApJ, 657, 286
Maccarone T. J., Long K. S., Knigge C., Dieball A., Zurek D. R., 2010, MNRAS, 406, 2087
McCrea W. H., 1964, MNRAS, 128, 147
Parise R. A. et al., 1994, ApJ, 423, 305
Portegies Zwart S., 2019, A&A, 621, L10
Richer H. B. et al., 1997, ApJ, 484, 741
Rodriguez C. L., Morscher M., Wang L., Chatterjee S., Rasio F. A., Spurzem R., 2016, MNRAS, 463, 2109
Rui N. Z., Kremer K., Weatherford N. C., Chatterjee S., Rasio F. A., Rodriguez C. L., Ye C. S., 2021, ApJ, 912, 102
Sahu S. et al., 2019, ApJ, 876, 34
Schiavon R. P. et al., 2012, ApJ, 143, 121
Shara M. M., Hurley J. R., 2006, ApJ, 646, 464
Siegel M. H. et al., 2014, ApJ, 148, 131
Siegel M. H., Porterfield B. L., Balzer B. G., Hagen L. M. Z., 2015, ApJ, 150, 129
Sills A., Karakas A., Lattanzio J., 2009, ApJ, 692, 1411
Simunovic M., Puzia T. H., Sills A., 2014, ApJ, 795, L10
Sosin C., 1997, AJ, 114, 1517
Stetson P. B., 1987, PASP, 99, 191
Subramaniam A. et al., 2017, ApJ, 154, 233
Thomson G. S., Dieball A., Knigge C., Long K. S., Zurek D. R., 2010, MNRAS, 406, 1084
Thomson G. S. et al., 2012, MNRAS, 423, 2901
Tody D., 1986, in Crawford D. L., ed., Proc. SPIE Conf. Ser. Vol. 0627, Instrumentation in Astronomy VI. SPIE, Bellingham, p. 733
Tody D., 1993, in Hanisch R. J., Brissenden R. J. V., Barnes J., eds, ASP Conf. Ser. Vol. 52, Astronomical Data Analysis Software and Systems II. Astron. Soc. Pac., San Francisco, p. 173
Tout C. A., Hall D. S., 1991, MNRAS, 253, 9
Tout C. A., Pols O. R., Eggleton P. P., Han Z., 1996, MNRAS, 281, 257
Wang L. et al., 2016, MNRAS, 458, 1450
Wood M., 1995, Theoretical White Dwarf Luminosity Functions: DA models, *White Dwarfs*. Springer-Verlag, Berlin, p. 41
Xin Y., Ferraro F. R., Lu P., Deng L., Lanzoni B., Dalessandro E., Beccari G., 2015, ApJ, 801, 67
Zurek D. R., Knigge C., Maccarone T. J., Dieball A., Long K. S., 2009, ApJ, 699, 1113
Zurek D. R., Knigge C., Maccarone T. J., Pooley D., Dieball A., Long K. S., Shara M., Sarajedini A., 2016, MNRAS, 460, 3660

SUPPORTING INFORMATION

Supplementary data are available at *MNRAS* online.

M30_Catalogue.txt

Please note: Oxford University Press is not responsible for the content or functionality of any supporting materials supplied by the authors. Any queries (other than missing material) should be directed to the corresponding author for the article.

This paper has been typeset from a TEX/LATEX file prepared by the author.

Appendix B

Far-ultraviolet investigation into the galactic globular cluster M30 (NGC 7099): II. Potential X-ray counterparts and variable sources

The paper **Mansfield et al., MNRAS, Volume 513, Issue 2, June 2022, DOI: 10.1093/mnras/stac1039** is provided below in its published form.

Monthly Notices of the ROYAL ASTRONOMICAL SOCIETY

MNRAS **513,** 3022–3034 (2022) https://doi.org/10.1093/mnras/stac1039
Advance Access publication 2022 April 15

Far-ultraviolet investigation into the galactic globular cluster M30 (NGC 7099) – II. Potential X-ray counterparts and variable sources

Santana Mansfield,[1★] Andrea Dieball,[1] Pavel Kroupa,[1,2] Christian Knigge,[3] David R. Zurek,[4] Michael Shara[4] and Knox S. Long[5]

[1]*Helmholtz-Institut für Strahlen- und Kernphysik (HISKP), Universität Bonn, Nußallee 14-16, D-53115 Bonn, Germany*
[2]*Astronomical Institute, Faculty of Mathematics and Physics, Charles University in Prague, V Holešovičkách 2, CZ-18000 Praha, Czech Republic*
[3]*School of Physics and Astronomy, University of Southampton, Highfield, Southampton SO17 1BJ, UK*
[4]*Department of Astrophysics, American Museum of Natural History, New York, NY 10024, USA*
[5]*Space Telescope Science Institute, 3700 San Martin Drive, Baltimore, MD 21218, USA*

Accepted 2022 April 10. Received 2022 April 8; in original form 2021 October 26

ABSTRACT

We present a far-ultraviolet (*FUV*) study of the globular cluster M30 (NGC 7099). The images were obtained using the Advanced Camera for Surveys (ACS/SBC, F150LP, *FUV*) and the Wide Field Planetary Camera 2 (WFPC2; F300W, *UV*) on board the *Hubble Space Telescope (HST)*. We compare the catalogue of *FUV* objects to 10 known X-ray sources and find six confident matches of two cataclysmic variables (CVs), one RS CVn, one red giant with strong *FUV* emission, and two sources only detected in the *FUV*. We also searched for variable sources in our data set and found a total of seven blue stragglers (BSs), four horizontal branch (HB) stars, five red giant branch stars, 28 main-sequence stars, and four gap objects that demonstrated variability. One BS star is a known W-UMa contact binary, one of the gap objects is a known CV identified in this work to be a dwarf nova, and the three other gap sources are weak variables. The periods and positions of two of the variable HB stars match them to two previously known RR Lyrae variables of types RRab and RRc.

Key words: techniques: photometric – stars: horizontal branch – novae, cataclysmic variables – stars: variable: general – globular clusters: individual: M30 (NGC 7099) – ultraviolet: stars.

1 INTRODUCTION

The high density of stars in the cores of globular clusters allows frequent interactions, which produces various exotic sources such as blue straggler (BS) stars that are located at brighter magnitudes in the colour–magnitude diagram (CMD) than the main sequence (MS) turnoff. BS stars are typically thought to have higher masses than MS stars by gaining mass from a companion (McCrea 1964), or from a direct collision (Hills & Day 1976), in order to remain in the location of the zero-age main sequence, while single MS stars of similar masses have turned off to become red giants. Other exotic sources include binary systems such as cataclysmic variables [CVs; a white dwarf (WD) star accreting mass from a companion], X-ray binaries, and millisecond pulsars (MSPs; Shara & Hurley 2006; Ivanova et al. 2008; Hong et al. 2016), as well as individual WDs.

CVs and low-mass X-ray binaries (LMXBs; a neutron star or black hole accreting material from a low-mass companion) are faint at optical wavelengths and not easily detectable in globular clusters as they are surpassed by the large number of MS stars that shine brightly in the optical. Instead, we search for these exotic sources in the ultraviolet and X-ray wavelengths. Since the accretion of material in these binary systems results in very hot temperatures in the accretion disc, as well as when material falls on to the surface of the compact object, the spectral energy distribution of this hot emission peaks in the far-ultraviolet (*FUV*) or X-ray wavelengths. Since the surfaces of the numerous MS and red giant branch (RGB) stars in globular clusters do not reach such high temperatures, they are faint at these wavelengths and the cluster core appears much less crowded. By taking observations in the ultraviolet, we can more easily detect and identify such exotic sources.

For the first part of this investigation (Mansfield et al. 2022, hereafter Paper I), we performed the photometry of ultraviolet observations of the globular cluster M30 (NGC 7099) and presented a $FUV - UV$ CMD and an analysis of the radial distributions of the different stellar populations. A more detailed overview of M30 and the previous studies on this cluster can be found in Paper I. We also presented an ultraviolet catalogue of sources.[1] We note that along with the strong central concentration of BSs, the radial distributions given in Paper I also show that the dominant stellar population in the central region is the WD/Gap sources, which has recently been theorised to be the case for core-collapsed globular clusters (Kremer 2020, 2021). In this present work, we continue our investigation into the properties of M30 and compare the positions of the sources detected in the ultraviolet to the locations of the known X-ray sources in M30. In this work, we also perform a variability study using the

★ E-mail: smansfield@astro.uni-bonn.de

[1] http://vizier.u-strasbg.fr/viz-bin/VizieR?-source = J/MNRAS/511/3785

FUV exposures to find active binary systems in M30, including those in the vicinity of X-ray sources.

Stars can exhibit brightness variability due to the orbit of a binary (or multiple) system, structural processes within single stars which generate pulsations, or from interactions between binary members such as mass transfer. For example, the emission from a hot accretion disc in a CV system, as well as the fall of material on to the surface of the WD, can produce strong variability, which helps distinguish CVs from isolated WDs. Investigating brightness fluctuations allows for precise stellar identification within the population groups. For instance, within M30, seven RR Lyrae variables have been observed on the horizontal branch (HB) in the optical and infrared (Pietrukowicz & Kaluzny 2004; Kains et al. 2013), and since Zurek et al. (2016) saw brightness variability on the HB in the *FUV* for NGC 1851, a variability study of M30 in the *FUV* will be valuable to find other potential RR Lyrae stars on the HB of M30, as well as possible CV candidates.

M30 also contains a number of X-ray sources which indicate exotic binary systems. Lugger et al. (2007) detected 13 X-ray sources that were also found by Zhao et al. (2020), who discovered an additional 10 sources, based on observations with *Chandra* ACIS-S. Some of these sources are thought to be CVs, and one is likely a quiescent low-mass X-ray binary (qLMXB). Two milli-second pulsars were also found in M30 by Ransom et al. (2004).

The observations and coordinate transformations used for this investigation are described in Section 2. The potential ultraviolet counterparts to the X-ray sources and their locations in the *FUV* − *UV* CMD are described in Section 3. The variable sources are described in Section 4, followed by a summary in Section 5.

2 DATA PROCESSING

2.1 Photometry

The *FUV* data were obtained with the Advanced Camera for Surveys (ACS) on board the *HST*, using the Solar Blind Channel (SBC) and the F150LP filter. The *UV* data were acquired using the Wide Field Planetary Camera 2 (WFPC2) and the F300W filtre, which was also on board the *HST*. These were both parts of the program GO-10561 (PI: Dieball) and were taken using 15 orbits distributed over three visits, from 2007 May 29 to June 9. The SBC has a field of view of 34.6 × 30.8 arcsec^2 and a pixel scale of 0.034 × 0.030 arcsec^2 pixel^{-1}. Sixty-four images were taken, each with an exposure time of 315 s, resulting in a total exposure time of 20 160 s. The WFPC2 consists of four cameras, the three Wide Field Cameras (WFCs) each with a field of view of 50 × 50 arcsec^2, and the PC with a field of view of 34 × 34 arcsec^2, and a pixel scale of 0.046 arcsec pixel^{-1}. As the PC was centred on the cluster core and the region observed for the *FUV* imaging, only the exposures from this camera were used in this work. Twenty-four images were taken with a total exposure time of 12 000 s. The observations, image processing, and data reduction are described in detail in Paper I. Out of 1934 sources detected in the *FUV*, 1569 have *UV* counterparts, including 1218 MS stars, 41 HB stars, 47 BSs, 185 RGB stars, and 78 WD/Gap objects (sources blueward of the MS and with *FUV* $\gtrsim$ 19 mag).

The optical data used in this work are the catalogue from Guhathakurta et al. (1998), the exposures of which were also taken with the WFPC2 on board the *HST* (program GO-5324, PI: Yanny). Eight exposures were taken on 1994 March 31, two using the F336W filtre with 100 s exposure time, two using the F439W filtre and 40 s exposure time, and four using the F555W filtre with 4 s exposure times. The data were accessed from VizeiR.[2]

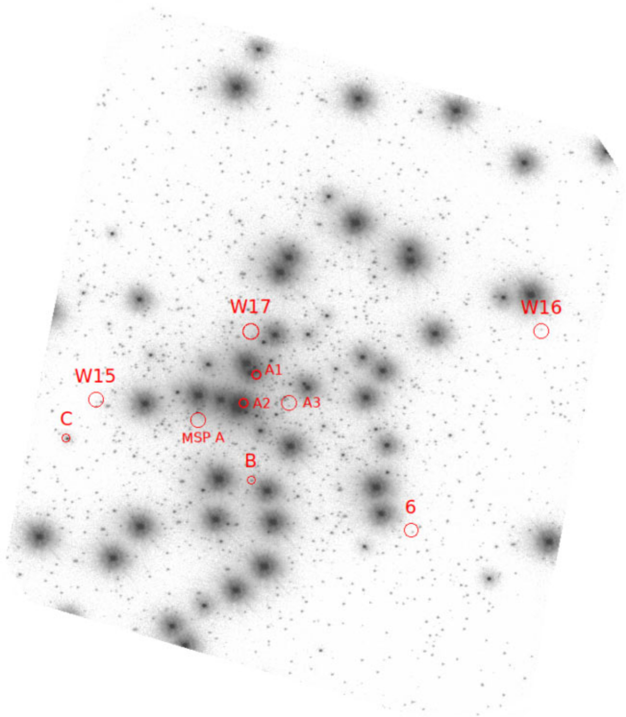

Figure 1. Positions of the 10 X-ray sources listed in Table 1, seen as red circles with sizes proportional to their positional uncertainties, superimposed on to the *FUV* master image of M30. North is up, east is to the left, and the image spans 34.6 × 30.8 arcsec^2.

2.2 X-ray coordinate transformation

Lugger et al. (2007) found 13 X-ray sources within the half-mass radius of M30 (1.15 arcmin, Harris 1996) using *Chandra* ACIS-S. In order to check the positions of these sources against our ultraviolet data set, we use the astrometric reference star adopted by Guhathakurta et al. (1998), a red giant (their source #3611), which in our catalogue is ID366. From our data set, the position of this star is:

$$\alpha = 21^h40^m22\overset{s}{.}31, \quad \delta = -23^\circ10'40\overset{''}{.}13 \quad \text{(J2000.0)}, \qquad (1)$$

which has a shift of $\Delta\alpha = +0.02$ arcsec, $\Delta\delta = +0.53$ arcsec from the position of $\alpha = 21^h40^m22\overset{s}{.}29$, $\delta = -23^\circ10'39\overset{''}{.}60$ given by Lugger et al. [2007; and also a relatively small shift of $\Delta\alpha = -0.004$ arcsec, $\Delta\delta = +0.03$ arcsec to the position of $\alpha = 21^h40^m22\overset{s}{.}314$, $\delta = -23^\circ10'40\overset{''}{.}10$ reported by Ransom et al. (2004)]. This is within the uncertainties of 0.70 arcsec in the world coordinate system (WCS) for both *HST* and *Chandra*. This positional shift is then applied to the Lugger et al. (2007) X-ray sources in order to match to our data set. These 13 sources were also detected by Zhao et al. (2020), as well as an additional 10 sources within the updated half-mass radius of 1.03 arcmin (Harris 2010). By comparing the coordinates given for the 13 sources discovered by Lugger et al. (2007) to those of Zhao et al. (2020), an additional shift can be applied to the new 10 sources to match them to our data set. Out of the 23 total sources,

[2]https://vizier.cds.unistra.fr/viz-bin/VizieR?-source = J/AJ/116/1757

Table 1. The positions and distances of the potential counterparts to the X-ray sources and their ultraviolet photometric quantities as found in this study. The radius r in column 2 is the distance of the X-ray source from the centre of the cluster, and the distance of the potential counterpart to the X-ray source is given in column 7. The X-ray sources A1–6 are from Lugger et al. (2007), sources W15–W17 are from Zhao et al. (2020), and the MSP from Ransom et al. (2004).

ID_{X-ray}	r (arcsec)	P^a_{err} (arcsec)	ID_{FUV}	RA (h:m:s)	Dec. (°:′:″)	Distance (arcsec)	Err^b	Type	*FUV* (mag)	*FUV−UV* (mag)
A1	1.312	0.24	ID272	$21^{\mathrm{h}}40^{\mathrm{m}}22^{\mathrm{s}}.16$	$-23^\circ10'45''.85$	0.238	0.992	BS	17.170 ± 0.004	–0.676 ± 0.006
A2	1.064	0.24	ID283	$21^{\mathrm{h}}40^{\mathrm{m}}22^{\mathrm{s}}.22$	$-23^\circ10'47''.65$	0.078	0.325	BS/RG	17.570 ± 0.013	–0.646 ± 0.016
			ID290	$21^{\mathrm{h}}40^{\mathrm{m}}22^{\mathrm{s}}.23$	$-23^\circ10'47''.71$	0.224	0.933	BS	14.676 ± 0.001	–1.612 ± 0.002
A3	1.599	0.42	ID181	$21^{\mathrm{h}}40^{\mathrm{m}}22^{\mathrm{s}}.03$	$-23^\circ10'47''.85$	0.134	0.319	RG	23.195 ± 0.066	5.677 ± 0.068
			ID187	$21^{\mathrm{h}}40^{\mathrm{m}}22^{\mathrm{s}}.03$	$-23^\circ10'47''.46$	0.289	0.688	RG	22.129 ± 0.034	3.971 ± 0.037
			ID191	$21^{\mathrm{h}}40^{\mathrm{m}}22^{\mathrm{s}}.04$	$-23^\circ10'47''.51$	0.336	0.800	RG	21.549 ± 0.023	5.444 ± 0.024
			ID806	$21^{\mathrm{h}}40^{\mathrm{m}}22^{\mathrm{s}}.00$	$-23^\circ10'47''.88$	0.405	0.964	MS	23.050 ± 0.054	3.801 ± 0.059
B	4.904	0.24	ID1647	$21^{\mathrm{h}}40^{\mathrm{m}}22^{\mathrm{s}}.18$	$-23^\circ10'52''.17$	0.005	0.021	–	21.582 ± 0.026	–
C	11.483	0.24	ID456	$21^{\mathrm{h}}40^{\mathrm{m}}22^{\mathrm{s}}.96$	$-23^\circ10'49''.74$	0.038	0.158	WD/Gap	19.748 ± 0.009	–0.821 ± 0.019
6	11.718	0.41	ID1700	$21^{\mathrm{h}}40^{\mathrm{m}}21^{\mathrm{s}}.51$	$-23^\circ10'55''.15$	0.090	0.220	–	23.256 ± 0.048	–
W15	9.559	0.43	ID449	$21^{\mathrm{h}}40^{\mathrm{m}}22^{\mathrm{s}}.81$	$-23^\circ10'47''.61$	0.292	0.679	MS	22.298 ± 0.029	3.464 ± 0.033
			ID452	$21^{\mathrm{h}}40^{\mathrm{m}}22^{\mathrm{s}}.83$	$-23^\circ10'47''.88$	0.364	0.847	MS	22.453 ± 0.031	3.483 ± 0.035
			ID912	$21^{\mathrm{h}}40^{\mathrm{m}}22^{\mathrm{s}}.83$	$-23^\circ10'47''.63$	0.109	0.253	WD/Gap	23.971 ± 0.071	2.233 ± 0.093
W16	16.672	0.44	ID1029	$21^{\mathrm{h}}40^{\mathrm{m}}20^{\mathrm{s}}.97$	$-23^\circ10'43''.43$	0.108	0.245	RG	23.692 ± 0.060	4.929 ± 0.064
W17	3.843	0.46	ID1681	$21^{\mathrm{h}}40^{\mathrm{m}}22^{\mathrm{s}}.18$	$-23^\circ10'43''.83$	0.297	0.646	–	22.648 ± 0.060	–
MSP A	3.870	0.43	ID1217	$21^{\mathrm{h}}40^{\mathrm{m}}22^{\mathrm{s}}.39$	$-23^\circ10'48''.35$	0.399	0.928	RG	22.272 ± 0.054	3.859 ± 0.057

(a) 95 per cent error circle.
(b) Characteristic uncertainty, Err = Distance/P_{err}.

10 are within the *FUV* field of view and are marked in Fig. 1. After comparing the data sets, we find six confident matches: ID283 to A2, ID1647 to B, ID456 to C, ID1700 to 6, ID912 to W15, and ID1029 to W16 (described in detail in Section 3). The average distance of these six sources to their X-ray counterparts was 0.148 arcsec, which is then used as an additional boresight correction to shift the X-ray catalogue into the *FUV* frame. After this shift, the confident matches have an average positional offset of 0.071 arcsec.

2.3 Brightness variability

For the variability study, the magnitudes of the individual 64 *FUV* exposures were measured using the DAOPHOT task (Stetson 1987), running under PYRAF (Greenfield & White 2000). As the individual images are slightly shifted with respect to one another, a specific coordinate list of the sources is first created for each exposure, using the coordinate list of the drizzled master image from Paper I. This list is transformed into individual coordinate lists using the task WCSCTRAN, which takes the WCS information from each exposure. Then the DAOPHOT task performs aperture photometry on each exposure using the specific coordinate list. This task was performed without recentring, which would measure the magnitude of a nearby bright star if the flux at the target coordinate is faint. Aperture and sky corrections to the measured fluxes are applied using the same method described in Paper I (section 2.1.2).

3 X-RAY SOURCE MATCHING

3.1 Positional error radii

The X-ray sources are given in Table 1, along with their potential counterparts. The positional 95 per cent error radii P_{err} is included for each X-ray source and is shown in Figs 1, 2, and 3 as red circles. For the bright sources (> 100 counts, i.e. sources A1, A2, B, and C), we calculate P_{err} using the positional uncertainties of the six confident matches and the formula:

$$\sigma_r^2 = \sigma_{RA}^2 + \sigma_{Dec}^2. \tag{2}$$

After applying the shifted boresight correction, the rms errors in RA and Dec. are 0.076 and 0.063 arcsec, respectively, correlating to 1σ in each of the two directions. A 95 per cent error radii corresponds to 2.45σ and as such the resulting P_{err} for the bright sources is 0.243 arcsec.

For the fainter sources, we take the 95 per cent error radii for *Chandra* ACIS-S given by Zhao et al. (2020) and calculated from the individual source count and offset (Hong et al. 2005). Then all *FUV* sources within P_{err} are marked with blue circles in Figs 2 and 3.

3.2 Chance coincidences

In the dense core of the cluster, there may be stars within the positional error radii that are chance coincidences. To estimate the number of chance coincidences of each stellar population within these radii, we follow the method of Zhao et al. (2020), and split the cluster into concentric annuli with 1 arcsec thicknesses over the 15 arcsec radius contained in our field of view. Assuming the populations are evenly distributed within each annulus, we can then calculate the number of chance coincidences, N_{C}, using the number of stars in each population in each annulus, N_{tot}, the area of each annulus, A_{ann}, and the area of the 95 per cent positional error radii, A_{err}, in the formula:

$$N_C = N_{tot} \times \frac{A_{err}}{A_{ann}} \tag{3}$$

which we have applied to the bright and faint X-ray sources separately, using the value $A_{\mathrm{err}} = 0.18$ arcsec^2 for the bright sources and the average value $A_{\mathrm{err}} = 0.58$ arcsec^2 for the faint sources. The number of chance coincidences found within the error circle for either a bright or a faint X-ray source is shown for each population, as well as the total chance of finding any type of star, is given in Fig. 4. As the area of the 95 per cent positional error is slightly more than three times as large for the fainter X-ray sources, the number

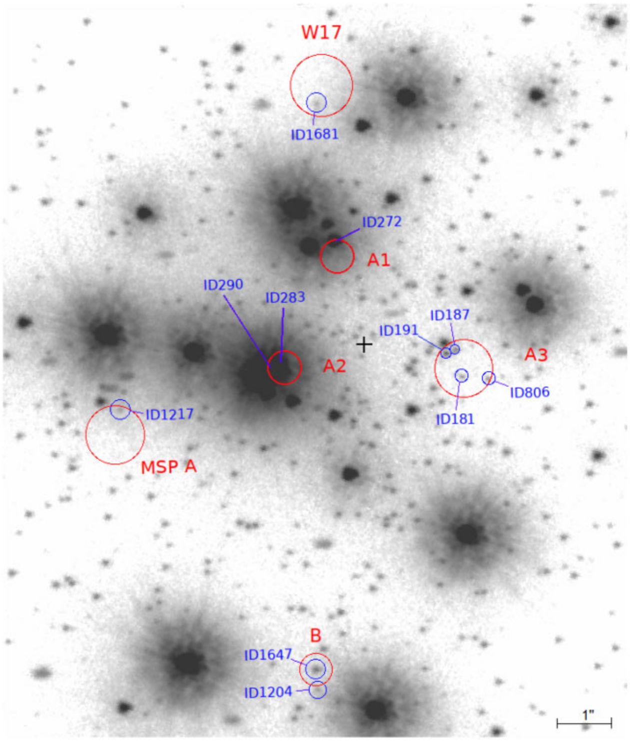

Figure 2. Position of X-ray sources with 95 per cent error radii marked with red circles. The potential counterparts are given in blue. The black cross indicates the centre of the cluster.

of chance coincidences within these radii are also slightly more than triple. Within the very core of the cluster the number of a chance coincidence of any type of star is 1.32 in the area around a bright X-ray source, but drops to an average of 0.52 over the rest of the *FUV* field of view. The average number of chance coincidences within a faint X-ray error circle is 1.66.

3.3 Cluster membership probability

Some of the ultraviolet sources discussed in this section and also in Section 4 have cluster membership probabilities calculated from their proper motions derived from the *Hubble Space Telescope UV Legacy Survey of Galactic Globular Clusters* (HUGS) catalogue (Piotto et al. 2015; Nardiello et al. 2018). The values for these sources are given in Table 2.

3.4 Potential X-ray counterparts

A total of 16 *FUV* sources are located within the 10 X-ray positional error radii. In order to see if we can already identify a number of these sources as confident matches based on their positions alone, we counted the number of *FUV* sources within the error radii at several small and increasing offsets. Due to the crowding in the centre of the cluster, the total number of *FUV* sources within all 10 error radii remained roughly the same at different offset positions. This indicates that a detailed examination into the characteristics of each potential X-ray counterpart is needed to evaluate the likelihood of associating it with the X-ray source. This examination will include an analysis of the photometric properties in both optical and ultraviolet wavelengths. The locations of these sources in the $FUV - UV$ CMD are marked in Fig. 5, which includes their optical counterpart locations in the $B - V$ CMD from the Guhathakurta et al. (1998) catalogue. The coordinate transformation to the optical catalogue was described in Paper I. The examination will also include a consideration of any variability which is discussed in Section 4 (Figs 6, 7 and 8).

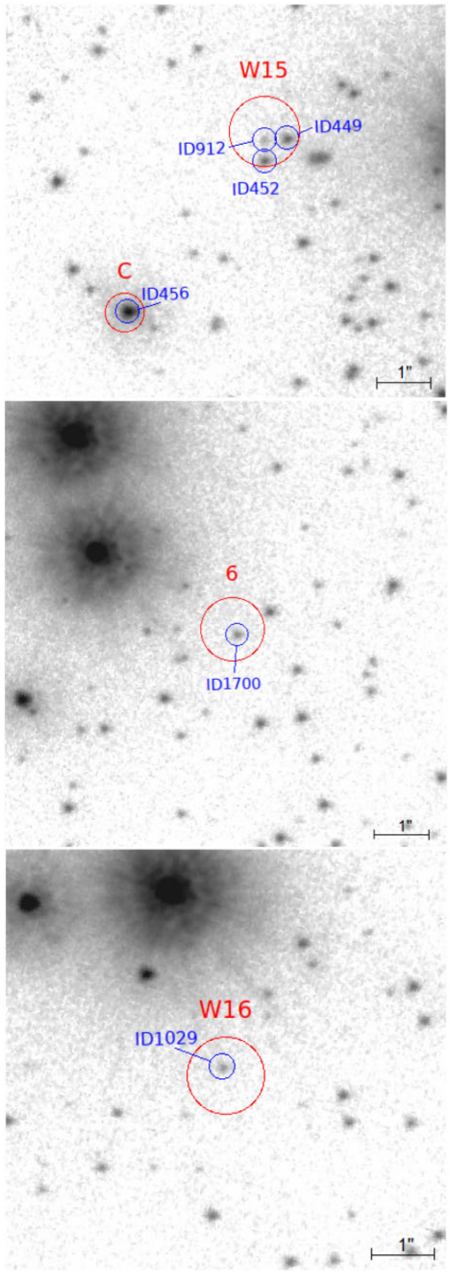

Figure 3. Same as Fig. 2.

3.4.1 Source A1

The X-ray source A1 (Lugger et al. 2007) is thought to be a qLMXB with a neutron star that has either a He atmosphere or a H atmosphere with significant hotspots (Echiburú et al. 2020). As LMXBs in a quiescent state have very reduced or no accretion, they are generally faint at ultraviolet and other wavelengths. Zhao et al. (2020) note that the donor star should be a He WD if the neutron star has a He atmosphere, and it could be a MS star if the neutron star has hotspots that distort the spectrum. Lugger et al. (2007) suggest two MS stars

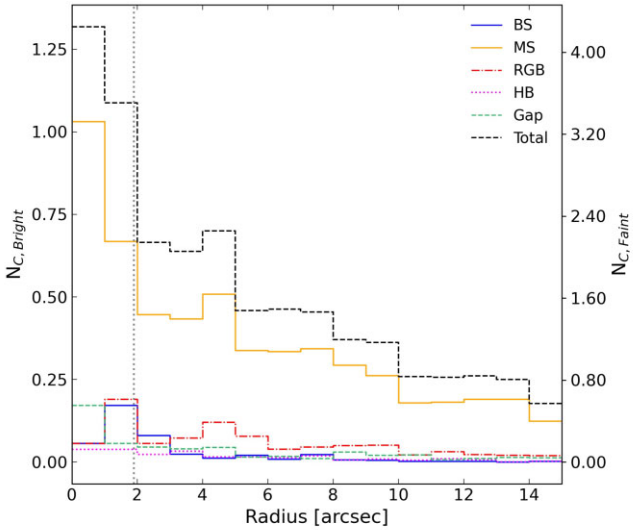

Figure 4 A number of chance coincidences within the error circle for either a bright or a faint X-ray source plotted as a function of radial distance from the centre of the cluster. For a bright source, the error radius Aerr = 0.18 arcsec2 is used and for a faint source Aerr = 0.58 arcsec2 is used. The dotted vertical line indicates the cluster core region. The group Total gives the chance of finding any coincidental star in the error radii.

Table 2. Cluster membership probabilities of some of the sources discussed in the text, from the HUGS catalogue (Piotto et al. 2015; Nardiello et al. 2018).

ID	P_{μ} (per cent)
93	92.6
179	44.2
181	90.2
187	88.5
191	88.5
268	97.5
272	97.1
276	98.0
277	96.9
350	85.1
456	94.3
912	96.7
1029	97.5
1217	95.6
1226	96.7
1230	96.7
1647	90.5
1681	90.5

that lie close to the MS turnoff in the optical CMD as possible companions, however they note that the area in the vicinity of A1 is severely crowded. As A1 lies within 2 arcsec of the cluster centre, the number of coincidental stars within the error radii at this radius is 1.09. From our data set, there is only one potential counterpart that lies on the edge of the error circle for A1, a BS star ID272 with a bright *FUV* magnitude (≈17.2 mag), making it one of the brightest BS sources, and it is also relatively bright in the optical, with $V =$ 18.16 mag [Guhathakurta et al. (1998), their source #3115]. As ID272 is a bright BS star and neither a WD or MS star, it is likely that ID272 is a chance superposition in this dense region of the cluster core, and the true counterpart is too faint to be seen in the *FUV*.

3.4.2 Source A2

Lugger et al. (2007) consider the brightest *FUV* source (#3327 in Guhathakurta et al. 1998, ID290 in this work) as a possible companion to the X-ray source A2 as it sits within 0.50 arcsec of it. However, they note that the crowding in this central region of the cluster (Fig. 2, $N_{\mathrm{C},\,Bright} = 1.09$) may mean that a different star may be the companion. From our data set, the error circle for A2 includes source ID290 at a distance of 0.224 arcsec, which is located in the BS region in the optical CMD (Fig. 5), but has the brightest *FUV* magnitude in this work. Lugger et al. (2007) conclude that this source is likely to be a sub-dwarf B star (sdB) with a WD companion. Yet, as noted by Lugger et al. (2007), not many sdB binaries are known to emit X-ray emission and thus its proximity to A2 could be a chance superposition. There is one other source within the error circle: ID283 at a distance of 0.078 arcsec from A2. This is an interesting counterpart candidate as in the $FUV - UV$ CMD it has the position of a bright BS star; however, in the optical CMD, it is located on the RGB. This likely represents a binary system in which the RGB star has overfilled its Roche Lobe and is transferring mass to a compact companion resulting in strong *FUV* emission. CVs undergoing substantial mass transfer appear considerably bluer in the ultraviolet relative to their optical colours. These objects are rare, although they have been found in other globular clusters (eg. Edmonds et al. 2003). Thus, it is likely that ID283 is the counterpart to the X-ray source A2 and is a CV system with a red giant donor star.

3.4.3 Source A3

The source A3 was a faint X-ray detection with no optical counterparts proposed by Lugger et al. (2007). In our work, there are four sources within the error circle of A3, all with optical counterparts. One MS star lies on the edge of the error circle, ID806, which is located in the MS in both optical and ultraviolet CMDs. As this source does not show significant variability (Section 4), this is unlikely to be the counterpart to A3. The number of chance coincidences within the faint X-ray source error radii at this distance from the centre is 1.60 for a MS star and 0.25 for a red giant (Fig. 4). Three RGB stars are also in the error circle, making one of these likely to be the correct counterpart. The closest to the X-ray source is ID181 at a distance of 0.134 arcsec, and the other two ID187 and ID191 are at distances of 0.289 and 0.336 arcsec, respectively. ID191 shows no variability, however ID181 and ID187 are interesting possibilities as counterparts to A3 as they are both slightly variable stars, which could result from instabilities in accretion if they are binary systems. As seen later in Section 4, ID187 has a larger standard deviation relative to sources of similar *FUV* magnitude than ID181, and it appears bluer in the ultraviolet CMD relative to the other red giants than the optical CMD. Thus, the most likely counterpart to A3 is the variable RGB star ID187, with the closer RGB star ID181 also a possibility.

3.4.4 Source B

Lugger et al. (2007) suggest a faint companion to X-ray source B that lies in the halo of a RGB star and is located on the MS in their infrared CMD, but has blue excess in the ultraviolet and concluded that source B is a potential CV. However, no MS star was detected at the location of source B in this present work, and the RGB star ID1204 is located just outside of the error circle for B, at a distance of 0.288 arcsec and did not show any significant variability. Only one

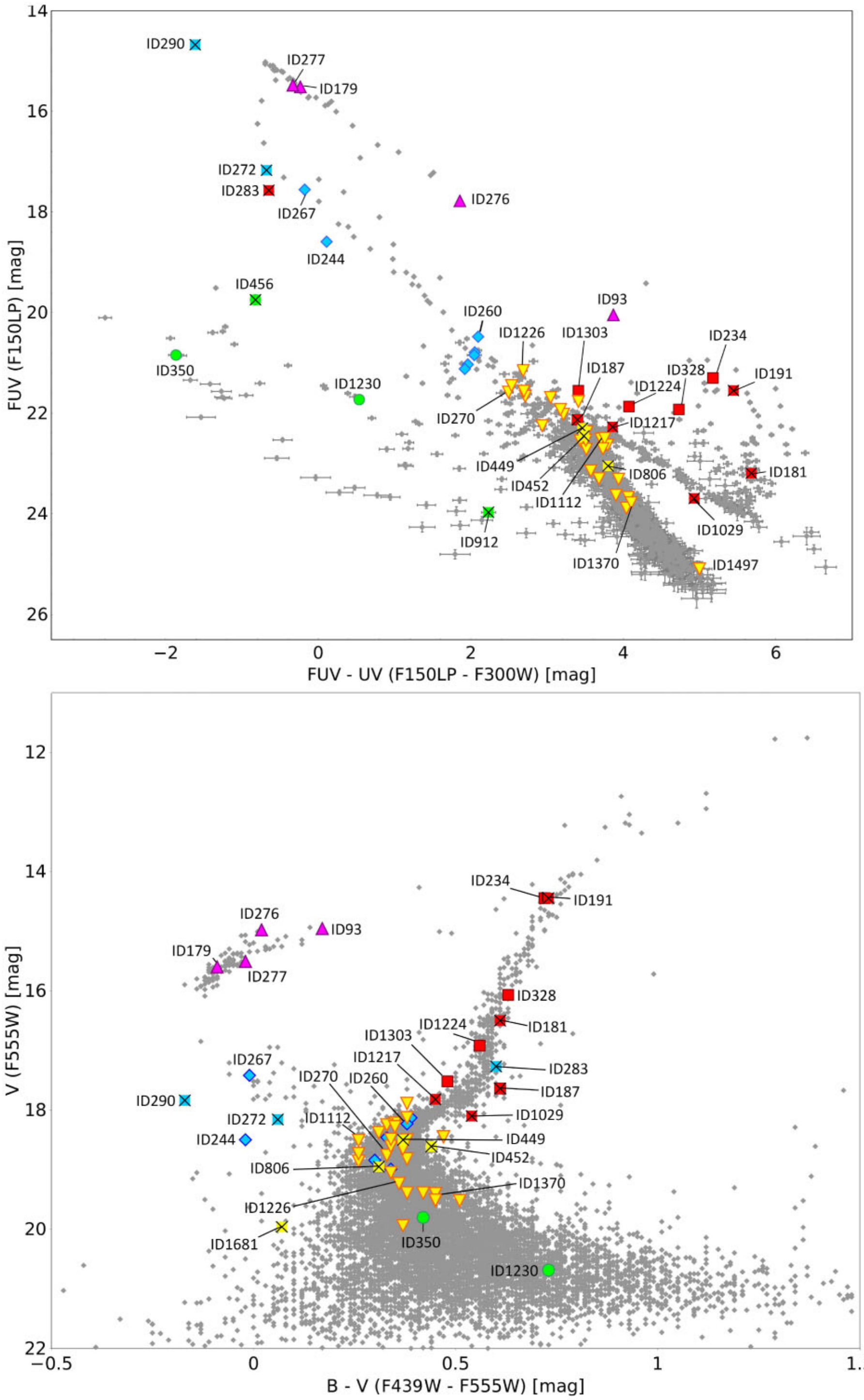

Figure 5. *FUV* − *UV* (top) and optical (Guhathakurta et al. 1998, bottom) CMDs with the positions of the variable BS (blue diamonds), HB (purple up triangles), MS (yellow down triangles), RGB (red squares), and WD/Gap (green circles) sources marked. The colours and shapes in one CMD are given based on the source location in the other CMD. Those with measured periods are numbered and those without can be found in Table A1. Additionally, the potential counterparts to the X-ray sources (Lugger et al. 2007; Zhao et al. 2020) are marked with crosses and are numbered. The reason that source ID283 is marked differently in the two CMDs is discussed in the text.

source is located within the error circle for source B, ID1647, which is only detected in the *FUV* and has no *UV* counterpart. At a distance of 0.005 arcsec from source B, this is the likely counterpart to B and the source which showed blue excess in Lugger et al. (2007). Piotto et al. (2015) and Nardiello et al. (2018) also find a source at this position with a cluster membership probability of 90.5 per cent. The light curve for ID1647 is given in Fig. 8 that shows little variability, and as the detection limit is $UV = 23.6$ (Paper I), it is likely that the companion to source B is a faint MS star, as suggested by Lugger et al. (2007).

3.4.5 Source C

One ultraviolet source is detected within the error circle of X-ray source C (Fig. 3), a WD/Gap object ID456 at a distance of 0.038 arcsec. This source was found by Lugger et al. (2007) to be a CV as it was fainter in the year 1999 by 1 mag than in 1994. ID456 is shown as a variable WD/Gap object in Section 4, where its magnitude in the first observing epoch was ≈1.5 mag brighter than in the latter two epochs . We agree then that ID456 is a CV that is experiencing a dwarf nova event. ID456 is one of the brightest Gap sources, with *FUV* ≈ 19.7 mag, however as no source was detected in the optical at this location, and the optical detection limit is $V \approx 22$, this suggests a very faint low-mass MS companion. Göttgens et al. (2019) also classify this source (ACS ID 23423) as a CV due to its broad H α and H β emission detected with the Multi Unit Spectroscopic Explorer (MUSE; Bacon et al. 2017).

3.4.6 Source 6

One source, ID1700, lies at a distance of 0.090 arcsec from X-ray source 6 from Lugger et al. (2007) and is detected in the *FUV* but is not seen in the *UV*. Due to the detection limit of $UV = 23.6$ (Paper I), the companion is likely a very faint MS star.

3.4.7 Source W15

Of the 10 additional X-ray sources detected by Zhao et al. (2020), three are in our *FUV* field of view: W15, W16, and W17. Three ultraviolet sources are detected within the error circle of W15: two MS stars, ID449 and ID452, and a gap source, ID912. The number of chance coincidences of MS stars in the error radius for W15 is 0.845 but for a gap source is only 0.068, meaning that the gap source is the more likely true counterpart. The gap object is also the closest to W15 at a distance of 0.109 arcsec and corresponds in position to the optical counterpart for W15 proposed by Zhao et al. (2020), who confirmed that it is a cluster member with a probability of 96.7 per cent (Piotto et al. 2015; Nardiello et al. 2018) and that this source has a blue excess in ultraviolet to infrared wavelengths, thus concluding that W15 is a CV. This source was not in the Guhathakurta et al. (1998) catalogue, but due to its location blueward of the MS in the *FUV*–*UV* CMD and its proximity to W15, we agree that ID912 is most likely a CV.

3.4.8 Source W16

Zhao et al. (2020) suggest a subgiant as a companion to W16 that correlates to the position of ID1029, a source that is located just below the RGB in both the *FUV* – *UV* and optical CMDs in this work. At a distance of 0.108 arcsec from W16, it is the only source detected in the *FUV* to be within the error circle of X-ray source W16. As Göttgens et al. (2019) find variable H α emission from this source using MUSE, Zhao et al. (2020) propose that this is an RS CVn type of AB. The *FUV* light curve for ID1029 illustrated in Section 4 shows that it is not more variable relative to other sources with similar *FUV* magnitudes (Fig. 6).

3.4.9 Source W17

Only one source was found within the error circle for W17, ID1681, another source with an *FUV* detection but no counterpart in the *UV*, however it does have a counterpart from the optical catalogue (Guhathakurta et al. 1998, their source #3175); a star located blueward of the MS in the optical CMD. Piotto et al. (2015) and Nardiello et al. (2018) also find a source at this position with a cluster membership probability of 98.1 per cent. Zhao et al. (2020) proposed two potential counterparts to W17, both MS stars that exhibited brightness variability, neither of which match to the position of ID1681. The light curve for ID1681 is shown in Fig. 8, which only shows a slight variation in magnitude.

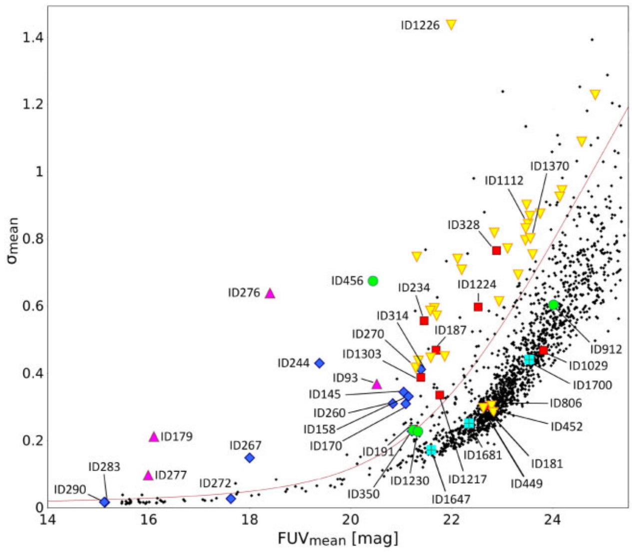

Figure 6. The standard deviation over time plotted against the mean *FUV* magnitude. Marked are the variable BS sources (blue diamonds), HB stars (purple up triangles), RGB stars (red squares), MS (orange down triangles), WD/Gap objects (green circles), and sources without *UV* measurements (blue squares). The light curves for these sources are presented in Figs 7 and A1. The faint red line indicates 20 per cent above the binned average σ_{mean}.

3.4.10 MSP A

Two MSPs were found in M30 by Ransom et al. (2004) using radio pulsar timing, one of which (PSR J2140–2310A, MSP A) was also faintly observed in X-ray wavelengths by Ransom et al. (2004) and is detected again by Zhao et al. (2020) who measure a higher number of X-ray counts for MSP A. Ransom et al. (2004) suggest a MS star companion within 0.09 arcsec of this pulsar that was seen in V_{555} images but not U_{336} or I_{814} images. This companion is not seen in our ultraviolet exposures, instead the only source within the error circle is a red giant, ID1217, located just off the MS turnoff, and at 0.399 arcsec away from the position of MSP A, is likely to be a chance superposition.

4 VARIABLE FUV SOURCES

In order to find objects in the *FUV* data set that exhibit significant variability, we plot the standard deviation σ_{mean} of the *FUV* magnitude over the mean *FUV* magnitude for each star (Fig. 6). Variable sources have a larger deviation than other sources with the same magnitude and the red line in the figure indicates 20 per cent above the binned average σ_{mean} as a rough criterion for variability. From this, seven BS, four HB, five RGB, and one WD/Gap source are identified as variable, and their light curves are plotted in Fig. 7. The two WD/Gap sources ID350 and ID1230 are also included as they are close to the variability criterion. Also included in Figs 6 and 7 are the Gap source ID912 and the RGB stars ID181 and ID1029

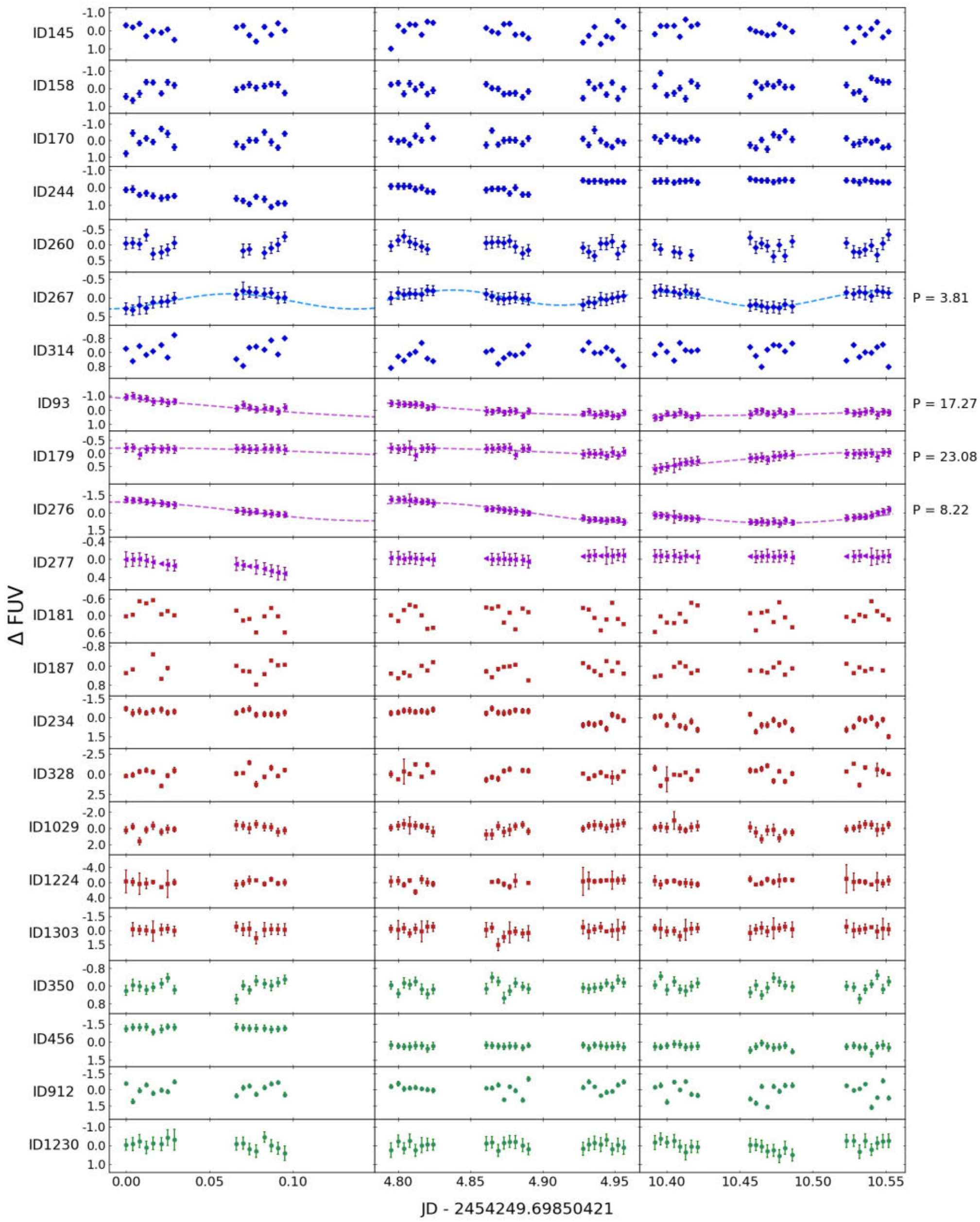

Figure 7. *FUV* mean-subtracted magnitudes ($\Delta FUV = FUV - FUV_{mean}$) are plotted over time for seven variable BS sources (blue diamonds), four HB stars (ID93 - ID277, purple triangles), seven RGB stars (red squares), and four gap objects (green circles). The sine curves represent the periods that are found for several sources, and the period in hours is given. The measured period of 3.81 h for ID267 is half of the true period for this contact binary (see text).

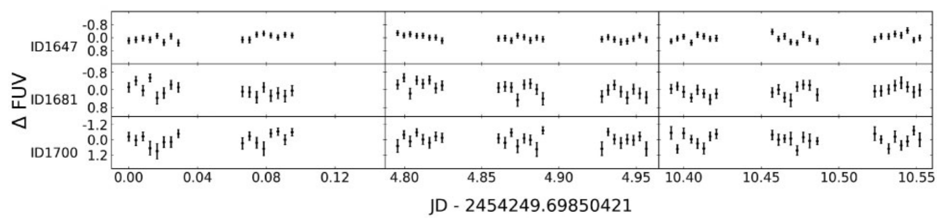

Figure 8. *FUV* light curves for the three potential X-ray counterparts that have no matching *UV* measurement. The mean-subtracted magnitude is plotted over time.

as these are potential X-ray counterparts. The light curves for the three sources within X-ray source error circles that are detected in the *FUV* but with no *UV* counterparts are given in Fig. 8. The light curves for 28 MS stars is shown in Fig. A1 in the Appendix. The other sources above the variability criterion that are not identified were unremarkable in their light curves. The cluster membership probabilities for some of the sources discussed are given in Table 2 (Piotto et al. 2015; Nardiello et al. 2018).

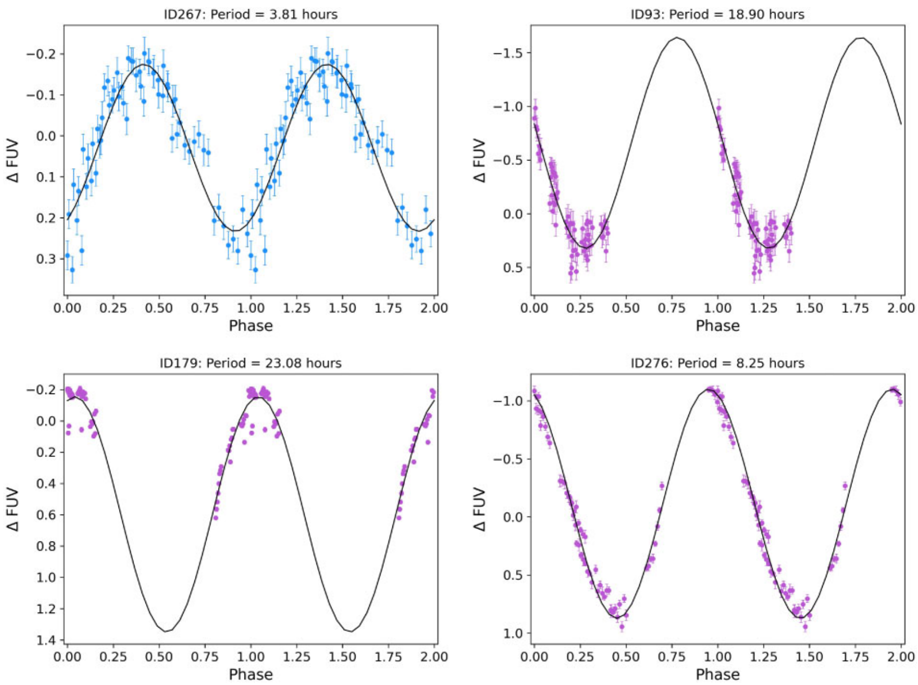

Figure 9. Folded light curves for the BS and HB stars with estimated periods shown in Fig. 7. The measured period of 3.81 h for ID267 is half of the true period for this contact binary (see text).

The periods of variable objects can be estimated by producing Lomb–Scargle periodograms (Lomb 1976; Scargle 1982), which performs a Fourier transform of the light-curve data points. In order to check for discrepancies in the data due to the observing window used, the window function is also calculated from a Lomb–Scargle periodogram with a non-floating mean model and without centering the data (VanderPlas 2018). The window function is plotted over the periodograms in Fig. A2 in the Appendix. The accuracy of this period is checked by comparing to the folded light curves. Four of our variable sources have periods measured and these are then used to plot sine curves representing this periodicity on to the light curves. The photometric properties and any found periods are given in Table A1 in the Appendix for all variable sources. The uncertainties in the FUV_{mean} magnitudes are larger than those for the $FUV - UV$ measurements since they are taken from the individual flat fielded exposures rather than the cleaner drizzled master image.

4.1 Blue stragglers

The light curves of the BS stars are shown in Fig. 7. The source ID267 corresponds within 0.07 arcsec to the position of the variable M30_5 identified as a W UMa-type contact binary by Pietrukowicz & Kaluzny (2004) who measure a period of 7.61 h. Due to the symmetry of such a system, the light curve would show a double-peak, and in our data set, we measure the half-period of 3.81 h (Figs 7, 9 and A2), however 7.61 h would be the true period for this system. Pietrukowicz & Kaluzny (2004) measured a maximum V magnitude for this star of 17.28 mag, which also agrees well to the value of 17.42 mag of the matched optical counterpart to ID267 from the Guhathakurta et al. (1998) catalogue (their source #3238).

4.2 Horizontal branch stars – RR Lyrae

RR Lyrae are variable giant stars with spectral class A−F and are generally found on the HB in globular clusters. The sub-group RRab have steep and asymmetrical light curves with periods in the range of 12–20 h, whereas the light curves for the sub-group RRc are more sinusoidal with shorter periods of 8–10 h (Bailey 1902; Smith 1995). Four HB stars in our data set were found to be variable, two of which have periods of 8.22 and 17.27 h, indicating that these are RR Lyrae variables. ID93 matches in position within 0.12 arcsec of M30_2, identified by Pietrukowicz & Kaluzny (2004) as an RRab variable. Our period of 17.27 h agrees well to the period of 16.54 h found for M30_2 (Pietrukowicz & Kaluzny 2004). These authors found a maximum V magnitude for this star of 15.21 mag, which also agrees well to the value of 14.96 mag of the matched optical counterpart to ID93 from Guhathakurta et al. (1998; their source #2105). ID93 also correlates in position to V15 from Kains et al. (2013) who find a period of 16.23 h and $V = 15.07$, as well as V15 from Göttgens et al. (2019), who find that it exhibits variable H α emission which is typical for RR Lyrae stars.

The other HB star, ID276, found in this work to have a period of 8.22 h, matches within 0.15 arcsec to M30_3, an RR Lyrae variable of type RRc, which has a period of 8.18 h (Pietrukowicz & Kaluzny 2004). These authors measured $V_{\rm max} = 15.08$ mag, in agreement to the optical counterpart #3009 from Guhathakurta et al. (1998) which had $V = 14.98$ mag. ID276 also corresponds to V19 from Kains et al. (2013) who find a period of 8.24 h. Our period of 8.22 h was found by taking the second highest peak from the periodogram (Fig. A2), which was double the frequency of the highest peak. This was done as the frequency of the highest peak did not produce a reasonable folded light curve and because the second highest peak corresponds well to the literature period values.

One of the other variable HB stars, ID179, is potentially a new RRab identification although it has a slightly long estimated period

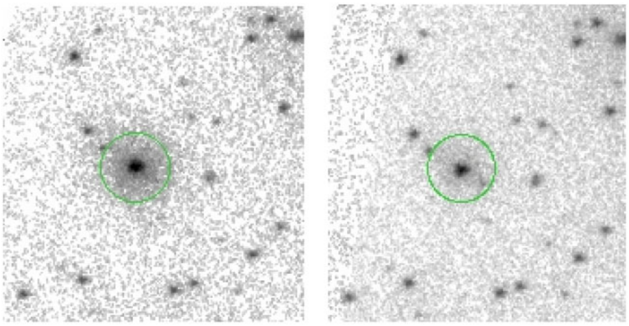

Figure 10. *FUV* image of the CV candidate ID456 during dwarf nova outburst (left) and quiescence (right).

of 23.08 h and also a low cluster member probability of 44.2 per cent (Piotto et al. 2015; Nardiello et al. 2018). No period was found for the other variable HB star ID277 but it is a cluster member with probability of 96.9 per cent (Piotto et al. 2015; Nardiello et al. 2018). Both sources are located on the HB in the *FUV* – *UV* CMD in Fig. 5, with $FUV = 15.51$ for ID179 and $FUV = 15.48$ for ID277. ID179 is found at the position $\alpha = 21^{h}40^{m}22^{s}.25$, $\delta = -23^{\circ}10'58''.51$ and ID277 at $\alpha = 21^{h}40^{m}22^{s}.03$, $\delta = -23^{\circ}10'39''.25$.

4.3 Red giant branch stars

As mentioned in Section 3, sources ID181 and ID187 are located at a distance of 0.134 and 0.289 arcsec of the X-ray source A3 (Lugger et al. 2007), respectively. As ID187 has a larger σ_{mean} relative to sources of similar *FUV* magnitudes, and ID181 only shows variations comparable to other stars at the same magnitude, this suggests that ID187 may have overfilled its Roche Lobe and is transferring mass to a low-mass compact companion, which results in X-ray and variable ultraviolet emission.

The RGB star ID234 is located at the tip of the RGB and shows stability in magnitude for the first and most of the second observing epochs but exhibits fluctuations in magnitude during the last epoch. This behaviour is also seen in MS stars ID268 and ID1226 in Section 4.5, the cause of which is unknown. The subgiant ID1029 was included in Fig. 7 as it was the only source within the error circle of X-ray source W16, however as seen in Fig. 6, it is no more variable in the ultraviolet than other sources of similar magnitudes.

4.4 WD/Gap sources

The *FUV* light curves for four of the WD/Gap sources are shown in Fig. 7. Source ID456 is, as indicated in Section 3, 0.038 arcsec from the X-ray source C and was proposed by Lugger et al. (2007) to be a CV, as it had decreased in the *UV* by 1 mag from 1994 to 1999. In the present work, ID456 decreases by roughly 1.5 mag in the *FUV* from the first observing epoch to the second which is representative of a dwarf nova and is pictured in Fig. 10. Göttgens et al. (2019) finds that this source exhibits broad Hα and Hβ emissions representative of accretion and it is thus very likely that this long-period CV candidate is the counterpart to the X-ray source C.

ID912 is the likely counterpart to X-ray source W15, making this source a potential CV, which was found by Zhao et al. (2020) to have a blue excess; however, the σ_{mean} for ID912 is not much larger than other sources of similar magnitudes.

Sources ID350 and ID1230 lie close to the variability criterion (Fig. 6), but their light curves only show slight variations. As such, these two sources can be considered weak variables.

4.5 Main sequence stars

The light curves for the MS stars that exhibit variability are given in Fig. A1 in the Appendix. The fluctuations of many of the MS stars seem more erratic than for the other populations which may indicate starspot activity (Brown et al. 2010). Some stars show little variance in magnitude over the course of one observing day, and then have large variations on another day, for example sources ID268 and ID1226 (this behaviour was also seen in the RGB star ID234). ID1226 has one of the highest σ_{mean} values and remains stable for almost two observing epochs and then exhibits a period of large variability before settling into a stable period again.

Source ID806 is on the edge of the error circle for X-ray source A3, and while it shows slight fluctuations in *FUV* magnitude, its σ_{mean} is no larger than sources of similar magnitude, and it remains likely that one of the RGB stars is the likely counterpart to A3.

5 SUMMARY

We performed a comparison of the positions of the sources detected in the FUV to known X-ray sources and possible companions or counterparts to these were discussed. The crowding in the centre of the cluster makes it difficult to determine the exact counterparts, and in this work all those that are within the 95 per cent error radii of the X-ray source are considered. Out of the 10 X-ray sources within our field of view, six confident counterparts are: the RGB star with strong *FUV* emission ID283 to X-ray source A2, the gap source ID456 to source C, agreeing with Lugger et al. (2007) that this is a CV, gap source ID912 to X-ray source W15, agreeing with Zhao et al. (2020) that this is also a CV, RGB star ID1029 to W16 that was proposed by Zhao et al. (2020) to be a RS CVn, and the two sources detected in the *FUV* but with no matching *UV* counterparts: ID1647 to X-ray source B and ID1700 to source 6. Although MS stars are much more numerous in the core region of globular clusters, if we include ID187 as the possible counterpart to A3, then three of the counterparts to the 10 X-ray sources are red giants.

Light curves were shown for *FUV*-variable objects and we found periods for four of these sources. Several of these variables were considered as potential X-ray counterparts. Out of the seven variable BS stars, the half period is measured for one of them that is a known W UMa-type contact binary. Four HB stars show variability, two are known RR Lyrae variables and one (ID179) is potentially a new RR Lyrae (RRab) classification, however it may be a field star. One gap source, ID456, a previously identified CV, shows a dwarf nova event and two other gap sources have weak variability. Twenty-eight MS stars also exhibit fluctuations.

Observations into the FUV allow us to detect and identify exotic stellar systems such as CVs, which are less easily observed at optical wavelengths among the numerous optically bright MS stars. Studies using ultraviolet wavelengths and multiwavelength comparisons continue to provide valuable insights into the different populations in dense stellar systems.

ACKNOWLEDGEMENTS

We thank the referee for the detailed and thoughtful comments. PK acknowledges support from the Grant Agency of the Czech Republic under grant number 20-21855S.

DATA AVAILABILITY

The data underlying this article are available in the *Mikulski Archive for Space Telescopes*: https://archive.stsci.edu. The data sets are derived from images in the public domain: https://archive.stsci.edu/proposal_search.php?mission=hst&id = 10561. The catalogue of sources is available at CDS via anonymous ftp to cdsarc.u-strasbg.fr (130.79.128.5) or via the VizieR catalogue access tool (Ochsenbein et al. 2000) at: http://vizier.u-strasbg.fr/viz-bin/VizieR?-source = J/MNRAS/511/3785. This research also made use of optical data also available at CDS: https://cdsarc.cds.unistra.fr/viz-bin/cat/J/AJ/116/1757.

REFERENCES

Bacon R. et al., 2017, A&A, 608, A1
Bailey S., 1902, Ann. Harv. Coll. Obs., 38, 1
Brown A. et al., 2010, Proc. IAU, 6, 78
Echiburú C. S., Guillot S., Zhao Y., Heinke C. O., Özel F., Webb N. A., 2020, MNRAS, 495, 4508
Edmonds P. D., Gilliland R. L., Heinke C. O., Grindlay J. E., 2003, ApJ, 596, 1177
Göttgens F. et al., 2019, A&A, 631, A118
Greenfield P., White R. L., 2000, in Manset N., Veillet C., Crabtree D., eds, ASP Conf. Ser. Vol. 216, Astronomical Data Analysis Software and Systems IX, Astron. Soc. Pac., San Francisco, p. 59
Guhathakurta P., Webster Z. T., Yanny B., Schneider D. P., Bahcall J. N., 1998, AJ, 116, 1757
Harris W. E., 1996, AJ, 112, 1487
Harris W. E., 2010, A New Catalog of Globular Clusters in the Milky Way, preprint (arXiv:1012.3224)
Hills J. G., Day C. A., 1976, Astrophys. Lett., 17, 87
Hong J., van den Berg M., Schlegel E. M., Grindlay J. E., Koenig X., Laycock S., Zhao P., 2005, ApJ, 635, 907
Hong J., Vesperini E., Belloni D., Giersz M., 2016, MNRAS, 464, 2511
Ivanova N., Heinke C. O., Rasio F. A., Belczynski K., Fregeau J. M., 2008, MNRAS, 386, 553
Kains N. et al., 2013, A&A, 555, A36
Kremer K., 2021, ApJ, 917, 28
Kremer K. et al., 2020, ApJS, 247, 48
Lomb N. R., 1976, Ap&SS, 39, 447
Lugger P. M., Cohn H. N., Heinke C. O., Grindlay J. E., Edmonds P. D., 2007, ApJ, 657, 286
Mansfield S., Dieball A., Kroupa P., Knigge C., Zurek D. R., Shara M., Long K. S., 2022, MNRAS, 511, 3785 (Paper I)
McCrea W. H., 1964, MNRAS, 128, 147
Nardiello D. et al., 2018, MNRAS, 481, 3382
Ochsenbein F., Bauer P., Marcout J., 2000, A&AS, 143, 23
Pietrukowicz P., Kaluzny J., 2004, Acta Astron., 54, 19
Piotto G. et al., 2015, ApJ, 149, 91
Ransom S. M., Stairs I. H., Backer D. C., Greenhill L. J., Bassa C. G., Hessels J. W. T., Kaspi V. M., 2004, ApJ, 604, 328
Scargle J. D., 1982, ApJ, 263, 835
Shara M. M., Hurley J. R., 2006, ApJ, 646, 464
Smith H., 1995, RR Lyrae Stars. Cambridge Univ. Press, Cambridge UK
Stetson P. B., 1987, PASP, 99, 191
VanderPlas J. T., 2018, ApJS, 236, 16
Zhao Y. et al., 2020, MNRAS, 499, 3338
Zurek D. R., Knigge C., Maccarone T. J., Pooley D., Dieball A., Long K. S., Shara M., Sarajedini A., 2016, MNRAS, 460, 3660

APPENDIX

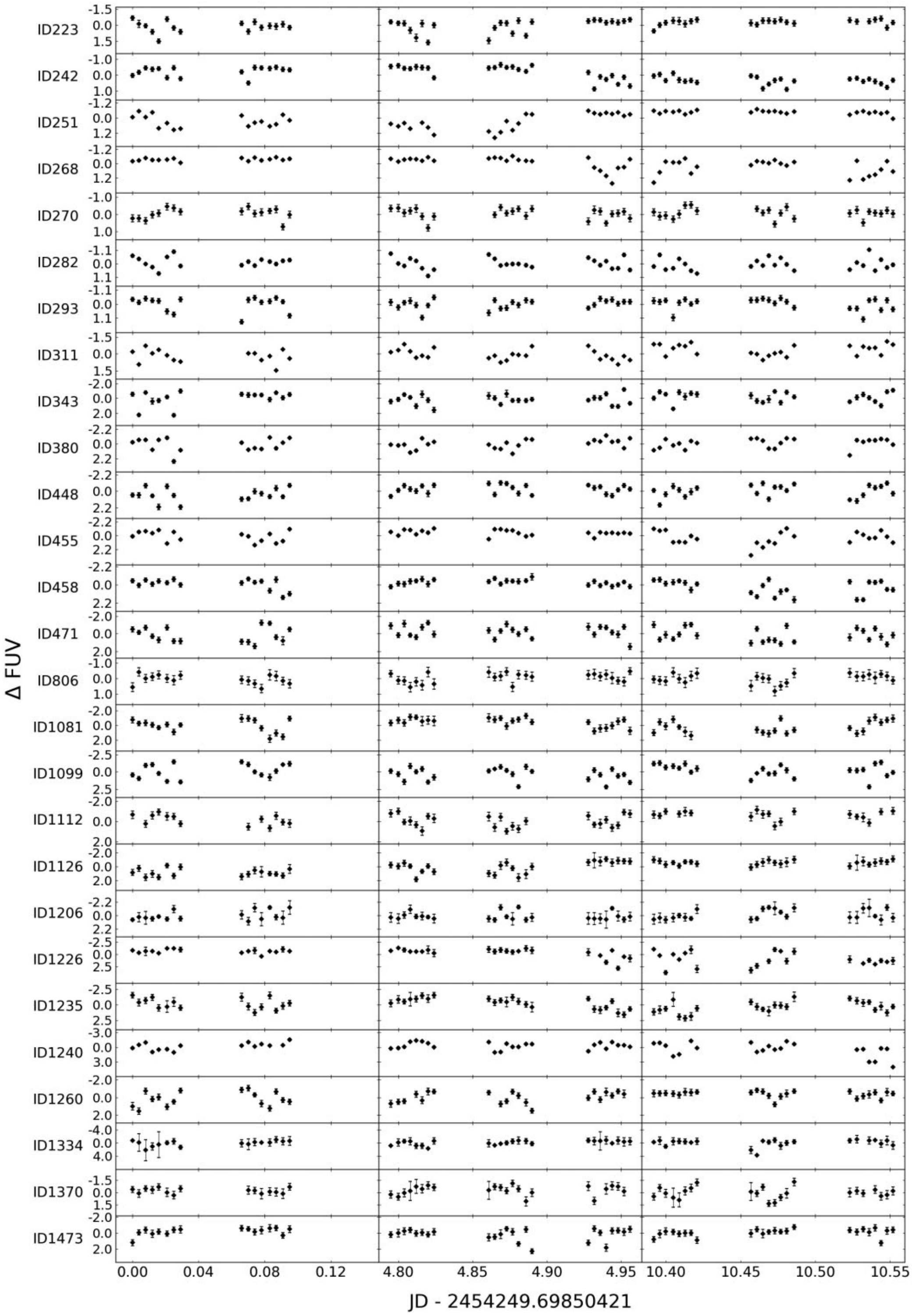

Figure A1. Light curves for the 28 MS stars that showed variability.

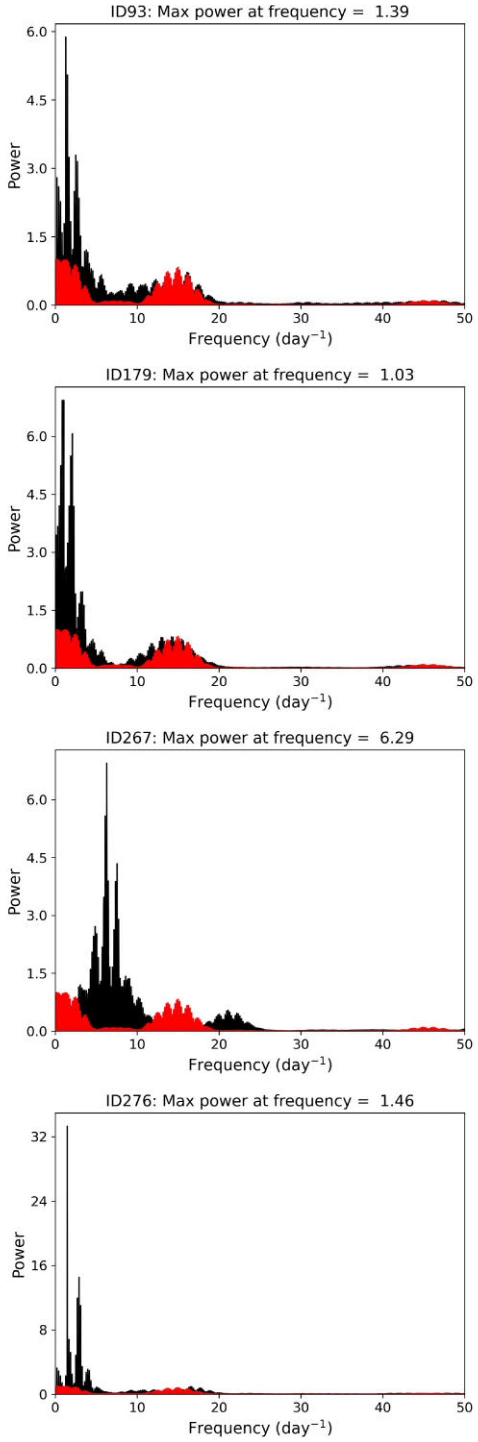

Figure A2. Lomb–Scargle periodograms (black) of the sources with periods measured along with the window function plotted in red.

Table A1. Photometric and variability parameters of all variable sources whose light curves are shown in this work.

ID	Type	*FUV - UV* (mag)	FUV_{mean} (mag)	σ_{mean}	Period (h)
93	HB	3.870 ± 0.011	20.518 ± 0.099	0.368	17.27
145	BS	1.961 ± 0.030	21.050 ± 0.152	0.344	
158	BS	1.923 ± 0.037	21.146 ± 0.161	0.331	
170	BS	2.054 ± 0.034	21.091 ± 0.158	0.309	
179	HB	0.234 ± 0.002	16.103 ± 0.013	0.212	23.08
181	RG	5.677 ± 0.068	22.726 ± 0.274	0.302	
187	RG	3.971 ± 0.037	21.690 ± 0.172	0.469	
223	MS	3.215 ± 0.091	21.658 ± 0.226	0.593	
234	RG	5.176 ± 0.044	21.455 ± 0.196	0.556	
242	MS	2.688 ± 0.052	21.340 ± 0.181	0.437	
251	MS	2.715 ± 0.058	21.581 ± 0.221	0.585	
260	BS	2.098 ± 0.043	20.835 ± 0.162	0.310	
267	BS	0.176 ± 0.007	17.999 ± 0.034	0.149	3.81
268	MS	3.175 ± 0.050	21.703 ± 0.229	0.571	
270	MS	2.495 ± 0.062	21.288 ± 0.170	0.416	
276	HB	1.857 ± 0.005	18.401 ± 0.038	0.638	8.22
277	HB	0.332 ± 0.002	15.989 ± 0.012	0.097	
282	MS	2.536 ± 0.032	21.862 ± 0.278	0.450	
293	MS	2.697 ± 0.046	21.585 ± 0.205	0.446	
311	MS	3.413 ± 0.056	22.200 ± 0.403	0.708	
314	BS	2.046 ± 0.092	21.390 ± 0.373	0.412	
343	MS	3.048 ± 0.066	22.120 ± 0.357	0.740	
350	Gap	-1.864 ± 0.098	21.238 ± 0.169	0.231	
380	MS	3.522 ± 0.038	23.109 ± 0.346	0.771	
448	MS	3.438 ± 0.038	23.462 ± 0.409	0.795	
455	MS	3.793 ± 0.038	23.552 ± 0.433	0.867	
456	Gap	0.821 ± 0.019	20.443 ± 0.099	0.675	
458	MS	3.706 ± 0.037	23.317 ± 0.377	0.693	
471	MS	3.513 ± 0.041	23.603 ± 0.430	0.753	
806	MS	3.801 ± 0.059	22.792 ± 0.282	0.303	
912	Gap	2.233 ± 0.093	24.019 ± 0.512	0.603	
1029	RG	3.929 ± 0.064	23.817 ± 0.429	0.468	
1081	MS	3.507 ± 0.041	23.753 ± 0.473	0.874	
1099	MS	4.067 ± 0.064	24.187 ± 0.486	0.944	
1112	MS	3.756 ± 0.036	23.513 ± 0.423	0.843	
1126	MS	3.732 ± 0.047	23.469 ± 0.412	0.830	
1206	MS	2.937 ± 0.049	21.309 ± 0.149	0.746	
1224	RG	4.074 ± 0.057	22.524 ± 0.471	0.597	
1226	MS	2.491 ± 0.064	21.992 ± 0.556	1.437	
1230	Gap	0.539 ± 0.054	21.333 ± 0.147	0.227	
1235	MS	3.682 ± 0.055	24.143 ± 0.570	0.924	
1240	MS	4.041 ± 0.065	24.577 ± 0.712	1.088	
1260	MS	3.903 ± 0.065	22.847 ± 0.312	0.817	
1303	RG	3.412 ± 0.036	21.391 ± 0.176	0.388	
1334	MS	3.937 ± 0.053	23.484 ± 0.422	0.900	
1370	MS	4.104 ± 0.070	23.560 ± 0.433	0.801	
1473	MS	3.573 ± 0.051	22.942 ± 0.314	0.613	

This paper has been typeset from a TEX/LATEX file prepared by the author.

Appendix C

A discontinuity in the luminosity-mass relation and fluctuations in the evolutionary tracks of low-mass and low-metallicity stars at the Gaia M-dwarf gap

The paper **Mansfield and Kroupa, A&A, Volume 650, A184, June 2021, DOI: 10.1051/0004-6361/202140536** is provided below in its published form.

The corrigendum **Mansfield and Kroupa, A&A, Volume 661, C1, May 2022, DOI: 10.1051/0004-6361/202140536e** is also included in its published form.

A&A 650, A184 (2021)
https://doi.org/10.1051/0004-6361/202140536

Astronomy & Astrophysics

A discontinuity in the luminosity–mass relation and fluctuations in the evolutionary tracks of low-mass and low-metallicity stars at the *Gaia* M-dwarf gap★

Santana Mansfield[1] and Pavel Kroupa[1,2]

[1] Helmholtz-Institut für Strahlen- und Kernphysik (HISKP), Universität Bonn, Nußallee 14-16, 53115 Bonn, Germany
e-mail: smansfield@astro.uni-bonn.de
[2] Astronomical Institute, Faculty of Mathematics and Physics, Charles University in Prague, V Holešovičkách 2, 18000 Praha, Czech Republic

Received 11 February 2021 / Accepted 23 April 2021

ABSTRACT

Context. The *Gaia* M-dwarf gap is a recently discovered feature in the colour-magnitude diagram that shows a deficiency of low-mass and low-metallicity stars at the lower end of the main sequence.

Aims. We aim at performing theoretical stellar modelling at low metallicities using a fine mass step and a fine time step, looking specifically for the transition of models from partially to fully convective since the convective kissing instability that occurs at this transition is believed to be the cause of the gap.

Methods. Stellar evolution models with metallicities of $Z = 0.01$, $Z = 0.001$, and $Z = 0.0001$ are performed using MESA, with a mass step of $0.00025\,M_\odot$ and a time step of 50 000 years.

Results. The small time step produced models that experience loops in their evolutionary tracks in the Hertzsprung-Russell (HR) diagram. The fluctuations in effective temperature and luminosity correspond to repeated events in which the bottom of the convective envelope merges with the top of the convective core, transporting ^{3}He from the core to the surface. In addition to the episodes of switching from partially to fully convective, several near-merger events that produced low amplitude fluctuations were also found. Low-metallicity models undergo the convective kissing instability for longer portions of their lifetime and with higher fluctuation amplitudes than models with higher metallicities. The small mass step used in the models revealed a discontinuity in the luminosity–mass relation at all three metallicities.

Conclusions. The repeated merging of the convective core and envelope, along with several near-merger events, removes an abundance of ^{3}He from the core and temporarily reduces nuclear burning. This results in fluctuations in the model's luminosity and effective temperature, causing loops in the evolutionary track in the HR diagram and leading to the deficiency of stars at the M-dwarf gap, as well as a discontinuity in the luminosity–mass relation.

Key words. stars: low-mass – convection – Hertzsprung-Russell and C-M diagrams – stars: luminosity function, mass function

1. Introduction

Stars are formed from the gravitational infall of material in molecular clouds, which produces many stars with masses lower than the mass of the Sun. A substantially greater amount of material is needed for stars with masses higher than the Sun, and so these stars are formed in much fewer numbers. Stars undergo nuclear reactions in their cores for masses $m \gtrsim 0.08\,M_\odot$, and thus the majority of all stars have masses from this lower limit up to the solar mass.

The stellar luminosity function and the stellar mass function are used to make comparisons across all types of stars, and these functions depend sensitively on the luminosity–mass relation. This relation has long been considered a smooth and differentiable function that exhibits structure correlating to the features of the stellar luminosity function (Kroupa et al. 1990). For example, an inflection in the luminosity–mass relation at $\approx 0.30\,M_\odot$ was first discussed by Copeland et al. (1970) as the H_2 dissociation zone having a lower adiabatic gradient. The minimum in the first derivative of the luminosity–mass relation, $dm/dM_{\rm bol}$, at this mass was found to correspond to the maximum of the observed luminosity function of low-mass stars (Kroupa et al. 1990; Kroupa & Tout 1997) due to H_2 formation as well as stars becoming fully convective at this mass. Thus, all mono-age and mono-metallicity stellar populations show a pronounced and sharp maximum in the stellar luminosity function at a visual absolute magnitude of $M_{\rm V} \approx 12$ (Kroupa 2002; Kroupa et al. 2013). The luminosity–mass relation has long been known to be metallicity dependant (Elson et al. 1995; Kroupa & Tout 1997).

A recently discovered and related feature, called the *Gaia* M-dwarf gap, or Jao gap, was found in the observational *Gaia* Data Release 2 (DR2) data (Jao et al. 2018) and coincides with the same stellar mass of the inflection in the luminosity–mass relation at $\approx 0.30\,M_\odot$. This feature lies at the lower end of the main sequence (MS) in the $G_{\rm BP}$–$G_{\rm RP}$, M_G colour-magnitude diagram (CMD) and represents a deficiency in the density of stars (and subsequently a dip in the luminosity function). This gap was recently confirmed in the *Gaia* Early Data Release 3 (EDR3) data (Gaia Collaboration 2021) at *Gaia* magnitudes $2.2 < G_{\rm BP}-G_{\rm RP} < 2.8$ and $10.0 < M_G < 10.3$ and portrays a drop in density by $17 \pm 6\%$ (Jao et al. 2018). It is postulated that this occurs due to M-dwarf stars with masses around ≈ 0.30–$0.35\,M_\odot$

★ Movie is available at https://www.aanda.org undergoing the transition from being partially to fully convective (Jao et al. 2018; Baraffe & Chabrier 2018).

The thermonuclear process for low-mass stars is governed by the proton-proton I (ppI) chain:

$$p + p \longrightarrow d + e^{+} + \nu_{\rm e} \tag{1}$$

$$p + d \longrightarrow {}^{3}{\rm He} + \gamma \tag{2}$$

$${}^{3}{\rm He} + {}^{3}{\rm He} \longrightarrow {}^{4}{\rm He} + 2p \tag{3}$$

where two protons (p) combine to make deuterium (d) by releasing a positron (e^+) and an electron neutrino ($\nu_{\rm e}$), and ultimately synthesise a ^{4}He nucleus with the release of a photon (γ) and via two ^{3}He nuclei. Equation (3) becomes important once the central temperature is $T \gtrsim 7 \times 10^6$ K (Dearborn et al. 1986), that is, $m \gtrsim 0.26\,M_\odot$. Without this reaction, the energy produced by the other two reactions (Eqs. (1) and (2)) is not great enough for the material in the core to become unstable to convection (Baraffe & Chabrier 2018), which occurs when the radiative temperature gradient is larger than the adiabatic gradient, $\nabla_{\rm rad} > \nabla_{\rm ad}$, where

$$\nabla_{\rm rad} \propto L\kappa/T^4. \tag{4}$$

When the reaction given by Eq. (2) dominates, the ^{3}He abundance grows, and at a temperature $T \gtrsim 7 \times 10^6$ K, Eq. (3) produces enough energy in the core for the centre to become convective (Chabrier & Baraffe 1997). Then, for example, as a $0.30\,M_\odot$ star approaches the MS, it has a radiative core, but the temperature increase due to the pre-MS contraction means that the production and destruction of ^{3}He by Eqs. (2) and (3) releases enough energy for the material in the core to become unstable to convection; as such, the star reaches the MS with a convective core and envelope, which are separated by a thin radiative layer (Ezer & Cameron 1967).

Before the discovery of the M-dwarf gap, van Saders & Pinsonneault (2012) theorised that at the mass directly above the convective boundary, stars undergo the 'convective kissing instability'. As ^{3}He is destroyed at a slower rate by Eq. (3) than is produced by Eq. (2) at these low-mass temperatures (Baraffe & Chabrier 2018), it cannot reach equilibrium abundance. The abundance of ^{3}He increases, and the core grows in size until it comes into contact with the convective envelope, resulting in periods of full convection (van Saders & Pinsonneault 2012). The mixing during these periods carries ^{3}He out towards the surface, nuclear reactions in the core subside, and the core contracts and becomes separated again from the envelope (van Saders & Pinsonneault 2012). This continues periodically, with variations in the star's luminosity and effective temperature, until the abundance of ^{3}He is high enough throughout the star that it remains fully convective for the remainder of its lifetime. The variations from this convective kissing instability are thought to result in the M-dwarf gap in the density of observed stars seen at these temperatures and luminosities. Baraffe & Chabrier (2018) produced models in steps of $0.01\,M_\odot$ and note the merging of the core and envelope in their $0.34\,M_\odot$ and $0.36\,M_\odot$ models, along with a decrease in central ^{3}He abundance and a change in the slope of the luminosity–mass relation at these masses. MacDonald & Gizis (2018) also find this relation and a dip in the luminosity function for their 0.33–0.35 $M_\odot$ models. Feiden et al. (2021) reproduced the M-dwarf gap in a CMD made from population synthesis models and also find periodic pulsations in luminosity, radius, and core temperature due to the ^{3}He instability.

The *Gaia* M-dwarf gap is prominent across the blueward edge of the MS, where lower-metallicity stars are found. Feiden et al. (2021) show that their models with low metallicity ([Fe/H] = −0.7) encounter this instability at lower masses (and thus cooler core temperatures) than models with higher metallicities; from this they conclude that the dependence of temperature on stellar mass is one of the critical factors for this instability. At low temperatures, the opacity dependence of the radiative temperature gradient (Eq. (4)) becomes important. For lower metallicity, the opacity is decreased and the central temperature needed for the energy transport in the core to occur by radiative transport is lower (Chabrier & Baraffe 1997) and thus requires less mass. As such, the convective kissing instability is expected to happen at lower masses for lower metallicities since the higher-mass models have the temperature necessary for radiative cores. This work aims to investigate the dependence of the M-dwarf gap on the very low metallicities found in old globular clusters. Based on this, we suggest that the M-dwarf gap should be well represented in metal-poor globular cluster CMDs, although the low stellar masses at which this effect is found will be difficult to detect in clusters at great distances.

This work uses stellar evolution models to reproduce the convection-mass transition and investigate a fine grid of masses and very low metallicities with a short-scale time step. These models are described in Sect. 2, the results are presented in Sect. 3, and we conclude with a discussion in Sect. 4.

2. Stellar models

The 1D stellar evolution code Modules for Experiments in Stellar Astrophysics (MESA, version 15140) was used (Paxton et al. 2011, 2013, 2015, 2018, 2019). The equations of state (EOSs) used in MESA are a combination of the SCVH (Saumon et al. 1995), OPAL (Rogers & Nayfonov 2002), HELM (Timmes & Swesty 2000), FreeEOS (Irwin 2004), and PC (Potekhin & Chabrier 2010) EOSs. The opacity tables relevant to this work are given by Grevesse & Sauval (1998) and OPAL (Iglesias & Rogers 1993, 1996); additionally, the electron conduction opacities are from Cassisi et al. (2007) and the opacity tables for the low temperatures of M-dwarf atmospheres in which molecules and dust grains are able to form are from Ferguson et al. (2005). For the outer boundary conditions we adopted the prescriptions provided by the Hauschildt et al. (1999) model atmosphere tables, taken at $\tau = 100$ (Paxton et al. 2011; Chabrier & Baraffe 1997). The nuclear reaction rates are from Cyburt et al. (2010), and we included additional weak reaction rates (Fuller et al. 1985; Oda et al. 1994; Langanke & Martínez-Pinedo 2000). Screening was included via the prescription of Chugunov et al. (2007). Thermal neutrino loss rates are from Itoh et al. (1996). The initial helium abundance is $Y = 0.24 + 2Z$ by mass fraction. Material becomes unstable to convection under the Schwarzschild criterion, and convective energy transport is described using mixing length theory.

Three initial metallicities were chosen ($Z = 0.01$, $Z = 0.001$, and $Z = 0.0001$) in order to investigate the M-dwarf gap on the blue edge of the MS and investigate the low metallicities found in globular clusters. An initial set of models for each metallicity was computed using a mass step of $0.01\,M_\odot$ to determine at which mass the models begin to have radiative cores. Once found, model sets were then produced using a smaller mass step of $0.00025\,M_\odot$. The models were calculated from the zero-age main sequence (ZAMS) up to 10 Gyr with a maximum time step of 50 000 years. One final model with an initial mass of $0.28\,M_\odot$ and $Z = 0.0001$ was computed up to 1 Gyr using a maximum time step of 1000 years.

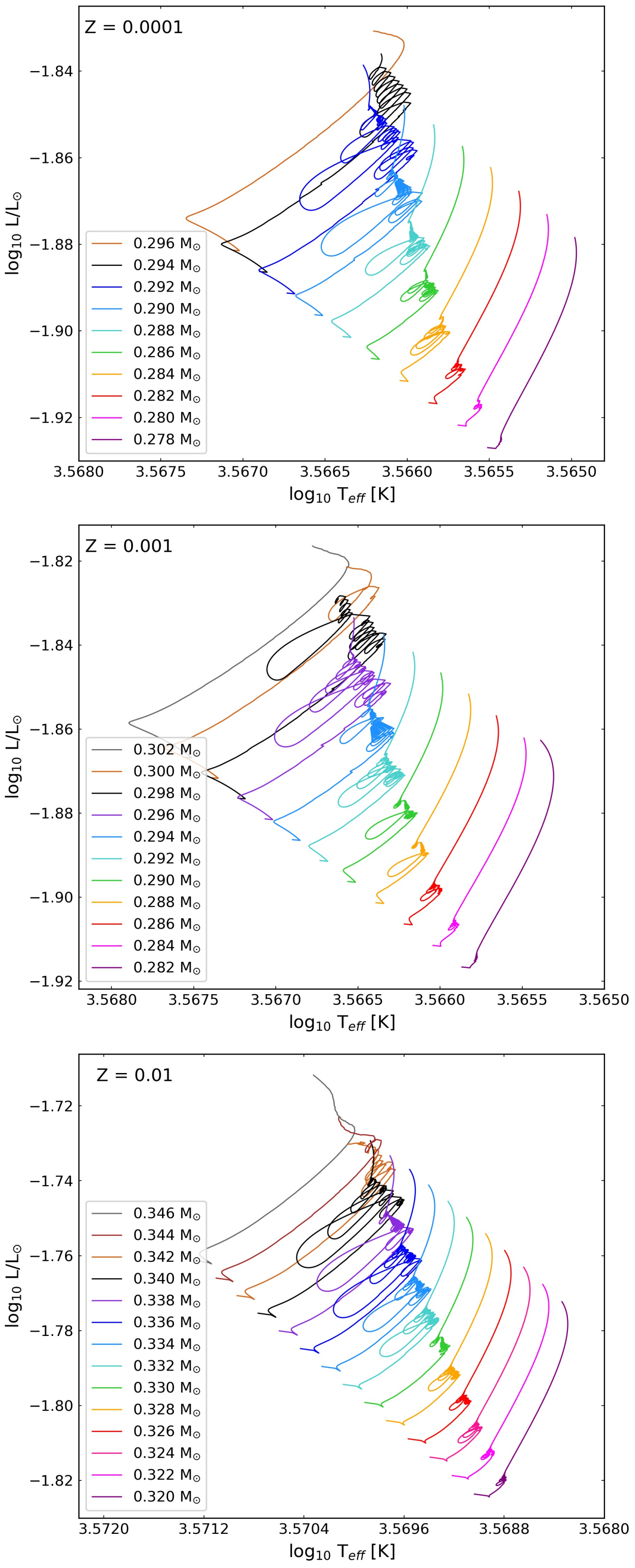

Fig. 1. Evolutionary tracks shown in the HR diagram for three sets of stellar models with metallicities $Z = 0.0001$ (*top*), $Z = 0.001$ (*middle*), and $Z = 0.01$ (*bottom*). The models begin their evolution on the left and move upwards along the tracks to reach the final points at 10 Gyr. The stars are on the MS throughout this evolution.

Table 1. Model mass ranges for the discontinuity in the luminosity–mass relation.

Age [Gyr]	$Z = 0.01$	$Z = 0.001$	$Z = 0.0001$
1	$0.32650{-}0.33875\,M_\odot$	$0.28600{-}0.29485\,M_\odot$	$0.28275{-}0.29000\,M_\odot$
3	$0.33450{-}0.34325\,M_\odot$	$0.29275{-}0.29925\,M_\odot$	$0.28850{-}0.29450\,M_\odot$
5	$0.34025{-}0.34325\,M_\odot$	$0.29500{-}0.30125\,M_\odot$	$0.29050{-}0.29500\,M_\odot$
7	$0.34175{-}0.34325\,M_\odot$	$0.29575{-}0.30150\,M_\odot$	$0.29175{-}0.29450\,M_\odot$
9	$0.34150{-}0.34350\,M_\odot$	$0.29775{-}0.30025\,M_\odot$	$0.29250{-}0.29525\,M_\odot$

3. Results

The low-mass MS models slowly undergo nuclear burning via the ppI chain described by Eqs. (1)–(3). By the time they reach an age of 10 Gyr, the hydrogen abundance in the core has only just begun to deplete. The Hertzsprung-Russell (HR) diagrams in Fig. 1 (and also later in Fig. 4) show the models experiencing a period of fluctuations that appear as loops along their evolutionary tracks during the MS. The age of the model at which this occurs increases with increasing mass. The mass range for this instability occurs at a higher mass for a higher metallicity, and the range of masses is larger for the higher-metallicity models. For the masses below the convective boundary, the models are fully convective throughout their lifetimes. Between a certain mass range for each metallicity (given in Table 1), the models begin their lives with a convective core, a thin radiative layer, and a convective envelope. They then undergo a period whereby they repeatedly switch from this structure to one of full convection and then relax into a fully convective state for the remainder of their lifetimes. This is illustrated in Fig. 2, which shows the mass coordinates of the convective and radiative regions of the $Z = 0.001$ models over time. At 1 Gyr, the models with mass $m < 0.28600\,M_\odot$ are fully convective, models with mass $0.28600\,M_\odot \leq m \leq 0.29845\,M_\odot$ have begun the convective kissing instability, and the models with higher masses have a stable convective core and radiative region. The $0.28550\,M_\odot$, $0.28900\,M_\odot$, and $0.29450\,M_\odot$ models are also fully convective at 1 Gyr, having undergone a merger of the convective core and envelope. At 3 Gyr, models with mass $m < 29275\,M_\odot$ and the $0.29550\,M_\odot$ model that has merged are fully convective. At 5 Gyr, the models with mass $m < 0.29500\,M_\odot$ along with the $0.29525\,M_\odot$ and $0.29550\,M_\odot$ models that are merged at this time are fully convective. By 9 Gyr, models with mass $m < 0.29775\,M_\odot$ are fully convective, and models with mass $m > 0.31150\,M_\odot$ have a radiative core.

3.1. *Convective kissing instability*

The luminosity, effective temperature, and central ^{3}He abundance over time are displayed in Fig. 3 for several models with a metallicity of $Z = 0.001$. For the sake of clarity, some models are not shown. At this metallicity, the models up to $0.30025\,M_\odot$ undergo fluctuations in luminosity and temperature, some over the course of several billion years, which correlate to the increase and decrease of ^{3}He in the core. There is a clear correlation between the dips in central ^{3}He abundance and both the peaks in luminosity and the troughs in temperature. The amplitude of the fluctuations generally decreases over time until the models settle into a fully convective state; however, the models also exhibit large changes in luminosity and temperature, corresponding to the larger loops seen in the HR diagrams in Fig. 1. Figure 4 shows the convective kissing instability for the $0.296\,M_\odot$,

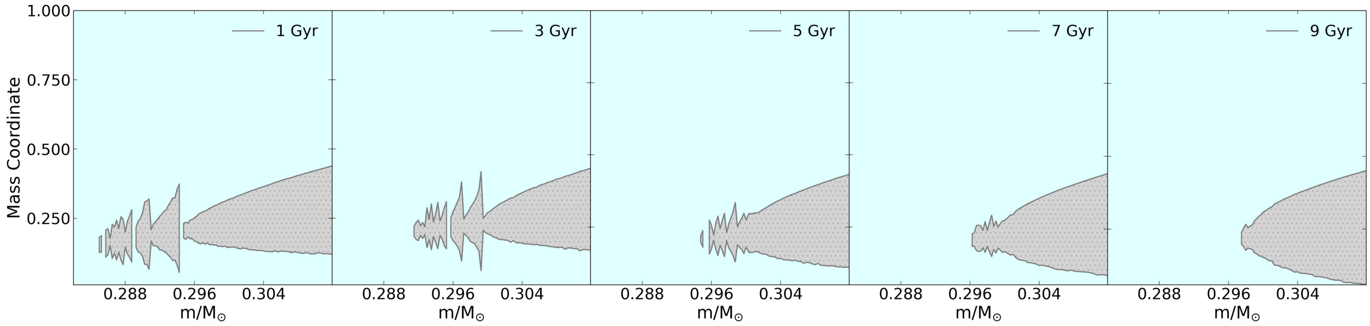

Fig. 2. Mass coordinates of the convective (blue) and radiative (grey dotted) regions within the $Z = 0.001$ models over 1, 3, 5, 7, and 9 Gyr. The models that experience a merger of the convective core and envelope can be seen as gaps in the radiative region. A movie of the full time lapse is available online.

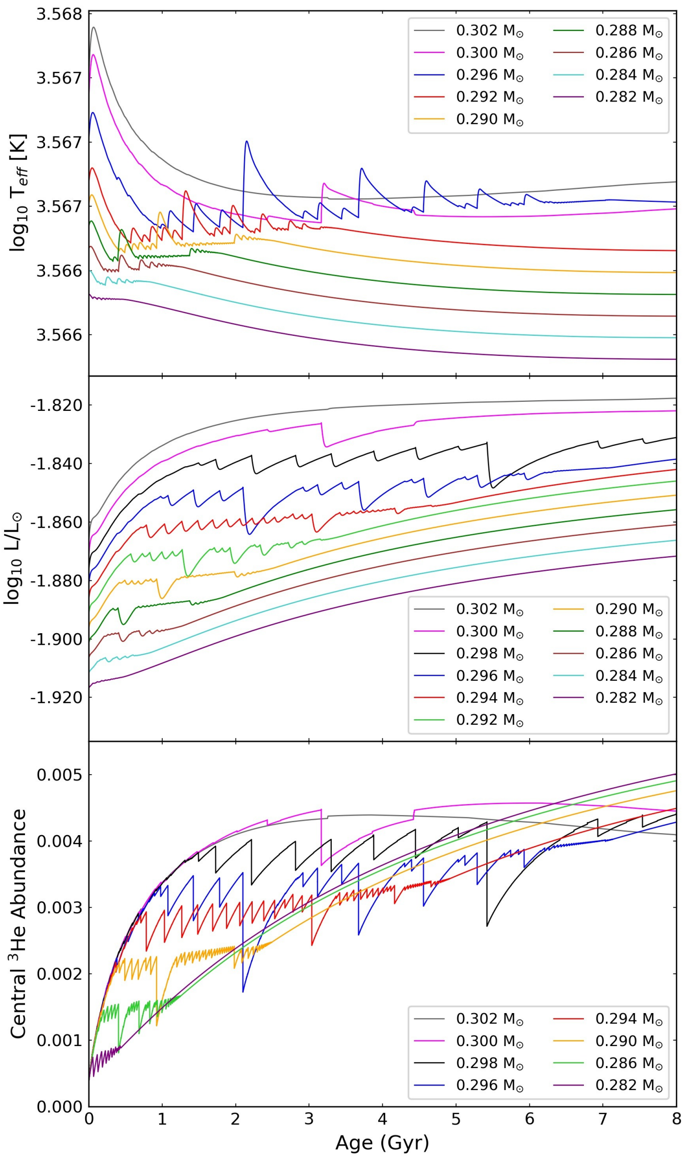

Fig. 3. Temperature (*top*) luminosity (*middle*), and central ^{3}He abundance (by mass fraction; *bottom*) over time for models with a metallicity of $Z = 0.001$. The fluctuations occur for several billion years for the higher-mass models.

$Z = 0.001$ model. The top panel shows the HR diagram, with each point representing 50 000 years, illustrating that the loops occur over a long period of time. The next panels down in the figure give the temperature, luminosity, radius, and ^{3}He abundance profiles over time, along with the mass coordinate positions of the top of the convective core and the bottom of the convective envelope; the region in between is radiative. Again, the correlation between these properties is clear. When the bottom of the convective envelope reaches down towards the core, the central ^{3}He abundance drops as the material is carried out towards the surface, and correspondingly the surface ^{3}He abundance rises. This results in a decrease in luminosity as the ^{3}He production is reduced. The temperature rises due to the now fully convective model contracting to compensate for the loss in nuclear energy output, which is represented by the drop in radius. Once the temperature is high enough to resume ^{3}He production, the abundance of ^{3}He in the core begins to rise along with the luminosity, and the model can increase again in radius. As the radius increases, the surface temperature drops. This repeated process, which results in the fluctuations in temperature and luminosity, produces the loops seen in the HR diagrams in Fig. 1. After ^{3}He reaches its equilibrium abundance, the fluctuations subside and the models remain fully convective. The time period during which the models undergo the convective kissing instability, as well as the amplitude in luminosity and temperature fluctuations, increases with increasing mass. The 1000 year time step model showed that the smallest pulsations took place on timescales of a few thousand years.

The models additionally exhibit several events where the bottom of the convective envelope reaches down towards the core but remains disconnected from it. These near-merger events correspond to small drops in central ^{3}He abundance and increases in surface ^{3}He, and they occur over a period of ≈1 Myr.

3.2. Metallicity dependence

The main effect due to metallicity is the convective kissing instability occurring at larger masses for models with higher metallicity. Correspondingly, the effective temperature is also higher for models with increased metallicity. Figure 5 shows the effect of metallicity for one chosen model with mass $m = 0.290\,M_\odot$. This figure includes the HR diagrams along with the temperature, luminosity, radius, and central ^{3}He abundance over time for metallicities of $Z = 0.001$ and $Z = 0.0001$. A comparison to $Z = 0.01$ could not be made here as the lowest mass to undergo the convective kissing instability for this metallicity is $0.32650\,M_\odot$. The higher-Z model begins the instability at an earlier age, around 0.3 Gyr, relative to the low-Z model, which begins at around 0.8 Gyr. The fluctuation period subsides and the higher-Z model becomes fully convective by 2.5 Gyr, compared

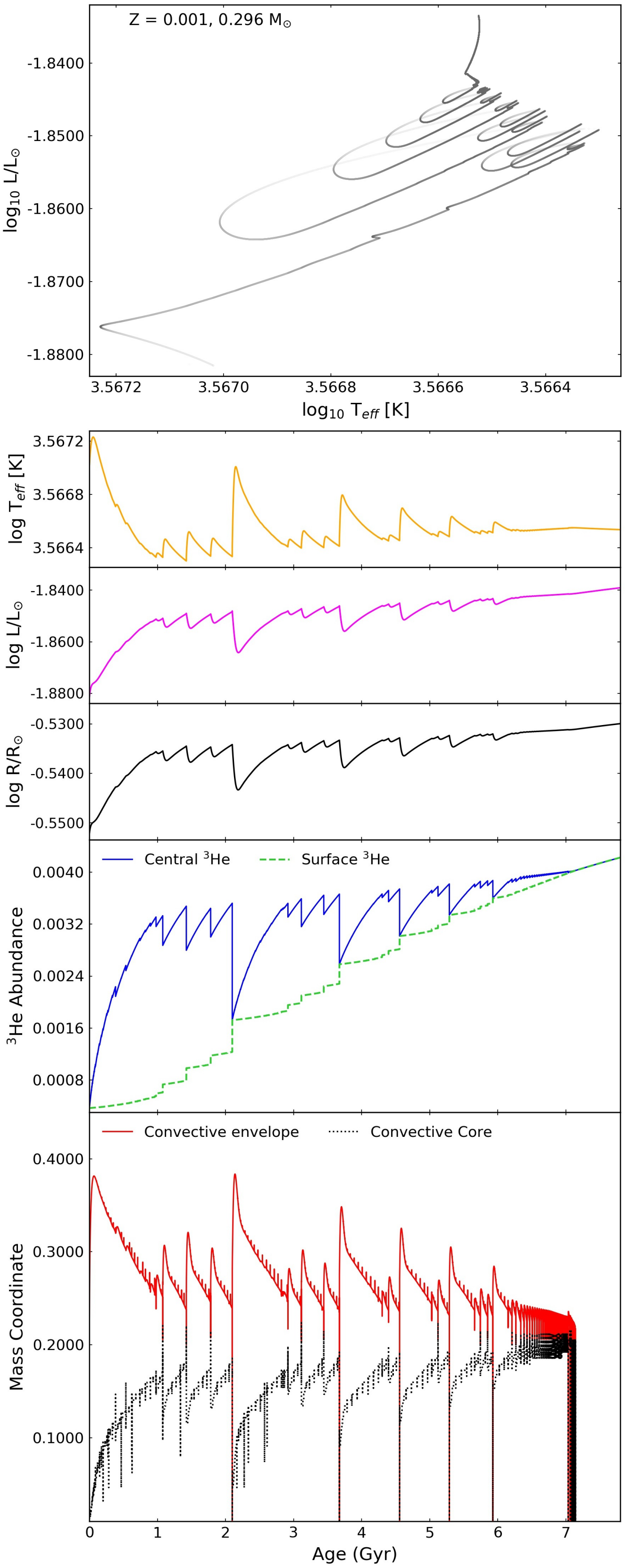

Fig. 4. HR diagram (*top*) for the 0.296 $M_\odot$, $Z = 0.001$ model, where each point represents 50 000 years. Also displayed are: the temperature, luminosity, and radius profiles for the same model (*middle*); and the centre and surface ^{3}He abundances (by mass fraction), along with the mass coordinate of the bottom of the convective envelope and the top of the convective core (*bottom*). A radiative region is found in between. After about 7 Gyr, this model has evolved to be fully convective.

to 5.5 Gyr for the low-Z model (more than twice as long). The amplitude of the fluctuations found in the luminosity, temperature, radius, and central ^{3}He abundance are much higher for the low-Z model.

3.3. Luminosity–mass relation

Figure 6 shows the luminosity–mass relation for the three metallicities investigated, at the model ages of 1, 3, 5, 7, and 9 Gyr. A discontinuity is seen at all metallicities. The discontinuity is present over many billions of years and is more prominent at the lower age. The mass ranges in which the discontinuity occurs are given in Table 1. By 9 Gyr, the lower-mass models that underwent the convective kissing instability at 1 Gyr have settled into a fully convective state, and as such the discontinuity shifts to higher masses and higher luminosities over time. Additionally, the discontinuity occurs at higher masses and luminosities for higher metallicities. Interestingly, the discontinuity is greatly reduced at 7 Gyr for $Z = 0.01$ to little more than a dip in the luminosity–mass relation, but then appears again at 9 Gyr. Also for $Z = 0.01$, the highest-mass model to undergo the instability remains 0.34325 $M_\odot$ at 3, 5, and 7 Gyr, whereas for the other metallicities the highest mass increases over time.

4. Discussion

The models in this work undergo luminosity, temperature, and radial fluctuations due to the convective kissing instability that was predicted by van Saders & Pinsonneault (2012), and found in models by Baraffe & Chabrier (2018) and Feiden et al. (2021) to be responsible for the *Gaia* M-dwarf gap. This work finds these fluctuations in the form of loops in the evolutionary tracks in the HR diagrams for models with metallicities down to $Z = 0.0001$, and our results agree with the conclusion that low-mass stars undergo these periods of fluctuations due to ^{3}He production and transport.

A dip in the luminosity–mass relation was found by MacDonald & Gizis (2018), and by using smaller mass steps, we see that there is in fact a discontinuity. We find that the discontinuity occurs at lower masses and luminosities for the lower-metallicity models, as a direct consequence of the convective kissing instability developing at higher masses for higher metallicities. The discontinuity is a result of the merging of the convective envelope and core with the production of ^{3}He, and of the model subsequently and periodically switching between partially and fully convective states. This affects the nuclear energy output, which results in the disruption in the luminosity–mass relation as well as the *Gaia* M-dwarf gap. This discontinuity, which is present over many billions of years, has a great impact on stellar physics as the luminosity–mass relation is no longer differentiable at these masses. For example, in order to constrain the stellar mass function, the slope of the luminosity–mass relation is used (Kroupa et al. 1990, 2013). This stellar mass function provides information on the nature of low-mass star formation and the contribution of low-mass stars to the dark matter problem (Kroupa et al. 1990).

The extra model with a maximum time step of 1000 years that ran up to 1 Gyr was calculated in order to check if the 50 000 year time step was able to provide an acceptable resolution for the computational time taken. The 1000 year time step model did reveal that the smallest pulsations took place on timescales of a few thousand years. However, the HR diagram as well as the luminosity and temperature profiles of the 1000 year

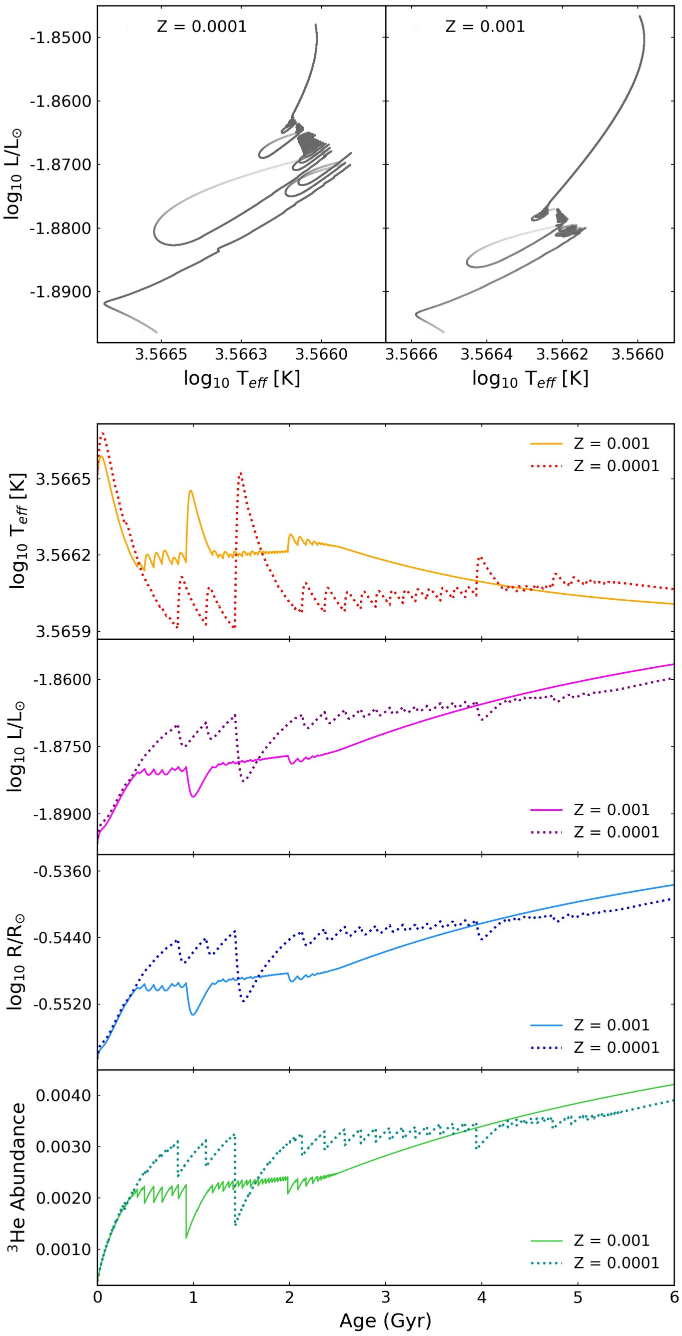

Fig. 5. HR diagrams for the 0.290 $M_\odot$ model with Z = 0.0001 (*top left*) and Z = 0.001 (*top right*). Each point represents 50 000 years. Also shown are the temperature, luminosity, radius, and central ^{3}He abundance profiles (bottom grid) for the two models.

model were visually comparable to the 50 000 year time step model. As the 1000 year model took 82 hours to complete, the computationally quicker 50 000 year time step was adequate for our purposes.

Feiden et al. (2021) find that the merger events between the convective core and envelope happen four to six times before their models settle into a fully convective state; however, the small time step used in this work reveals a much higher number of merger events. Additionally, some models experience several near-merger events during which the convective envelope reaches down into the radiative layer but not all the way to the core. These mixing events transport ^{3}He-rich material into the radiative region, into which the convective envelope reaches and pulls ^{3}He outwards to the surface. Whilst the core and envelope do not merge during these events, there exists a million-year-long instability between the two that results in small fluctuations in the ^{3}He abundance, as well as in the surface temperature and luminosity. Further investigation is needed to fully resolve and determine the processes occurring during these near-merger events which was beyond the scope of this work.

The convective kissing instability occurs at higher masses for higher metallicities. This was expected due to the increased opacity for higher metallicities. Convection occurs when the radiative temperature gradient is higher than the adiabatic gradient, and by increasing the opacity, a higher temperature (and thus mass) is needed for the growth of a radiative core than for a lower opacity. For lower metallicities, the central temperature required for radiative transport is lower (Chabrier & Baraffe 1997), and thus the low-Z models have a radiative core at lower masses than the models with high metallicities. For a given mass, the convective kissing instability occurs earlier in the model lifetime for a higher metallicity since the evolution of the central temperature occurs earlier (see Chabrier & Baraffe 1997, Fig. 10a). Additionally, the convective kissing instability occurs for longer portions of the model lifetime for lower metallicities (Fig. 5), in agreement with Feiden et al. (2021) and Jao et al. (2018), who note that the observational M-dwarf gap is more prominent at the blue edge of the MS in the HR diagram that represents stars of low metallicities. The instability is found in models with metallicities down to Z = 0.0001, which would be well represented in old globular clusters; this is especially true since the instability period was found to be almost twice as long for the Z = 0.0001 models relative to the Z = 0.001 models. It would be of great importance to find the M-dwarf gap in the observations of these star clusters, although the great distances of the clusters create difficulties in finding these faint low-mass stars. Infrared observations of the nearest globular clusters may be able to achieve this.

5. Summary

Stellar evolution models were computed using three different metallicities over a range of masses in order to reproduce the M-dwarf gap observed in the lower region of the MS. The models used a mass step of 0.00025 $M_\odot$ and a time step of 50 000 years and ran until 10 Gyr. A final model used a 1000 year time step up to 1 Gyr; however, this was computationally time consuming, and the time step of 50 000 years was adequate for the purposes of this investigation. A discontinuity was found in the luminosity–mass relation for masses 0.32650–0.34350 $M_\odot$ for the metallicity Z = 0.01, masses 0.28600–0.30025 $M_\odot$ for Z = 0.001, and masses 0.28275–0.29525 $M_\odot$ for Z = 0.0001. The HR diagrams for these models show loops during the MS, which results in fluctuations in luminosity and effective temperature. The lower-metallicity models undergo the convective kissing instability at lower masses than the higher-metallicity models, due to the lower opacity and thus the lower temperature (and mass) required for radiative transport in the core. The instability occurs for a longer portion of the model's lifetime for a given mass with decreasing metallicity.

Comparing the central and surface ^{3}He abundances, as well as the mass coordinates of the convective core and envelope, the loops and pulsations correspond to the merging of the core and envelope, resulting in the switching of the model from a partially to fully convective state and the transport of ^{3}He from the core to the surface. These loops would lead to the deficiency of stars in

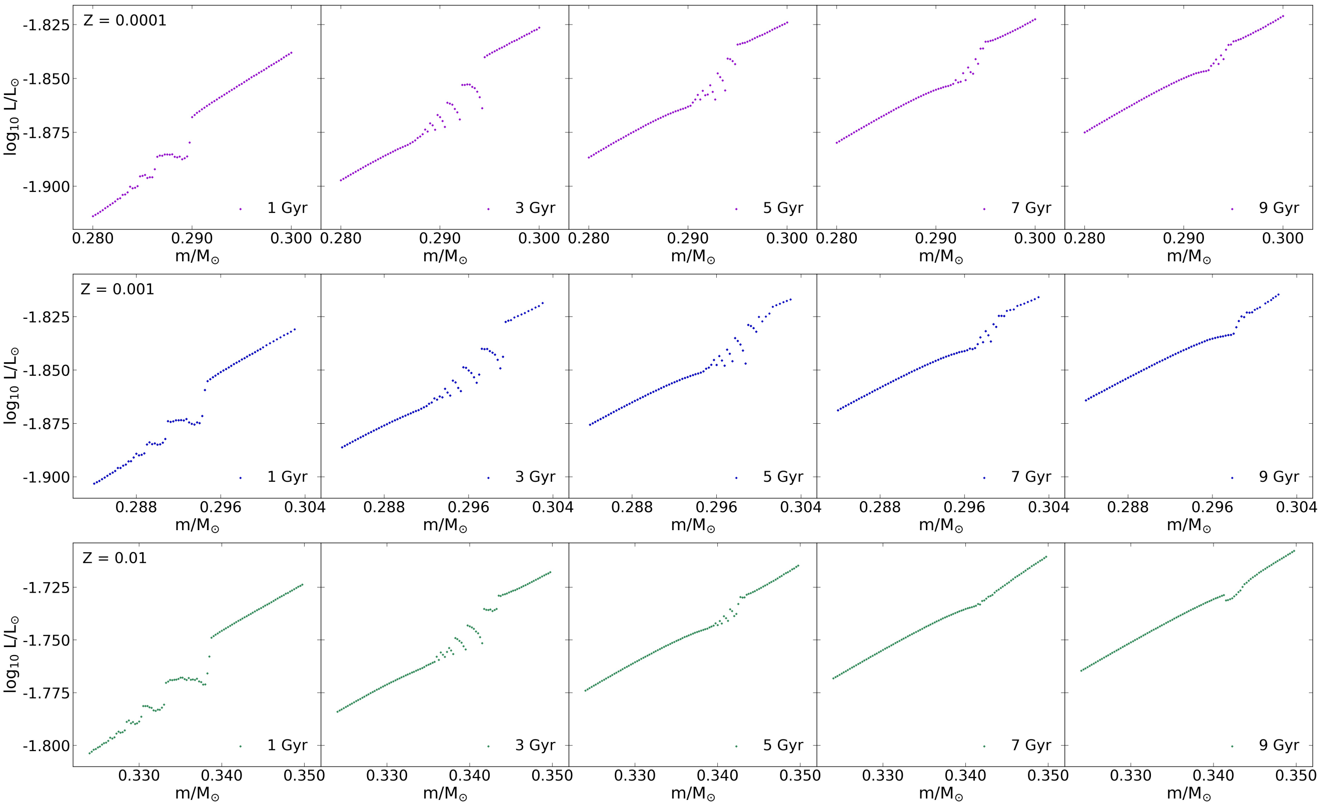

Fig. 6. Luminosity–mass relation for metallicities $Z = 0.0001$ (*top*), $Z = 0.001$ (*middle*), and $Z = 0.01$ (*bottom*) at model ages 1, 3, 5, 7, and 9 Gyr. A movie of the full time lapse is available online for the $Z = 0.001$ model set.

the *Gaia* M-dwarf gap and are due to the production and mixing of ^{3}He throughout the star from the merging of the convective core and envelope.

Acknowledgements. We thank the referee for the detailed and thoughtful comments. PK acknowledges support from the Grant Agency of the Czech Republic under grant number 20-21855S.

References

Baraffe, I., & Chabrier, G. 2018, A&A, 619, A177
Cassisi, S., Potekhin, A. Y., Pietrinferni, A., Catelan, M., & Salaris, M. 2007, ApJ, 661, 1094
Chabrier, G., & Baraffe, I. 1997, A&A, 327, 1039
Chugunov, A. I., Dewitt, H. E., & Yakovlev, D. G. 2007, Phys. Rev. D, 76, 025028
Copeland, H., Jensen, J. O., & Jorgensen, H. E. 1970, A&A, 5, 12
Cyburt, R. H., Amthor, A. M., Ferguson, R., et al. 2010, ApJS, 189, 240
Dearborn, D., Schramm, D., & Steigman, G. 1986, ApJ, 302, 35
Elson, R. A. W., Gilmore, G. F., Santiago, B. X., & Casertano, S. 1995, AJ, 110, 682
Ezer, D., & Cameron, A. G. W. 1967, Can. J. Phys., 45, 3461
Feiden, G. A., Skidmore, K., & Jao, W.-C. 2021, ApJ, 907, 53
Ferguson, J. W., Alexander, D. R., Allard, F., et al. 2005, ApJ, 623, 585
Fuller, G. M., Fowler, W. A., & Newman, M. J. 1985, ApJ, 293, 1
Gaia Collaboration (Smart, R. L., et al.) 2021, A&A, 649, A6
Grevesse, N., & Sauval, A. J. 1998, Space Sci. Rev., 85, 161
Hauschildt, P. H., Allard, F., & Baron, E. 1999, ApJ, 512, 377
Iglesias, C. A., & Rogers, F. J. 1993, ApJ, 412, 752
Iglesias, C. A., & Rogers, F. J. 1996, ApJ, 464, 943
Irwin, A. 2004, http://freeeos.sourceforge.net/
Itoh, N., Hayashi, H., Nishikawa, A., & Kohyama, Y. 1996, ApJS, 102, 411
Jao, W.-C., Henry, T. J., Gies, D. R., & Hambly, N. C. 2018, ApJ, 861, L11
Kroupa, P. 2002, Science, 295, 82
Kroupa, P., & Tout, C. A. 1997, MNRAS, 287, 402
Kroupa, P., Tout, C. A., & Gilmore, G. 1990, MNRAS, 244, 76
Kroupa, P., Weidner, C., Pflamm-Altenburg, J., et al. 2013, in The Stellar and Sub-Stellar Initial Mass Function of Simple and Composite Populations, eds. T. D. Oswalt, & G. Gilmore (Dordrecht: Springer), 115
Langanke, K., & Martínez-Pinedo, G. 2000, Nucl. Phys. A, 673, 481
MacDonald, J., & Gizis, J. 2018, MNRAS, 480, 1711
Oda, T., Hino, M., Muto, K., Takahara, M., & Sato, K. 1994, At. Data Nucl. Data Tables, 56, 231
Paxton, B., Bildsten, L., Dotter, A., et al. 2011, ApJS, 192, 3
Paxton, B., Cantiello, M., Arras, P., et al. 2013, ApJS, 208, 4
Paxton, B., Marchant, P., Schwab, J., et al. 2015, ApJS, 220, 15
Paxton, B., Schwab, J., Bauer, E. B., et al. 2018, ApJS, 234, 34
Paxton, B., Smolec, R., Schwab, J., et al. 2019, ApJS, 243, 10
Potekhin, A. Y., & Chabrier, G. 2010, Contrib. Plasma Phys., 50, 82
Rogers, F. J., & Nayfonov, A. 2002, ApJ, 576, 1064
Saumon, D., Chabrier, G., & van Horn, H. M. 1995, ApJS, 99, 713
Timmes, F. X., & Swesty, F. D. 2000, ApJS, 126, 501
van Saders, J., & Pinsonneault, M. 2012, ApJ, 751, 98

A&A 661, C1 (2022)
https://doi.org/10.1051/0004-6361/202140536e

Astronomy & Astrophysics

A discontinuity in the luminosity–mass relation and fluctuations in the evolutionary tracks of low-mass and low-metallicity stars at the *Gaia* M-dwarf gap (*Corrigendum*)

Santana Mansfield[1] and Pavel Kroupa[1,2]

[1] Helmholtz-Institut für Strahlen- und Kernphysik (HISKP), Universität Bonn, Nußallee 14-16, 53115 Bonn, Germany
e-mail: smansfield@astro.uni-bonn.de
[2] Astronomical Institute, Faculty of Mathematics and Physics, Charles University in Prague, V Holešovičkách 2, 18000 Praha, Czech Republic

A&A, 650, 184 (2021), https://doi.org/10.1051/0004-6361/202140536

Key words. stars: low-mass – convection – Hertzsprung-Russell and C-M diagrams – stars: luminosity function, mass function – errata, addenda

The initial helium abundance used in the models was $Y = 0.28$ and not the stated metallicity-dependent value of $Y = 0.24 + 2Z$. The mass ranges for models that undergo the convective kissing instability with this initial helium abundance are: $0.33000\,M_\odot \leq m \leq 0.37100\,M_\odot$ for $Z = 0.01$, $0.34300\,M_\odot \leq m \leq 0.36900\,M_\odot$ for $Z = 0.001$, and $0.35600\,M_\odot \leq m \leq 0.39033\,M_\odot$ for $Z = 0.0001$. All conclusions remain accurate except that the instability here occurs at a higher mass range for lower metallicity.

Appendix D

The convective kissing instability in low-mass M-dwarf models: convective overshooting, semi-convection, luminosity functions, surface abundances and star cluster age dating

The paper **Mansfield and Kroupa, MNRAS, Volume 525, Issue 4, August 2023, DOI: 10.1093/mnras/stad2587** is provided below in its published form.

Monthly Notices of the ROYAL ASTRONOMICAL SOCIETY

MNRAS **525,** 6005–6014a (2023)
Advance Access publication 2023 August 31

https://doi.org/10.1093/mnras/stad2587

The convective kissing instability in low-mass M-dwarf models: convective overshooting, semi-convection, luminosity functions, surface abundances, and star cluster age dating

Santana Mansfield [1]★ and Pavel Kroupa [1,2]

[1] *Helmholtz-Institut für Strahlen- und Kernphysik (HISKP), Universität Bonn, Nußallee 14-16, D-53115 Bonn, Germany*
[2] *Astronomical Institute, Faculty of Mathematics and Physics, Charles University in Prague, V Holešovičkách 2, CZ-18000 Praha, Czech Republic*

Accepted 2023 August 23. Received 2023 August 23; in original form 2023 March 1

ABSTRACT

Low-mass models of M-dwarfs that undergo the convective kissing instability fluctuate in luminosity and temperature resulting in a gap in the main sequence that is observed in the *Gaia* data. During this instability, the models have repeated periods of full convection where the material is mixed throughout the model. Stellar evolution models are performed using MESA with varying amounts of convective overshooting and semi-convection. We find that the amplitude and intensity of the instability is reduced with increasing amounts of overshooting but sustained when semi-convection is present. This is reflected in the loops in the evolutionary tracks in the Hertzsprung–Russell diagram. The surface abundances of ^{1}H, ^{3}He, ^{4}He, ^{12}C, ^{14}N, and ^{16}O increase or decrease over time due to the convective boundary, however the relative abundance changes are very small and not likely observable. The mass and magnitude values from the models are assigned to a synthetic population of stars from the mass–magnitude relation to create colour–magnitude diagrams, which reproduce the M-dwarf gap as a large indent into the blueward edge of the main sequence (MS). This is featured in the luminosity function as a small peak and dip. The width of the MS decreases over time along with the difference in width between the MS at masses higher and lower than the instability. The parallel offset and relative angle between the upper and lower parts of the MS also change with time along with the mass–magnitude relation. Potential age-dating methods for single stars and stellar populations are described.

Key words: convection – instabilities – stars: abundances – Hertzsprung–Russell and C–M diagrams – stars: low-mass – stars: luminosity function, mass function.

1 INTRODUCTION

The M-dwarf gap is a recently discovered deficiency of stars at the lower end of the main sequence (MS) in the *Gaia* Data Release 2 (DR2) data (Jao et al. 2018), and the early *Gaia* Data Release 3 (eDR3) data set (Gaia Collaboration 2021). The drop in density of stars at this location is understood to be due to the stars undergoing the convective kissing instability at the boundary between less-massive stars that are fully convective and slightly higher-mass ones with radiative cores and convective envelopes (van Saders & Pinsonneault 2012; Baraffe & Chabrier 2018; Feiden, Skidmore & Jao 2021; Mansfield & Kroupa 2021; Boudreaux & Chaboyer 2023).

The phenomenon is a consequence of a delicate balance between temperature and luminosity in the criteria for convection which leads to a convective region growing at the centre of a star, and the unequal abundance of hydrogen and helium throughout the star due to the radiative region between the convective core region and convective envelope (illustrated in Fig. 1). According to the Schwarzschild criterion (Schwarzschild & Härm 1958), convection occurs in the stellar material when the radiative temperature gradient is larger than the adiabatic gradient, $\nabla_{\rm rad} > \nabla_{\rm ad}$, where

$$\nabla_{\rm rad} \propto \frac{L\kappa}{T^4}. \quad (1)$$

Simplified, if the term on the right side of equation (1) is small then the material is radiative, and if it is large then it is convective. Within the small mass range at which stars undergo the convective kissing instability, the luminosity and temperature compete to dominate equation (1) such that there is a persistent unbalancing of the equation, leading to the material at the very centre of the star repeatedly switching between a convective and radiative state. As described in Mansfield & Kroupa (2021), the pp-I chain is the primary thermonuclear process for M-dwarf stars

$$p + p \longrightarrow d + e^+ + \nu_e, \quad (2)$$

$$p + d \longrightarrow \; ^3He + \gamma, \quad (3)$$

$$^3He + \; ^3He \longrightarrow \; ^4He + 2p, \quad (4)$$

where equation (3) dominates. At around 0.35 M$_\odot$, a star begins on the zero-age main sequence (ZAMS) with sufficient central temperature (equation 1) to have a radiative core. Then with the onset of nuclear burning, which primarily produces ^{3}He in equation (3), enough luminosity is produced in the core that a convective

★ E-mail: smansfield@astro.uni-bonn.de

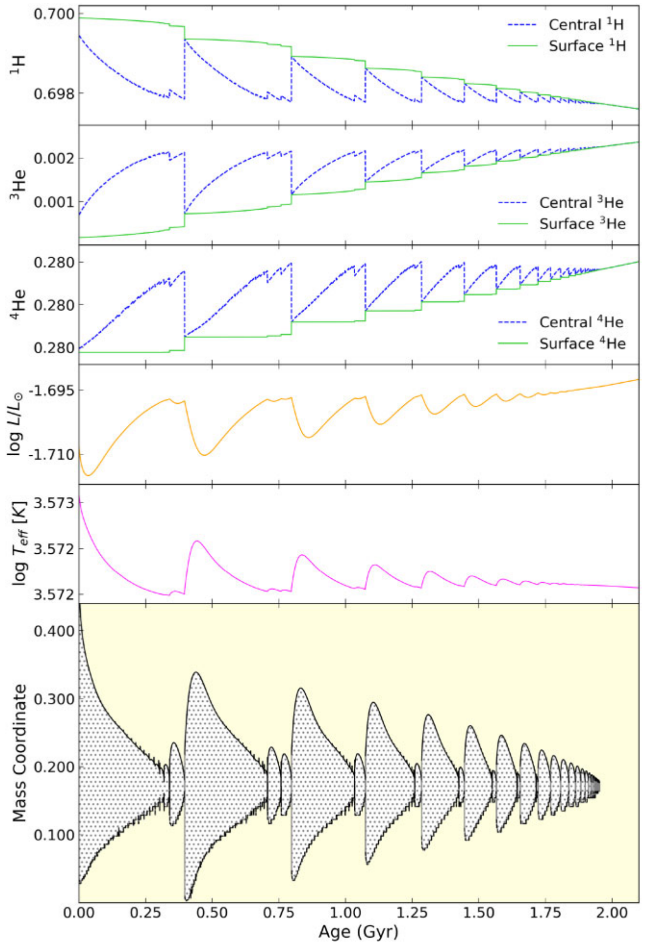

Figure 1. The top five plots give the surface and central abundances by mass fraction of hydrogen and helium, luminosity, and effective temperature over time for a 0.37 $M_\odot$, $Z = 0.02$ model without overshooting or semi-convection. The bottom plot shows the convective (solid yellow) and radiative (dotted grey) regions for the same model in which the convective kissing instability can be seen.

region forms within the radiative one (equation 1). The abundance of ^{3}He rises in the convective core but is unable to reach equilibrium abundance with the rest of the star due to the radiative region. As nuclear production proceeds, greater amounts of the material in the core region becomes convective until it finally merges with the convective envelope. The star undergoes a short ($\approx$1 Myr) period of full convection, resulting in a mixing of the stellar material. As ^{3}He and ^{4}He are pulled out of the core, the pp-I chain is disrupted and the nuclear productivity, and thus luminosity, subsides. A reduction in nuclear generation means the star contracts and the temperature increases. With the decrease in luminosity and rise in temperature, the material in the central region becomes radiative again according to equation (1). Once the central temperature becomes high enough to produce sufficient ^{3}He, which is now no longer being transported out towards the surface due to convection, equation (4) can resume and the pp-I chain is restored. Then, the luminosity is sufficient again to once more begin growing an inner convective region as per equation (1). The fluctuations in luminosity and temperature result in loops in the Hertzsprung–Russell (HR) diagram of stellar evolution models (Mansfield & Kroupa 2021), and is understood to produce the M-dwarf gap.

The process of the convective kissing instability occurs repeatedly over time but is also dampened with time due to the equilibrium abundances. Each time there is a merging of core and envelope, the helium abundance drops in the centre and rises at the surface, as helium becomes equally distributed throughout the star. When the nuclear production resumes, the central helium abundance rises but only to a certain 'critical' amount before falling again at the next merging event. At this time, because the surface abundance of helium is higher than that of the previous merging event, the decrease of central helium abundance is less before it reaches equilibrium. And so with each moment of full convection, the time it takes to reach equilibrium abundance becomes increasingly less, and correspondingly the time at which the nuclear production is diminished is lower. Accordingly then, the amount by which the luminosity drops is also reduced, resulting in a smaller region of the stellar material becoming radiative. This is what we see in Fig. 1 with the radiative region becoming smaller over time. Once the surface abundance reaches the critical central abundance, true equilibrium is attained and the pp-I chain can finally run without disruption. Now that luminosity is steadily produced, it is high enough (equation 1) to retain the stellar material in a prevailing fully convective state.

Whilst it is now understood that the convective kissing instability is a possible cause of the M-dwarf gap, some questions about the nature of the instability remain, namely how certain convective and mixing processes may alter and affect the intensity and duration of the convective kissing instability due to the blurring of boundaries between convective and radiative regions and the added mixing of material towards equilibrium abundance. These processes are primarily convective overshooting and semi-convection. The effects of these processes will be investigated in this publication along with the consequences of the instability on the surface abundances and the stellar luminosity function.

Convective overshooting occurs when the material in a convective cell has a non-zero velocity when it reaches the boundary of the cell and so continues to move a small distance past it, mixing the material into the radiative region. The extent of overshooting is mass dependent (Claret 2007) and so for low-mass stars only a small amount of overshooting will be present. Yet even at these small numbers, the ability for material to be mixed across the boundary will alter the distribution of helium abundance and likewise the amplitude of the convective kissing instability.

Semi-convection is a diffusive process in a material that occurs in a region that is unstable to convection as per the Schwarzschild criterion, but stable according to the Ledoux criterion (Ledoux 1947). This happens when:

$$\nabla_{\rm ad} < \nabla_{\rm rad} < \nabla_L, \qquad (5)$$

with the Ledoux temperature gradient:

$$\nabla_L = \nabla_{\rm ad} + \frac{\varphi}{\delta}\nabla_\mu, \qquad (6)$$

and

$$\varphi = \left(\frac{\delta \ln \rho}{\delta \ln \mu}\right)_{P,T}, \delta = \left(\frac{\delta \ln \rho}{\delta \ln T}\right)_{P,\mu}, \nabla_\mu = \left(\frac{\delta \ln \mu}{\delta \ln P}\right), \qquad (7)$$

where ρ is the density, μ is the mean molecular weight, P is the pressure, and T is the temperature. When a non-homogeneous composition of material remains after a convective region shrinks, a discontinuity of density and molecular weight results in a slow mixing of material called semi-convection. This process would happen in M-dwarf stars undergoing the convective kissing instability due to convective regions repeatedly growing and shrinking.

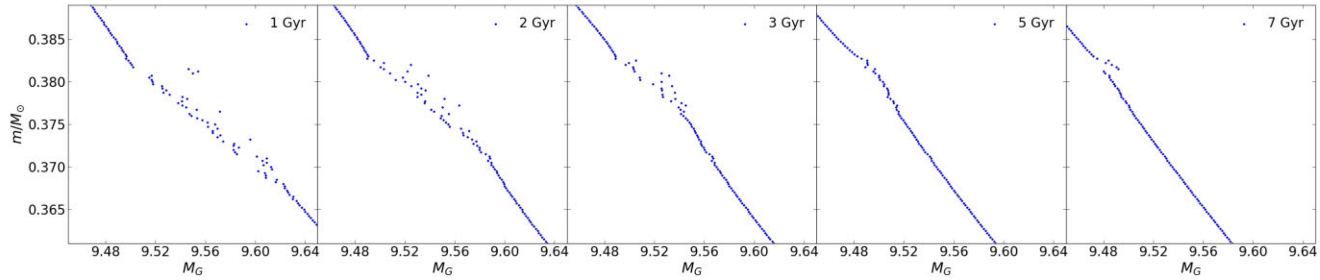

Figure 2. Mass–magnitude relation in the photometric G band for models with $Z = 0.02$, without overshooting or semi-convection, at five time intervals of 1, 2, 3, 5, and 7 Gyr. The fluctuations in magnitude caused by the convective kissing instability create a discontinuity in the relation.

This work will also look at the changes in surface abundances of the models, as the abundance of ^{3}He is seen to increase each time the core and envelope merges (Mansfield & Kroupa 2021). Until now only the effects of the instability on ^{3}He have been previously investigated. We will look to see if the convective kissing instability influences the surface abundances of other light elements, particularly ^{1}H, ^{12}C, and ^{16}O as these affect the spectra of M-dwarfs. The cool temperatures of M-dwarf atmospheres allows for the formation of molecules and dust particles, which leads to considerable molecular absorption in their spectra (Allard & Hauschildt 1995). The main molecules responsible for the opacity of M-dwarf atmospheres are those which contain either C, O or H, namely TiO and VO that dominates the optical spectrum (Allard et al. 1997), and H_2O and CO that prevails in the infrared (Rajpurohit, et al. 2013; Veyette et al. 2016). Changes in the surface abundances may result in alterations of the atmosphere properties. For example, a reduction of carbon and oxygen would lead to less TiO, CO, and H_2O forming, and thus a different configuration of the surface material for stars of lower masses. This would then affect the properties and structure of M-dwarf atmospheres, which are sensitive to these abundances. For example, Allard et al. (1997) found that a reduction in H_2O and TiO in models results in a cooling of the atmosphere.

Additionally we will explore the consequence of the convective kissing instability on the stellar luminosity function (LF), which is given by:

$$\phi_{\mathrm{p}} = \frac{\mathrm{d}N}{\mathrm{d}M_{\mathrm{p}}} = -\frac{\mathrm{d}N}{\mathrm{d}m}\frac{\mathrm{d}m}{\mathrm{d}M_{\mathrm{p}}} = -\xi\frac{\mathrm{d}m}{\mathrm{d}M_{\mathrm{p}}}, \tag{8}$$

where N is the number of stars per cubic parsec, M_{p} is the absolute magnitude in a photometric pass band p, m is the stellar mass, and $\xi(m)\mathrm{d}m$ is the number of stars per cubic parsec with masses between m and $m + \mathrm{d}m$. Specific features are present in the stellar LF which are due to the internal material of stars at certain masses. For solar metallicity stars, the LF has a minimum at $M_{\mathrm{V}} \approx 7$ called the Wielen dip (Wielen 1974), due to H^- becoming a more important source of opacity for decreasing mass. Once it becomes the primary source, there is a flattening of the luminosity–mass relation and the dip in the luminosity function (Kroupa, Tout & Gilmore 1990). The stellar LF also has a maximum at $M_{\mathrm{V}} \approx 11$–$12$ due to the onset of H_2 formation in a thin outer shell (Kroupa et al. 1990). For lower metallicities, these features become shifted to brighter magnitudes (Kroupa & Tout 1997). Upon discovering the M-dwarf gap, Jao et al. (2018) predict that there should be a dip in the LF at around $M_{\mathrm{V}} \approx 10.5$–$11.5$ for solar metallicities.

The fluctuations in luminosity during the convective kissing instability causes a discontinuity in the luminosity–mass relation (Mansfield & Kroupa 2021). The LF depends on the slope of the luminosity–mass relation, and as such, the discontinuity means that the relation is indifferentiable and thus the slope, $\mathrm{d}m/\mathrm{d}M_{\mathrm{p}}$, cannot be calculated at the mass range of the convective kissing instability. In this work, we will use an alternative method to determine the LF by creating a synthetic population of stars with properties that are assigned using the results from stellar evolution models. As the LF represents the number of stars per magnitude bin, we can recreate the LF from a count of the number of stars within the magnitude bins. We also consider the mass–magnitude relation and its derivative, as well as potential age-dating methods for single stars and populations such as star clusters.

This investigation uses stellar evolution models which are detailed in Section 2. The set-up for a synthetic population of stars using the results of these models is described in Section 3. The results are presented in Section 4, a discussion is given in Section 5, followed by a summary in Section 6.

2 STELLAR MODELS

The 1D stellar evolution code Modules for Experiments in Stellar Astrophysics (MESA, version r22.11.1) is utilized (Paxton et al. 2011, 2013, 2015, 2018, 2019). The equations of state (EOSs) applied in MESA are a combination of the SCVH (Saumon, Chabrier & van Horn 1995), HELM (Timmes & Swesty 2000), OPAL (Rogers & Nayfonov 2002), FreeEOS (Irwin 2004), and PC (Potekhin & Chabrier 2010) EOSs. Molecules and dust grains are able to form in the low temperatures of M-dwarf atmospheres and the opacity tables for these temperatures are from Ferguson et al. (2005). The nuclear reaction rates are from Cyburt et al. (2010), with additional weak reaction rates (Fuller, Fowler & Newman 1985; Oda et al. 1994; Langanke & Martínez-Pinedo 2000). The opacity tables are those given by OPAL (Iglesias & Rogers 1993; Iglesias & Rogers 1996) and Grevesse & Sauval (1998), as well as electron conduction opacities from Cassisi et al. (2007). Thermal neutrino loss rates are from Itoh et al. (1996). Screening was included using the prescription of Chugunov, Dewitt & Yakovlev (2007). For the outer boundary conditions of M-dwarfs, the Hauschildt, Allard & Baron (1999) model atmosphere tables were used, taken at $\tau = 100$ (Chabrier & Baraffe 1997; Paxton et al. 2011). The initial helium abundance is $Y = 0.24 + 2Z$ by mass fraction. Convective mixing is described using mixing length theory (mixing length parameter $\alpha_{\mathrm{MLT}} = 2$), with the convective premixing scheme (CPM, Paxton et al. 2019) which iterates over each cell and instantaneously applies mixing to the cells which are found to be convective (Ostrowski et al. 2020). Sets of models are calculated at solar metallicity ($Z = 0.020$) and a lower metallicity of $Z = 0.001$ to represent a globular cluster. They begin at the ZAMS and run until 9 Gyr. A maximum time step of 2×10^5 yr is used in order to slow the code down during the MS where the convective kissing instability occurs. Similarly to that described

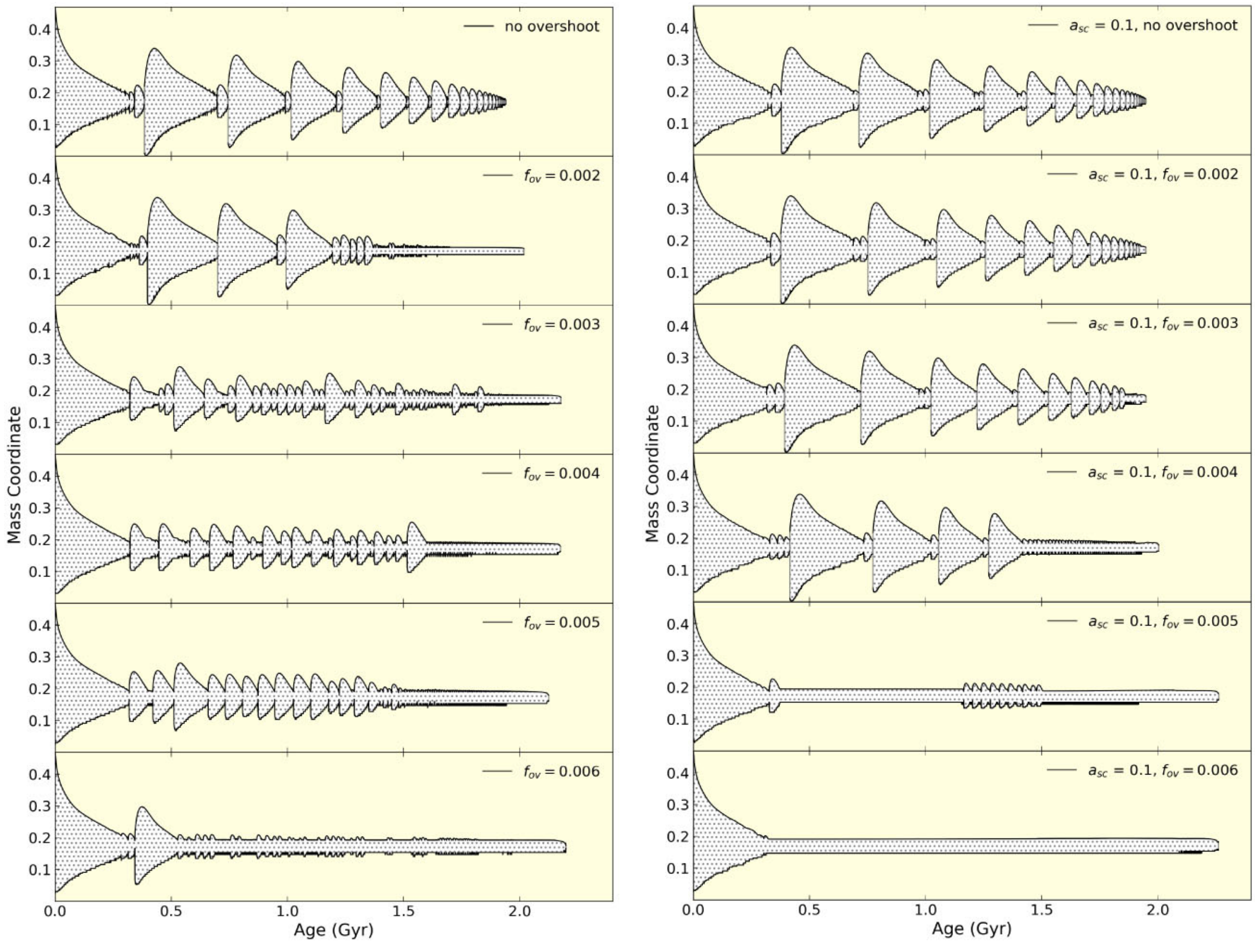

Figure 3. Mass coordinate of the convective (yellow solid) and radiative (grey dotted) regions plotted over time for a 0.37 $M_\odot$, $Z = 0.02$ model. The models on the left used the Schwarzschild criterion for convection with no semi-convection but increasing overshooting parameter $f_{\rm ov}$, and the models on the right used the Ledoux criterion with semi-convection parameter $\alpha_{\rm sc} = 0.1$ and also increasing $f_{\rm ov}$.

in Mansfield & Kroupa (2021), this time step is small enough to see the instability with sufficient resolution, but large enough that the computational time is reasonable. Binary systems were considered but not applied here for simplicity. The conclusions drawn should be similar for binary systems as the convective kissing instability affects the stars individually.

Convective overshooting is administered by an exponentially decaying, time-dependent diffusive processes past the convective boundary given by

$$D_{\rm ov} = D_0 \exp\left(-\frac{2r}{f_{\rm ov} H_{\rm p}}\right), \tag{9}$$

where D_0 is the diffusion coefficient inside the boundary, r is the radial distance past the boundary, $f_{\rm ov}$ is the free overshooting parameter, and $H_{\rm p}$ is the pressure scale height (Herwig 2000; Paxton et al. 2011). The amount of convective core overshooting is strongly dependent on mass for $m \lesssim 2$ $M_\odot$ with $f_{\rm ov}$ increasing sharply up to $f_{\rm ov} \approx 0.0160$ where it stays constant for masses higher (see Claret 2007, fig. 10). As such, M-dwarf stars of this mass range will have a very small amount of overshooting. We used $0.0005 \le f_{\rm ov} \le 0.0060$ in this work to see the effect on the models, but note that it is likely that $f_{\rm ov} \ll 0.0050$.

For semi-convection to be implemented, the Ledoux criterion for convection is used (equations 5–7). Mixing in regions satisfying equation (5) is via a time-dependent diffusive process with diffusion coefficient

$$D_{\rm sc} = \alpha_{\rm sc}\left(\frac{\kappa_{\rm r}}{6 c_p \rho}\right)\frac{\nabla_{\rm rad} - \nabla_{\rm ad}}{\nabla_L - \nabla_{\rm rad}}, \tag{10}$$

where $\kappa_{\rm r}$ is the radiative conductivity and c_p is the specific heat at constant pressure. The values applied in this work for the dimensionless semi-convection parameter $\alpha_{\rm sc}$ are 0.1 and 1.

The models do not include thermohaline mixing as it is not an important mixing process for M-dwarfs on the MS. This is because for thermohaline mixing to occur, the mean molecular weight decreases inwards, which can occur in low-mass stars after the first dredge up (Charbonnel & Zahn 2007; Cantiello & Langer 2010), but is not present during the early MS at which the convective kissing instability occurs.

3 POPULATION SYNTHESIS

To construct colour–magnitude diagrams (CMDs) and the luminosity function, three sets of 100 000 stars are given masses ranging from 0.08 $M_\odot$ to 0.60 $M_\odot$ according to the canonical initial mass function, $\xi(m) \propto m^{-\alpha}$, with $\alpha = 1.3$ for $m \le 0.50\,M_\odot$ and $\alpha = 2.3$ for $m > 0.50\,M_\odot$ (Kroupa 2001; Kroupa et al. 2013). These are then assigned an age and corresponding magnitude values due to the mass–magnitude relation determined from the MESA models which is

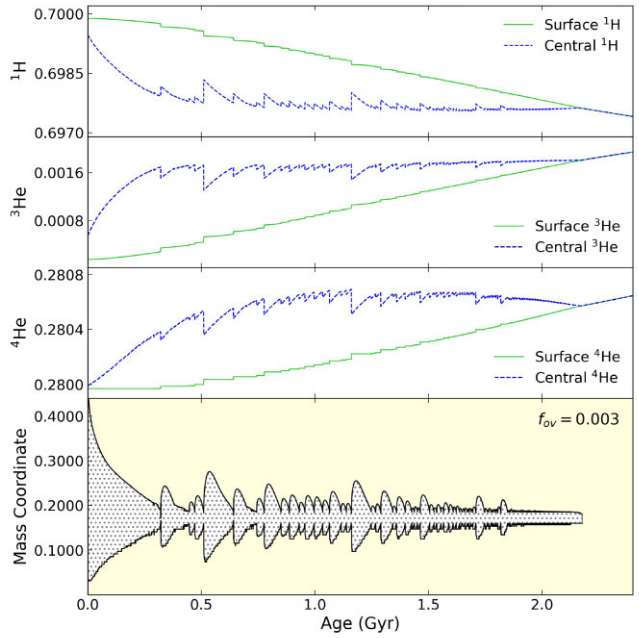

Figure 4. Central and surface abundances by mass fraction for the 0.37 $M_\odot$, $Z = 0.02$ model with overshooting parameter $f_{\rm ov} = 0.003$, along with the mass coordinate of the radiative (grey dotted) and convective (yellow solid) regions over time.

shown in Fig. 2, where there is a discontinuity due to the fluctuations in luminosity. The slope of the mass–magnitude relation differs at masses lower than and larger than the discontinuity, and changes over time. Thus in order to assign magnitude values to masses higher and lower than the discontinuity, the equation of the line is determined at each point in time. For the masses within the instability range, the magnitude is taken directly from the corresponding MESA models. This method is applied because the slope, dm/dM_p, within the instability range cannot be determined, as the relation is indifferentiable across the discontinuity.

Following Paxton et al. (2018), the absolute magnitude of a star in a photometric pass band p is determined by

$$M_p = M_{\rm bol} - BC_p, \tag{11}$$

with the absolute bolometric magnitude

$$M_{\rm bol} = -2.5 \log_{10}(L/L_\odot) + M_{\rm bol,\odot}, \tag{12}$$

where $M_{\rm bol,\odot} = 4.74$ is the absolute bolometric magnitude of the Sun. The bolometric corrections BC_p are taken from a pre-processed set of tables provided within MESA that are described in Paxton et al. (2018) as computed from atmosphere models, and defined as functions of the stellar photosphere including the effective temperature $T_{\rm eff}$ (Code et al. 1976; Houdashelt, Bell & Sweigart 2000). The conversion to the *Gaia G*-band magnitudes follows Jordi, C. et al. (2010).

The first set has a metallicity of $Z = 0.020$ to represent stars in the local neighbourhood and the second set uses a metallicity of $Z = 0.001$ to represent stars in a globular cluster. Both of these sets have no overshooting or semi-convection applied. The third set is calculated using semi-convection with an efficiency of $\alpha_{\rm sc} = 0.1$ and an overshooting parameter of $f_{\rm ov} = 0.006$, with a metallicity of $Z = 0.020$. All other parameters of the sets remain the same.

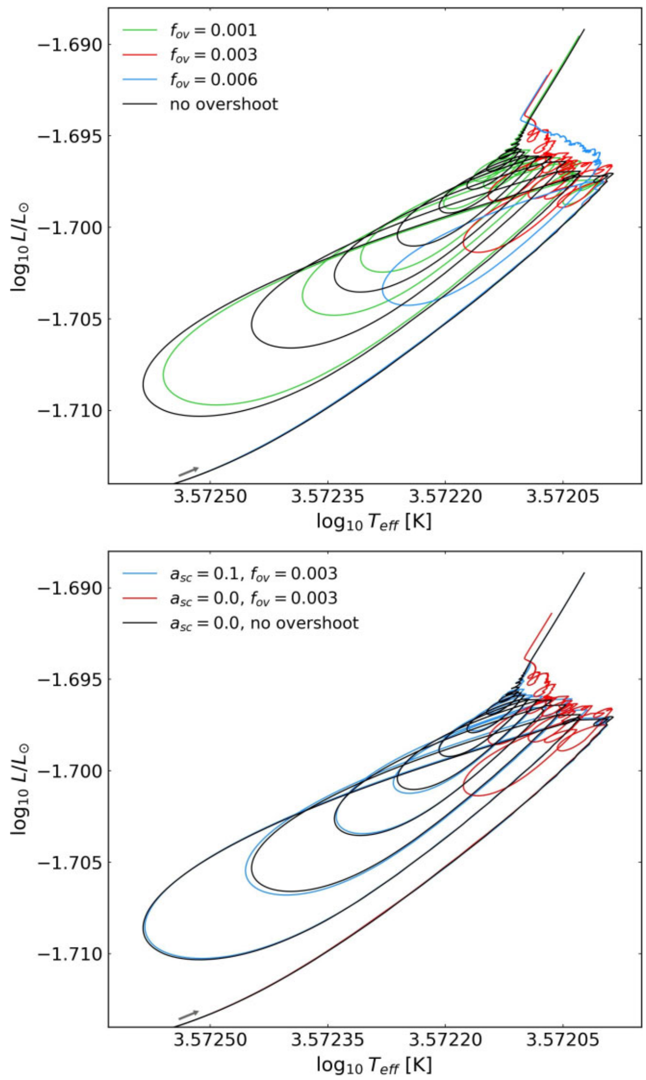

Figure 5. HR diagram showing the evolutionary track of the 0.37 $M_\odot$, $Z = 0.02$ model with varying amounts of overshooting (*top*), where increasing overshooting diminishes the loops. The models evolve from the lower left as indicated by the arrow. The bottom plot shows the tracks with no overshooting or semi-convection (black), with overshooting added (red) and with both overshooting and semi-convection (blue) which sustains the loops.

4 RESULTS

Models with masses 0.3440–0.3825 $M_\odot$ undergo the convective kissing instability for $Z = 0.020$.

4.1 Convective overshooting and semi-convection

Fig. 3 illustrates the effects of overshooting up to $f_{\rm ov} = 0.006$ and semi-convection with efficiency $\alpha_{\rm sc} = 0.1$ for a 0.37 $M_\odot$ model. As $f_{\rm ov}$ increases, the amplitude of the convective kissing instability is lessened, and there are fewer mergers of the core and envelope into a fully convective state. Instead, the core and envelope come close enough together that the remaining distance is small enough for material to cross the radiative region due to overshooting. As the abundance of helium is able to gradually increase throughout the model by passing through the radiative region (as seen by the steady increase of surface ^{3}He abundance in Fig. 4), there is no longer the dampening of the convective kissing instability over time that was

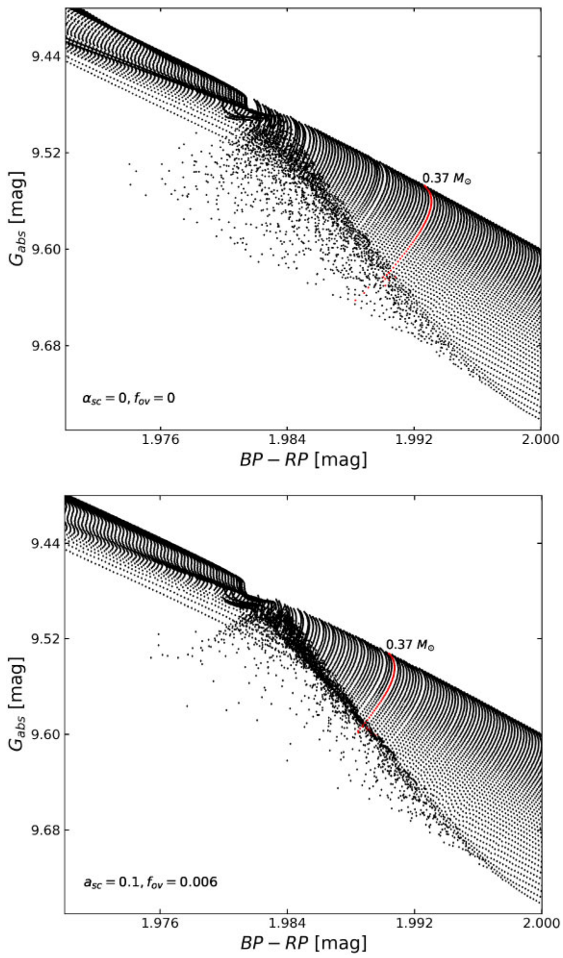

Figure 6. Colour–magnitude diagram showing the main sequence for $Z = 0.02$ across all ages, for no overshooting or semi-convection (*top*), and for $a_{\rm sc} = 0.1$ and $f_{\rm ov} = 0.006$ (*bottom*). The convective kissing instability causes an indent into the blueward edge of the MS. This instability region is more sparsely populated for models with high amounts of overshooting, however it is still present. Marked in red is the 0.37 $M_\odot$ model.

seen when no overshooting is present (Fig. 1). The results here are shown up to $f_{\rm ov} = 0.006$ however we again note that real M-dwarfs are likely to have a low amount of overshooting (Claret 2007).

Fig. 5 shows that the loops in the evolutionary tracks of the models in the HR diagrams become much smaller for an increasing amount of overshooting. Whilst overshooting reduces the convective instability, adding semi-convection to the models can retain it. For example, the $f_{\rm ov} = 0.003$ model on the left hand side of Fig. 3 does not fully merge at any point, yet when semi-convection is present, the results become comparable to the model without any overshooting. The radiative region gradually shrinks until the model is fully convective, then a large portion of the material becomes radiative again. With semi-convection, the loops in the HR diagrams are prominent once more, as seen in Fig. 5. The same is true for a more efficient semi-convection with parameter $\alpha_{\rm sc} = 1$ which is not shown here.

A comparison of the colour–magnitude diagrams created by the population synthesis for models with no semi-convection or overshooting and for models with $a_{\rm sc} = 0.1$ and $f_{\rm ov} = 0.006$ is given in Fig. 6. The indent into the blueward edge of the MS represents the instability region, where the luminosity and temperature of the models fluctuate (as indicated by the loops in Fig. 5). This instability

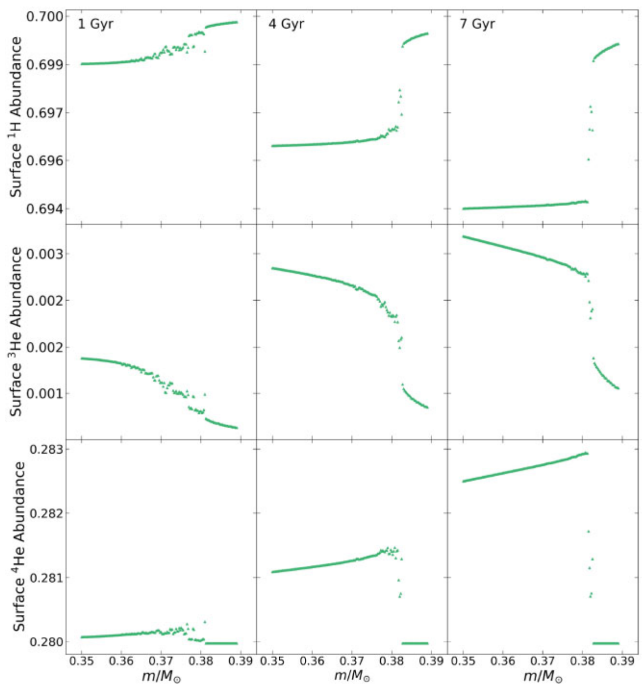

Figure 7. Surface abundances by mass fraction of ^{1}H, ^{3}He, and ^{4}He, taken at time intervals of 1, 4, and 7 Gyr, plotted against the mass range for $Z = 0.02$, with no overshooting or semi-convection applied.

region is more sparsely populated for the models with high amounts of overshooting, as expected, however it is still distinguishable, meaning that if M-dwarfs were to have high amounts of overshooting, the M-dwarf gap would still be present in the observational CMD. The 0.37 $M_\odot$ model is marked in Fig. 6 which shows a reduction (from top panel to bottom panel) in the area of the instability region over which the model proceeds.

4.2 Surface abundances

An illustration of the changes to the central and surface ^{1}H, ^{3}He, and ^{4}He abundances over time is given in Fig. 1. For a model without overshooting, the rise and drops in the abundances occur when the model becomes fully convective and mixes the stellar material throughout the model. When overshooting is applied (Fig. 4) the material is mixed without the model being fully convective. In either case, the surface abundance of helium continuously rises (and hydrogen decreases) until it is equal to the central abundance.

If we view the surface abundances across the mass range, we can see the difference between the models which are fully convective and those that are not. Fig. 7 shows the surface abundances of ^{1}H, ^{3}He, and ^{4}He by mass fraction plotted against the mass range, given at time intervals of 1, 4, and 7 Gyr. As the models age, a drop forms within the model sets, which represents the convective boundary. The models with masses higher than the drop are those with radiative cores and convective envelopes, and as such the surface abundances of these do not vary significantly over time. The models with masses lower than the drop are fully convective, and so the surface abundances of ^{3}He and ^{4}He steadily increase with time as these isotopes that are being produced in the core are carried outward to the surface by convection. Conversely, the surface abundance of ^{1}H decreases over time for the fully convective models, as ^{1}H is mixed downward re-fuelling the core.

The drop illustrated in Fig. 7 moves to higher masses with time. This was seen in Mansfield & Kroupa (2021) as the lower mass models undergo the instability at an earlier point in their lifetimes than the higher mass models, and once the instability ceases, the models remain fully convective. This drop would still be present in the absence of the convective kissing instability, however it would likely be a sudden discontinuity which would not change with time.

The average relative changes in surface abundance by the end of the model lifetime is approximately a 1.0 per cent decrease for ^{1}H and a 1.2 per cent increase of ^{4}He and as such are unlikely to be detected over observational noise. The surface abundance of ^{3}He has quadrupled although it still remains a small fraction of the overall stellar material.

Similarly to hydrogen and helium, once the lower mass models have undergone the convective kissing instability and remain fully convective, the surface ^{12}C and ^{16}O values decrease, and ^{14}N increases, however these abundances change by less than 0.2 per cent during the total model evolution. As the differences are so small, they are not shown here.

4.3 The width of the MS: the solar neighbourhood

As seen in Section 4.1, the convective kissing instability presents as an indent into the blueward edge of the MS (Fig. 6) in the colour–magnitude diagram from our population synthesis. The width of the MS varies significantly across this region. Fig. 8 shows the CMD at increasing population age, representing composite Galactic-field populations, where the overall width of the MS decreases over time. Additionally, the width of the MS is larger for stars with masses lower than the instability than for masses higher, and with time the difference between these two widths also becomes smaller.

4.4 Age dating: star clusters

Fig. 9 gives a set of CMDs for $Z = 0.020$ and a lower metallicity of $Z = 0.001$ with stars of the same age, representing a solar-neighbourhood open cluster and a Galactic halo globular cluster, respectively. Although the absence of an age spread does not show the development in MS width in this case, we can still see the change in parallel offset between the upper and lower parts of the MS, as well as the large kink due to the convective kissing instability. The offsets Ψ_i measured at four points ($BP - RP = 1.972$, 1.978, 1.992, and 1.998 for $Z = 0.020$, and $BP - RP = 1.506$, 1.510, 1.520, and 1.524 for $Z = 0.001$) are quantified in Tables 1 and 2 and illustrated in Fig. 10, along with the relative angle from vertical, $\theta = \theta_1 - \theta_2$, between the upper and lower MS. For $Z = 0.020$, the directions of the MS at masses higher (upper MS) and lower (lower MS) than the convective kissing instability are considerably divergent by 2 Gyr and then become more in line with each other as the models evolve, except for at 4 Gyr when the sign of the relative angle becomes reversed. Similarly for $Z = 0.001$, the MS is roughly parallel at the beginning of the evolution, the upper and lower parts of the MS diverge by 2 Gyr, then become increasingly more aligned until 7 Gyr when they are nearly parallel again. By measuring the parallel offset and the relative angle between the upper and lower MS, the age of a star cluster could be estimated.

4.5 Age dating: single M-dwarf stars

A method for potential age dating of an M-dwarf star with known distance, metallicity, and mass is by the star's position in the CMD, if the mass is lower than the convective kissing instability. This is illustrated in Fig. 11 where the time-dependent location in the CMD of a single mass model is given. As the model evolves, it moves redward and towards higher luminosities, but only up to a point, meaning that this method could only be used to estimate the age of a star up until around 7 Gyr.

4.6 Mass–magnitude relation and the luminosity function

Fig. 12 shows the mass–magnitude relation and its derivative, dm/dM_V, with the convective kissing instability shown in the inset plot. The gap in the peak of the derivative at $M_V = 10.20$ is due to the discontinuity being indifferentiable. Just as the width of the MS in the CMD is wider for models with masses below the instability when viewed over time, the mass–magnitude relation and its derivative also exhibits a time dependence for these masses.

Fig. 13 shows the stellar luminosity function in different wavebands. At the magnitude where the convective kissing instability occurs, there is a small peak and dip in the number of stars at $M_V = 10.20$ and $M_K = 6.63$. The inset plots give a closer view of this feature. The dip corresponds to the indent into the blueward edge of the MS, and the small peak that is brighter in magnitude indicates a slight over-density which can be seen in Fig. 6 as the wave-like overlapping of models just above the gap. This peak is likely to correlate to the same slight over-abundance of stars seen close to the gap in observations (Jao & Feiden 2020).

5 DISCUSSION

The convective kissing instability is reduced with increasing amounts of overshooting. The loops in the evolutionary tracks of the models in the HR diagram also become suppressed for increasing overshooting. This brings into question whether M-dwarf stars undergoing the convective kissing instability with overshooting can still be responsible for the M-dwarf gap. The CMD created from the population synthesis (Fig. 6) using a relatively high amount of overshooting indicates that there are fewer models within the instability region, yet it does remain. If the amount of overshooting is low, and semi-convection is also present, then the loops in the HR diagram are sustained (Fig. 5). Therefore in order to reproduce sufficient fluctuations in luminosity and temperature to cause the observed M-dwarf gap, stars at this mass range may have overshooting, with less overshooting being preferable (we suggest an upper limit of $f_{\mathrm{ov,max}} = 0.004$), and semi-convection should also be present.

The indent that lies in the blueward edge of the MS is more pronounced for the younger models, similar to the larger kinks found in lower-age isochrones given by Baraffe & Chabrier 2018 (their fig. 6). This is due to the models settling into a fully convective state after several gigayear (Mansfield & Kroupa 2021) and the cessation of the fluctuations in luminosity and temperature. From our models we see that there is a reduction in the width of the MS over time for composite Galactic-field populations, and a difference in width of the MS at masses lower than the instability compared with masses higher (Figs 8). For star clusters, which can be assumed to have members of all the same age, the parallel offset and relative angle between the upper and lower MS changes with time (Figs 9 and 10). This is detected in a recently observed CMD of the Hyades cluster, which finds a difference in MS direction for stars higher and lower than $0.35\,\mathrm{M}_\odot$ (for a super-solar metallicity of [Fe/H] = +0.25, Brandner, Calissendorff & Kopytova 2022, their fig. 1). These findings then have the potential to be used as an age estimator of stellar populations. The width of the MS may also be used to estimate the age of single M-dwarf stars if the precise metallicity and mass are known (Fig. 11).

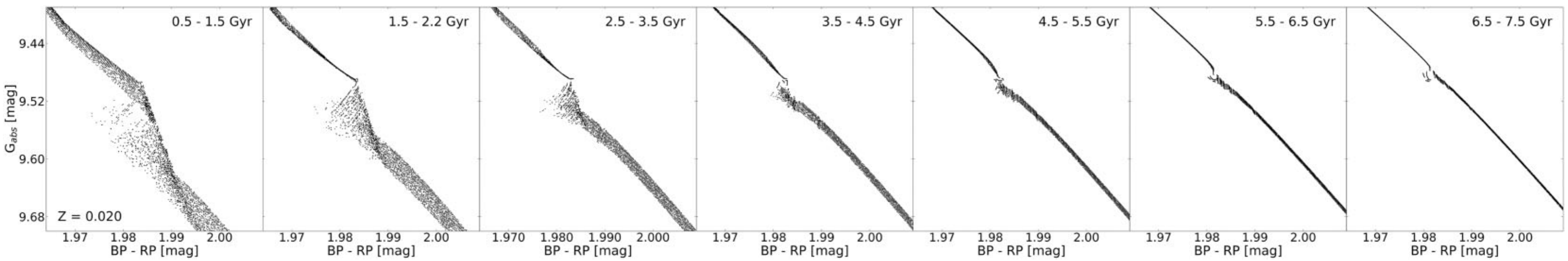

Figure 8. Composite Galactic-field populations grouped into age bins spanning 1 Gyr at increasing population age, showing that the width of the MS decreases with time. Here no overshooting or semi-convection is used.

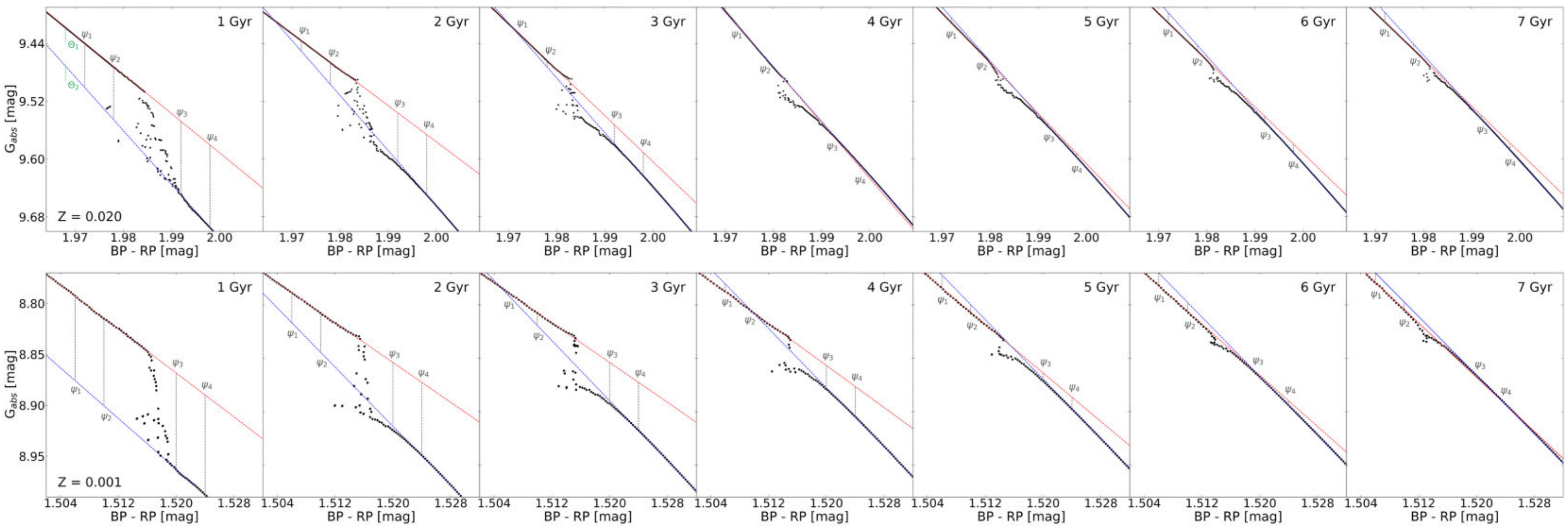

Figure 9. A set of solar metallicity stars (*top*) and with $Z = 0.001$ (*bottom*) are given where the stars have the same age and no overshooting or semi-convection is used. The changes in width can no longer be seen without any age distribution, but the parallel offset of the MS and the kink due to the convective kissing instability remain. The offsets, Ψ_i, and the relative angle, $\theta = \theta_1 - \theta_2$, of the upper and lower parts of the MS are detailed in Fig. 10.

Table 1. The parallel offsets and relative angle between the upper and lower parts of the MS as shown in Fig. 9, for $Z = 0.02$.

Age (Gyr)	Ψ_1 (M_G)	Ψ_2 (M_G)	Ψ_3 (M_G)	Ψ_4 (M_G)	θ (°)
1	0.062	0.073	0.102	0.113	2.551
2	0.013	0.029	0.067	0.083	4.155
3	0.001	0.007	0.026	0.031	1.042
4	0.000	– 0.001	– 0.002	– 0.003	– 0.094
5	– 0.006	– 0.003	0.002	0.005	0.094
6	– 0.013	– 0.007	0.006	0.115	1.029
7	– 0.014	– 0.007	0.005	0.010	0.992

Table 2. Same as Table 1 but for $Z = 0.001$.

Age (Gyr)	Ψ_1 (M_G)	Ψ_2 (M_G)	Ψ_3 (M_G)	Ψ_4 (M_G)	θ (°)
1	0.081	0.085	0.092	0.099	0.960
2	0.029	0.037	0.059	0.068	5.181
3	0.002	0.011	0.036	0.045	4.437
4	– 0.008	0.000	0.021	0.028	3.403
5	– 0.013	– 0.008	0.007	0.010	0.943
6	– 0.011	– 0.010	0.000	0.005	1.146
7	– 0.011	– 0.008	– 0.002	0.000	0.775

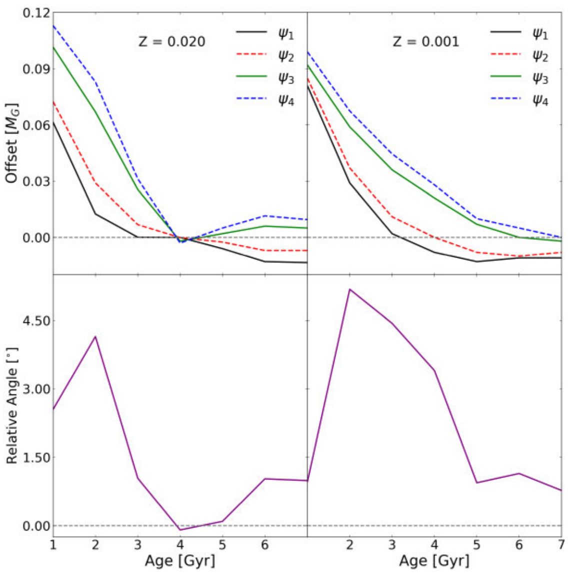

Figure 10. The offsets Ψ_i (*top*), and the relative angle (*bottom*) between the upper and lower parts of the MS shown in Fig. 9.

The stellar luminosity function shows a small feature located at around $M_\mathrm{V} \approx 10.20$ (Fig. 13), which is at a slightly brighter magnitude than the prediction by Jao et al. (2018) of finding a gap in the stellar luminosity function at around $M_\mathrm{V} \approx 10.5$–$11.5$. A dip in the luminosity function at $M_\mathrm{K} = 6.71$ is also predicted by MacDonald & Gizis (2018), which is in agreement to the dip seen in Fig. 13 at $M_\mathrm{K} \approx 6.63$. MacDonald & Gizis 2018 propose an alternative theory to explain the M-dwarf gap in which convective mixing is treated as a diffusive process, resulting in their models undergoing a single merger event rather than the convective kissing instability. However, they report that the central ^{3}He abundance is increased during this merger from the mixing of ^{3}He from the envelope, yet we find the opposite relation in our models. The central ^{3}He abundance is

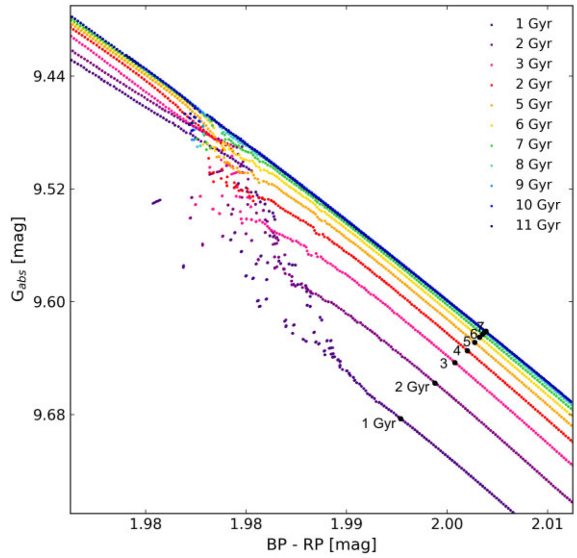

Figure 11. A CMD showing the MS of M-dwarf stars at different snapshots in time, without overshooting or semi-convection applied and a metallicity of $Z = 0.02$. Marked on the diagram is a single model at different ages. If the position in the CMD of a star can be accurately known, along with its metallicity, then the age of the star could be determined, until around 7 Gyr.

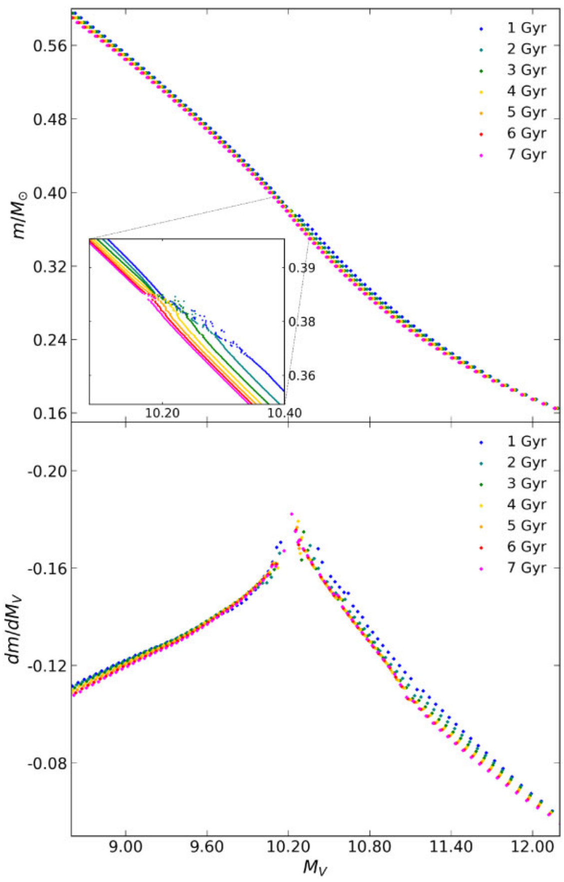

Figure 12. Mass–M_V relation (*top*) and its derivative (*bottom*) for solar metallicity and no overshooting or semi-convection applied, showing a slight dependence in time for the models with masses lower than the convective kissing instability. Inset is a zoomed in region of the instability, showing the discontinuity.

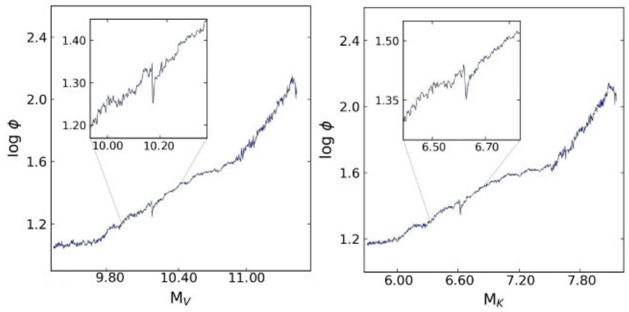

Figure 13. Stellar luminosity function in the *V* and *K* wavebands for $Z = 0.02$ and all ages and no overshooting or semi-convection applied, showing a peak and dip due to the convective kissing instability.

reduced when the model becomes fully convective and material is mixed throughout the star (Fig. 1).

The convective kissing instability effects the surface abundance values of the elements ^{1}H, ^{3}He, ^{4}He, ^{12}C, ^{14}N, and ^{16}O through the core and envelope merger events when the models are fully convective and material is transported throughout the model. The instability effects higher mass models over time and the lower masses settle into a fully convective state. This can be seen as the relative changes in abundance values move to higher masses over time. If the abundance values of a star could be measured and the metallicity is also known, this could be used to estimate the age and mass of the star. However, the relative changes for all elements and isotopes studied are very small and likely will not be larger than observational noise, as well as being within the normal variations of abundances due to stars being formed at different locations and times. Thus, whilst interesting from the evolutionary model standpoint, the predicted changes in surface abundances will be challenging to detect in observations.

6 SUMMARY

The amplitude and intensity of the convective kissing instability is reduced with increasing amounts of overshooting but sustained when semi-convection is also present. This effect is seen to modify the loops in the evolutionary tracks in the HR diagram.

The surface abundance values of M-dwarf models are altered by moments of full convection as well as once the models settle into a fully convective state. However the relative changes are small and unlikely to be detected significantly enough to be separated from observational noise or natural variation.

The merging of the convective core and convective envelope produces a discontinuity in the mass–magnitude relation and we are able to take the magnitudes from the models at multiple moments in time to create the stellar luminosity function. This synthetic population of stars shows the M-dwarf gap as an indent into the blueward edge of the MS as well as an overabundance of stars at slightly brighter magnitudes where the models overlap. This results in a feature consisting of a small peak and dip in the luminosity function near $M_{\mathrm{V}} \approx 10.20$.

The width of the MS for a Galactic-field composite population decreases over time, as well as the difference in width of the MS from stars with masses higher and lower than the instability. The parallel offset and relative angle between the upper and lower MS for a single-age star cluster changes with time. This may be used to estimate the ages of stellar populations. Due to the large width of the lower MS, the position of a star in the CMD with known metallicity and mass may also be used to estimate the age of the star if the mass is close to but lower than the convective kissing instability. Furthermore, the width of the lower MS also correlates to a time dependence in the mass–magnitude relation and its derivative.

Finally, a consideration for future study is to investigate different mixing lengths and rotation. Rotation can drive strong mixing of material within stars, and M-dwarfs have been observed to rotate quickly at the young ages, and thus an investigation into rotation would also be beneficial for further study.

ACKNOWLEDGEMENTS

We thank the referee for the detailed and thoughtful comments.

DATA AVAILABILITY

The data sets were derived from MESA which is in the public domain: https://docs.mesastar.org/

REFERENCES

Allard F., Hauschildt P. H., 1995, ApJ, 445, 433
Allard F., Hauschildt P. H., Alexander D. R., Starrfield S., 1997, ARA&A, 35, 137
Baraffe I., Chabrier G., 2018, A&A, 619, A177
Boudreaux T. M., Chaboyer B. C., 2023, ApJ, 944, 129
Brandner W., Calissendorff P., Kopytova T., 2022, MNRAS, 518, 662
Cantiello M., Langer N., 2010, A&A, 521, A9
Cassisi S., Potekhin A. Y., Pietrinferni A., Catelan M., Salaris M., 2007, ApJ, 661, 1094
Chabrier G., Baraffe I., 1997, A&A, 327, 1039
Charbonnel C., Zahn J.-P., 2007, A&A, 467, L15
Chugunov A. I., Dewitt H. E., Yakovlev D. G., 2007, Phys. Rev. D, 76, 025028
Claret A., 2007, A&A, 475, 1019
Code A. D., Davis J., Bless R. C., Brown R. H., 1976, ApJ, 203, 417
Cyburt R. H. et al., 2010, ApJS, 189, 240
Feiden G. A., Skidmore K., Jao W.-C., 2021, ApJ, 907, 53
Ferguson J. W., Alexander D. R., Allard F., Barman T., Bodnarik J. G., Hauschildt P. H., Heffner-Wong A., Tamanai A., 2005, ApJ, 623, 585
Fuller G. M., Fowler W. A., Newman M. J., 1985, ApJ, 293, 1
Gaia Collaboration 2021, A&A, 649, A6
Grevesse N., Sauval A. J., 1998, Space Sci. Rev., 85, 161
Hauschildt P. H., Allard F., Baron E., 1999, ApJ, 512, 377
Herwig F., 2000, A&A, 360, 952
Houdashelt M. L., Bell R. A., Sweigart A. V., 2000, ApJ, 119, 1448
Iglesias C. A., Rogers F. J., 1993, ApJ, 412, 752
Iglesias C. A., Rogers F. J., 1996, ApJ, 464, 943
Irwin A., 2004, http://freeeos.sourceforge.net, Accessed June 2022
Itoh N., Hayashi H., Nishikawa A., Kohyama Y., 1996, ApJS, 102, 411
Jao W.-C., Feiden G. A., 2020, ApJ, 160, 102
Jao W.-C., Henry T. J., Gies D. R., Hambly N. C., 2018, ApJ, 861, L11
Jordi C. et al., 2010, A&A, 523, A48
Kroupa P., 2001, MNRAS, 322, 231
Kroupa P., Tout C. A., 1997, MNRAS, 287, 402
Kroupa P., Tout C. A., Gilmore G., 1990, MNRAS, 244, 76
Kroupa P., Weidner C., Pflamm-Altenburg J., Thies I., Dabringhausen J., Marks M., Maschberger T., 2013, in Oswalt T. D., Gilmore G., eds, Planets, Stars and Stellar Systems. Volume 5: Galactic Structure and Stellar Populations, Vol. 5. Springer Netherlands Dordrechtp. 115–242
Langanke K., Martínez-Pinedo G., 2000, Nucl. Phys. A., 673, 481
Ledoux P., 1947, ApJ, 105, 305
MacDonald J., Gizis J., 2018, MNRAS, 480, 1711
Mansfield S., Kroupa P., 2021, A&A, 650, A184
Oda T., Hino M., Muto K., Takahara M., Sato K., 1994, At. Data Nucl. Data Tables, 56, 231
Ostrowski J., Baran A. S., Sanjayan S., Sahoo S. K., 2020, MNRAS, 503, 4646

Paxton B., Bildsten L., Dotter A., Herwig F., Lesaffre P., Timmes F., 2011, ApJS, 192, 3
Paxton B. et al., 2013, ApJS, 208, 4
Paxton B. et al., 2015, ApJS, 220, 15
Paxton B. et al., 2018, ApJS, 234, 34
Paxton B. et al., 2019, ApJS, 243, 10
Potekhin A. Y., Chabrier G., 2010, Contrib. Plasma Phys., 50, 82
Rajpurohit A. S., Reyle C., Allard F., Homeier D., Schultheis M., M. Bessell, , A. Robin, , 2013, A&A, 556, A15
Rogers F. J., Nayfonov A., 2002, ApJ, 576, 1064
Saumon D., Chabrier G., van Horn H. M., 1995, ApJS, 99, 713
Schwarzschild M., Härm R., 1958, ApJ, 128, 348
Timmes F. X., Swesty F. D., 2000, ApJS, 126, 501
van Saders J., Pinsonneault M., 2012, ApJ, 751, 98
Veyette M. J., Muirhead P. S., Mann A. W., Allard F., 2016, ApJ, 828, 95
Wielen R., 1974, Highlights Astron., 3, 395

This paper has been typeset from a TEX/LATEX file prepared by the author.